Diagnostics of evolving planetary nebulae: observation and simulation of atomic and molecular emission lines

Author:

Alexander Martin Jones

Principal Supervisor:

Dr T. M. Gledhill

Centre for Astrophysics Research

School of Physics, Astronomy and Mathematics

University of Hertfordshire

Submitted to the University of Hertfordshire in partial fulfilment of the requirements of the degree of Doctor of Philosophy.

October 2020

Abstract

Planetary nebulae (PNe) are the glowing, gaseous remnants of low to intermediate mass stars. As light from the star passes through the layers of gas and dust, a distinct spectrum is produced, with a variety of emission, absorption and continuum features. This means that a large number of physical properties can be inferred from a single spectroscopic observation. This thesis concentrates on the properties of evolving PNe which are bright in the 1-0 S(1) emission line of molecular hydrogen (H_2), observed by the UWISH2 survey.

The first part of this thesis is the reduction and analysis of K-band spectra of 29 true and candidate PNe from this survey. The Brγ line is identified in all but two objects, signifying the presence of H^+. 13 candidate PNe have spectra with the Brγ line, but show no signs of Hα emission in optical surveys, confirming the need for infrared observations to reveal PNe obscured by dust in the Galactic Plane. Ratios of fluxes of H_2 and hydrogen recombination lines are used to link the dominant H_2 excitation mechanism with PN morphology and evolution. In line with previous results, we find that UV-fluorescence plays a greater role in W-BPNe (bipolar PNe with pinched waists), while R-BPNe (bipolar PNe with ring structures) are predominantly thermally excited. Using the relative spatial extents of H$_{II}$ and H_2 emission, which act as a proxy for evolution, we find that W-BPNe are likely to be younger objects, while the R-BPNe are more evolved.

The second part focusses on Abell 53 - a little-studied PN consisting of a bright ring of H$_{II}$ and H_2 emission. Multi-wavelength observations are obtained, including photometry from the near-UV to radio, along with optical and near-IR long-slit spectra. After correcting for extinction, these observations are used to conduct a detailed analysis in order to determine the properties of Abell 53, including gas temperature and density, along with physical dimensions of radius and distance. The photoionisation code Cloudy is used with the Markov-Chain Monte Carlo (MCMC) optimisation procedure in order to find a best-fit set of parameters to describe the optical observations. A good fit is found using a star approximated by a blackbody with an effective temperature and luminosity of 104 kK and 400 $L_\odot$ respectively, surrounded by a spherical shell spanning from 0.09 to 0.17 pc, with density 830 cm^{-3} and filling factor 0.48. Observed line ratios of H_2 1-0 S(1) to Hα and 2-1 S(1) are reproduced by replacing the outer portion of the previous shell with a higher-density region of ~ 15000 cm^{-3}, thickness 0.010 pc and a constant temperature of 2100 K.

The third part uses a sequence of photoionisation models, such as the one used for Abell 53, in order to replicate H_2 emission from an evolving PN. Each model in the sequence represents a PN at a particular evolutionary stage, defined by parameters describing the incident radiation field, expansion and density. Using values representative of a typical PN, Hα surface brightnesses were obtained, comparable to observations and hydrodynamical models, leading us to

believe that this method is reliable. The downside of using a sequence of static models, rather than a time-dependent radiation-hydrodynamic model, is that the timescales over which certain reactions take place must not exceed the time intervals between successive models. In order to try to match the surface brightnesses in the UWISH2 survey, constant density models were developed with densities up to the highest observed in knots in PNe. We paid special attention to the reaction rates of H_2 formation on grain surfaces, and total H_2 destruction, which are highly dependent on density. Unless the density is at the highest end of possibilities, the timescales required to reform H_2 on grains is much longer than the intervals between successive models, meaning that the CS flux changes before the models have time to react to the changes. The H_2 surface brightness for the 10^7 cm^{-3} density model while on the cooling track are of the same order as those in the UWISH2 survey, and so it is likely that this emission is compatible with emission from dense knots.

Declaration

I declare that no part of this work is being submitted concurrently for another award of the University or any other awarding body or institution. This thesis contains a substantial body of work that has not previously been submitted successfully for an award of the University or any other awarding body or institution.

The following parts of this submission have been published previously and/or undertaken as part of a previous degree or research programme:

1. Chapter 1: some sections are taken from the introduction of my published paper: Jones, A.M., Gledhill, T.M., Froebrich, D., et al., 2018. MNRAS, 480(2):1563

2. Chapter 2: the majority of this chapter is published as Jones, A.M., Gledhill, T.M., Froebrich, D., et al., 2018. MNRAS, 480(2):1563

Except where indicated otherwise in the submission, the submission is my own work and has not previously been submitted successfully for any award.

Acknowledgements

My biggest thanks go to my supervisor Tim Gledhill, whose support and encouragement have been invaluable throughout the course of this PhD. He has been an incredible teacher and mentor, and I could not have completed this thesis without his constant guidance. Conversations with Janet Drew and Maria Monguió have helped me understand techniques such as aperture photometry and extinction corrections, while meetings with Jim Dale offered an insight into the workings of photoionisation models. I am grateful to Dirk Froebrich and Michael Smith, who, along with Tim, obtained the original observations that set this project into motion. I'd also like to thank Martin Hardcastle, for allowing me access to his parallel versions of the Markov Chain Monte Carlo fitting procedures. Finally, a big thank you to my fellow postgraduate students, for enduring my countless Python questions and for sharing thoughts, coffees, and pints.

Contents

List of Figures

List of Tables

List of Acronyms

2MASS   2 Micron All Sky Survey

AGB   Asymptotic Giant Branch

CCD   Charge-Coupled Device

CS/CSPN   Central Star of a **PN**

FITS   Flexible Image Transport System

FWHM   Full Width at Half Maximum

(G)ISW   (Generalised) Interacting Stellar Wind model

GLIMPSE   Galactic Legacy Infrared Mid-Plane Survey Extraordinaire

HR   Hertzsprung-Russell diagram

INT   Isaac Newton Telescope

IPHAS   INT Photometric H-Alpha Survey

IRAC   InfraRed Array Camera

IRAF   Image Reduction and Analysis Facility

IRAS   InfraRed Astronomical Satellite

ISIS   Intermediate-dispersion Spectrograph and Imaging System

ISM   Inter-Stellar Medium

LIRIS   Long-slit Intermediate Resolution Infrared Spectrograph

LIS   Low-Ionisation Structure

LSST   Large Synoptic Survey Telescope

MASH   Macquarie/AAO/Strasbourg Hα planetary nebulae catalogue

MCMC   Markov-Chain Monte Carlo method

MIPS   Multi-Band Imaging Photometer for Spitzer

NGC   New General Catalogue of Nebulae and Clusters of Stars

PAH   Polycyclic Aromatic Hydrocarbons

Pan-STARRS   Panoramic Survey Telescope And Rapid Response System

PDR	**P**hoto**D**issociation **R**egion
PN/PNe	**P**lanetary **N**ebula/**N**ebulae
PPN	**P**roto-**P**lanetary **N**ebula
PS1	**P**an-**STARRS1** data archive
PSF	**P**oint **S**pread **F**unction
SB	**S**urface **B**rightness
SED	**S**pectral **E**nergy **D**istribution
SHS	**S**uperCOSMOS **H**α **S**urvey
SNR	**S**ignal to **N**oise **R**atio
UKIDSS GPS	**UK**IRT **I**nfrared **D**eep **S**ky **S**urvey **G**alactic **P**lane **S**urvey
UKIRT	**U**nited **K**ingdom **I**nfra-**R**ed **T**elescope
UVEX	**U**ltra**V**iolet **EX**cess Survey
UWISH2	**U**KIRT **W**idefield **I**nfrared **S**urvey for **H**$_2$
VLA	**V**ery **L**arge **A**rray
WFCAM	**W**ide-**F**ield **CAM**era
WHT	**W**illiam **H**erschel **T**elescope
WISE	**W**ide-field **I**nfrared **S**urvey **E**xplorer
YSO	**Y**oung **S**tellar **O**bject
ZAMS	**Z**ero **A**ge **M**ain **S**equence

Chapter 1

Introduction

1.1   Observing planetary nebulae

A planetary nebula (PNe plural, or PN singular) is an expanding gaseous shell, formed from the material released during periods of heavy mass loss on the asymptotic giant branch (AGB) phase of stellar evolution. UV radiation from the star responsible for the PN (central star, or CS) excites and ionises the gaseous material, creating strong emission lines in the optical and infrared. PNe are the penultimate stage of evolution for low to intermediate mass stars ($0.8\,M_\odot$ to $8\,M_\odot$). Shklovsky (1956) was the first to propose that PNe were the result of stars at the end of their lives, rather than the beginning, as previously thought. Evidence of ionisation, in the form of recombination lines of hydrogen or helium, and collisionally excited lines of heavier elements such as oxygen, nitrogen and sulphur, are required to formally classify an object as a PN. Collisionally-excited lines are important in PNe due to the low electron densities (10^0-10^5 per cm^3). Other observational constraints include evidence of free-free emission at radio wavelengths, and emission from cool dust at $\sim 30\,\mu$m, and polycyclic aromatic hydrocarbons (PAHs) at $\sim 8\,\mu$m. PNe usually have radii < 1.5 pc, however young PNe will have typical radii < 0.05 pc (Frew and Parker, 2010). They have lifetimes of the order 10^4 years, before fading away back into the ISM. Over 90% of evolved stars will result in a PN phase (Zijlstra, 2015). PNe are very important as a means of chemical enrichment of the Milky Way. During the red and asymptotic giant branch phases, elements such as carbon are synthesised, and recycled back into the ISM during the PN phase (Bensby and Feltzing, 2006).

1.1.1 A brief history of PN observation

The complex structures and symmetries of PNe make them some of the most fascinating objects in the Milky Way to observe. The first accidental discovery of a PN occurred in 1764, while Charles Messier was searching for comets. Objects that clearly did not resemble comets, being too diffuse and not appearing to move across the sky, were compiled into the famous Messier Catalogue (Messier, 1781), with objects such as the Orion Nebula (Messier 42, or M 42) still using that same naming convention. The source Messier had in fact discovered would later be known as the Dumbbell Nebula (M 27); an optical three-colour image of which is shown in Figure 1.1.
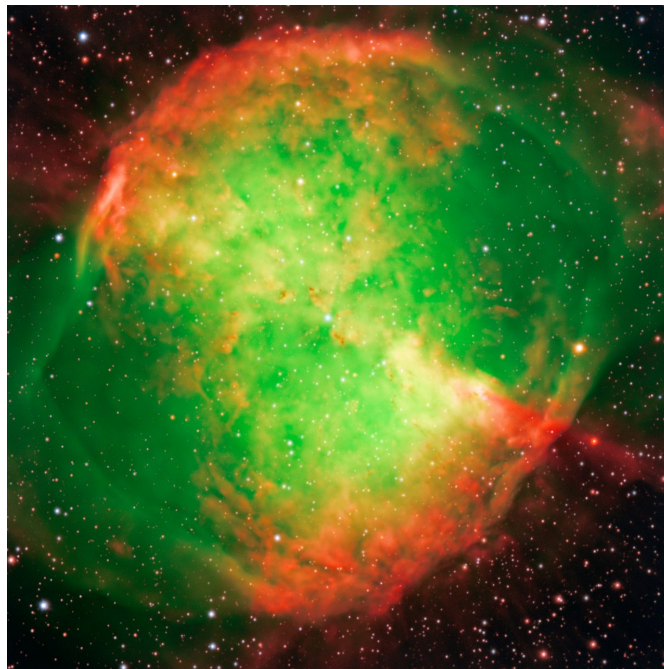
FIGURE 1.1: VLT three-colour image of M 27 (the Dumbbell Nebula). The three colours come from a wide-band blue filter, along with two interference filters at emission lines of doubly-ionised oxygen (green) and ionised hydrogen (red). Source: `https://www.eso.org/public/images/eso9846a/`

It would not be until 1864 that the true nature of the PN was revealed, when William Huggins created the first spectrum of a PN - NGC 6543. It was found that light from the source, rather than being continuous, as would be expected from a group of stars, was actually concentrated at a specific wavelength, corresponding to an emission line from a gaseous nebula being heated by an external energy source. While observing reflection nebulae, Hubble (1922) suggested that the source of their energy could be from nearby stars; he found that the area of light a nebula reflects is proportional to the apparent magnitude of the star. This principle would then be applied to PNe, with the central star acting as the energy source. Menzel (1926) theorised

that the central star must be hot, in order to generate a high flux of Lyman-continuum photons which can ionise the nebula. A considerable puzzle was solved in 1927, when the mysterious source of certain emission lines in Huggins' spectrum of NGC 6543 were finally identified. Rather than originating from a proposed new element 'Nebulium', they were actually the result of 'forbidden' transitions of ionised nitrogen and oxygen (Bowen, 1928). They were known as 'forbidden' transitions as they would violate normal selection rules, and not be observed under the experimental conditions that could be re-created on Earth.

As technology advanced, observations of PNe improved significantly, from X-ray to radio wavelengths. One of the most powerful tools available is integral field unit (IFU) spectroscopy, allowing simultaneous high-resolution imaging of PNe at multiple wavelengths (e.g. NGC 7293: Matsuura et al. 2007; IC 2501, Hen-2-7 and PB 4: Ali and Dopita 2019). The dusty molecular envelopes of the youngest PNe can be probed with radio interferometry (e.g. IRAS 15103–5754; Gómez et al. 2018). Sub-arcsecond angular resolutions are now possible (e.g. NGC 2346; Manchado et al. 2015), and will continue to improve. The launch of the James Webb Space Telescope (JWST), with its high angular-resolution and high-sensitivity at near and mid-IR wavelengths, will allow many issues to be addressed, from searching for binary companions and disks around central stars, to revealing the smallest structures in evolving post-AGB stars (Sahai, 2020).

1.1.2 Surveys

There are currently over 3000 PNe known in the Milky Way (Parker et al., 2016); knowledge of their number plays a crucial role in galaxy simulations. Many of them were discovered by Hα emission surveys, including the SuperCOSMOS Hα Survey (SHS; Parker et al. 2005), which provided the objects that make up the Macquarie/AAO/Strasbourg Hα (MASH) catalogues (Parker et al. 2006; Miszalski et al. 2008), and the INT Photometric Hα Survey of the Northern Galactic Plane (IPHAS; Drew et al. 2005)[1]. However it is likely that many PNe are yet to be discovered, obscured by dust in the Galactic Plane. It is therefore necessary to switch to infrared instruments, such as Spitzer and WISE; the lower ISM dust extinction at infrared wavelengths means that a variety of new objects can be observed (e.g. Cohen et al. 2011; Parker et al. 2012). This was one of the motivations behind the UWISH2 survey (see Sect 1.1.4.1), results from which form the backbone behind this thesis.

---

[1] Data for all of these PNe are available on the University of Hong Kong/Australian Astronomical Observatory/Strasbourg Observatory Hα Planetary Nebula (HASH PN) database, at `http://hashpn.space`; an interactive catalogue of imaging, spectroscopic and other observational data (Parker et al., 2016).

1.1.3   Separating PNe from imposters

There are many astronomical objects with properties similar to PNe, such as HII regions, reflection nebulae, supernova remnants, symbiotic stars, cataclysmic variables and young stellar objects. Frew and Parker (2010) gives a good review of the various observational methods that have been developed to attempt to separate the true PNe from these so called imposters. Optical emission lines are a commonly used tool (e.g. Sabin et al. 2014), where photoionised and shocked regions occupy distinct areas of the [NII] / Hα vs [SII] / Hα plane. Ratios of other optical lines, including [OIII] lines to Hβ and HeII (4686 Å) are also used. Other indicators of a PN include the detection of an obvious central star, a typical morphology often showing a degree of symmetry, the presence of a clear ionised structure, and consistent near and mid-IR colours. Cohen et al. (2011) used IRAC mid-IR colours to help separate PNe from other sources, and Gledhill et al. (2018) adapted this method for objects in the UWISH2 survey (see next section). IRAC colours are particularly useful for distinguishing PNe from ultra compact (UCHIIs) and diffuse HII regions. This is because deep 10 μm silicate absorption features are present in UCHIIs but not in diffuse regions. Also, the ratio of the 6.2 μm and 7.7 μm PAH features is greater in HII than in PNe (Cohen et al., 1989).

1.1.4   H$_2$ in PNe

The first detection of H$_2$ in a PN was in NGC 7027 (Treffers et al., 1976), whose spectra revealed a weak emission line at 2.122 μm, corresponding to the 1-0 S(1) transition (see Sect. 1.4 for more details). They surmised that for H$_2$ to be detected in the PN, it must either be located in dense shielded regions inside the nebula, or outside the ionised region, preventing the molecules from dissociating. Ever since, many more PNe have been shown to have H$_2$ emission, by observing not only the 1-0 S(1) line, but other ro-vibrational transitions at infrared and ultraviolet wavelengths. Notable examples include the Helix nebula (e.g. Matsuura et al. 2009; Meixner et al. 2005) and the Ring nebula (Speck et al., 2003), both of which have been observed to contain dense cometary knots of H$_2$ emission scattered throughout the nebula. H$_2$ has been observed in low ionisation structures (LISs); these are small, localised regions in PNe located far from the centre, and characterised by more prominent emission of low-ionisation lines, such as those of [NII], [OII], [OI] and [SII] (e.g. Akras et al. 2017; Akras et al. 2020). However H$_2$ has been detected in the centres of nebulae (e.g. Luhman and Rieke 1996) and in clumps and

filaments in the equatorial regions of bipolar PNe (Marquez-Lugo et al., 2013). Models have shown that H_2 emission can originate from the ionised region (Aleman and Gruenwald, 2011).

H_2 is therefore an excellent tracer of the morphology of PNe, and many studies have been conducted to investigate relationships between morphology and H_2 emission. For example, there is strong observational evidence that bipolar PNe (BPNe), that have higher mass central stars which reach higher temperatures, have brighter H_2 emission; this is known as Gatley's Rule (Zuckerman and Gatley 1988; Kastner et al. 1994). However, H_2 can also be detected in ellipsoidal or barrel-like PNe (Marquez-Lugo et al., 2013). Bipolar PNe can be further divided into those showing broad, ring-like features (R-BPNe) and those with narrow waists or compact centres (W-BPNe) (Manchado et al., 1996). The nature of this divide is uncertain - they may form an evolutionary sequence, or originate from different progenitor populations (Guerrero et al., 2000).

The K-band (2 - 2.4 μm) lies in the near-infrared region of the electromagnetic spectrum, and is home to a wide range of ro-vibrational lines of H_2, including the 1-0 S(1) (2.1218 μm) and 2-1 S(1) (2.2477 μm) lines. Ratios of these lines can indicate the mechanisms responsible for the excitation of the H_2 (Black and Dalgarno, 1976). Also in this waveband lie recombination lines of hydrogen and helium. The detection of the Brγ H recombination line at 2.1661 μm signifies that the CSPN has begun to photoionise its environment, however this line can also be produced in shocks. Imaging of H_2 and H recombination lines is a powerful tool for studying the evolution of PNe, especially in the transition from proto-planetary nebulae (PPNe) to PNe (Gledhill and Forde, 2015). During this fast evolutionary phase, the ionisation front begins to break out the central region, while the surrounding material is predominantly molecular. Studies such as these can reveal the changing morphologies and degrees of excitation, providing key evidence for possible formation and evolution mechanisms. The close wavelength proximity of these emission lines makes the K-band particularly advantageous to study both the molecular and ionised components of PNe.

1.1.4.1   The UWISH2 survey

The UKIRT Widefield Infrared Survey for H_2, or UWISH2, was an unbiased Galactic Plane imaging survey of the Milky Way, focussed on the 2.1218 μm H_2 line. This was the first non-targeted H_2 survey of the Milky Way, on a larger scale than anything previously. The purpose of the survey was to both uncover new objects, and complement existing observations of H_2
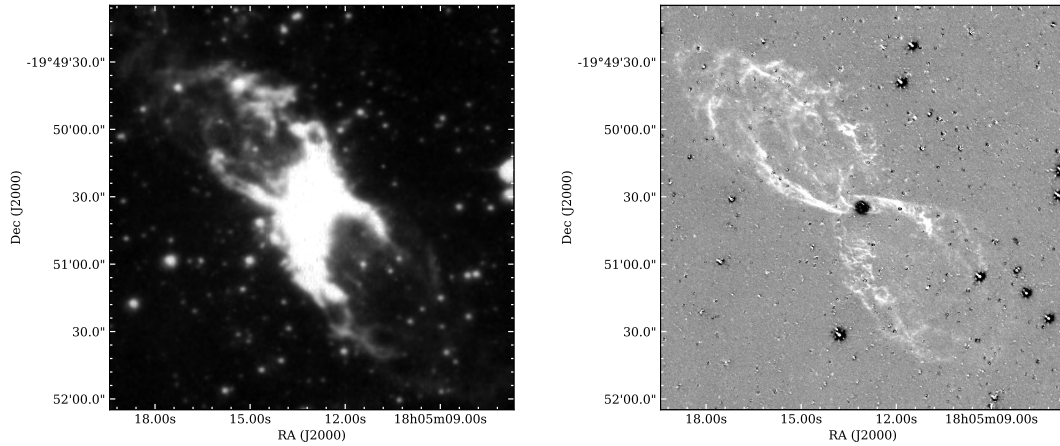
FIGURE 1.2: Images of NGC 6537 in Hα (left) and H$_2$ 1-0 S(1) (right) emission, taken from the IPHAS and UWISH2 surveys respectively.

in star-forming regions, around evolved stars, and in supernova remnants with good spatial resolution. The 2.1218 μm line was chosen as it traces well the hot, dense molecular gas found in these kinds of objects. Observations were carried out from 2009 - 2011, targeting the Northern hemisphere between 357° and 65° longitude, and $|b| < 1.5°$ latitude, with an area of 209 square degrees. Two additional regions were targeted in the Cygnus and Auriga constellations, with areas 42 and 35.5 square degrees respectively. These areas were chosen due to having numerous giant molecular clouds and massive star forming regions.

The observations were taken using the Wide-Field Camera (WFCAM, Casali et al. 2007) on the 3.8m United Kingdom Infrared Telescope (UKIRT), at the Mauna Kea Observatory in Hawaii. The arrays making up WFCAM have a pixel scale of 0.4 arcsec, however a 'micro stepping' procedure was used so the scale in the final tiles is 0.2 arcsec. A custom H$_2$ filter was used, with a central wavelength of 2.122 μm and a width of 0.021 μm. In order to make sure only the H$_2$ flux would contribute to the images, great care was taken to remove the K-band continuum flux, by aligning the K-band images from the UKIRT Infrared Deep Sky Survey of the Galactic plane (UKIDSS GPS: Lawrence et al. 2007; Lucas et al. 2008).

In total, 33200 individual extended H$_2$ features were detected. Of these, 700 were found to be groups of jets and outflows, 284 were individual (candidate) planetary nebulae, 30 were supernova remnants (SNRs) and about 1300 were photo-dissociation regions (PDRs). These classifications were made mainly based on shape and location. For example, isolated, extended, and bright H$_2$ knots located in or near known star forming regions are designated as jets or outflows. Whereas, objects located far from star-forming regions with typical morphologies were classified as candidate PNe, with further observations needed to classify as true PNe. The

classifications were cross-checked through comparison with near-infrared surveys of the same regions, including the UKIDSS GPS survey. The main findings of the survey are described in Froebrich et al. (2015). An example of an image of a PN from the survey, namely NGC 6537, is shown in Figure 1.2, alongside the same view but in Hα emission.
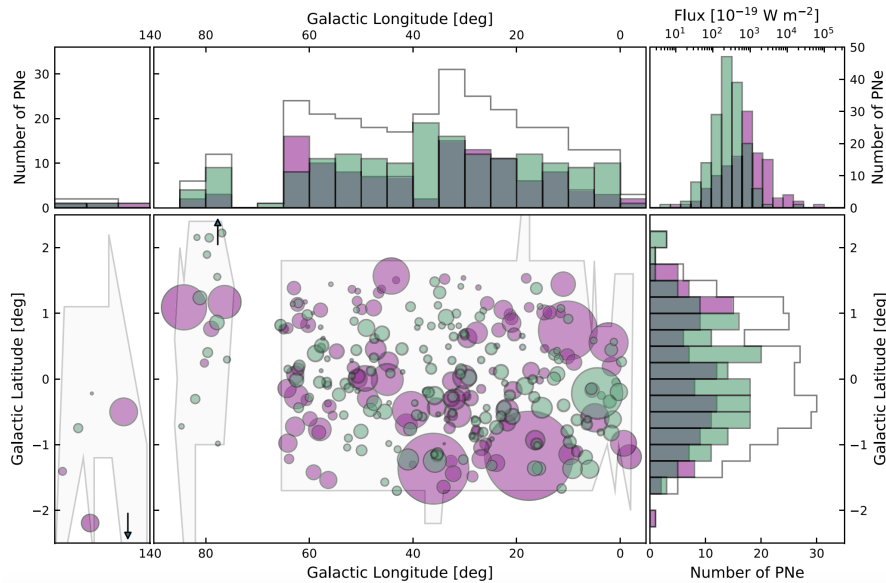
FIGURE 1.3: Figure 4 from Gledhill et al. (2018) showing the distribution of PNe in the UWISH2 field. Objects detected in Hα emission are purple and those not detected are green. The darker green regions correspond to an overlap of the two regions, with the total PN numbers given by the stepped black line. The diameter of the circles is proportional to the area of H$_2$ emission on the sky.

The 284 candidate PNe detected in the survey included those already known to us through optical surveys, in addition to many new discoveries with no known optical counterparts. Gledhill et al. (2018) have since updated this number to 295 candidates. The median surface area of H$_2$ emission for objects with and without Hα detection is 162 and 70 arcsec^2 respectively. The smallest candidate PN has a diameter of 3 arcsec, while the largest has a major axis of 5 arcmin. Figure 1.3, their figure 4, shows the distribution of these PNe in the survey, and whether or not they are also detected in Hα surveys - a primary indicator of the presence of H$^+$.

1.2 The formation and evolution of PNe

The most important factor determining the fate of a star is its mass. Stars with masses <0.8 M$_\odot$ spend the longest time on the main sequence as they slowly burn their supply of fuel. They do not reach sufficient temperatures to ignite helium fusion in their cores, and end their lives as He-rich white dwarfs. The lowest mass stars, known as brown dwarfs (<0.07 M$_\odot$), never
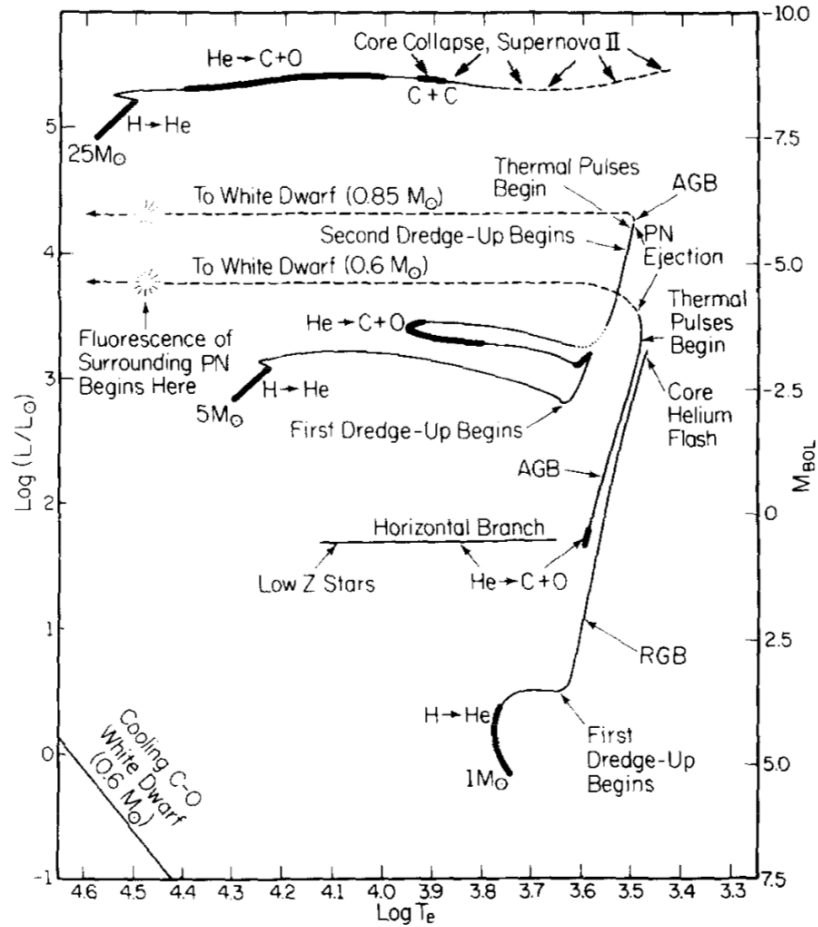
FIGURE 1.4: Hertzsprung-Russell diagram for three stars of initial masses 1, 5 and 8 M$_\odot$, taken from Iben (1995).

manage to fuse hydrogen due to insufficient core temperatures, but instead can fuse deuterium. High mass stars (>8 M$_\odot$) will race though their main sequence stage, burning fuel at massive rates. They end their lives in the most extreme way, exploding as supernovae to leave behind a neutron star or a black hole. It is the stars with masses 0.8 M$_\odot$ <M <8 M$_\odot$ that have a chance of becoming planetary nebulae. Their journey from the main sequence to the white dwarf stage are described in the following sections.

1.2.1   Main sequence

Stars spend the vast majority of their lives on the main sequence (MS) of the Hertzsprung-Russell (HR) diagram. These diagrams typically have temperature, or colour, on their x-axis, and luminosity, or magnitude, on the y-axis, and show how the surface properties of a star of certain mass evolve with age. An example is given in Figure 1.4, where the main sequence is depicted as the initial bold segments of the various tracks shown. In this phase, stars fuse

hydrogen into helium in their cores, generating tremendous amounts of energy. The two methods in which this occurs are the proton-proton (PP) chain, which dominates for stars with solar masses, or the carbon-nitrogen-oxygen (CNO) cycle, which is more important for higher mass stars. The first step for the PP chain involves fusing two hydrogen atoms together to create deuterium, with one of the protons undergoing beta plus decay:

$$H^1 + H^1 \longrightarrow H^2 + e^+ + \nu_e \tag{1.1}$$

This is the slowest step, taking billions of years and limiting the overall timescale of the process. The next step is much faster ($\sim$ seconds) and involves the creation of a helium isotope, He-3:

$$H^2 + H^1 \longrightarrow He^3 + \gamma \tag{1.2}$$

Two He-3 nuclei can then fuse to form a regular helium atom, He-4:

$$\textbf{PP-I} \qquad He^3 + He^3 \longrightarrow He^4 + 2H^1 \tag{1.3}$$

This is known as the PP-I branch, and is the most common among solar-type stars. However, two other PP reactions can occur, known as PP-II and PP-III:

$$
\begin{aligned}
& He^3 + He^4 \longrightarrow Be^7 + \gamma \\
\textbf{PP-II} \qquad & Be^7 + e^- \longrightarrow Li^7 + \nu_e \\
& Li^7 + H^1 \longrightarrow 2He^4
\end{aligned}
\tag{1.4}
$$

$$
\begin{aligned}
& He^3 + He^4 \longrightarrow Be^7 + \gamma \\
\textbf{PP-III} \qquad & Be^7 + H^1 \longrightarrow Bo^8 + \gamma \\
& Bo^8 \longrightarrow Be^8 + e^+ + \nu_e \\
& Be^8 \longrightarrow 2He^4
\end{aligned}
\tag{1.5}
$$
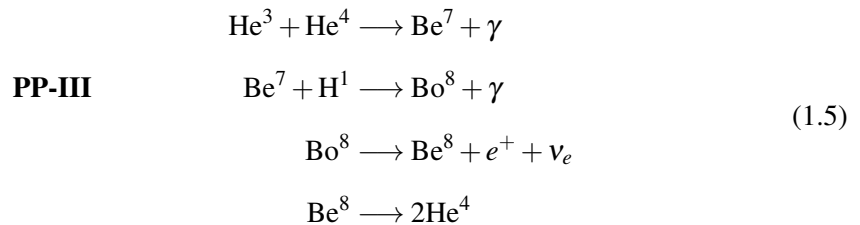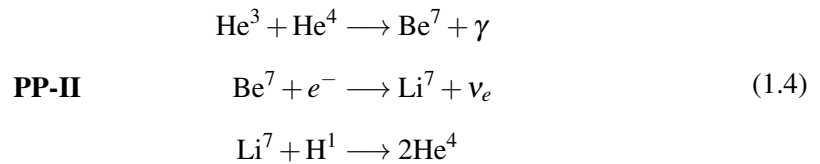
Core temperatures are much higher in stars with masses greater than that of the Sun, at which point the CNO cycle becomes the dominant fusion mechanism, however a small percentage of He-4 is produced in the Sun via this method. The most common branch, CNO-I, requires some carbon to already be present, at which point a cycle of fusions with hydrogen and subsequent decays occur:

$$C^{12} + H^1 \longrightarrow N^{13} + \gamma$$
$$N^{13} \longrightarrow C^{13} + e^+ + \nu_e$$
$$C^{13} + H^1 \longrightarrow N^{14} + \gamma$$
$$N^{14} + H^1 \longrightarrow O^{15} + \gamma \tag{1.6}$$
$$O^{15} \longrightarrow N^{15} + e^+ + \nu_e$$
$$N^{15} + H^1 \longrightarrow C^{12} + He^4$$
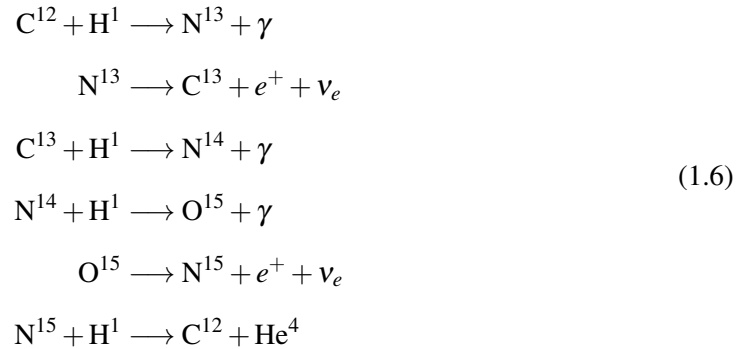
The process is limited by the relatively slow timescale of the proton capture of the N-14 nucleus.

1.2.2   Red giant branch (RGB)

At the end of its main sequence, the star will eventually run out of hydrogen in its core to fuse. At this point, it begins instead to fuse hydrogen in a shell surrounding the now inert helium core, marking the end of the main sequence and the beginning of the red giant phase. Throughout the main sequence, the outward gas and radiation pressure is balanced by the inward force of gravity. Now, as the rate and location of fusion changes, the star is no longer in equilibrium, and the size and temperature of the star can change rapidly. As the core mass increases, the star expands and cools, pushing it towards the right of the HR diagram. However, the luminosity increases significantly, following a particular mass-luminosity relation. The outer layers of the star are convective, which means that products from the CNO cycle now occurring in the burning shell are brought up to the surface. This is known as the first dredge-up. The He core grows and its temperature increases, leading to helium ignition in the core at the tip of the RGB. New elements at the surface of the star provide evidence for operation of the CNO cycle.

1.2.3   Horizontal branch (HB)

Lower mass stars (0.8 $M_\odot$ <M <1.8 $M_\odot$) develop degenerate cores[2] (Herwig, 2005), meaning that the onset of He fusion increases the temperature, which in turn increases the fusion rate, without being able to expand to regulate the temperature. This leads to a thermonuclear runaway, where vast quantities of helium are produced very quickly - known as a helium flash. The mechanism for He-fusion is known as the triple alpha process:

$$He^4 + He^4 \longrightarrow Be^8$$
$$Be^8 + He^4 \longrightarrow C^{12} + 2\gamma \tag{1.7}$$

The helium flash causes the core to expand, reducing the rate of fusion. The star contracts, causing its temperature to increase and its luminosity to decrease. The star reaches a state of equilibrium and sits on the horizontal branch of the HR diagram. For stars with MS masses above $\sim$2.5 $M_\odot$, the core is non-degenerate at the point of He ignition, so they avoid a flash.

1.2.4   Asymptotic giant branch (AGB)

The asymptotic giant branch (AGB) occurs when the star runs out of core helium to burn. At this point, the star will have developed an electron-degenerate carbon-oxygen (C-O) core. A second dredge-up occurs for stars with masses >4 $M_\odot$ (Karakas and Lugaro, 2016). In this early phase of AGB evolution, there is almost no hydrogen burning occurring, which is now located in the outer layers of the star. Instead, helium burning in the shell increases the mass of the C-O core, until the separation between the hydrogen-rich envelope and the electron-degenerate core becomes so small, that hydrogen is reignited. This is the beginning of the thermally pulsing AGB (TPAGB) phase, where shells of hydrogen and helium burn alternately, and further helium flashes can occur in the process. Many dredge-ups (collectively known as the third dredge-up) occur during the TPAGB phase, where material is brought from deep within the star to the surface by the convective envelope, leading to the richness of chemical abundances found in PNe.

---

[2]In degenerate matter, the fermions all occupy high energy states so that the Pauli Exclusion Principle, which states that identical fermions can not occupy the same quantum state within the same system, is obeyed.

Paczyński (1970) was the first to suggest that significant mass loss of the stellar envelope during the AGB phase was necessary to cause the CSPN to evolve to the left of the HR diagram. This is required in order to increase the temperature of the CSPN to a point at which it can ionise the surrounding envelope, while remaining at constant luminosity. The mass is removed in the form of a stellar wind, and the mechanisms for this process can be thought of as either radiative (transfer of momentum from the photons to the gas), coronal (driven by wave energy) or a combination of the two (Cassinelli, 1979). Infrared observations led to the first evidence of this large-scale mass loss (Woolf and Ney, 1969). The dust emission which dominates the flux of these infrared observations was vital in explaining the huge mass loss rates on the AGB. Radiation pressure on dust grains initiates their outward-movement, and momentum transfer from the dust grains to the gas drives the overall outflow, containing both gas and dust.

In order to transform the material ejected from the AGB star into a structure which will eventually become the PN, Kwok suggested the Interacting Stellar Wind model (ISW) (Kwok et al. 1978; Kwok 1982). This model says that the mass loss rate from the stellar envelope greatly increases towards the end of the AGB phase - the superwind. As the envelope mass falls, the photospheric radius of the star decreases, and thus its temperature increases. The mass loss rate drops at this point, but the speed of the wind greatly increases. This new fast wind sweeps up and ploughs into the previously ejected superwind. Subsequent models (termed Generalised Interacting Stellar Wind, or GISW models) introduced additional winds causing a departure from spherical symmetry (e.g. Balick 1987; Frank et al. 1993; Mellema and Frank 1995), matching observations which show that the vast majority of PNe are asymmetric. GISW models have been modified since their creation, but still remain the most accepted evolutionary model. Further improvements using radiation-hydrodynamics models have since been developed in order to explain the increasing level of detail of observations of AGB stars.

1.2.5   Post-AGB to PN

The end of the AGB phase is marked by the complete removal of the hydrogen envelope from the star, while leaving behind a thin hydrogen burning shell. This is the beginning of the proto-planetary nebula (PPN) stage, or more generally the post-AGB phase (van Winckel, 2003). The PPN is an object where the central star rises appreciably in temperature due to the now lost envelope, however is still not hot enough to ionise the surrounding material; the stellar type can range anywhere from M to B type. These are very dusty objects, often obscuring the star, but

are clearly visible in the infrared (Kwok, 1993). One of the first PPNe to be identified, AFGL 2688, is very bright at mid-IR wavelengths due to dust emission (Ney et al., 1975). The mass loss rate is reduced appreciably during this fast phase of evolution, which can be as short as a few hundred years.

PPNe and consequently PNe have a variety of shapes with complex symmetries, the likes of which are determined by the mass loss history on the AGB. One of the leading explanations for observations of axisymmetric PPNe and PNe is the presence of a binary companion to the CS (De Marco, 2009). It has been suggested that shaping through the action of stellar rotation and magnetic fields alone could be sufficient to generate axisymmetric PNe (García-Segura et al., 1999), although it seems difficult for a single star to attain a magnetic field strong enough to significantly affect the shape of the nebula (Soker 2006; Nordhaus et al. 2007). The addition of a binary companion could make this possible. Understanding these transition objects will prove vital for constraining evolutionary models, and may be the key to understanding the shaping mechanisms.

Eventually, the effective temperature of the CSPN will exceed around 25000 K, allowing it to begin ionising the detached envelope. Objects observed to have this ionisation front concentrated at the centre of the nebula are named hot post-AGBs, and so they are just becoming PNe. The ionisation front travels outwards, meaning more material becomes ionised, thus leading to the PN phase. The CS will move to the left of the HR diagram as its surface temperature increases. As the remnant star sheds its outer layers to create the PN, its C-O core becomes exposed, becoming both cooler and less luminous. These white dwarfs exist in the bottom left region of the HR diagram, and will continue to radiate for Gyrs.

1.3 PNe as physical laboratories

The effect of the energy input from the CS on the surrounding gaseous nebula means that PNe harbour a wide range of physical processes. As photoionisation models of PNe will be utilised in Chapters 4 and 5, it is important to understand these processes, as they are the basis of these models. A typical model of a PN will consist of an inner ionised region and an outer PDR signalling the transition from ionised to atomic, and then molecular hydrogen. The physics governing these regions are described in the following sections.

1.3.1 The ionised region

1.3.1.1 Ionisation vs recombination

If a photon with enough energy is absorbed by an atom, an electron within that atom can either be excited to a higher energy level, or removed entirely. The former case is known as photoexcitation, described by a bound-bound transition, while the latter case is called photoionisation, described by a bound-free transition. In a hydrogen atom, the minimum energy required by a photon to remove an electron from the ground state is known as the Lyman limit, and occurs at a wavelength of 912 $\text{\AA}$. Photons with at least this amount of energy, known as Lyman continuum photons, travel only short distances in PNe before being absorbed or scattered by nearby atoms or ions. This sets a limit on the outer radius at which the hydrogen exists in its ionised form - known as the Strömgren radius (Strömgren, 1939).

The photoelectrons removed from the hydrogen atoms will have a range of energies depending on the energy of the incident photon that caused the ionisation. Some of the electrons will recombine with the ionised hydrogen (protons), in a process called recombination. However, they are more likely to interact with themselves, and these collisions give rise to a state of local thermal equilibrium (LTE). The free electrons can be described by a single temperature - the kinetic temperature. After a recombination, the electron can either be found in a higher energy level, where it will quickly drop down the levels until reaching the ground state, or it can directly recombine into the ground level. Case A recombination occurs in optically-thin nebulae, and assumes that all the photons emitted can escape the nebula without further absorption. Case B recombination occurs in optically-thick nebulae, and assumes that the emitted photons are scattered many times, and never manage to escape the nebula. The real scenario will be an intermediate between these two extremes. At a point in the nebula, the balance between the rate at which atoms become ionised and the rate at which the protons and electrons recombine is described by the ionisation equilibrium equation (Osterbrock and Ferland, 2006):

$$n(\text{H}^0) \int_{\nu_0}^{\infty} \frac{4\pi J_\nu}{h\nu} a_\nu(\text{H}^0) d\nu = n_e n_p \alpha(\text{H}^0, T) \ [\text{cm}^{-3}\text{s}^{-1}] \tag{1.8}$$

where $n(\text{H}^0)$, n_e and n_p are the atomic hydrogen, electron and proton number densities, J_ν is the mean intensity of radiation at that location, h is Planck's constant, ν is the photon frequency, $a_\nu(\text{H}^0)$ is the ionisation cross section for H^0 and $\alpha(\text{H}^0, T)$ is the recombination coefficient of H^0.

In the ionised regions of PNe, it is the rate of ionisation (LHS) that dominates. The temperature of a PN is controlled by heating and cooling mechanisms. The main heating source is that due to the energy of the photoelectrons produced via ionisation, while recombination is a type of cooling mechanism, removing thermal electrons from the plasma and radiating away their energy as photons.

1.3.1.2 Line and continuum radiation
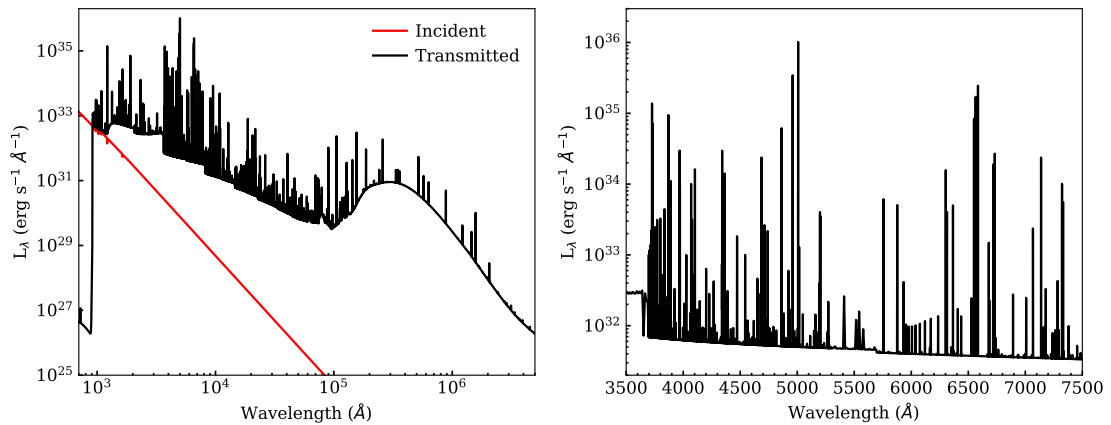
FIGURE 1.5: Left: The SED transmitted from a basic PN simulation using the photoionisation code Cloudy (see Sect. 4.1) in black, with the incident CS field in red. Notable features include the 2γ continuum in the near-UV, the 30 μm bump due to dust emission, the Balmer jump at 3650 Å, and a range of RLs and CELs in the optical. Right: A zoom-in on the optical region (3500 - 7500 Å).

The spectra of gaseous nebulae such as PNe are rich in emission lines (bound-bound transitions), and are categorised as either recombination lines (RLs) or collisionally excited lines (CELs). RLs are produced when a free electron combines with an ion, while CELs are the result of a collision with a free electron. Both result in an electron being found in a higher energy level, which then cascades down the levels, producing photons. RLs are permitted lines, meaning they follow quantum mechanical selection rules, and have a high probability of occurring. Hydrogen has many RLs, for example Hα at 6563Å, which is used in many surveys as an indicator of H^+. CELs, also called forbidden lines, obey the same electric dipole selection rules as any other transition, except that those selection rules result in the transition probability being extremely low compared with "permitted" transitions. In terrestrial conditions, the atom would collide with a species and collisionally de-excite before it had chance to radiate, whereas in extreme low density environments, such as those found in PNe, it can stay in the excited state long enough to see the radiative transition. Common CELs found in PNe include [OIII] $\lambda 5007$ and [NII] $\lambda 6584$. As the excitation potentials of metal ions such as these are much lower than those

of hydrogen and helium, the strength of CELs are often greater than those of RLs, and are therefore responsible for most of the cooling in PNe.

While bound-bound transitions produce most of the observed emission lines, free-bound radiation in the optical region, and free-free emission at infrared and radio wavelengths contribute largely to the continua of PNe. Free-bound emission occurs when an electron recombines with a proton into a higher-energy state, releasing a photon. As the free electrons can have a range of energies, so too can the energies of the emitted photons, thus producing a continuum of possibilities. The Balmer jump (3646 $\mathring{A}$) is a notable feature of optical PN continua; at wavelengths greater than this, the energy is too low for a free electron to recombine directly into the $n = 2$ energy level. Similar jumps in the continuum exist for other ground energy levels. Free-free emission, or Bremsstrahlung radiation, occurs when an electron passes near an ion, causing it to decelerate; the reduction of its kinetic energy is emitted as a photon. The range of possible kinetic energies of the electrons, and varying distance between them and the ion, means that the resultant energy distribution is a continuum, mostly in the radio region. As the radiation from free-free emission and recombination lines both originate in the ionised region, comparison of observed radio fluxes and optical Balmer lines to theoretical values can be used to estimate extinction to PNe (see Sect. 3.2.3.2). In addition to free-free and free-bound emission, another contributor to the SED of a PN is two photon radiation. In low density environments, an electron can be found in a virtual energy state between the $n = 2$ and $n = 1$ levels of the H atom. De-excitation from this state into the ground state leads to the emission of 2 photons, whose total energy must match that of a single Lyman-α photon (1215 $\mathring{A}$), however the individual energies can be a range of values, leading to a continuum.

In Figure 1.5, the SED from a basic simulation of a PN using the photoionisation code Cloudy (Ferland et al., 2017) is given, and displays some of the contributions to the total energy output of a PN. This includes bound-bound transitions, in the form of emission lines, and the underlying continuous emission (from bound-free, free-free and 2-photon transitions).

1.3.2 The neutral region

Moving radially outwards in the nebula, the number of ionising photons decrease, and so does the nebula temperature. The point at which the temperature drops to a few 1000s of K typically marks the end of the ionised region, and the beginning of the photodissociation region, or PDR. A PDR is the transition region into a molecular envelope, consisting mainly of atomic gas (such

as H, C and O) but also molecules such as H_2 and CO, and larger dust grains including silicates and graphites. Unlike the ionised region, whose chemistry is controlled by the Lyman continuum photons, the chemistry in the PDR is dominated by FUV (far ultraviolet) photons (<13.6 eV), which are absorbed by gas and dust grains. At the inner edge of the PDR, the FUV photons dissociate the molecules to neutral and singly ionised atoms (e.g. H^0, C^+, O^+). At larger radii, hydrogen atoms/ions can combine to form H_2, and further away, CO will form.

1.3.2.1 Thermal balance

The thermal equilibrium of the PDR is balanced by heating and cooling mechanisms. One of the most important heating mechanisms is grain photoelectric heating. This involves dust grains, including polycyclic aromatic hydrocarbons (PAHs), absorbing FUV photons and in turn creating energetic electrons, which given enough energy, can escape and add their excess kinetic energy to the gas. This process is much more efficient for smaller grain sizes. H_2 has an important role in heating the surrounding gas. FUV dissociation releases thermal electrons, while collisional de-excitation of vibrationally excited H_2 and formation of H_2 molecules on dust grains both add energy to the system. Many soft X-rays (>100 eV) can escape the H^+ region and penetrate into the PDR, where they ionise atoms and molecules. Other mechanisms include the photoionisation of C, gas-grain collisions and the dissipation of turbulence.

Cooling mechanisms remove energy from the nebula in the form of photons, which we observe as an SED. Some of the strongest emission lines observed include the ro-vibrational transitions of H_2, far-infrared fine-structure lines[3] (e.g. [CII] 158μm, [OI] 65μm, [CI] 609 μm), molecular rotational lines from species such as CO, OH and H_2O, various forbidden lines (e.g. [FeII] 1.26 and 1.64 μm, [OI] 6300 Å) and grain cooling of the gas.

1.3.2.2 Dust

Since dust was first observed in a PN (Gillett et al., 1967), many PNe have appeared in mid and far infrared surveys (e.g. IRAC, IRAS, WISE) where both line and continuum emission is present. Continuum emission radiated from dust grains can be approximated by Wien's law, which says that the position of the peak of a blackbody (λ_{max}) depends only on its temperature:

---

[3]These are produced though the splitting of spectral lines due to electron spin.

$$\lambda_{max} T = 0.0029 \ \text{m} \cdot \text{K} \tag{1.9}$$

Emission from dust at 100 K would peak at roughly 30 μm; a feature commonly observed in the SED of PNe, known as the 30 μm bump, and is present in simulations (see Figure 1.5). Dust grains are categorised as either graphites (carbon chemistry) or silicates (silicon chemistry), and form as atoms condense out of the gas at temperature $\sim$ 1400 K. PAH molecules are organic compounds consisting of rings of atoms, and are commonly observed in PNe (e.g. Otsuka et al. 2014).

1.3.3 Shocks

The motions of gases in the AGB and PN phases are governed by the laws of fluid dynamics. A supersonic flow is one in which the speed of the flow exceeds the local sound speed of the medium. As a supersonic flow travels towards a slower moving fluid, there is not enough time for information describing the flow to reach the fluid. On impact, the gas is compressed, heated and accelerated, setting up a strong discontinuity in quantities such as density, velocity and temperature. This phenomenon, known as a shock, can thermally excite any H_2 molecules present (see Sect. 1.4.2). Shock waves can arise around stars at the beginning and end of their lives. In post-AGB stars, a shock front is set up where the fast stellar wind ploughs into the slower AGB wind. Much theoretical work has been dedicated to re-creating the physics in shock-waves in proto-PNe/young PNe (e.g. Novikov and Smith 2018). Shocks associated with molecular outflows are usually categorised as either J-type (jump) of C-type (continuous), the latter of which takes into account the additional effects of magnetic fields.

1.4 The H_2 molecule

H_2 is the most abundant molecule in the PDR, and so has a large influence on the chemistry in this region. As observations and simulations of emission lines of H_2 are the main focus of this thesis, it is vital to understand the physics behind this molecule, including how the various molecular transitions arise, along with how it is formed and destroyed.

1.4.1 Physics of the diatomic H_2 molecule

The energy levels of a hydrogen atom, which is simply a proton and electron, are described by a principal quantum number ($n = 1$ to ∞), an orbital angular momentum ($l = 0, 1, 2, 3$, or s, p, d, f), and a spin quantum number of the electron ($s = \pm 1/2$). Using this notation, the first excited states of hydrogen are $1s, 2s$ and $2p$. As the only force in the H atom is the electromagnetic attraction between the proton and electron, the energy difference, ΔE, of an electron transitioning between levels n_i and n_f, which is inversely proportional to the wavelength of the emitted photon, is only dependent on the two quantum numbers. This is known as the Rydberg formula:

$$\frac{\Delta E}{hc} = \frac{1}{\lambda} = R_H \left(\frac{1}{n_f^2} - \frac{1}{n_i^2} \right)$$

(1.10)

where h is Planck's constant, c is the speed of light and R_H is the Rydberg constant. The energy levels of H_2, even being the simplest possible molecule, consisting of two protons and two electrons, are much more complex to describe. This is because there is no longer a single central force acting between a proton and an electron, but instead there are two nuclei, whose relative motions give rise to two additional sets of energy levels: rotational and vibrational. Using the Born-Oppenheimer approximation, which allows the nuclei and electrons to be treated separately[4], and assuming the rotational and vibrational motions of the nuclei can also be treated separated, the total wave function is given by:

$$\psi_{tot} = \psi_{el} \psi_{vib} \psi_{rot}$$

(1.11)

where ψ_{el}, ψ_{vib} and ψ_{rot} are the electronic, vibrational and rotational wave functions respectively. The most energetic motions are the electronic, followed by the vibrational and then the rotational modes. The various electronic states in a diatomic molecule (those formed from two atoms) such as H_2 depends on the separation of the nuclei. At small separations, there are strong repulsive potentials between the two positive nuclei, and between the negative electrons, but more importantly due to exchange interactions between electrons. This is a consequence of the Pauli Exclusion Principle, which prevents the electrons occupying the same space. At large separations, the molecule is pulled apart - called dissociation.

---

[4]This approximation is valid because the mass of the electron is much less than that of the proton (~ 2000 times less), and so the electrons can move much faster relative to the protons.
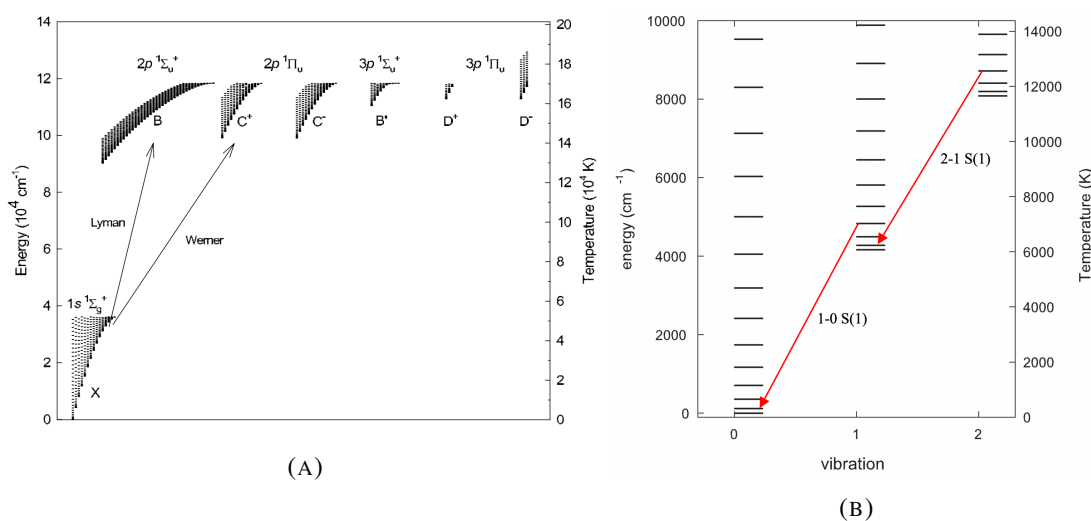
FIGURE 1.6: (A) Energy levels for the first seven electronic states of H_2, with the ground state in the bottom left corner. (B) The first three vibrational levels of the ground state, showing the lowest energy rotational levels. The 1-0 S(1) and 2-1 S(1) transitions are denoted by the red arrows. Both original figures were taken from Shaw et al. (2005) - their figures 1 and 3.

In general, the electronic state of a diatomic molecule (those formed from two atoms) is denoted by $^{2S+1}\Lambda_\Omega$. 2S+1 is called the spin multiplicity, where S is the sum of the individual electron spin angular momenta. As molecules are not spherical, the orbital angular momentum of the electrons is not conserved. However, the total orbital angular momentum along the nuclear axis (that which joins the two nuclei) is conserved. This momentum, denoted Λ, can be positive or negative (doubly degenerate), unless $\Lambda = 0$, in which case it is singly degenerate. $\Lambda = 0$, 1, 2, 3 and 4 are denoted by the Greek letters $\Sigma, \Pi, \Delta, \Phi$ and Γ respectively. Interchanging the two nuclei can result in either a positive or negative solution of the wavefunction, as the two nuclei are identical. This symmetry is denoted by Ω, the projection of the total electronic angular momentum onto the nuclear axis, which is given by 'g' if positive, or 'u' if negative. For Σ states, another symmetry exists when reflecting the molecule through a plane. If the sign of the wavefunction does not changes upon reflection, the state is followed by a '+' superscript; if it does change, a '-' is used. In addition, a letter is placed before the state to help distinguish the levels further. 'X' is the ground state, 'A', 'B', 'C' and 'D' are levels with spin multiplicity identical to the ground state, and 'a', 'b', 'c' and 'd' are levels with spin multiplicity different to the ground state. For example, the ground state of H_2 is denoted $X^1\Sigma_g^+$, and its energy levels are shown in Figure 1.6.

H_2 is a homo-nuclear molecule (consisting of identical atoms) and so has no permanent electric or magnetic dipole moment. Therefore the only observable transitions are electric quadrupole

transitions, with ΔJ, the change in rotational quantum number = -2, 0 and 2 (O, Q and S branches). One of the most commonly observed H_2 lines is v = 1-0 S(1) at 2.122 μm. This designation refers to the fact that it is the transition from the $v = 1$ to $v = 0$ vibrational levels, the S implies a change in rotational quantum number of +2, and the 1 in parentheses is the value of the lower J level (i.e. from $J = 3$ to $J = 1$). This transition, along with 2-1 S(1), is demonstrated in Figure 1.6b.

1.4.2 Thermal vs non-thermal excitation

The two methods of exciting electrons in the H_2 molecule are thermal and non-thermal excitation. In the thermal process, H_2 molecules are collisionally heated to a few thousand degrees (often occurring in shocks), and radiate near-IR photons as they cool (Burton, 1987). In the non-thermal process, a H_2 molecule is excited when it absorbs a UV photon, and quickly decays to a vibrationally-excited level of the electronic ground state. Further decays result in the emission of infrared photons, known as fluorescence (Black and Dalgarno, 1976). A mixture of these processes contribute to the emission lines commonly observed in spectra, especially in the K-band. To produce strong H_2 in a PN, there needs to be hot, molecular gas, heated close to the dissociation temperature of the molecule. Thermal processes populate the H_2 levels from the lowest ($v = 0$) to the highest ($v \geq 2$) states, whereas non-thermal processes populate from the top ($v \geq 3$) down. Therefore, ratios such as the 1-0 S(1) / 2-1 S(1) and 1-0 S(1) / 3-2 S(3) will have typical values depending on the excitation environment. A purely UV pumped spectrum will have a 1-0 S(1) / 2-1 S(1) ratio equal to 1.8 (Black and Dalgarno 1976, Black and van Dishoeck 1987), while in the thermal case, indicative of shocks, this ratio will be at least 10 (Hollenbach and Shull 1977, Burton et al. 1992). However, there is also a density dependence - at densities above $\sim 10^5$ cm^{-3}, the 1-0 S(1) / 2-1 S(1) ratio can begin to resemble that of a shocked gas, even in a fluoresced case (Burton et al., 1990).

1.4.3 Formation and destruction of H_2

In the PDR, there is a cycle in which H_2 is created and destroyed, depending on its environment. H_2 molecules are primarily formed on the surfaces of dust grains, which act as a catalyst allowing the reaction to take place. A H atom will adsorb onto a dust grain, either through van der Waals forces (the physisorbed mechanism, occurring at T $<$100 K) or through chemical bonds (the chemisorbed mechanism, T $>$100 K) (Cazaux and Tielens, 2002). It can then diffuse across

the surface moving to another adsorption site. Here it has the opportunity to react with another H atom either still in the gas phase, or also adsorbed. The newly formed H_2 molecule can then desorp from the grain. This molecule can only survive if it can avoid being bombarded by FUV photons - self and dust shielding can provide this protection. Other methods for forming H_2 include the associative detachment reaction, where a H^- ion combines with a H atom (i.e. $H^- + H^0 \longrightarrow H_2 + e^-$), and charge exchange reactions between H atoms and H_2^+ ions - Aleman and Gruenwald (2004) showed that these are important in PNe.

In PNe, it is not always clear whether H_2 molecules primarily form within the nebula after the onset of ionisation, or whether they formed during the AGB phase, and survive through to the PN phase. In the latter case, the density would need to be high enough for H_2 molecules to form within the atmosphere of the star. After expulsion from the surface, they would then need to be shielded by dust grains in order to prevent dissociation by the intense UV field of the CS. Matsuura et al. (2009) estimated densities and H_2 formation timescales of knots in the Helix nebula, and found they are likely remnants of gas that have survived from the AGB phase.

In the harsh environment of the PDR, there are many ways that a H_2 molecule is destroyed. The primary mechanism is photodissociation, where combination with an FUV photon in the 912 - 1100 Å range (Lyman and Werner transitions) breaks the molecule apart, given by $H_2 + 2\gamma \longrightarrow 2H^+ + 2e^-$. However, H_2 can protect itself from the UV photons in a process known as shielding - either though continuous dust absorption, or absorption by other H_2 molecules. The latter of these processes is known as self-shielding. Other destruction methods include photoionisation; collisional dissociation between H, H_2 and electrons; ionisation induced by soft X-rays and cosmic rays, and reactions with atoms and ions (including O^+, C^+ and O).

1.5   Thesis Outline

This thesis is a combination of three separate pieces of work; the first of which has been published, while there are plans to transform Chapters 3 and 4 into a second paper (Jones and Gledhill (in prep.)). The motivation behind this thesis is the desire to contribute some understanding to the physical processes driving the emission of H_2 in PNe of different morphologies and ages, through observation and modelling. Some questions on which I hope to gain insight include:

1. How effective are K-band observations at helping to identify optically-obscured PNe?

2. How does H_2 emission correlate with PN age and morphology for a sub-sample of PNe?

3. Can a photoionisation model be used to reproduce observations of both the ionised and molecular regions of a particular PN?

4. Can this model be used to determine an evolutionary state, and a possible origin for the H_2 emission?

5. How applicable can a sequence of static models be in modelling the H_2 emission in an evolving PN?

The thesis is organised as follows:

Chapter 2: This chapter describes the analysis of a set of K-band spectroscopic observations of PN candidates from the UWISH2 survey. As many of these objects are optically-obscured by dust in the ISM, attempts are made to confirm or reject the objects as PNe, by searching for the Brγ emission line in their spectra. This line, along with those of H_2, are used to make links between excitation mechanisms of H_2 with morphology and evolutionary stage. The work in this chapter has been published as Jones et al. (2018).

Chapter 3: This chapter describes a detailed analysis of a round PN observed in the UWISH2 survey - Abell 53. Multi-wavelength observations, including photometry from various surveys, and optical and near-infrared spectroscopy obtained through telescope proposals, are characterised and used to estimate some of the physical conditions within the nebula.

Chapter 4: The photoionisation code Cloudy is described, and used to create a 'simple' model of Abell 53, in order to replicate observations of both the ionised and molecular regions for the first time. A Markov-Chain Monte Carlo method is used to find the best set of parameters of the model.

Chapter 5: This chapter investigates how effective a sequence of static Cloudy models can be in simulating an evolving PN, in order to reproduce observed H_2 surface brightnesses in the UWISH2 survey.

Chapter 2

K-band spectroscopy of UWISH2 PN candidates

2.1 Introduction

In this chapter, K-band long-slit spectra of a sample of PNe and candidate PNe taken from the UWISH2 imaging survey (UKIRT Widefield Infrared Survey for H_2) (Froebrich et al., 2011) are presented. The focus is on confirmation (or rejection) of these objects as PNe, along with investigating the mechanisms governing the excitation of H_2, and how these relate to the evolutionary stages and morphologies. Along with spectra, we make use of near-IR H_2 and optical $H\alpha$ imaging, and mid-IR colours where available. This work was published in the Monthly Notices of the Royal Astronomical Society (MNRAS) journal (Jones et al., 2018). In Sect. 2.2, the sample and the available data are presented. Sections 2.3 and 2.4 outline the observations and the methods used to reduce the data. In Sect. 2.5, the spectra and images of the objects are described, while the links between morphology, line ratios and evolution are discussed in Sect. 2.6. Finally, the conclusions are made in Sect. 2.7.

TABLE 2.1: Observation log and additional information for the 29 targets. Coordinates refer to the central position of the slit used in the spectroscopy. Morphologies and sizes in H_2 and $H\alpha$ are taken from table A1 of Gledhill et al. (2018). Morphologies make use of the 'ERBIAS' classification system (Parker et al., 2006), and sizes are the major and minor axis dimensions in arcsec. Where no $H\alpha$ morphology is given, the object is not detected in $H\alpha$ emission. PN status comes from the HASH PN database (Parker et al., 2016), where 'T', 'L', 'P' and 'C' refer to true, likely, possible and candidate PNe respectively - see text for details.

PN G	Other names	RA	Dec	Integration (s)	Airmass	H_2		$H\alpha$		PN status
						Morph.	Size	Morph.	Size	
004.7-00.8	—	269.95542	-25.26527	1200	1.71	Bams	25x12	—	—	C
009.7-00.9	SSTGLMC G009.7612-00.9575	272.71231	-20.96230	1200	1.56	Bs	18x6	—	—	C
020.7-00.1	—	277.37398	-10.94099	1200	1.46	Bs	14x9	A	15x9	C
020.8+00.4	SSTGLMC G020.8543+00.4857	276.84922	-10.50625	1200	1.34	B	2.8x1.2	—	—	C
024.8+00.4	SSTGLMC G024.8959+00.4586	278.76581	-6.93617	1200	1.23	Bs	14x6	—	—	C
025.9-00.5	—	280.21143	-6.44546	1200	1.46	Ers	8x5	—	—	C
032.6-01.2	MPA J1855-0048	283.85720	-0.80638	1200	1.31	Bps	12x5	E	10x5	T
034.8+01.3	—	282.55901	+2.30305	1200	1.17	Bs	14x7	—	—	C
035.7-01.2	NVSS 190102+015727	285.26293	+1.95644	1200	1.17	Bs	26x12	—	—	C
036.4+00.1	GPSR5 36.481+0.155	284.34075	+3.23021	1200	1.25	Bps	12x5	—	—	C
037.4-00.1	—	285.07885	+3.90133	1080	1.28	Er	6x5	—	—	C
040.4+01.1	—	285.32726	+7.20967	1200	1.11	Bs	12x4	—	—	C
040.5-00.7	—	287.02679	+6.41554	1200	1.24	Bs	12x7	—	—	C
042.1+00.4	—	286.67062	+8.38580	1200	1.55	Bs	9x9	—	—	C
047.1+00.4	—	289.05872	+12.86745	1200	1.27	Brs	25x14	S?	—	C
047.5-00.3	—	289.95370	+12.76896	1200	1.24	Es	12x8	—	—	C
048.2-00.4	—	290.40474	+13.37742	1200	1.47	Bs	10x8	—	—	C
050.0-00.7	—	291.57894	+14.80423	1320	1.41	Bs	12x12	—	—	C
050.5+00.0	NVSS J192414+153909	291.06046	+15.65315	1320	1.23	Bs	16x5	S	—	L
057.9-00.7	Kn 7	295.60822	+21.75634	1080	1.33	Brs	26x20	B	27x30	T
058.1-00.8	IPHASX J194301.3+215424	295.75604	+21.90672	1320	1.61	Bs	20x12	B	15x12	L
059.7-00.8	IPHASX J194633.0+231659	296.63714	+23.28371	1440	1.17	Bs	12x9	Ea	13x9	P
060.5-00.3	K 3-45	296.56513	+24.18437	1200	1.93	Bps	11x6	Bs	11x6	T
061.8+00.8	—	296.14467	+25.92826	1200	1.40	Bs	12x13	B?	12x12	C
062.1+00.1	—	297.01712	+25.81331	1200	1.71	Ear	12x10	E?	10x8	C
062.2+01.1	—	296.15164	+26.44203	1200	1.00	Bs	16x10	E?	11	C
062.7+00.0	IPHASX J194940.9+261521	297.42017	+26.25520	1200	2.20	Bs	17x8	Bps	13x7	T
064.1+00.7	—	297.57807	+27.89812	1080	1.05	Bs	11x4.5	E?	2.3x4	C
064.9+00.7	—	298.03161	+28.54425	1200	1.96	Brs	10x8	B?	10x8.5	C

2.2 Sample

Our sample for spectroscopic follow-up consisted of 29 targets[1] from the UWISH2 survey, selected mainly due to their bright H_2 fluxes, and mix of interesting morphologies. The objects lie at low Galactic latitudes ($-1.5° < b < 1.5°$) and have longitudes in the range ($0° < l < 65°$). Table 2.1 lists all the targets observed, while images of the targets in H_2 and $H\alpha$ emission are shown in Figure 2.1. The 'ERBIAS' classification system used in Table 2.1 separates PN morphologies as either Elliptical (oval), Round, Bipolar, Irregular, Asymmetric or quasi-Stellar (point source). The lower case letters 'amprs' are used to highlight additional features: a one-sided enhancement/asymmetry 'a', multiple shells/external structure 'm', point symmetry 'p', a well-defined ring structure/annulus 'r' or a resolved internal structure 's' (Parker et al., 2006).

Four of the targets have a PN status of 'true'; these are confirmed PNe with multi-wavelength PN-like morphologies, PN spectral features and sometimes the presence of an obvious CSPN. Two have the status 'likely', for objects that are likely to be PNe but do not have completely

---

[1]The original sample consisted of 32 targets, however spectra for 3 of these had SNRs too low for the data to be useful.

TABLE 2.2: Observations of 15 standard stars, given in the order they were observed. The air mass is the average taken over the image sequence. The spectral types and K-band magnitudes were taken from SIMBAD.

HIP ID	RA	DEC	Air Mass	Integration (s)	Spec. Type	K-mag
98347	299.72083	+30.36528	1.09	20	A2	8.416
92177	281.79583	+10.76361	1.18	120	A0	7.468
96518	294.32500	+15.25056	1.50	240	B8	7.902
90967	278.34167	-5.91167	1.27	60	B9	6.163
92386	282.40417	+0.83611	1.37	80	A1	6.040
94478	288.43333	+5.51556	1.70	80	A3	6.078
98699	300.69583	+28.51472	1.62	80	A1	6.833
92386	282.40417	+0.83611	1.49	60	A1	6.040
92386	282.40417	+0.83611	1.23	60	A1	6.040
87819	269.0875	-21.95583	1.58	60	A1	4.779
90991	278.4125	-14.85361	1.46	60	A0/1	5.631
90967	278.34167	-5.91167	1.59	60	B9	6.163
95002	289.97083	+11.53472	1.33	60	A2	5.767
96518	294.32500	+15.25056	1.73	100	B8	7.902
98186	299.29167	+30.85639	1.74	80	B8	7.615

conclusive or available morphology/spectroscopy data. One is labelled 'possible', indicating a possible PN with insufficient morphology/spectroscopy data; usually due to a mix of low SNR, poor wavelength coverage, low surface brightness or unclear nebulosity. These statuses are taken from the HASH PN database (Parker et al., 2016). The remaining 22 targets have the status 'new candidate' - these have been classified as candidate PNe by the UWISH2 survey on the basis of morphology and lack of association with known star-forming regions. These statuses come from the HASH PN database. Hα images are available for all 29 targets, however only 14 show evidence of Hα emission, with 7 of these having been previously reported.

It is also apparent that some of the targets are bright in the mid-IR, with Spitzer/IRAC imaging available at 3.6, 4.5, 5.8, and 8.0 μm from the GLIMPSE survey[2]. Mid-IR colour-colour plots can be used as an additional diagnostic to imaging and spectroscopy, to distinguish PNe from possible mimics, as their various infrared properties cause them to populate different regions of the diagrams (e.g. Robitaille et al. 2008; Cohen et al. 2011). Gledhill et al. (2018), hereafter G18, have measured IRAC colours for targets in the UWISH2 survey, with detectable mid-IR emission, which includes the targets from this work. Fluxes in all four bands are available for 18 of the targets.
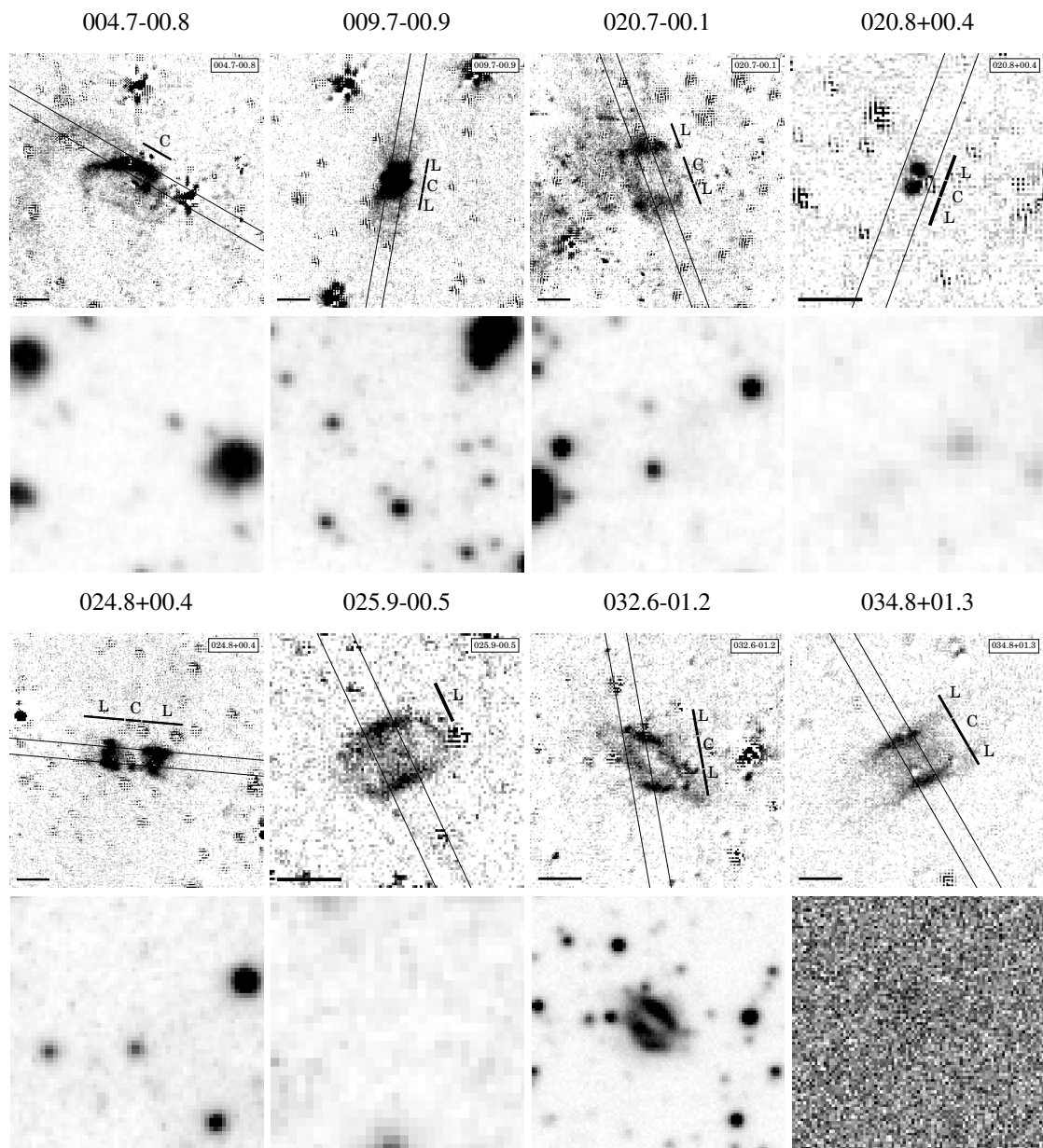
FIGURE 2.1: H_2 (top) and $H\alpha$ (bottom) images of the candidate PNe investigated in this work, in order of increasing galactic longitude. H_2 images are K-band continuum subtracted, and are taken from the UWISH2 survey, found at `http://astro.kent.ac.uk/uwish2/`. $H\alpha$ images are taken from either the SHS or IPHAS surveys, depending on their location, and were obtained through the HASH PN database. We overlay the LIRIS slit size and position, and the sections used for extraction - these are denoted 'C' for the centre, 'L' for a lobe and 'A' for all the target. The horizontal bars in the bottom left corner of the H_2 images are scale bars representing 5 arcsec.

035.7-01.2   036.4+00.1   037.4-00.1   040.4+01.1

040.5-00.7   042.1+00.4   047.1+00.4   047.5-00.3
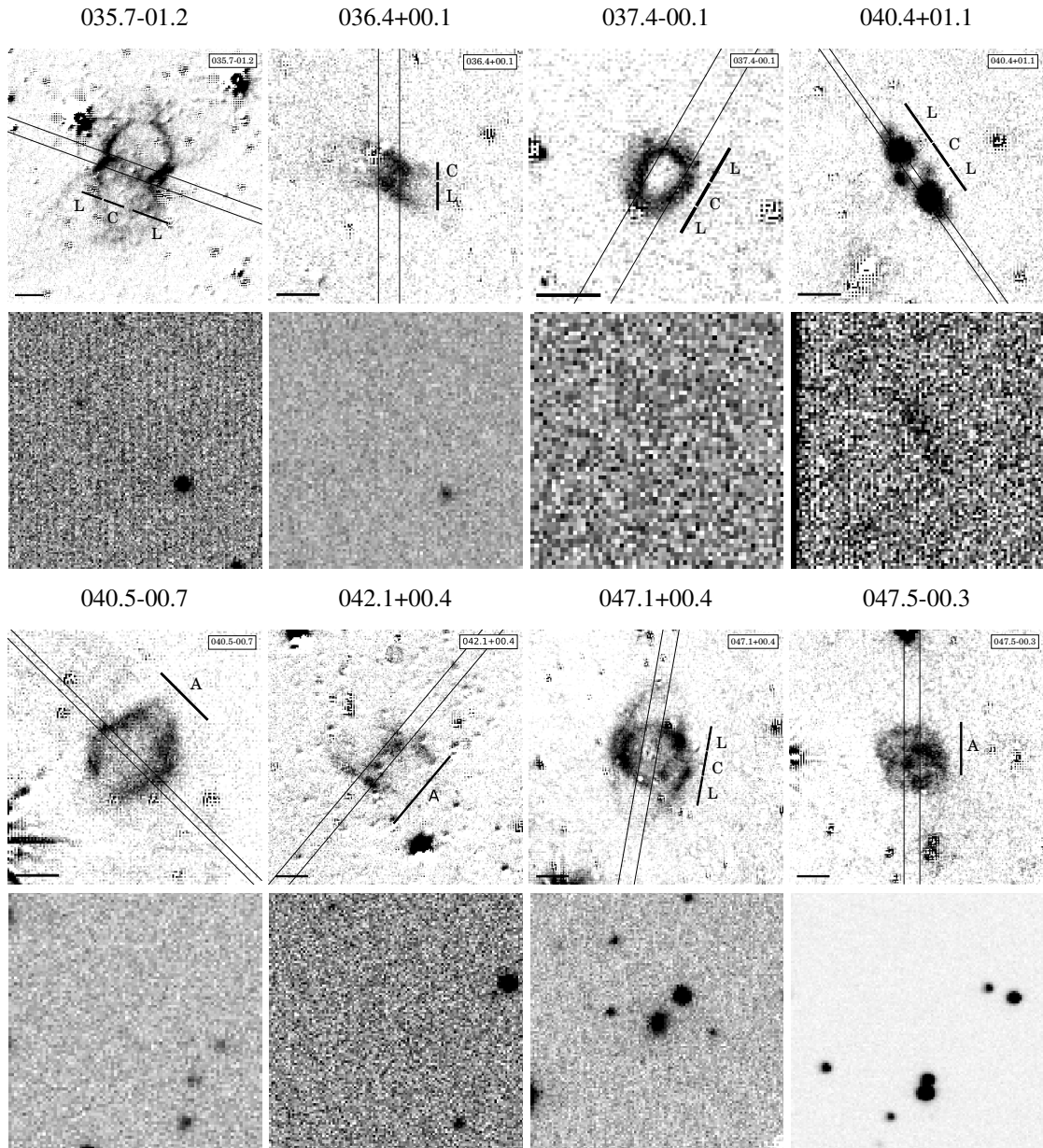
FIGURE 2.1: continued

2.3 Observations

Spectroscopic observations were obtained on the 22nd - 24th July, 2016, using the Long-slit Intermediate Resolution Infrared Spectrograph (LIRIS: Manchado et al. 2003; Acosta Pulido et al. 2003) on the 4.2m William Herschel Telescope (WHT), located at the Observatorio del Roque de los Muchachos on La Palma, Canary Islands. LIRIS uses a 1024 × 1024 HAWAII detector, with a pixel scale of 0.25 arcsec pixel^{-1}, yielding a field of view of 4.27 arcmin x 4.27 arcmin. Using the 'hkspec' filter and 'hr_k' grism, the available wavelength range was 2.05

[2]http://irsa.ipac.caltech.edu/data/SPITZER/GLIMPSE/index_cutouts.html

048.2-00.4 050.0-00.7 050.5+00.0 057.9-00.7

058.1-00.8 059.7-00.8 060.5-00.3 061.8+00.8
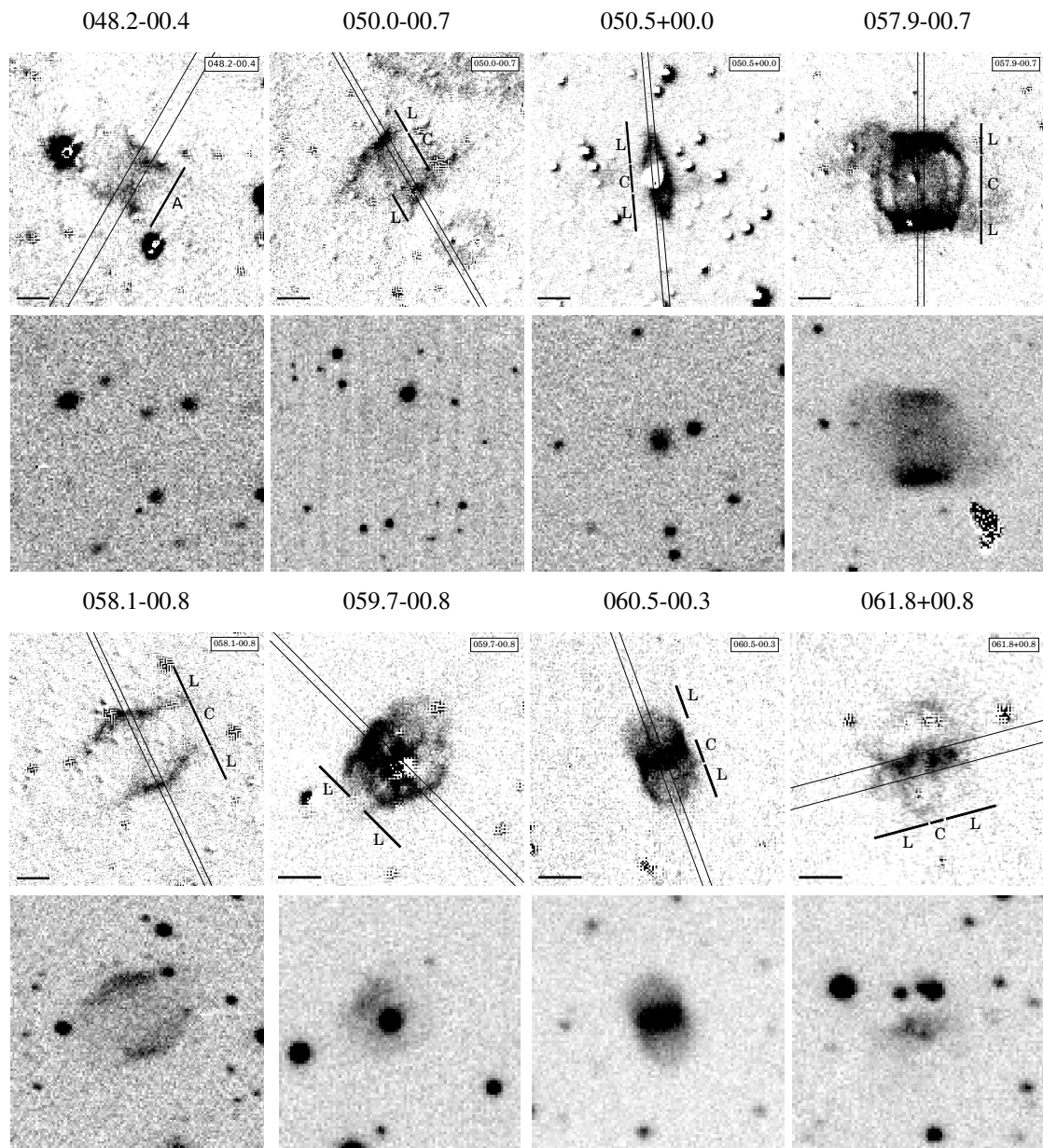
FIGURE 2.1: continued

to 2.41 μm, and the resolution, R $= \Delta\lambda/\lambda = 2500$, corresponding to a wavelength resolution of 3.6 Å/pixel.

Observing conditions were in general quite good, as indicated by the airmass and the seeing. Airmass is the amount of air the light has to travel through the atmosphere before reaching the telescope. This meant that targets observed close to twilight generally had the worse conditions; some of these targets had signals too low for any useful information to be extracted. The average airmass for the targets over the three nights were 1.31, 1.37 and 1.54 respectively. Seeing describes how turbulence in the atmosphere results in observations appearing more spread out.

062.1+00.1   062.2+01.1   062.7+00.0   064.1+00.7

064.9+00.7
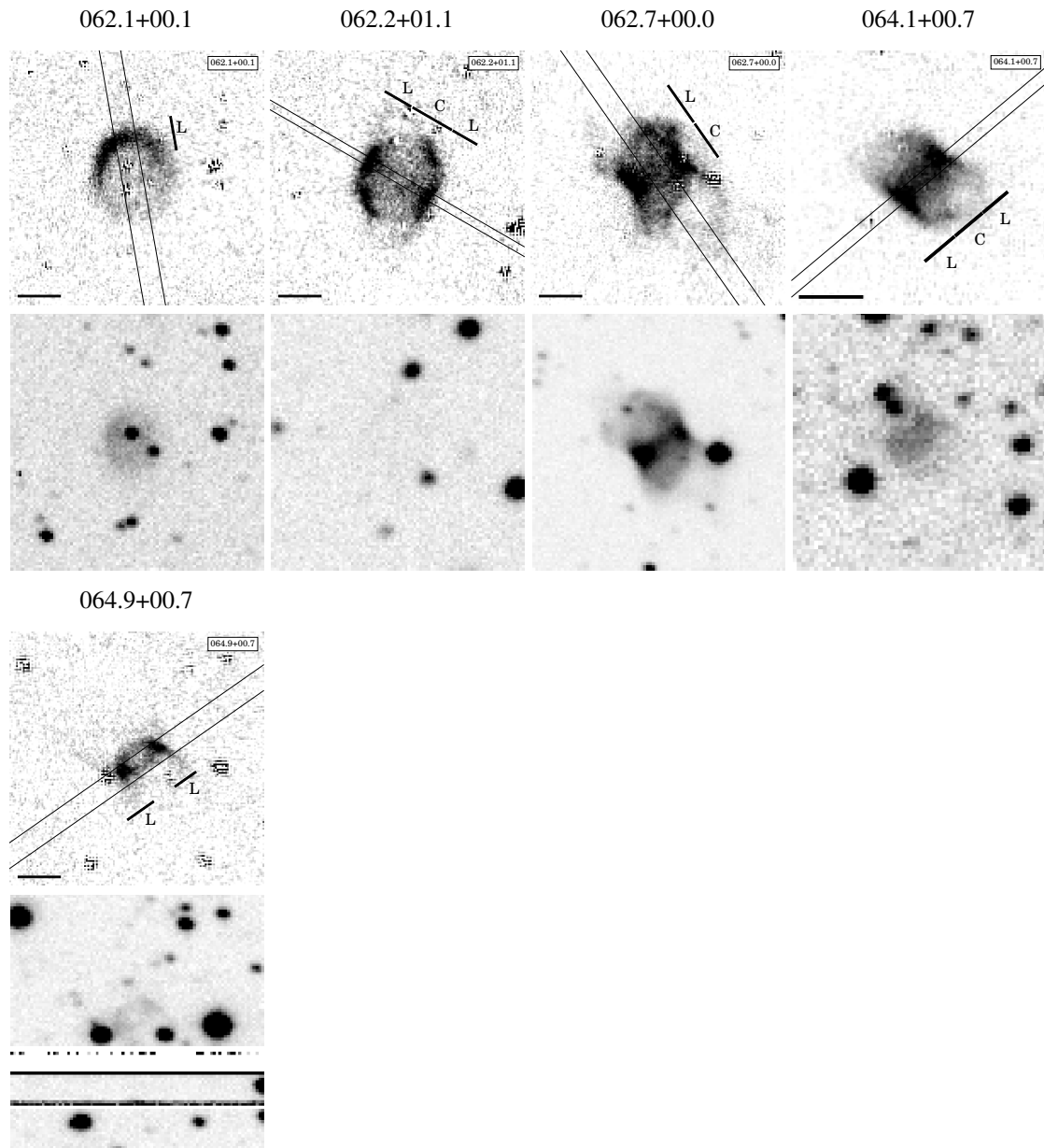
FIGURE 2.1: continued

The seeing can be estimated from the full-width at half-maximum (FWHM) of the signal from a point source, such as a star - this was measured to not usually exceed ~ 1 arcsec.

For most of the targets, 20 exposures of 60s were obtained. These were observed in a A-B-B-A nodding sequence, with A and B images offset from each other by a number of arcseconds, depending on the size of the nebula, in order to effectively subtract the sky contribution. We also obtained flat-fields, arcs and spectra of standard stars; details of the latter of these are given in Table 2.2.

In order to place the slit in the correct position on the target, J-band images were first taken to

determine the star field, and compared to the UWISH2 H_2-K difference images. The difference image allows the source to be clearly visible in H_2, which would be otherwise invisible in the J-band image. The offsets were calculated, and the telescope re-positioned in order to centre the slit onto the target. We used a slit width of 1 arcsec for the brighter targets, and increased it to 2.5 arcsec for the fainter ones. The slit was generally oriented along the major axis of the nebula, as defined by UWISH2 images, or to contain the brightest H_2 features. However, this sometimes led to nearby stars falling within the slit, rendering certain sections of the data unusable. The extraction sections are marked on the UWISH2 H_2-K images in Fig. 2.1. Table 2.1 gives observational details for each target.

2.3.1 Additional observations

As part of a programme that also included observations of Abell 53 (see Chapter 3), we acquired K-band spectroscopy of PN G077.7+03.1 using 2 positions, in order to cover both high and low surface brightness regions. The original purpose of this programme was to investigate how properties determined from K-band spectra vary across PNe of different physical sizes, and hence different stages of evolution. We also obtained follow-up narrow-band imaging of PN G050.5+00.0, using LIRIS. The observations were carried out on the 26th September, 2017, using the Brγ and K-band continuum filters, which included flat-field frames. The average airmass of the target frames was 1.33, with a seeing of ≈ 1 arcsec.

2.4 Data reduction and processing

2.4.1 Spectroscopy

The process to transform the raw data from the telescope into a final product which can be used for scientific purposes is known as data reduction. The steps used here to generate fully-calibrated one-dimensional spectra of the 29 original PN candidates are shown in Figure 2.2. IRAF (Image Reduction and Analysis Facility; Tody 1993) is a collection of software packages used extensively by astronomers when dealing with telescope data. Various packages are used here for flat-field correction, wavelength calibration, telluric correction, flux calibration and image combination. Additionally, PYTHON with the ASTROPY module (Astropy Collaboration et al., 2013) was used to extract the spectra. We describe these steps in the following sections.
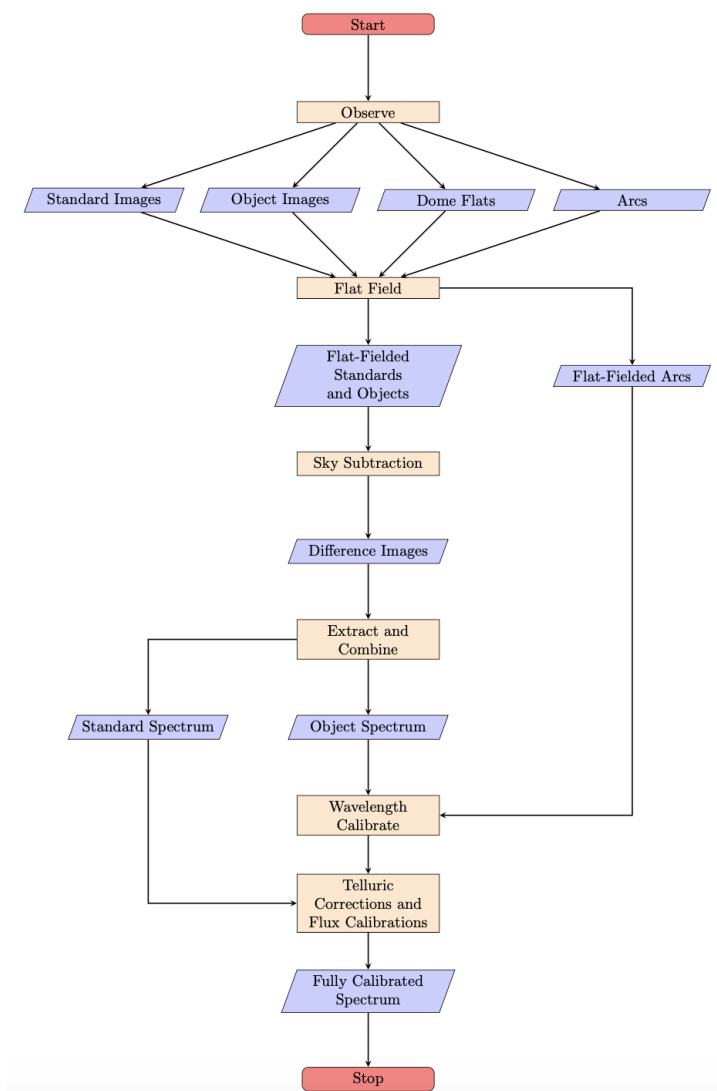
FIGURE 2.2: Flowchart for LIRIS data reduction procedure.

Flat-field   The first stage of the procedure is to flat-field the data, in order to account for the pixel to pixel variation of the detector, and any vignetting caused by telescope or instrumental optics (note that bias and dark corrections are automatically carried out with each exposure). The individual dome flat images were stacked to create a master flat. This was then normalised (average pixel value = 1), and divided into the target images in order to remove the variations in the response of the detector.

Sky subtraction   The purpose of taking measurements at two positions (A and B in the A-B-B-A sequence) was to remove both the bright emission lines and the continuum emission due to the sky, as the atmosphere is very bright in the K-band. The best way to do this is by taking a short, 60 second exposure of the target (position A), then slightly moving the telescope while
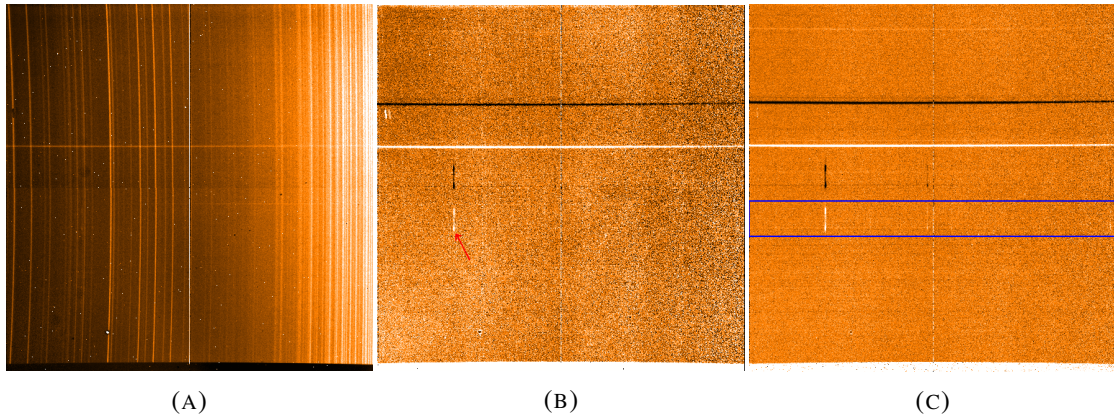
FIGURE 2.3: Various stages in the reduction procedure for PN G057.9-00.7. The x-axis represents wavelength, while the y-axis represents distance along the slit. (A) Raw data - vertical lines are sky lines due to atmosphere (B) Flat-fielded A-B image - the sky lines have disappeared due to subtracting the A nodding position from the B. The 1-0 S(1) line is located with a red arrow. (C) Combined A-B - the median of all the A-B images. The blue box is the region used to extract the spectrum. The bright horizontal lines in the images come from the continuum of a background star located within the slit.

ensuring the target still lies within the slit and taking an exposure (position B), and repeating in the sequence A-B-B-A, so as to not waste time moving the telescope between each successive exposure. Each A image was subtracted from each B image, and vice versa, to remove the sky emission lines and continuum. The effect of this is visible in Figure 2.3, which shows different stages of the reduction procedure for one particular target, namely PN G057.9-00.7. Figures 2.3b and 2.3c are A-B difference images, with the white regions (positive values) coming from the A images, while the black regions (negative) come from the B images. The corresponding B-A difference image would be the opposite way round. The separation between the regions corresponds to the separation between the two noddings, around 30 arcsec in this case.

Stacking To improve the signal to noise, the individual A-B images are median-stacked together, as are the B-A images. The result is two combined difference images, one for A-B, and the other for B-A. At this stage, some of the brighter emission lines can be seen. The 1-0 S(1) line is indicated by a red arrow in Figure 2.3b, and the effect of stacking the images makes it much more prominent in Figure 2.3c. The 1-0 S(0) line can also be seen, almost halfway along the image. By inspecting the combined difference images, it was clear that for three of the targets, it would be very difficult to extract spectra - it was decided these would not be used. In the case of PN G026.8+00.2, many background stars were located within the slit, causing the image to be confused with different sources. PN G056.3-01.5 and PN G064.2-00.1 were extremely faint, and there was no real signal detected.

Cosmetic changes   Detectors can have bad pixels; those which have some sort of defect, and can effect part or all of a row or column of the chip, or those that are struck by cosmic rays, which will have much larger values than surrounding pixels. The stacked A-B images are inspected for each target, and any bad pixels are removed using the PATCH routine within GAIA, a STARLINK software package (Currie et al., 2014). Near-IR detectors are different from the CCDs used in optical instruments. In LIRIS images, there are clear discontinuities between the 4 quadrants, visible in Figure 2.3, caused by a detector reset anomaly. This is a consequence of the build up of an unstable component when the detector switches between being exposed and not being exposed, and are removed using PYTHON.

Extraction   The images at this point are two-dimensional spectra, that is they contain wavelength and spatial information. In order to clearly see which emission lines are present, and enable the calculation of the fluxes of the lines, a spectrum needs to be extracted from the difference images. This is a one-dimensional plot with wavelength on the x-axis and flux density (flux per unit wavelength) on the y-axis. As the target data only lies in a small region of the image, an extraction window was made, which essentially crops the region where the target data is. This is represented by the blue box in Figure 2.3c. The boundaries of this region lie where the signal from the target falls to the noise level. The data in this window could then be collapsed to a single row, by summing the counts in each of the columns. This was done for both the A-B, and B-A combined difference images, and averaged together to form a one-dimensional array. This could be plotted to generate an uncalibrated spectrum of the target. However, there would be no wavelength scale on the x-axis, or physical flux on the y-axis, and the effects of the atmosphere would also be included. For most targets, we choose 2 regions to extract data from: a central region, usually where HII emission is stronger, and an outer region containing flux from the lobes, where often the H_2 emission is strongest. For some targets, foreground/background stars would lie within the slit, and therefore they would appear in the data as continua. Unfortunately, these could not be removed from the data, and so the flux from these sections could not be extracted.

Wavelength calibration   Arc images were taken using an argon lamp within the telescope. The strong emission lines in these images are due to the electron transitions within the argon atom, and so have well-known wavelengths. By combining this information with the wavelengths of known sky lines, it is possible to convert the x-positions of these lines (in pixels) to wavelengths (in microns). A polynomial function could be fitted to a section of the arc data,
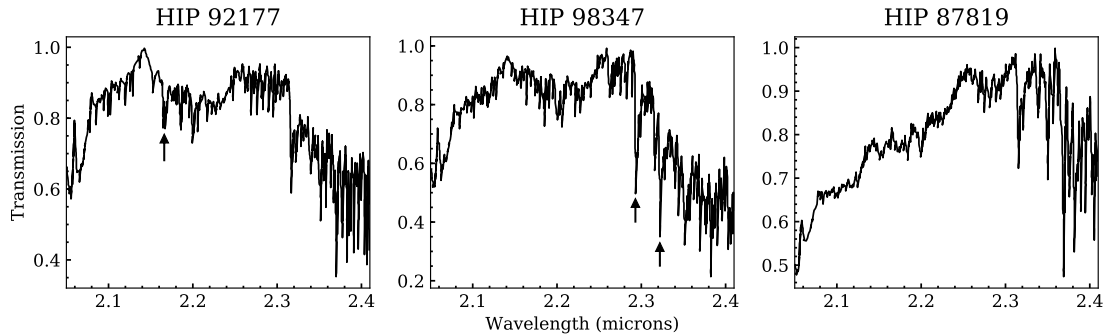
FIGURE 2.4: Transmission curves for 3 standard stars, with the maximum set to 1.0. Left: HIP 92177 - a typical standard star. The arrow indicates the position of the Brγ absorption feature. Middle: HIP 98347 - SIMBAD classes this star as A2, however we note the presence of CO bandheads (shown with arrows) in the K-band. Right: HIP 87819 - a Herbig Ae/Be star with a highly reddened spectrum.

at the same part of the chip as where the targets were observed, in order to find this dispersion relation; however, it became clear that a linear function would be adequate. Once each pixel along the x-axis has its own wavelength, the smallest separation (i.e. between two consecutive pixels) could be calculated, which equaled 3.6 $\mathring{A}$/pixel. The wavelength calibration was checked by noting the approximate position of the bright 1-0 S(1) line[3] and any other obvious lines which should be present in a PN. It is also worth noting that there is a slight curvature in the sky emission lines when moving along the y-axis, which is evident in Figure 2.3a. This is an optical effect, and found not to be a significant issue at the target positions on the chip, where the curvature is minimal.

Telluric corrections   As with any ground-based observations, the effect of the atmosphere has to be accounted for. While the sky lines can be removed through subtracting the images, some transmission effects of the atmosphere remain in the data. Standard stars were observed throughout the 3 nights, chosen on the basis of having relatively few features in their spectra, and for their proximity to the PN candidates to ensure they closely represented the atmosphere through which the targets were observed. Details of the chosen stars are given in Table 2.2. Late B-type, and early A-type main sequence stars should have very few features (such as metal lines) in their spectra in the K-band, apart from Brγ absorption (Lancon and Rocca-Volmerange 1992; Wallace and Hinkle 1997). In order to remove the atmosphere from the spectra of the targets, a blackbody spectrum was created with the same temperature as the standard star. Theoretically, this is what the spectrum of the standard star would look like if it was observed from space. The

---

[3]The H_2 1-0 S(1) line has a rest wavelength of 2.1218 μm, however its position in a spectrum may be shifted slightly due to a radial velocity component for part or all of a PN.

temperature of the standard comes from its spectral type, found using the SIMBAD database (Wenger et al., 2000). For late B-type and early A-types, this is usually around 10000 K. The blackbody curve is normalised, and divided into the spectrum of the standard - this creates an atmospheric transmission spectrum. Dividing the spectrum of the PN candidate by this removes the transmission effects of the atmosphere. The left panel of Figure 2.4 shows the transmission curve for a typical standard star, with an arrow indicating the position of the Brγ absorption feature. This is intrinsic to the stellar spectrum, and is removed using PYTHON before being divided into the spectrum of the PN candidate. All the other features are due to the atmosphere. The middle and right panels of Figure 2.4 are the transmission curves for HIP 98347 and HIP 87819 respectively. These stars may have featureless spectra in the optical, which is why they were listed as standard stars for observing. However in the K-band, this is not the case. HIP 98347 is labelled as an ordinary main-sequence star of spectral type A2. Therefore we would expect to see a relatively featureless spectrum, with Brγ absorption. Instead, we see no clear evidence of Brγ, and the addition of two absorption features These are identified as the CO v = 2-0 band head at 2.2935 μm, and the v = 3-1 band head at 2.3227 μm (Tokunaga, 2000). The presence of these lines in absorption would suggest they originate from the photospheres of cool, mostly evolved stars, or from circumstellar material (Hoffmeister et al., 2006). HIP 87819 is actually a Herbig Ae/Be star, which is a pre-main-sequence star. It is found to have a very high projected rotational velocity (Mora et al., 2001), with a protoplanetary disk (Isella et al., 2016). Dust grains in this disk may explain its reddened spectrum. As these two stars cannot be considered as standards, it was decided to not use these spectra for telluric corrections.

Flux calibration   In order to put a physical scale on the y-axis of the spectra, e.g. W m^{-2}, three IRAF routines are used: STANDARD, SENSFUNC and CALIBRATE. The basic principle involves integrating over the standard star spectrum, and using a broad-band magnitude (i.e. from the K-band) to find a wavelength-dependent function that translates raw data units to physical units. This assumes that the standard stars can be well approximated by blackbodies, with effective temperatures and K-band magnitudes taken from SIMBAD. These functions can then be applied to the target spectra.

Emission line fitting   At this point, we have fully-calibrated K-band spectra for 29 targets, with usually 2 spectra for each target, one for the central region and one for the outer lobes. We now need to estimate the flux contained within emission lines in the spectra, relative to a

continuum level, if any. Firstly, the emission lines need to be located, by searching the spectra in wavelength space where known nebula lines are present. In order to calculate these emission line fluxes, Gaussian profiles were fitted to the spectra using the CURVE FIT function from the PYTHON SCIPY module (Jones et al., 2001), which uses non-linear least squares in order to fit a function to the data. The equation for a Gaussian is given by

$$y = A \cdot \exp\left(\frac{-(x-\mu)^2}{2\sigma^2}\right) + B \tag{2.1}$$

The four parameters to be found from each fit to an emission line are the amplitude (A), position (μ), standard deviation (σ) and a shift in the y-direction (B) if a continuum is present. An estimate of the covariance matrix from the fit gives 1σ uncertainties on the parameters. The equation for the area under a Gaussian is

$$F = \sqrt{2\pi} \cdot A \cdot \sigma \tag{2.2}$$

which gives the flux of an emission line. The uncertainties in the parameters from the fit are propagated through this equation to yield an estimate on the flux. The fluxes and uncertainties for all emission lines identified in the 29 targets are given in Table 2.3.

2.4.2 Imaging

As mentioned in Sect 2.3, narrow-band images were acquired for PN G050.5+00.0. Images were taken at 5 offset pointings - stacking the unaligned images together created a sky frame, which was subtracted from each target frame to remove the sky contribution. These were then aligned and stacked to form the final image. Standard IRAF routines were used in flatfielding, image alignment and stacking. In order to highlight any structures within the bright central region of PN G050.5+00.0, we deconvolved the image using the Richardson-Lucy algorithm (Richardson 1972; Lucy 1974). This was achieved using a star within the same field to act as a point spread function, in order to improve the resolution. The procedure was carried out using the LUCY routine in the STARLINK package KAPPA.

2.5 Results and analysis

Figure 2.5d for PN G050.5+00.0, 2.6b and 2.6c for PN G059.7-00.8, and Fig. A.1 for the remaining targets, show the fully calibrated emission spectra, with identified features labelled. All targets have the v = 1-0 S(1), 1-0 S(0) and 1-0 Q(1) H_2 emission lines, albeit the latter line is often weak due to poor atmospheric transmission. Higher vibrational level H_2 lines are identified in some objects, including the 3-2 S(2) and 3-2 S(3) lines. Brγ (2.1661 μm) is seen in all but 4 objects[4], signifying the presence of ionised hydrogen. We detect the HeI (2.0587 μm) line in 9 targets, which means their central stars have become hot enough that their UV photons are capable of ionising He. We also see the weaker HeI (2.1127 μm) line in 3 targets, and the HeII (2.1891 μm) line in 4 targets. These, and a range of other H_2 emission lines seen in the targets are listed in Table 2.3, along with their fluxes. In the following sections, some of the more interesting objects are described.

2.5.1 PN G050.5+00.0

PN G050.5+00.0 is a particularly interesting object, as morphological and kinematic evidence suggests the presence of fast outflows - the only object in our initial sample with such properties. With a range of radio data available, it has been classed as a 'likely PN', (e.g. the CORNISH 5.0 GHz survey; Hoare et al. 2012; and the RMS survey; Urquhart et al. 2009), while the Green Bank Telescope (GBT) HII Region Discovery Survey (Anderson et al., 2011) classes PN G050.5+00.0 as a HII region. The UWISH2 image is shown in Fig. 2.5a, without K-band subtraction[5]. PN G050.5+00.0 has a cigar-shaped H_2 morphology, surrounded by a rim of stronger emission. The object has a very bright central region, which is likely a combination of H_2 and K-band continuum emission (K_c). We also find strong Brγ emission here, which extends slightly into the lobes where there is a void of H_2; more noticeable in the northern lobe (Fig. 2.5c).

We overlay contours on Fig. 2.5a to highlight structure in the centre. We find the emission here is not uniform, but instead peaks at a point slightly to the south-east. This encouraged us to attempt narrow band Brγ and K_c imaging, to see if it would be possible to further resolve

---

[4]We do not detect Brγ in PN G062.1+00.1 or 064.9+00.7, however these objects have clear Hα emission in their IPHAS images. We attribute this lack of detection to a combination of high airmass during observations, and nearby stars preventing extraction of the central regions, where the H^+ is thought to be concentrated.

[5]We include the H_2 image to give a better view of the central region, as the H_2-K image of the centre is dominated by negative flux, due to a strong Brγ flux in the K-band leading to an over-subtraction.

TABLE 2.3: Continuum-subtracted line fluxes and errors ($\times 10^{-19}$ Wm^{-2}) for K-band emission lines. Rest wavelengths of the emission lines are given in μm. Note these values are not corrected for extinction.

ID	Region	HeI 2.0587	H$_2$ 2-1 S(3) 2.0735	HeI 2.1127	H$_2$ 1-0 S(1) 2.1218	H$_2$ 2-1 S(2) 2.1542	Brγ 2.1661
004.7-00.8	Centre	—	47 ± 7	—	398 ± 22	17	—
009.7-00.9	Centre	99 ± 6	41 ± 5	9	412 ± 16	16 ± 3	169 ± 6
	Lobes	—	33 ± 4	—	280 ± 10	11 ± 4	—
020.7-00.1	Centre	—	—	—	99 ± 7	—	16 ± 4
	Lobes	—	29 ± 6	—	282 ± 17	—	15 ± 5
020.8+00.4	Centre	—	12 ± 2	—	56 ± 2	—	—
	Lobes	—	14 ± 4	—	104 ± 4	—	—
024.8+00.4	Centre	78 ± 3	—	5.4 ± 0.9	57 ± 8	—	115 ± 3
	Lobes	—	91 ± 8	—	805 ± 65	27 ± 5	—
025.9-00.5	North lobe	—	—	—	95 ± 5	—	8.6 ± 2.9
032.6-01.2	Centre	16 ± 3	11 ± 2	—	155 ± 9	—	53 ± 2
	Lobes	—	—	—	211 ± 12	—	28 ± 3
034.8+01.3	Centre	8.7 ± 2.5	6.2 ± 2.8	—	117 ± 12	—	34 ± 3
	Lobes	11 ± 3	14 ± 3	—	234 ± 15	—	22 ± 3
035.7-01.2	Centre	—	—	—	108 ± 10	—	17 ± 3
	Lobes	—	—	—	480 ± 28	—	53 ± 6
036.4+00.1	Centre	14 ± 2	—	—	67 ± 5	—	42 ± 2
	South lobe	15 ± 2	13 ± 3	—	102 ± 7	—	47 ± 3
037.4-00.1	Centre	21 ± 5	—	—	33 ± 5	—	75 ± 4
	Lobes	15	8.9 ± 3.5	—	199 ± 16	—	54 ± 4
040.4+01.1	Centre	36 ± 7	—	—	99 ± 4	—	72 ± 4
	Lobes	—	75 ± 6	—	579 ± 12	—	—
040.5-00.7	All	—	—	—	204 ± 5	—	21 ± 8
042.1+00.4	All	—	—	—	244 ± 12	—	21 ± 4
047.1+00.4	Centre	48 ± 6	—	—	61 ± 3	—	104 ± 3
	Lobes	—	—	—	143 ± 5	—	16 ± 4
047.5-00.3	All	—	18 ± 4	—	202 ± 13	—	37 ± 4
048.2-00.4	All	—	—	—	180 ± 14	—	15 ± 3
050.0-00.7	Centre	—	—	—	140 ± 6	—	23 ± 6
	Lobes	—	—	—	234 ± 6	—	—
050.5+00.0	Centre	1920 ± 30	—	212 ± 19	209 ± 9	—	3890 ± 80
	Lobes	109 ± 10	45 ± 12	15 ± 6	518 ± 15	28 ± 10	256 ± 9
057.9-00.7	Centre	—	35 ± 10	—	277 ± 8	—	43 ± 5
	Lobes	—	57 ± 6	—	669 ± 10	—	29 ± 9
058.1-00.8	Centre	—	—	—	127 ± 7	—	16 ± 7
	Lobes	—	—	—	244 ± 6	—	24 ± 6
059.7-00.8	Lobes	—	52 ± 10	—	503 ± 8	—	59 ± 7
060.5-00.3	Centre	—	—	—	177 ± 5	—	39 ± 2
	Lobes	—	—	—	215 ± 7	—	18 ± 5
061.8+00.8	Centre	—	—	—	61 ± 3	—	8.8 ± 1.5
	Lobes	—	—	—	409 ± 17	—	36 ± 8
062.1+00.1	North lobe	—	—	—	145 ± 13	—	—
062.2+01.1	Centre	—	—	—	166 ± 4	—	14 ± 3
	Lobes	—	—	—	255 ± 4	—	—
062.7+00.0	Centre	—	—	—	309 ± 22	—	113 ± 8
	North lobe	—	—	—	191 ± 11	—	30 ± 5
064.1+00.7	Centre	—	20 ± 5	—	206 ± 6	—	23 ± 4
	Lobes	—	24 ± 6	—	282 ± 4	—	14 ± 4
064.9+00.7	Lobes	—	7.4 ± 2.3	—	58 ± 6	—	—

TABLE 2.3: continued

ID	Region	HeII 2.1891	H$_2$ 3-2 S(3) 2.2014	H$_2$ 1-0 S(0) 2.2233	H$_2$ 2-1 S(1) 2.2477	H$_2$ 3-2 S(2) 2.2870	H$_2$ 1-0 Q(1) 2.4066
004.7-00.8	Centre	—	—	78 ± 7	32 ± 5	—	343 ± 22
009.7-00.9	Centre	17 ± 2	7.6 ± 2.6	98 ± 5	56 ± 4	15 ± 3	332 ± 14
	Lobes	—	11 ± 3	59 ± 3	39 ± 4	—	147 ± 9
020.7-00.1	Centre	—	—	17 ± 2	—	—	59 ± 8
	Lobes	—	—	64 ± 5	25 ± 5	—	49 ± 14
020.8+00.4	Centre	—	—	15 ± 1	7.9 ± 1.4	—	23 ± 3
	Lobes	—	—	25 ± 2	17 ± 3	—	57 ± 6
024.8+00.4	Centre	13 ± 1	—	23 ± 6	10 ± 3	—	46 ± 7
	Lobes	—	19 ± 4	185 ± 15	94 ± 9	—	597 ± 51
025.9-00.5	North lobe	—	—	22 ± 2	—	—	23 ± 7
032.6-01.2	Centre	—	—	34 ± 3	13 ± 2	—	44 ± 7
	Lobes	—	—	43 ± 4	15 ± 2	—	77 ± 8
034.8+01.3	Centre	—	—	25 ± 3	—	—	61 ± 8
	Lobes	—	—	50 ± 5	21 ± 2	—	140 ± 14
035.7-01.2	Centre	—	—	20 ± 2	—	—	69 ± 10
	Lobes	—	—	95 ± 8	40 ± 7	—	359 ± 27
036.4+00.1	Centre	—	—	15 ± 2	10 ± 2	—	44 ± 4
	South lobe	—	—	24 ± 3	12 ± 2	—	55 ± 6
037.4-00.1	Centre	—	—	10 ± 2	5 ± 1	—	13 ± 4
	Lobes	—	—	49 ± 5	22 ± 4	—	130 ± 20
040.4+01.1	Centre	—	—	20 ± 4	13 ± 4	—	67 ± 12
	Lobes	—	—	135 ± 9	75 ± 6	—	228 ± 14
040.5-00.7	All	—	—	49 ± 9	—	—	171 ± 11
042.1+00.4	All	—	—	46 ± 7	—	—	92 ± 11
047.1+00.4	Centre	21 ± 3	—	18 ± 3	—	—	43 ± 11
	Lobes	—	—	40 ± 5	—	—	75 ± 14
047.5-00.3	All	—	—	40 ± 3	—	—	100 ± 11
048.2-00.4	All	—	—	51 ± 5	—	—	60 ± 14
050.0-00.7	Centre	—	—	30 ± 4	—	—	123 ± 12
	Lobes	—	—	62 ± 7	—	—	222 ± 18
050.5+00.0	Centre	93 ± 4	—	67 ± 8	46 ± 4	182 ± 7	175 ± 20
	Lobes	—	32 ± 6	136 ± 10	89 ± 5	21 ± 7	364 ± 21
057.9-00.7	Centre	—	—	61 ± 6	20 ± 6	—	158 ± 13
	Lobes	—	—	141 ± 8	51 ± 6	—	148 ± 19
058.1-00.8	Centre	—	—	32 ± 6	—	—	64 ± 15
	Lobes	—	—	58 ± 7	18 ± 6	—	95 ± 15
059.7-00.8	Lobes	—	—	119 ± 7	38 ± 6	—	378 ± 14
060.5-00.3	Centre	—	—	40 ± 3	15 ± 3	—	121 ± 10
	Lobes	—	—	49 ± 4	16 ± 5	—	137 ± 13
061.8+00.8	Centre	—	—	15 ± 2	—	—	61 ± 8
	Lobes	—	—	107 ± 7	31 ± 5	—	327 ± 25
062.1+00.1	North lobe	—	—	35 ± 4	—	—	103 ± 12
062.2+01.1	Centre	—	—	41 ± 5	—	—	148 ± 13
	Lobes	—	—	55 ± 4	—	—	269 ± 15
062.7+00.0	Centre	—	—	67 ± 11	25 ± 6	—	244 ± 42
	North lobe	—	—	43 ± 5	—	—	168 ± 26
064.1+00.7	Centre	—	—	52 ± 4	22 ± 4	—	146 ± 10
	Lobes	—	—	64 ± 4	21 ± 6	—	204 ± 15
064.9+00.7	Lobes	—	—	18 ± 4	—	—	65 ± 9

the central region, and to investigate the structure of the ionised and continuum emission. We show the deconvolved Brγ - K$_c$, and K$_c$ images in (Fig. 2.5b). Both have elongated structures, slightly offset from the centre of the object, which are similar to the structure seen in Fig. 2.5a. This leads us to believe that the Brγ and continuum emission both originate from the unresolved central region, and are being scattered by the same spatially extended dusty structure. This is because at 2μm, dust-scattered light is more important than thermal dust emission, unless the dust is very hot, and would need to be at the sublimation temperature.

FIGURE 2.5: K-band images and spectra for PN G050.5+00.0. (A) H_2 image from UWISH2, showing position and width of slit, and extraction sections. Contours range from 2400 to 3600 counts, in steps of 400. North is up, East is left. (B) Deconvolved narrow-band Brγ-K_c (left) and K-band continuum (right) images of the central region. Contours range from 500 to 3000 counts, in steps of 500. (C) Two-dimensional spectra for the 1-0 S(1) and Brγ lines, with dotted lines drawn through their centres. (D) K-band spectra of central region and lobes.

Higher vibrational level H_2 lines, and recombination lines of helium (including those of HeI and HeII) are seen in the spectra of PN G050.5+00.0 (Figure 2.5d). The Pfund series is also visible in the spectrum of the central region, from 2.3 μm onwards. In the two-dimensional spectrum of PN G050.5+00.0, we find the H_2 emission lines are slanted, indicating that the northern lobe is blueshifted, while the southern lobe is redshifted. We suggest two possible scenarios - either the object has curved outflows (where the northern lobe curves towards us, while the southern lobe curves away), or a range of initial speeds in the outflow causes faster-moving matter to be found at larger distance. We show a region of the two-dimensional spectrum, centred on the 1-0 S(1) line, in Fig. 2.5c, which is essentially a position-velocity diagram. We measure the wavelength shift from the centre to the end of each lobe to be 7.2 ± 3.6 Å, which gives a line-of-sight velocity of 100 ± 50 km s^{-1}, relative to the systemic velocity. A previous study using ^{13}CO observations (Ellsworth-Bowers et al., 2015) found a line-of-sight velocity of 83.7 kms^{-1}. These measurements are lower limits on the actual expansion velocity of the nebula, as any inclination to the line-of-sight will act to raise this value. These findings, along with mid-IR

colours measured by G18 (see Figure 2.8), suggest that PN G050.5+00.0 is more likely to be a PN rather than a HII region.
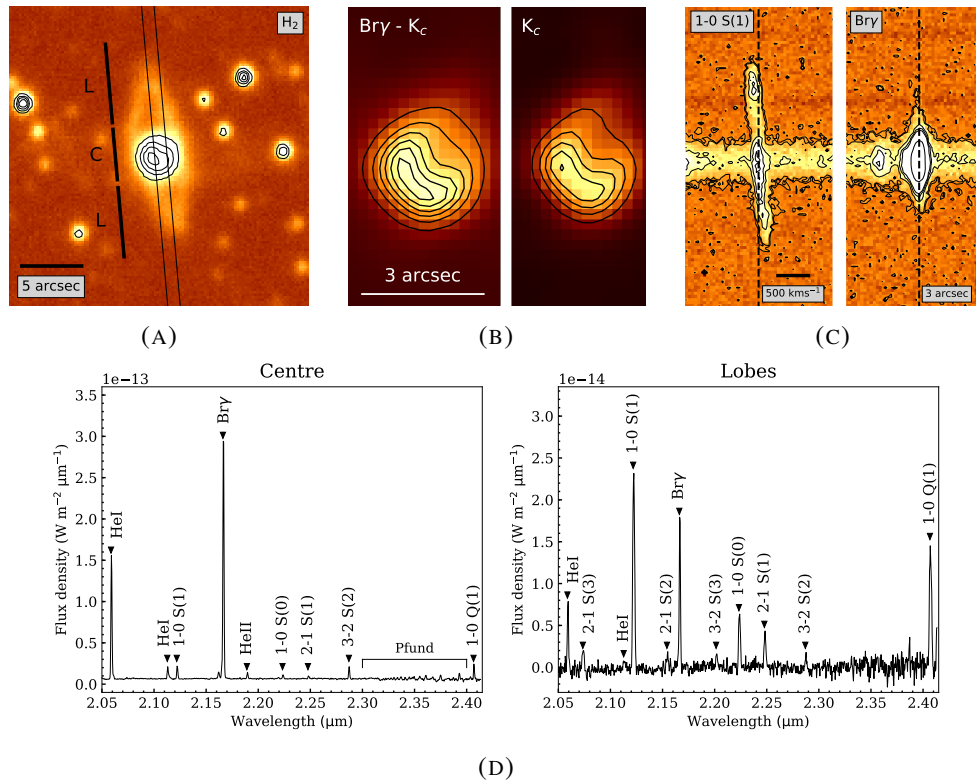
2.5.2 PN G059.7-00.8
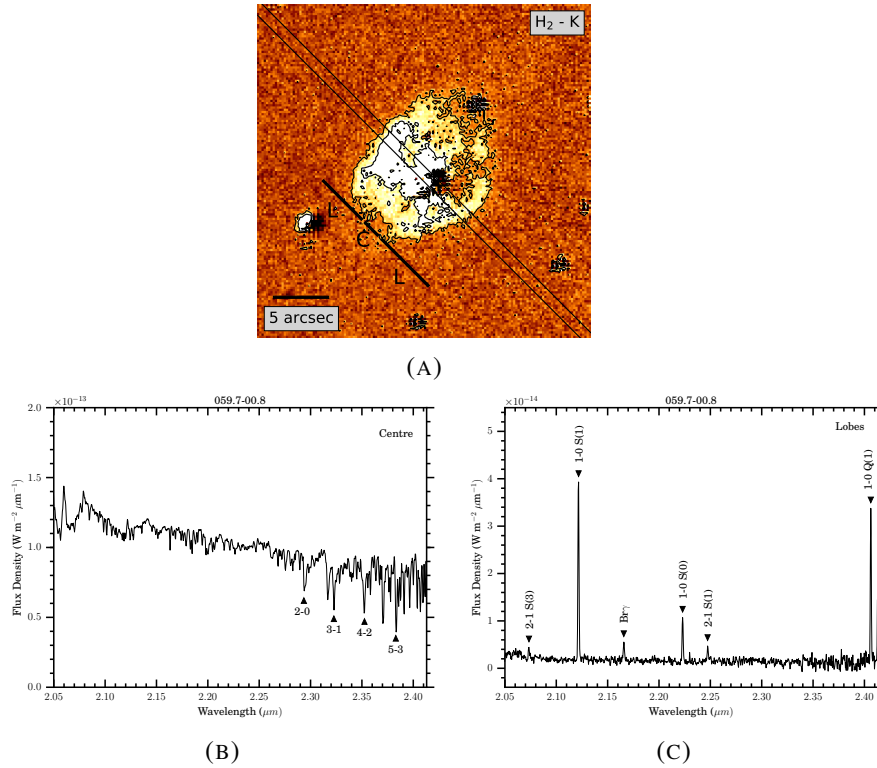
FIGURE 2.6: K-band image and spectra for PN G059.7-00.8. (A) H_2-K image from UWISH2, showing position and width of slit, and extraction sections. Contours are located at 50 and 150 counts. (B) K-band spectrum of central region, with CO bandheads labelled (C) K-band spectrum of the sum of the lobes.

PN G059.7-00.8 is a 'possible' PN, with an optical spectrum and imaging available[6]. The object has a steady rising continuum in the optical (4000 to 8000 Å), with strong emission lines of [OIII], [NII] and Hα (Sabin et al., 2014). It has an elliptical morphology in Hα emission, however its H_2 structure is spider-like, with stronger shells of emission to the north-east and south-west. In the centre of PN G059.7-00.8, we find a very bright source, and investigate to see if it is related to the object. The spectrum of this source, with a bright continuum, is shown in Fig. 2.6b. The continuum falls at longer wavelengths, and we find multiple CO bandheads in absorption, including the v = 2-0 (2.2935 μm), 3-1 (2.3227 μm), 4-2 (2.3535 μm) and 5-3 (2.3829 μm). These are characteristics common among cool giant stars of spectral types K and M (figure 8 in Rayner et al. (2009)), however can also be indicators of a YSO (Casali and Eiroa

---

[6]These can be found on the HASH PN database.

1996; Reipurth and Aspin 1997). K-giants are much more common and brighter than YSOs or main sequence stars, and so it seems that this is likely the identify of this star. If it were a dwarf star, it would need to be a bright mid to late M-type in order to have such strong CO bandheads. This means it would also need to be fairly local, however parallax measurements by Gaia give a distance of 2.9 kpc (Gaia Collaboration et al., 2018). G18 measure mid-IR colours of the nebula consistent with a YSO (see Figure 2.8), however this bright star dominates the observations, making this method much less accurate at determining its identity. We suspect, therefore, that the bright central source is an unrelated field star projected onto the PN.

2.5.3   PN G077.7+03.1

PN G077.7+03.1 was not observed as part of the original programme, but as a separate run that also included observations of Abell 53 (see Chapter 3). It was therefore not mentioned in Jones et al. (2018), but it is included here as its spectra reveal some interesting kinematic properties. Previous measurements of PN G077.7+03.1 include mid-IR and radio photometry (Phillips and Marquez-Lugo 2011a; Condon and Kaplan 1998), optical spectrophotometry (Kazarian et al., 1998) and spectroscopy (Acker et al., 1992). We report here the first evidence of fast outflows in this PN. Figure 2.7a shows the IPHAS Hα image of PN G077.7+03.1 with contours from the UWISH2 H_2 image overlaid. The Hα image, which traces HII emission, reveals a bipolar structure, with the strongest emission concentrated in a small central rectangular region (2×1 arcsec), but extends towards the North-East and South-West as curved, almost spider-like arms out to radii of roughly 5 to 6 arcsec (regions 1 and 2). These arms continue out to much larger radii as H_2 emission, in a twisting, corkscrew-like manner (regions 3 and 4). H_2 emission can be found out to radii of $\approx$20 arcsec, and perhaps even further out towards the North-West as diffuse clumps.

Its 1D spectrum in Figure 2.7b reveals bright lines of Brγ, H_2 1-0 S(1) and HeII, and a faint continuum. In Figures 2.7c and 2.7d we show the the position-velocity diagrams for the H_2 1-0 S(1) and Brγ lines for the two slit positions used. Similarly to PN G050.5+00.0, there is evidence for accelerating molecular outflows, in that the H_2 1-0 S(1) line in regions 1 and 3 are redshifted, and region 2 and 4 are blueshifted, relative to the systemic velocity. Again, limited by the wavelength resolution of LIRIS, we can only roughly estimate the line-of-sight outflow velocities, which appear to be around 100 kms^{-1}. Combining this kinematic information with

(A)

(B)

(C)

(D)
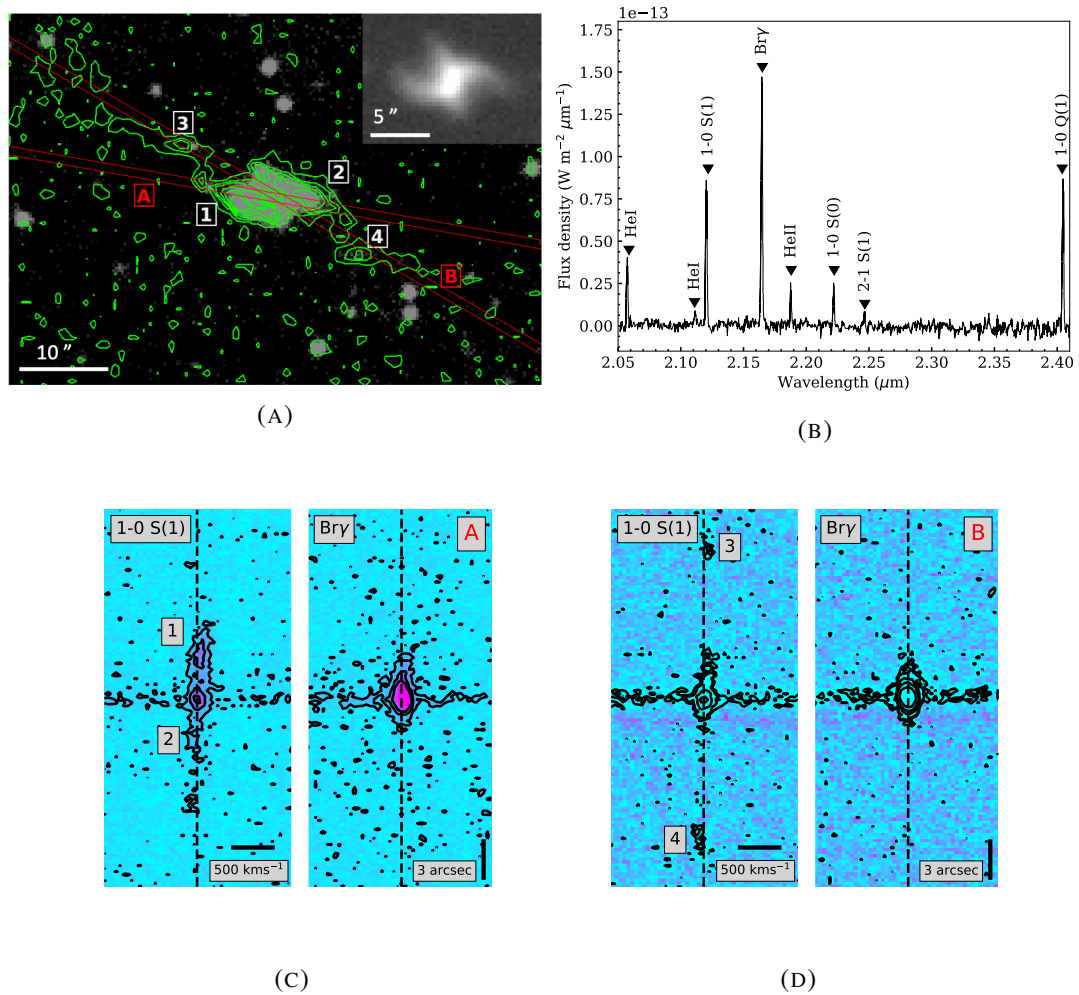
FIGURE 2.7: Images, spectra and P-V diagrams of PN G077.7+03.1. (A) IPHAS Hα image, with UWISH2 H$_2$ contours overlaid. The two LIRIS slit positions are also drawn: 'A' for the slit passing through the two bright central regions (labelled 1 and 2), and 'B' for the slit that covers the outer lobes (labelled 3 and 4). The smaller image in the corner highlights the structure within the Hα image. Scale bars for both images are given. North is up, East is left. (B) K-band spectrum at slit position 'A', with emission lines labelled. (C) and (D) Position-velocity diagrams for the H$_2$ 1-0 S(1) and Brγ emission lines at slit positions 'A' and 'B' respectively. The 4 regions from the IPHAS image are labelled.

the outflows' twisting morphologies, it appears that there is a rotational component, perhaps either due to the presence of a binary companion, or as a consequence of the environment.

2.5.4 Candidate PNe

22 targets in the sample are candidate PNe selected by the UWISH2 survey, with the remaining 7 targets either true, likely or possible PNe. Their Hα and H$_2$ images can be found in Figure 2.1, and their K-band spectra in Appendix A.1. 7 of the candidates have Hα emission in either IPHAS or SHS images (see Table 2.1). 13 candidate PNe have the Brγ line, but show no signs
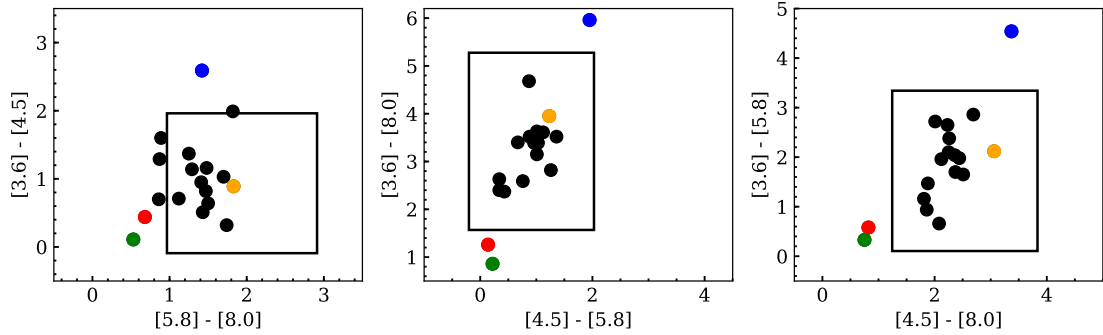
FIGURE 2.8: IRAC colour-colour plots for all objects observed with LIRIS, taken from Gledhill et al. (2018). The black rectangles give the regions where PNe are expected to lie, as defined in Gledhill et al. (2018). The lower left region in each plot represents the area where YSOs are expected to be found. The red, blue, orange and green points are the colours for PN G004.7-00.8, PN G020.8+00.4, PN G050.5+00.0 and PN G059.7-00.8 respectively.

of Hα emission in optical surveys. These are likely to be members of the optically-obscured PN population. Two of the candidates, PN G004.7-00.8 and PN G020.8+00.4, show no signs of Brγ or Hα emission - a lack of H$^+$ suggests these may not be PNe. Both objects have bipolar morphologies, however the former has multiple extended structures, including a large sweeping tail of H$_2$ extending eastward before turning south, while the latter consists of two small blobs of H$_2$ emission. G18 find mid-IR colours which place PN G004.7-00.8 in the YSO region, while the mid-IR colours of PN G020.8+00.4 are not consistent with PNe, YSOs or H$\textsc{ii}$ regions; instead it seems more likely to be a proto-planetary nebula (PPN) (see Figure 2.8).

We class 4 of the candidates as W-BPNe, including PN G009.7-00.9, G024.8+00.4, G036.4+00.1 and G040.4+01.1. These objects have either a compact core or a narrow, pinched waist in H$_2$ emission. All of these have strong Brγ and He$\textsc{i}$ (2.0587 μm) lines in their central regions, while the first two have v = 3 H$_2$ lines and additional helium lines He$\textsc{i}$ at 2.1127 μm and He$\textsc{ii}$ at 2.1891 μm) in their spectra. None show evidence of Hα emission, implying strong line-of-sight extinction. The cores of PN G009.7-00.9 and G036.4+00.1 can be resolved into two knots of H$_2$, which could be signs of molecular tori being viewed side-on (Kerber and Claeskens, 1997). PN G024.8+00.4 has well-separated H$_2$ lobes, with a smaller knot of emission just south of the centre. Its spectrum has a continuum gradually rising with wavelength, which is often a sign of dust. PN G040.4+01.1 also has two separated lobes, with two smaller knots to the north-west and south-east of the centre, which again could be due to a molecular torus.

Most of the remaining candidates we consider to be R-BPNe, which are bipolars with equatorial

ring structures[7], with the exception of PN G025.9-00.5, G037.4-00.1 and G047.5-00.34, whose H_2 morphologies are more elliptical. The R-BPNe in the sample have fairly similar spectra which lack the v = 3 H_2 lines. The HeI (2.0587 μm) line is observed in 3 of these objects, and one of the elliptical PNe (PN G037.4-00.1). The most impressive of the R-BPNe is PN G035.7-01.2, with the largest angular size of the sample. The object has arcs of H_2, which are likely to be cavity walls. It is invisible in Hα, but Brγ lines are present in the spectra. PN G047.1+00.4 is another good example, with a point-symmetric morphology resembling an eye rotated by 90°. It has a ring of H_2 emission, and two curved arms extending in the north and south directions. Spectra and Hα images reveal an ionised region localised to the centre, where we also observe the HeII (2.1891 μm) line - this is the only R-BPN in the sample which shows this feature. However, this could be an orientation effect, where we are looking down the major axis of the object, and from another viewing angle, the object could look more like a W-BPN.

2.6 Discussion

A simple means of determining the evolutionary stage of a PN is to observe the spatial extent of ionised material, traced by Brγ emission, in relation to the extent of H_2 emission. It follows that in PPNe, Brγ emission should be absent, as their central stars are not yet hot enough to ionise the surrounding envelope. When the temperature reaches $\approx$ 25000 K, ionisation produces Brγ emission localised to the central region. As the PN evolves, the ionisation front moves outwards, gradually replacing the molecular material. This process can be clearly seen in young PNe (Gledhill and Forde, 2015). As not all of the targets are visible at Hα, we can use the two-dimensional spectra to measure the radius of the Brγ emission along the slit as a proxy of the ionised radius, which can then be compared to the radius of H_2 1-0 S(1) emission. In Fig. 2.9, we demonstrate how the Brγ and H_2 radii are estimated using this technique for two objects, PN G024.8+00.4 (left) and PN G032.6-01.2 (right). The position along the slit is given on the x-axis, and the flux (summed over the slit width) is on the y-axis. The flux of the H_2 and Brγ emission lines along the slit are given by the black and red lines respectively. The point at which the flux reaches the noise level, determined by visual inspection, is the maximum extent of the emission line, and therefore the radius. The shaded areas show the regions where the radii are estimated to lie.

---

[7]It is sometimes difficult to see a clear ring feature, however we label any bipolar objects as R-BPNe if their morphology is obviously not of the W-BPN or elliptical type.
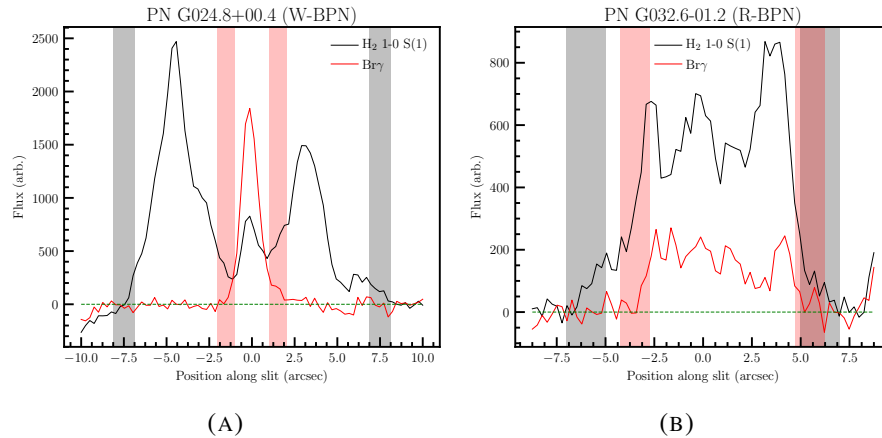
FIGURE 2.9: Slices showing the variation of the flux along the slit for PN G024.8+00.4 (A) and PN G032.6-01.2 (B), where the black and red lines are for the 1-0 S(1) and Brγ hydrogen emission lines respectively. The shaded regions represent the regions where the radii are estimated to lie. The green dotted line represents zero flux.

For the two objects in Fig. 2.9, we estimate the ratio of the diameters (or equivalently the radii) of the Brγ and 1-0 S(1) lines to be 0.2 ± 0.07 and 0.75 ± 0.18 for PN G024.8+00.4 and PN G032.6-01.2 respectively. We plot the ratio of the Brγ to H_2 radius on the x-axis of Fig. 2.10a for the bipolar objects in the sample. Error bars on these values reflect the regions in which the radii are estimated to lie, as the exact point at which the emission reaches the background level when using plots such as Fig. 2.9 is not always clear. This is certainly the case when the signal to noise ratio is low, or when nearby stars contaminate the two-dimensional spectra. In cases where it was deemed too difficult to estimate a radius using this technique alone, H_2 and Hα imaging were also inspected when available.

We use the UWISH2 images to separate the objects in Fig. 2.10a according to their bipolar type, with W-BPNe (compact core or narrow waist) in red and the R-BPNe (broad ring structures) in blue. We class five of the targets as W-BPNe, including PN G009.7-00.9, G024.8+00.4, G036.4+00.1, G040.4+01.1 and G050.5+00.0. Most of the remaining sample we class as R-BPNe. Three of the W-BPNe have Brγ regions localised to their centres, so they are positioned to the very left of the figure. These values are upper limits, indicated by hollow arrows, as their Brγ extents match the average seeing of the observations, given by the width of stellar continua in the same field of view. Fig. 2.9a, for PN G024.8+00.4, clearly shows the small angular extent of the Brγ emission when compared to the much more extended 1-0 S(1) emission. PN G050.5+00.0 lies to the right of this group, however we showed in Sec 2.5.1 that this object's Brγ emission is likely to be generated in an unresolved central region, and then scattered, possibly by a dusty torus, which increases its apparent Brγ extent. If this scattering process were

not occurring, PN G050.5+00.0 would move to the left, which we indicate by a solid arrow in Fig. 2.10a. PN G036.4+00.1 lies to the right of PN G050.5+00.0, however we note the slit was not positioned along the major axis of the nebula, which we believe to run north-east to south-west. Therefore, we have no information as to what extent the ionisation front has travelled into the lobes. We believe if the slit were positioned along the major axis, the Brγ to H_2 radius would decrease, and so we mark this object with a solid arrow to show it could also move to the left.

TABLE 2.4: Key line ratios and errors - uncorrected for extinction.

ID	Region	H_2 1-0 S(1) / 2-1 S(1)	H_2 1-0 S(1) / 3-2 S(3)	H_2 1-0 S(1) / Brγ	HeI (2.0587 μm) / Brγ
004.7-00.8	Centre	12 ± 2	—	—	—
009.7-00.9	Centre	7.3 ± 0.6	54 ± 19	2.4 ± 0.1	0.58 ± 0.04
	Lobes	7.2 ± 0.7	25 ± 7	—	—
020.7-00.1	Centre	—	—	6.4 ± 1.5	—
	Lobes	12 ± 2	—	19 ± 6	—
020.8+00.4	Centre	7.1 ± 1.3	—	—	—
	Lobes	6.3 ± 1.0	—	—	—
024.8+00.4	Centre	5.7 ± 2.0	—	0.50 ± 0.07	0.67 ± 0.03
	Lobes	8.6 ± 1.0	43 ± 9	—	—
025.9-00.5	North lobe	—	—	11 ± 4	—
032.6-01.2	Centre	12 ± 2	—	2.9 ± 0.2	0.30 ± 0.05
	Lobes	14 ± 2	—	7.5 ± 0.8	—
034.8+01.3	Centre	—	—	3.4 ± 0.4	0.25 ± 0.08
	Lobes	11 ± 2	—	11 ± 1	0.48 ± 0.14
035.7-01.2	Centre	—	—	6.4 ± 1.3	—
	Lobes	12 ± 2	—	9.1 ± 1.1	—
036.4+00.1	Centre	7.0 ± 1.5	—	1.6 ± 0.1	0.34 ± 0.06
	South lobe	8.4 ± 1.7	—	2.2 ± 0.2	0.31 ± 0.04
037.4-00.1	Centre	6.3 ± 1.7	—	0.44 ± 0.07	0.28 ± 0.07
	Lobes	9.3 ± 1.7	—	3.7 ± 0.4	0.28 ± 0.0
040.4+01.1	Centre	7.4 ± 2.5	—	1.4 ± 0.1	0.50 ± 0.10
	Lobes	7.8 ± 0.7	—	—	—
040.5-00.7	All	—	—	9.8 ± 3.7	—
042.1+00.4	All	—	—	12 ± 2	—
047.1+00.4	Centre	—	—	0.59 ± 0.03	0.46 ± 0.06
	Lobes	—	—	9.2 ± 2.6	—
047.5-00.3	All	—	—	5.5 ± 0.7	—
048.2-00.4	All	—	—	12 ± 3	—
050.0-00.7	Centre	—	—	6.0 ± 1.5	—
	Lobes	—	—	—	—
050.5+00.0	Centre	4.5 ± 0.4	—	0.05 ± 0.01	0.49 ± 0.01
	Lobes	5.8 ± 0.4	16 ± 3	2.0 ± 0.1	0.43 ± 0.04
057.9-00.7	Centre	14 ± 4	—	6.4 ± 0.7	—
	Lobes	13 ± 1	—	23 ± 7	—
058.1-00.8	Centre	—	—	7.9 ± 3.2	—
	Lobes	14 ± 4	—	10 ± 3	—
059.7-00.8	Lobes	13 ± 2	—	8.5 ± 1.0	—
060.5-00.3	Centre	12 ± 2	—	4.6 ± 0.3	—
	Lobes	14 ± 5	—	12 ± 3	—
061.8+00.8	Centre	—	—	7.0 ± 1.2	—
	Lobes	13 ± 2	—	11 ± 3	—
062.1+00.1	North lobe	—	—	—	—
062.2+01.1	Centre	—	—	12 ± 3	—
	Lobes	—	—	—	—
062.7+00.0	Centre	12 ± 3	—	2.7 ± 0.3	—
	North lobe	—	—	6.3 ± 1.0	—
064.1+00.7	Centre	9.3 ± 1.8	—	9.1 ± 1.6	—
	Lobes	13.3 ± 3.7	—	20 ± 5	—
064.9+00.7	Lobes	—	—	—	—

Once these considerations are taken into account, Fig. 2.10a shows a clear divide between the two morphological types, where, using this fairly simple tracer of evolution, the W-BPNe have
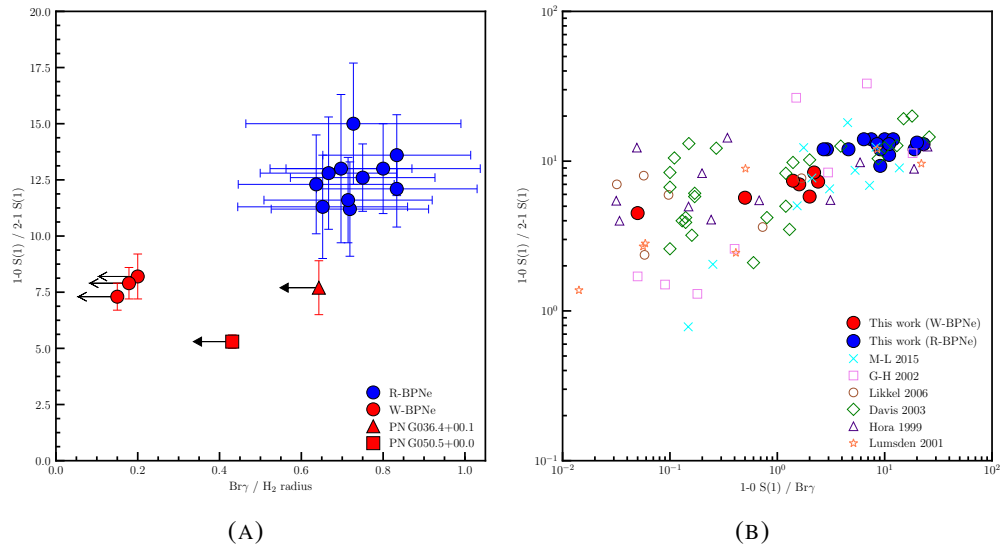
FIGURE 2.10: (A) Brγ to H$_2$ radius ratio versus 1-0 S(1) / 2-1 S(1) ratio for bipolar PNe. Error bars for radii are estimated from two-dimensional spectra. We mark solid arrows (not to scale) on two objects as we believe these should move to the left of the diagram, and hollow arrows on objects thought to represent upper limits (see text for details) (B) Line ratio plot with data from this work overlaid onto previous results. This includes the individual ratios extracted at different positions along the slit.

a smaller ratio of Brγ to H$_2$ radius, and so are less evolved, while the R-BPNe have larger Brγ to H$_2$ radii and are therefore more evolved. Fig. 2.9b compares the extents of the Brγ and H$_2$ emission for an R-BPN (PN G032.6-01.2), and it can be seen these are comparable. This idea makes sense, considering that many PPNe, in the stage of evolution immediately before the PN phase, have morphologies closely resembling those of W-BPNe. It is also known that strong emission lines of HeI (2.0587 μm) and Brγ are seen in young PNe (Gledhill and Forde, 2015), which is what we observe. On the other hand, the fact that the ionisation front in the R-BPNe has moved further from the central region approaching the outer bound of the H$_2$ radius, means that R-BPNe have had more time to form broad, ring-like structures. Ramos-Larios et al. (2017) measure physical sizes, kinematic ages and luminosities of a sample of bipolar PNe, and also find that R-BPNe are more evolved than W-BPNe. However, they suggest that R-BPNe and W-BPNe are likely formed from different progenitors, rather that forming an evolutionary sequence where one type evolves into the other.

Information about how the H$_2$ is being excited can be found by comparing the fluxes of emission lines. These line ratios have the advantage that the effect of differential extinction on their values is relatively small, due to small wavelength separations between lines. As explained in Chapter 1, H$_2$ can be excited thermally (e.g. in shocks) or non-thermally (e.g. UV-fluorescence), and various line ratios can be used to distinguish between the two. In general, values of 1-0 S(1)

to 2-1 S(1) of around 2 signify a UV-pumped spectrum (Black and Dalgarno 1976; Black and van Dishoeck 1987), while values of 10 or higher can be found in shocks (Hollenbach and Shull 1977; Burton et al. 1992). On the y-axis of Fig. 2.10a we plot the 1-0 S(1) / 2-1 S(1) ratio, summed over the object, and again there is good evidence for a dichotomy between the two bipolar types. Using Fig. 2.10a, the mean 1-0 S(1) / 2-1 S(1) ratios for the W-BPNe and R-BPNe are 7.3 ± 1.0 and 12.6 ± 1.1 respectively. This leads us to believe that on average, thermal excitation is the main mechanism exciting H_2 in R-BPNe, while the lower ratios of W-BPNe, and the fact that we only observe v = 3 H_2 transitions in these objects, could mean that UV-fluorescence plays a more important role in their excitation. While a mean 1-0 S(1) / 2-1 S(1) ratio of 7.3 is higher than the theoretical value for a purely UV pumped spectrum (~ 2.0), a fluoresced dense gas ($n \geq 10^5$ cm^{-3}) subjected to intense UV radiation will have an increased 1-0 S(1) / 2-1 S(1) ratio due to collisional heating (Sternberg and Dalgarno 1989, Hollenbach and Natta 1995). Further observational evidence is provided by Marquez-Lugo et al. (2015), who find UV excitation is likely occurring in the cores of W-BPNe, while R-BPNe are dominated by shock excitation. If R-BPNe are more evolved than W-BPNe, then it follows that UV-fluorescence is a process associated with younger objects, while thermal excitation prevails as the PN evolves; a trend found observationally by Davis et al. (2003). This broadly agrees with the theoretical work of Natta and Hollenbach (1998), however once high resolution integral field spectroscopy is obtained, it is evident that line ratios, and therefore excitation mechanisms, can vary across the surface of young PNe, and highlights the importance of the dependence of line ratios on density (Gledhill and Forde, 2015).

There are also indications that the 1-0 S(1) / Brγ ratio is linked with the evolutionary stage, for example Guerrero et al. (2000) find this ratio is low for young PNe, while more evolved objects have larger ratios. This is supported by G18, who find that for a small sample of 23 PNe covering a range in physical radii of 0.03 to 0.6 pc, the H_2 surface brightness is approximately independent of radius, and therefore age. Combining this with the fact that the Hα, and therefore Brγ, surface brightness decreases with radius (Frew et al., 2016), it follows that the H_2 1-0 S(1) / Brγ surface brightness ratio increases with increasing radius and age. The trend between the 1-0 S(1) / Brγ and 1-0 S(1) / 2-1 S(1) ratios has been investigated in Marquez-Lugo et al. (2015). We have taken fig. 7 from this work, included our data, and reproduced the graph here as Fig. 2.10b. Additional data comes from Hora et al. (1999), Lumsden et al. (2001), García-Hernández et al. (2002), Davis et al. (2003), Likkel et al. (2006) and Marquez-Lugo et al. (2015). This plot shows a loose positive correlation between the 1-0 S(1) / 2-1 S(1) and 1-0 S(1) / Brγ ratios, and our

data is no exception to this trend. Again, we separate our targets into W-BPNe and R-BPNe, and there is a clear separation between the two bipolar types, where W-BPNe have lower 1-0 S(1) / Brγ ratios than the R-BPNe (mean values of 1.5 ± 0.8 and 10.6 ± 6.0 respectively). Fig. 2.10b may then suggest an evolutionary sequence, where bipolar PNe move to larger 1-0 S(1) / Brγ and 1-0 S(1) / 2-1 S(1) ratios as they evolve.

PN G050.5+00.0 has the lowest 1-0 S(1) / 2-1 S(1) and 1-0 S(1) / Brγ ratios in the sample, with values of 4.5 and 0.05 respectively in the central region. If PNe do generate higher line ratios as they evolve, this would mean that PN G050.5+00.0 is the youngest PN in the sample. It is likely that UV fluorescence is largely contributing to the excitation of H$_2$ here, in regions closer to the central star. Assuming a fluoresced gas, a 1-0 S(1) / 3-2 S(3) value of 16 for PN G050.5+00.0 could indicate a high FUV flux with a density $\geq 10^5$ cm^{-3} (Burton et al., 1990). We find good evidence for fast outflows in the lobes of PN G050.5+00.0 (see Sec 2.5.1), which increase the chance of the H$_2$ being shock-excited. This is likely the reason behind the small increase of the 1-0 S(1) / 2-1 S(1) ratio to 5.8 in the lobes.

With no data available for physical sizes, we have needed to rely on a very simple method for determining the potential evolutionary stages of our sample. This method of comparing the spatial extents of Brγ (ionised) and H$_2$ 1-0 S(1) (molecular) emission is most effective if the PN is spherical, consisting of a inner shell of ionised emission, defined by a Strömgren radius, and an outer shell of molecular emission. Clearly some of the radiation needs to be able to reach the outer molecular material for it to become excited, and therefore visible in observations. As our sample consists mainly of non-spherical objects, this means there will be some issues using this method, as it is likely that ionised and molecular material will not be distributed evenly. However, assuming the velocity of the material is directed along the major axis, this method should still have some merit for bipolar PN. The radius-age relation for PNe is well established for elliptical or round PNe (Jacob et al., 2013), but how applicable this relation is to bipolar PNe is uncertain, and will depend on the formation mechanism. There will likely be a deviation from the general relation, especially if the H$_2$ arises in the outflows of such bipolars, or in structures at the ends of the outflows rather than in the ionised region close to the central star.

2.7 Summary

In this chapter, medium-resolution, K-band spectra of a sample of 29 Galactic Plane objects taken from the UWISH2 survey, including 4 true, 2 likely, 1 possible and 22 candidate PNe, have been presented. Additionally, the spectra of PN G077.7+03.1, not part of the original target selection, was presented. The candidate PNe were selected on the basis of their morphologies, and lack of association with known star-forming regions. Evidence for ionised material, in the form of either Brγ emission in the spectra or Hα emission in narrow-band surveys, is found in all but 2 of the targets. One of these, PN G020.8+00.4, is likely to be a PPN - at an earlier stage of evolution with a central star not yet hot enough to ionise its surrounding environment. PN G004.7-00.8 has mid-IR colours indicative of a YSO. 13 of the candidate PNe show no clear Hα emission, however we detect Brγ emission in their spectra. These objects potentially contribute to the optically-obscured PN population, and their discovery clearly highlights the need for multi-wavelength studies of PNe, to accurately predict the number of PNe in the Milky Way.

We have used the spectra to calculate line ratios, which have been used to constrain the mechanisms dominating the excitation of H$_2$. Most of the targets that we believe to be PNe are either R-BPNe (large ring structures) or W-BPNe (pinched waist), while the remaining 3 are considered to be elliptical. In agreement with previous studies, we find the former are predominantly thermally excited, while in the latter, UV fluorescence may have more influence. The link between line ratios and the spatial extent of ionised emission could mean that W-BPNe are younger objects, while the R-BPNe are more evolved, and an evolutionary scheme in which one class evolves into the other is worth further investigation.

Chapter 3

Observational analysis of Abell 53

3.1 Introduction

(A)

(B)
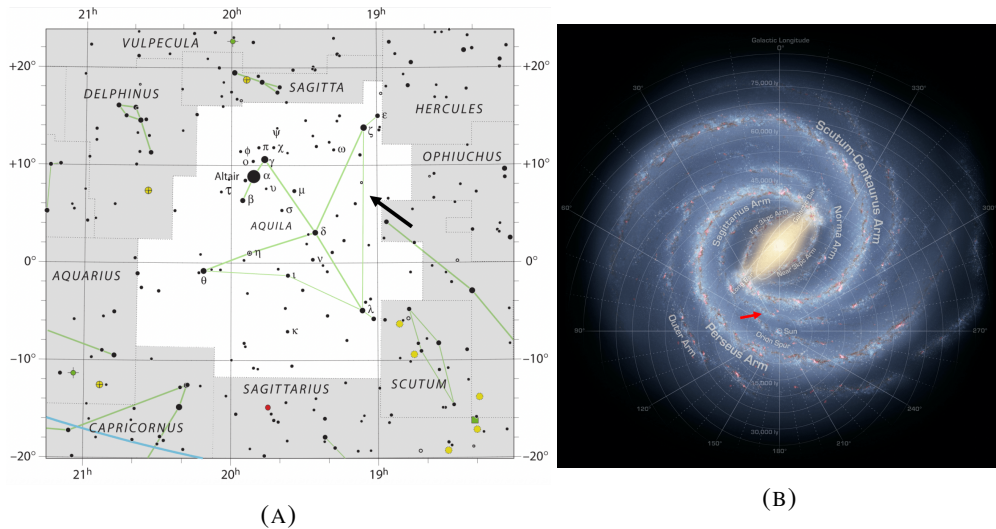
FIGURE 3.1: The location of Abell 53 within the constellation Aquila (left) and in the Milky Way (right), marked by the arrows. Image credits: IAU and Sky & Telescope magazine (Roger Sinnott & Rick Fienberg) (left) and NASA/JPL-Caltech/R. Hurt (SSC/Caltech) (right)

Abell 53, also known as PN A66 53 or PN G040.3-00.4, is a planetary nebula located in the Aquila constellation in the plane of the Milky Way (RA/DEC 19:06:45.90 +06:23:52.48, or l/b 40.3704 -0.4752). The location of Abell 53 in the sky is given in Figure 3.1a. Using the Hα surface brightness - radius relation (Frew et al., 2016), it is located at a distance of 2.3 kpc. Using this estimate, Figure 3.1b shows its place in the Milky Way. Images of the object in Hα and H$_2$ emission lines are shown in Figure 3.2, and it is clear to see that unlike many PNe, with their often axisymmetric structures, Abell 53 appears nearly completely round, and has a strong
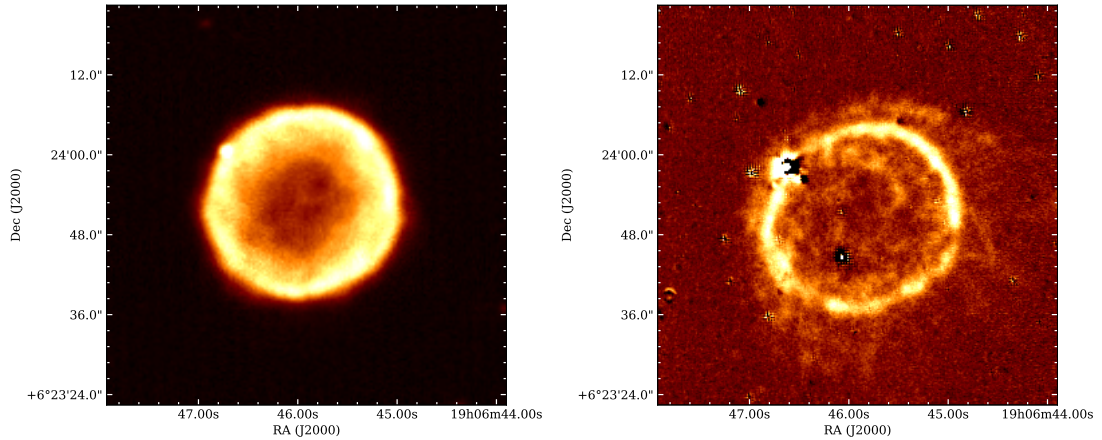
FIGURE 3.2: Hα+[NII] (left) and H$_2$-K (right) images of Abell 53, taken from the IPHAS and UWISH2 surveys respectively.

ring-like appearance in both ionised and molecular emission. H$_2$ emission is seen to extend beyond the bright ring, as wispy clumps trailing towards a south-west direction.

Using the SIMBAD database, Abell 53 has appeared in 56 papers and surveys. The first study to include Abell 53 and classify it as a planetary nebula was Abell (1955), which used blue and red photographs from the Palomar Observatory, comprising of 73 PNe and 13 globular clusters. A revised list was composed in 1966 (Abell, 1966), which added another 13 PNe and included more reliable position measurements. Their list of PNe included objects with low surface brightnesses and large angular diameters, and so they surmise that these PNe are at a more evolved stage of evolution. They record values for the magnitudes and surface brightnesses of the nebula and the central star, the angular diameter (31 arcsec), the physical diameter (0.25 pc), the distance (between 1.69 and 2.44 kpc), the electron density (853 cm^{-3}) and the temperature and luminosity of the central star (138 kK and 219 L$_\odot$ respectively).

Since this work, Abell 53 has appeared in multiple survey and catalogue papers, including optical (e.g. Perek and Kohoutek 1967, Acker et al. 1992, Frew et al. 2013), infrared (e.g. Kwok et al. 2008, Phillips and Marquez-Lugo 2011a, Froebrich et al. 2015) and radio (e.g. Milne and Aller 1982, Condon and Kaplan 1998, Pazderska et al. 2009). The first targeted study of Abell 53 was by Phillips and Ramos-Larios (2008), who use Spitzer/IRAC images as part of the GLIMPSE survey (Benjamin et al., 2003) to investigate how the flux at 3.6, 4.5, 5.8 and 8.0 μm varies with radius. The images are shown in Figure 3.3 (their figure 3), and the spatial profiles in Figure 3.3b (their figure 4). They find particularly strong 8 μm emission, which is roughly twice as strong in the outer regions than the inner, and extends beyond the emission observed in optical imaging, out to radii of around 18 arcsec. Within this band, strong ionic transitions,

including [ArII] ($\lambda 6.985$ μm), [NeVI] ($\lambda 7.642$ μm) and [ArIII] ($\lambda 8.991$ μm) can be found, as well as polycyclic aromatic hydrocarbons (PAH) features at 7.7 and 8.6 μm.

(A)

(B)
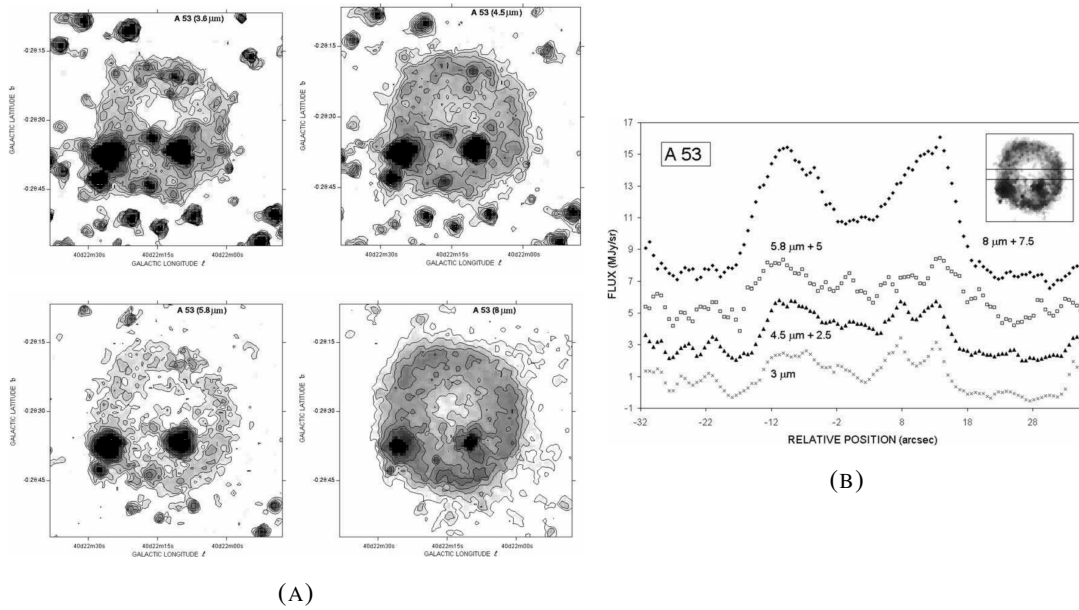
FIGURE 3.3: Spitzer/IRAC images (left) and spatial profiles (right) of Abell 53 taken from Phillips and Ramos-Larios (2008).

In another study, Abell 53 appeared in a series of papers looking at objects with rings, discs or shells (known as bubbles) in 24 μm emission from the MIPSGAL Legacy Survey (Carey et al., 2009). Ingallinera et al. (2014b) made radio observations of Abell 53 with the Very Large Array at 1.4 and 5 GHz, and calculated the most precise flux densities to date (59.7 ± 0.5 mJy and 64.1 ± 0.8 mJy respectively for 5 and 1.4 GHz). They find a flat spectra index, $\alpha = -0.06 \pm 0.01$, suggesting thermal free-free emission from the ionised region. Using the 5 GHz radio map, they find a distance of 2.1 ± 0.3 kpc, and assuming an electron temperature of 10000 K, an ionised mass of 0.2 M$_\odot$. Figure 10 from their work is shown here as Figure 3.4, where the ring structure can be distinguished in the 1.4 GHz image.

In this Chapter, a range of observations at different wavelengths of Abell 53 are presented (Sect. 3.2). These include photometric measurements of images from surveys calculated in this work but also found in the literature, along with spectroscopy from telescope proposals. Using a range of techniques, these observations will then be used to estimate some physical properties of Abell 53 (Sect. 3.3). In Chapter 4, the observations will be used to create a model of Abell 53 using the photoionisation code Cloudy, by finding an optimum set of physical parameters.
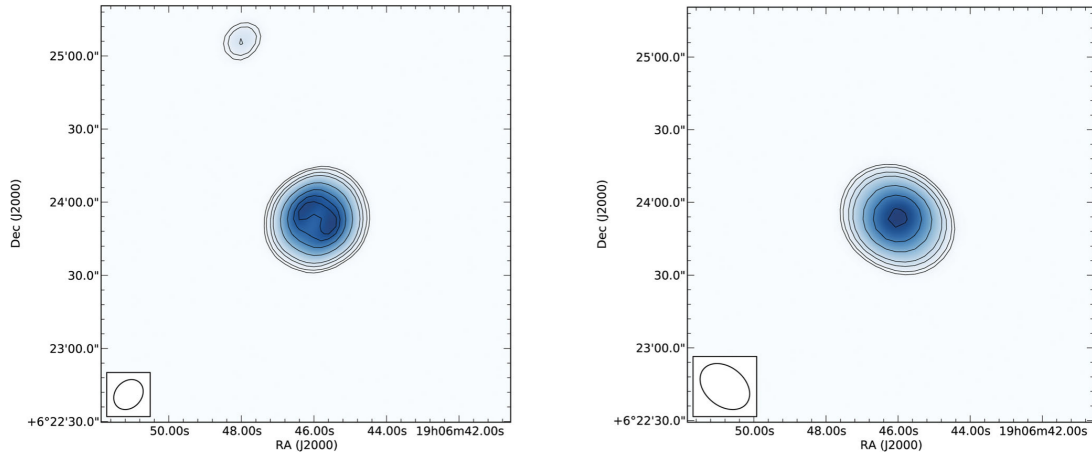
FIGURE 3.4: VLA image of Abell 53 at 1.4 GHz (left) and 5 GHz (right), taken from In-
gallinera et al. (2014b).

3.2 Multi-wavelength observations

3.2.1 Photometry

Photometry involves measuring the total amount of light from an object, and converting the raw data units into something physically useful, such as flux in Wm^{-2}. A wide range of images are available for Abell 53, ranging from the near-UV all the way to radio wavelengths. It is the aim here to obtain the flux of Abell 53 at as many wavelengths as possible, in order to create an SED (Spectral Energy Distribution), which will provide a useful comparison for the models. For cases where the data is available, and no fluxes are found in the literature, we attempt to measure our own using aperture photometry (Sect. 3.2.1.1). Otherwise, we collect fluxes from the literature (Sect. 3.2.1.2).

3.2.1.1 Calculated photometry: near-UV to near-IR

Aperture photometry is the process of measuring the counts (raw data units) of an object, relative to the background noise level, by placing a circular aperture at the maximum extent of the signal (characterised by a point spread function, or PSF, for stars). We have performed aperture photometry on images taken from surveys ranging from the near-UV to the near-IR. These include:

- The UV-Excess Survey of the Northern Galactic Plane (UVEX, Groot et al. 2009); an imaging survey of the northern Galactic plane in the optical RGO U, Sloan g and r filters,

as well as the narrowband HeI $\lambda\lambda 5875$ filter. Its main aim was to look for objects with a UV excess, such as white dwarfs, metal-deficient stars and background quasars.

- The INT Photometric Hα Survey of the Northern Galactic Plane (IPHAS; Drew et al. 2005); a survey of the Northern plane in Sloan r and i filters, and narrow-band Hα, using the Isaac Newton Telescope on La Palma (the same used for UVEX). IPHAS images distinguish objects such as post-AGB stars, PNe, Be stars, young stellar objects (YSOs), white dwarfs, binary systems and many main-sequence A stars and M giants.

- The Panoramic Survey Telescope and Rapid Response System data archive 1 (Pan-STARRS1, or PS1; Chambers et al. 2016); using g, r, i, z and y broadband filters at a purpose-built telescope at Haleakala Observatory, Hawaii. Its science targets included anything from solar system objects to high-redshift QSOs.

- The UKIRT Infrared Deep Sky Survey Galactic Plane Survey (UKIDSS/GPS; Lucas et al. 2008); designed as the successor to 2MASS (Skrutskie et al., 2006), using the J, H and K near-infrared filters on the United Kingdom Infrared Telescope. Its focus was on cool, local brown dwarfs, high-redshift dusty starburst galaxies, elliptical galaxies, galaxy clusters and extremely distant quasars.

- The UKIRT Widefield Infrared Survey for H$_2$ (UWISH2; Froebrich et al. 2011), a narrowband 2.122 μm H$_2$ survey of the Galactic plane. Its objects of interest include PNe, supernova remnants and young stellar objects.

Apart from the UVEX images, which were obtained by special request, all other images were downloaded directly from the corresponding survey websites. The PS1 images are stacks, and are the optimal combination of the data best suited for photometry purposes - these are described in Waters et al. (2016). A selection of images from these surveys are shown in Figure 3.5. The overall shape of Abell 53 is fairly consistent in the different filters; nearly completely round, with its surface brightness increasing with increasing radial distance. The H$_2$-K image shows a thinner, ring-like appearance with a bright rim of molecular emission.

The counts are extracted from the images using the interactive image display tool GAIA, part of the STARLINK software package (Currie et al., 2014). An aperture with radius either 15 or 16 arcsec is used, depending on the visible extent of emission, centred on the object, and the counts summed. Uncertainties are estimated from the noise in the images, where the total noise is given by:
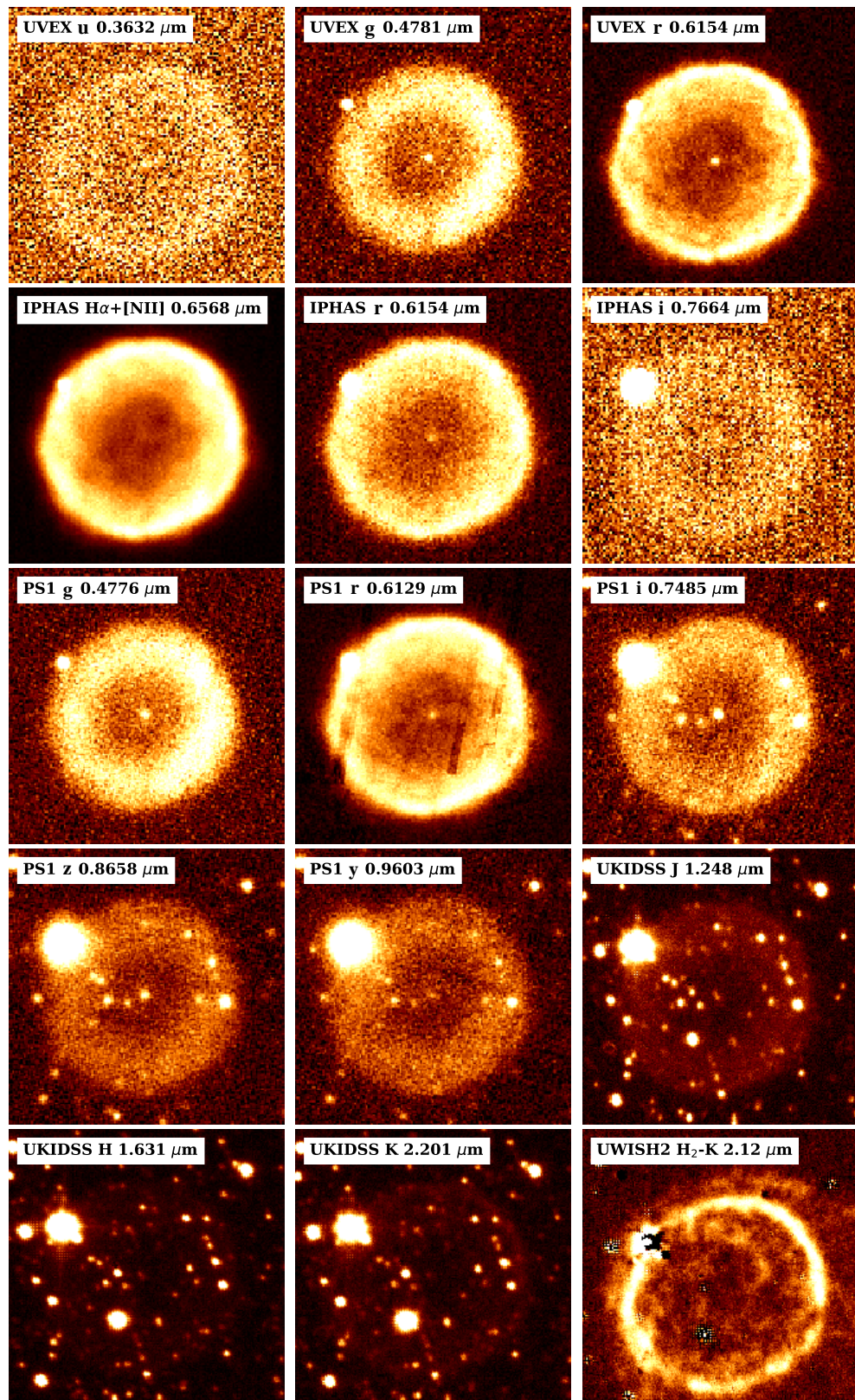
FIGURE 3.5: Abell 53 images from near-UV to near-IR used for photometry. All images are 40 arcsec across. North is up, East is left.

TABLE 3.1: Details of the optical/near-infrared photometry. Columns are: Band (name of the survey and the filter used); λ_{eff} (effective wavelength of the filter); W_{eff} (effective width of the filter); T_{exp} (integration time); m_{zp} (magnitude zero point); X (airmass); E (extinction coefficient) and $F_{\lambda,\text{zp}}$ (flux zero point).

Band	λ_{eff} (Å)	W_{eff} (Å)	T_{exp} (s)	m_{zp}	X	E	$F_{\lambda,\text{zp}}$ (erg cm^{-2} s^{-1} Å^{-1})
UVEX U	3632	618	120	22.97 ± 0.01	1.118682	0.46	3.859×10^{-9}
UVEX G	4781	1201	30	25.09 ± 0.01	1.11638	0.19	5.151×10^{-9}
UVEX R	6154	1219	30	24.58 ± 0.02	1.121133	0.09	2.490×10^{-9}
IPHAS Hα+[NII]	6568	94	120	26.2616 ± 0.03	1.0	0.0	1.661×10^{-9}
IPHAS r	6154	1220	30	27.898 ± 0.03	1.0	0.0	2.490×10^{-9}
IPHAS i	7664	1472	10	26.0487 ± 0.03	1.0	0.0	1.280×10^{-9}
PS1 G	4776	1166	894	25.0	1.0	0.0	4.773×10^{-9}
PS1 R	6130	1318	872	25.0	1.0	0.0	2.897×10^{-9}
PS1 I	7485	1243	930	25.0	1.0	0.0	1.943×10^{-9}
PS1 Z	8658	966	540	25.0	1.0	0.0	1.452×10^{-9}
PS1 Y	9603	615	620	25.0	1.0	0.0	1.180×10^{-9}
UKIDSS J	12483	1590	10	24.465 ± 0.018	1.09	0.05	3.014×10^{-10}
UKIDSS H	16313	2920	10	24.727 ± 0.023	1.09	0.05	1.183×10^{-10}
UKIDSS K	22010	3510	5	24.05 ± 0.01	1.09	0.05	4.026×10^{-11}
UWISH2 H$_2$-K	21220	210	720	21.121 ± 0.051	1.0	0.05	4.283×10^{-11}

$$N_{total} = \sqrt{N^2 + N_{sky}^2 + N_{dark}^2 + N_{ron}^2} \tag{3.1}$$

where $N = \sqrt{n}$, *n* being the number of photons from the source, N_{sky} is the noise from the sky underneath the source, N_{dark} is the noise from the dark current due to the thermal radiation from the detector, and N_{ron} is the read-out noise, which occurs when the signal is amplified.

Any bright foreground stars within the aperture are subtracted from the total using additional apertures, the most notable of these is a bright star at the north-east edge. This is demonstrated in Figure 3.6a. For three of the PS1 images (I, Z, Y) and the UKIDSS images, many foreground stars lie within the extraction region, and have a significant effect on the total counts measured. Their contribution was removed using their magnitudes obtained through the VizieR service. We then overlay an annulus at the same central position, with an inner radius of 20 arcsec, and an outer radius of 25 arcsec, in order to correct for the local background level. An example of the positions of the target and background annuli are shown in Figure 3.6a, along with that of the bright foreground star.

To convert the sky-subtracted counts into flux densities, F_λ, we use the following general equation

$$F_\lambda = \frac{\text{counts}}{t_{\text{exp}}} \cdot F_{\lambda,\text{zp}} \cdot 10^{-m_{\text{zp}}/2.5} \cdot 10^{(X-1)(E/2.5)} - F_{\lambda,\text{FG}} \tag{3.2}$$
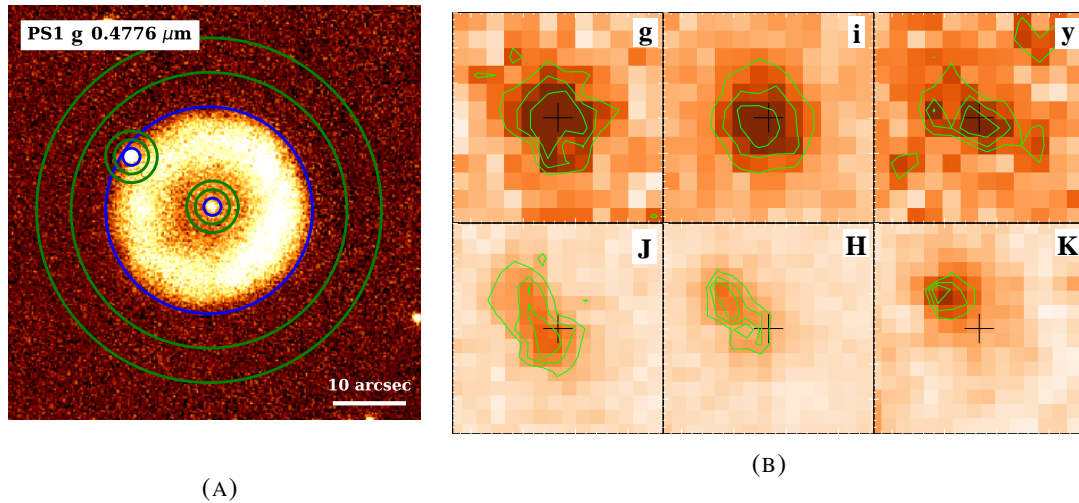
FIGURE 3.6: Left: g-band image of Abell 53 from the Pan-STARRS1 survey. North is up, East is left. This image demonstrates where various apertures were placed in order to calculate the photometry. Signal contained within the blue apertures are associated with the source, while the green annuli give the background regions. The possible central star is visible at the centre of the image, while a bright foreground/background star is located to the North East. Right: The changing position of the possible central star with wavelength. The top frames are from the Pan-STARRS1 survey (g, i and y bands), and the bottom frames are from the UKIDSS survey (J, H and K bands). All frames are 3×3 arcsec cutouts. Each frame has the same coordinates at its centre, marked by the black cross-hair. Green contours are shown to make the signal clearer.

where t_{exp} is the exposure time in seconds, $F_{\lambda,zp}$ is the flux zero point, m_{zp} is the magnitude zero point, X is the airmass, E is the extinction coefficient and $F_{\lambda,FG}$ is the total flux density from foreground/background stars within the target aperture, if required. Flux density, F_λ, is the flux per unit wavelength (or frequency), and its usual units are erg cm^{-2} s^{-1} Å^{-1}. These are converted into flux units (erg cm^{-2} s^{-1}) by simply multiplying by the effective width of the filter (W_{eff}). F_{zp} are usually taken from the SVO Filter Service[1], while the other parameters can be found in the FITS headers. For the UWISH2 image, we follow the same procedure as Froebrich et al. (2015), using the 2MASS filter properties in order to apply the conversion (filter width = 0.2620 μm). Photometry for UWISH2 is performed on the H$_2$-K image, so the continuum level has been removed. All the parameters used in the aperture photometry are given in Table 3.1, while the measured counts and flux densities are given in Table 3.2. Uncertainties in flux density are calculated by propagating[2] the detector noise and m_{zp} uncertainty through Equation 3.2.

---

[1]The SVO Filter Profile Service. Rodrigo, C., Solano, E., Bayo, A. http://ivoa.net/documents/Notes/SVOFPS/index.html. The Filter Profile Service Access Protocol. Rodrigo, C., Solano, E. http://ivoa.net/documents/Notes/SVOFPSDAL/index.html

[2]Uncertainty propagation in general made use of the following two Python packages: UNCERTAINTIES for first order approximations (`http://pythonhosted.org/uncertainties/`) and MCERP for a Monte Carlo approach (`https://pythonhosted.org/mcerp/`).

TABLE 3.2: Optical/near-infrared photometry fluxes for the main nebula and proposed central star. Columns are: Band (survey and filter); Counts (sky-subtracted counts, with an estimation of the noise); F_λ (flux density, calculated using Equation 3.2) and F (flux, i.e. $F_\lambda \cdot W_{\mathrm{eff}}$).

Band	Counts	F_λ (erg cm^{-2} s^{-1} Å^{-1})	F (erg cm^{-2} s^{-1})
		Nebula + Central Star	
UVEX U	21242 ± 592	$4.66(\pm0.14) \times 10^{-16}$	$2.88(\pm0.08) \times 10^{-13}$
UVEX G	143920 ± 798	$2.32(\pm0.03) \times 10^{-15}$	$2.78(\pm0.03) \times 10^{-12}$
UVEX R	647750 ± 1312	$7.98(\pm0.15) \times 10^{-15}$	$9.73(\pm0.18) \times 10^{-12}$
IPHAS Hα+[N II]	1499900 ± 1350	$7.79(\pm0.21) \times 10^{-14}$	$7.32(\pm0.20) \times 10^{-12}$
IPHAS r	446360 ± 1298	$7.70(\pm0.21) \times 10^{-15}$	$9.39(\pm0.26) \times 10^{-12}$
IPHAS i	55855 ± 696	$2.72(\pm0.08) \times 10^{-15}$	$4.00(\pm0.12) \times 10^{-12}$
PS1 G	4276700 ± 5983	$2.283(\pm0.003) \times 10^{-15}$	$2.663(\pm0.004) \times 10^{-12}$
PS1 R	24404000 ± 9730	$8.108(\pm0.003) \times 10^{-15}$	$1.0687(\pm0.0004) \times 10^{-11}$
PS1 I	12403000 ± 13391	$1.32(\pm0.03) \times 10^{-15}$	$1.64(\pm0.04) \times 10^{-12}$
PS1 Z	15688000 ± 14564	$1.45(\pm0.02) \times 10^{-15}$	$1.40(\pm0.02) \times 10^{-12}$
PS1 Y	41687000 ± 43738	$3.30(\pm0.02) \times 10^{-15}$	$2.03(\pm0.02) \times 10^{-12}$
UKIDSS J	2294700 ± 5603	$1.68(\pm0.19) \times 10^{-15}$	$2.66(\pm0.30) \times 10^{-12}$
UKIDSS H	8295300 ± 14515	$4.33(\pm0.27) \times 10^{-15}$	$1.26(\pm0.08) \times 10^{-11}$
UKIDSS K	4896300 ± 10882	$8.91(\pm0.90) \times 10^{-16}$	$3.13(\pm0.32) \times 10^{-12}$
UWISH2 H$_2$-K	1830600 ± 2223	$3.88(\pm0.18) \times 10^{-16}$	$1.02(\pm0.05) \times 10^{-12}$
		Central Star	
Band	Counts	F_λ (erg cm^{-2} s^{-1} Å^{-1})	F (erg cm^{-2} s^{-1})
UVEX U	133 ± 66	$2.91(\pm1.44) \times 10^{-18}$	$1.80(\pm0.89) \times 10^{-15}$
UVEX G	309 ± 65	$4.97(\pm1.04) \times 10^{-18}$	$5.97(\pm1.25) \times 10^{-15}$
UVEX R	1182 ± 96	$1.46(\pm0.12) \times 10^{-17}$	$1.78(\pm0.15) \times 10^{-14}$
PS1 G	11014 ± 540	$5.88(\pm0.29) \times 10^{-18}$	$6.86(\pm0.33) \times 10^{-15}$
PS1 R	32713 ± 1150	$1.09(\pm0.04) \times 10^{-17}$	$1.43(\pm0.05) \times 10^{-14}$
PS1 I	45938 ± 1239	$9.60(\pm0.26) \times 10^{-18}$	$1.19(\pm0.03) \times 10^{-14}$
PS1 Z	41481 ± 1127	$1.12(\pm0.03) \times 10^{-17}$	$1.08(\pm0.03) \times 10^{-14}$
PS1 Y	45952 ± 3749	$8.75(\pm0.71) \times 10^{-18}$	$5.38(\pm0.44) \times 10^{-15}$
UKIDSS J	1800 ± 363	$8.93(\pm1.79) \times 10^{-18}$	$1.42(\pm0.29) \times 10^{-14}$
UKIDSS H	3176 ± 953	$4.86(\pm1.45) \times 10^{-18}$	$1.42(\pm0.42) \times 10^{-14}$
UKIDSS K	568 ± 709	$1.10(\pm1.37) \times 10^{-18}$	$3.87(\pm4.80) \times 10^{-15}$

The process is repeated in a similar fashion for the proposed central star, found at the centre of the nebula. Apertures with 1 or 2 arcsec diameters are used, and the background region carefully placed over the nearby nebula region so as to cover a region with a similar background level of the target. We attempt to measure a signal for UVEX, PS1 and UKIDSS images, however very few counts are available at the short and long wavelength ends, making the photometry unreliable for UVEX U, and UKIDSS H and K images. It also needs to be assumed that there is little difference in the background noise level from the CS location to the background annulus region. Interestingly, we discovered that the position of the central point source in the PS1 images was slightly different to its position in the UKIDSS data (see Figure 3.6b). The offset between the centre of the PSFs in the G and K images is measured at just over 1 arcsec. This suggests that the point source may actually consist of two separate stars, a brighter optical star at

the centre of Abell 53, and an infrared star positioned slightly to the north-east. Whether this is a chance alignment, or we are in fact seeing a binary system, is unclear. However, this scenario makes extracting the flux from the proposed central star, presumably the brighter optical star, more challenging. We attempt to only include counts from the optical star in our measurements, however blending of the two PSFs in the UKIDSS images means that the accuracy of these measurements is limited.

3.2.1.2 Photometry from the literature: IR to radio

TABLE 3.3: List of mid-infrared fluxes of Abell 53 from the literature, in chronological order. Uncertainties are given where measured.

Reference	Telescope/Detector	Wavelength (μm)	Flux density / magnitude
Acker et al. (1992)	IRAS	12	2.31 Jy
		25	1.44 Jy
		60	75.46 Jy
		100	152 Jy
Phillips and Ramos-Larios (2008)	Spitzer/IRAC	3.6	9.89 mag
		4.5	8.23 mag
		5.8	8.21 mag
		8.0	7.1 mag
Kwok et al. (2008)	Spitzer/IRAC	3.6	31 mJy
		4.5	26 mJy
		5.8	69 mJy
		8.0	180 mJy
	IRAS	12	2.856 Jy
		25	0.724 Jy
		60	<8.540 Jy
		100	<96.5 Jy
Mizuno et al. (2010)	Spitzer/MIPS	24	1100 mJy
Phillips and Marquez-Lugo (2011b)	Spitzer/MIPS	24	1180 $\pm$ 25.5 mJy
Phillips and Marquez-Lugo (2011a)	AKARI	18	1043 mJy
		65	11713 mJy
		90	10097 mJy
		140	19476 mJy
Gledhill et al. (2018)	Spitzer/IRAC	3.6	9.76 $\pm$ 0.02 mag
		4.5	8.65 $\pm$ 0.01 mag
		5.8	8.53 $\pm$ 0.02 mag
		8.0	6.36 $\pm$ 0.01 mag

TABLE 3.4: List of radio fluxes of Abell 53 from the literature, in chronological order.

Reference	Telescope	Frequency (GHz)	Flux density (mJy)
Milne and Aller (1982)	Parkes 64m	14.7	76
Reich et al. (1984)	Effelsberg 100m	2.7	360
Condon and Kaplan (1998)	VLA	1.4	34.1 $\pm$ 1.1
Pazderska et al. (2009)	OCRA-p	30	54.9 $\pm$ 6.5
Hoare et al. (2012)	VLA	5	9.12
Ingallinera et al. (2014b)	VLA	5	59.7 $\pm$ 0.5
		1.4	64.1 $\pm$ 0.8

We searched the literature for any measured mid-IR flux densities of Abell 53, which are given in Table 3.3. The various telescopes and detectors used include:

- The Spitzer Space Telescope, with two photometers: the Infrared Array Camera (IRAC) (Fazio et al., 2004) and the Multiband Imaging photometer (MIPS) (Rieke et al., 2004). IRAC has filters at 3.6, 4.5, 5.8 and 8.0 μm, while MIPS has filters at 24, 70 and 160 μm.

- The Infrared Astronomical Satellite (IRAS) (Neugebauer et al., 1984), with bands at 12, 25, 60 and 100 μm.

- AKARI; the first Japanese satellite dedicated to infrared astronomy (Murakami et al., 2007). It has 2 scientific instruments: the infrared camera (IRC), with filters from 2.4 to 23 μm; and the far-infrared surveyor (FIS), with filters from 67 to 163 μm.

The reliability of some of the mid-IR photometry is uncertain, due to the presence of 2 foreground/background stars within the main shell of Abell 53. This is demonstrated in images from the Wide-field Infrared Survey Explorer (WISE; Wright et al. 2010), shown in Figure 3.7. As the wavelength of the observations increase, the angular resolution of the images worsens, making it difficult to distinguish between flux from the nebula and flux from the stars. However, we still feel they are of some use, and we will include the measurements in our SED of Abell 53 (see Section 3.3.1), to compare to our models.
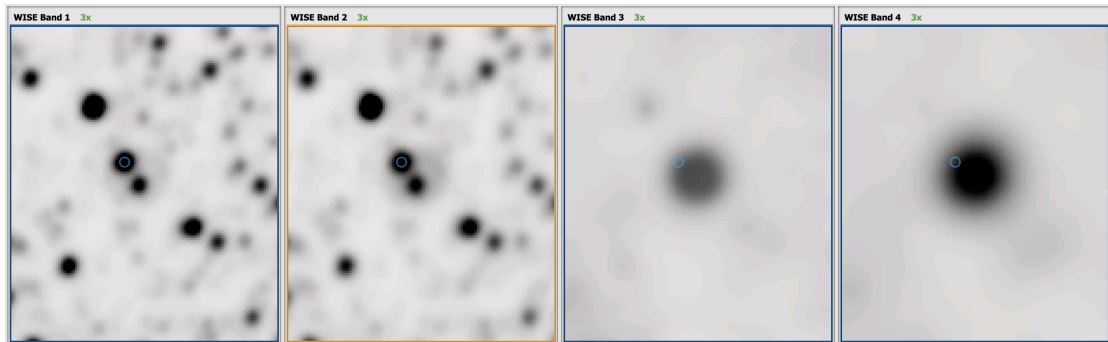
FIGURE 3.7: Images of Abell 53 in the 4 WISE bands: 3.3, 4.6, 12 and 22 μm.

In 1970, the first radio measurements (2 cm) were recorded of Abell 53 (Rubin, 1970), using the National Radio Astronomy Observatory. Since then, more detailed radio observations have been taken at different frequencies, including the 64m Parkes Observatory in Australia; the Effelsberg 100m telescope in Germany; the Very Large Array (VLA) in the USA; and the One Centimetre Receiver Array Prototype (OCRA-p) in Poland. Measured flux densities can be found in Table 3.4.

TABLE 3.5: Mid-infrared and radio photometry fluxes of Abell 53, which are displayed graphically in the SED (Figure 3.18). Columns are: Band (name of the survey/instrument and the filter used); λ_{eff} (effective wavelength of the filter); W_{eff} (effective width of the filter); F_{ν} (flux density per unit frequency); F_{λ} (flux density per unit wavelength) and F (the flux, i.e. $F_{\lambda} \cdot W_{\text{eff}}$).

Band	λ_{eff} (Å)	W_{eff} (Å)	F_{ν} (mJy)	F_{λ} (erg cm^{-2} s^{-1} Å^{-1})	F (erg cm^{-2} s^{-1})
IRAC 3.6	3.508×10^4	6836	32.4 ± 2.3	$7.90(\pm0.56) \times 10^{-16}$	$5.40(\pm0.38) \times 10^{-12}$
IRAC 4.5	4.437×10^4	8650	60.0 ± 32.9	$9.15(\pm5.02) \times 10^{-16}$	$7.91(\pm4.34) \times 10^{-12}$
IRAC 5.8	5.628×10^4	12561	57.8 ± 12.4	$5.47(\pm1.17) \times 10^{-16}$	$6.87(\pm1.47) \times 10^{-12}$
IRAC 8.0	7.589×10^4	25288	153.1 ± 51.4	$7.97(\pm2.68) \times 10^{-16}$	$2.02(\pm0.68) \times 10^{-11}$
MIPS 24	2.321×10^5	52963	1180 ± 26.0	$6.57(\pm0.14) \times 10^{-16}$	$3.48(\pm0.08) \times 10^{-11}$
IRAS 12	1.015×10^5	60670	2856	8.32×10^{-15}	5.05×10^{-10}
IRAS 25	2.173×10^5	100174	724	4.60×10^{-16}	4.61×10^{-11}
IRAS 60	5.199×10^5	305160	<8540	$<9.48 \times 10^{-16}$	$<2.89 \times 10^{-10}$
IRAS 100	9.530×10^5	332640	<96500	$<3.19 \times 10^{-15}$	$<1.06 \times 10^{-9}$
AKARI 18	1.761×10^5	99690	1043	1.01×10^{-15}	1.01×10^{-10}
AKARI 65	6.295×10^5	183383	11713	8.87×10^{-16}	1.63×10^{-10}
AKARI 90	7.690×10^5	330800	10097	5.12×10^{-16}	1.69×10^{-10}
AKARI 140	1.409×10^6	433116	19476	2.94×10^{-16}	1.28×10^{-10}
OCRA-p 30	1.000×10^8	-	54.9	1.65×10^{-22}	-
PARKES 14.7	2.041×10^8	-	76.0	5.47×10^{-23}	-
VLA 5	6.000×10^8	-	59.7	4.98×10^{-24}	-
VLA 1.4	2.140×10^9	-	64.1	4.20×10^{-25}	-

To plot these measurements on an SED, we convert all flux densities to erg cm^{-2} s^{-1}Å^{-1}. For the IRAC observations, with 3 independent sets of measurements, we take the means as the values and standard deviations as the uncertainties. The mid-IR/radio measurements we decide to include in our SED are given in Table 3.5, chosen for either being the more reliable measurement, if multiple observations exist, or an average is taken.

3.2.2 Optical and near-infrared spectroscopy

3.2.2.1 ISIS

TABLE 3.6: Optical line fluxes for Abell 53 from Kaler (1983) (given relative to Hβ) and Acker et al. (1992) (relative to Hα).

Line + λ (Å)	Kaler (1983)	Line + λ (Å)	Acker et al. (1992)
Hβ 4861	100	Hα 6563	100
HeII 4686	35 ± 28	[OIII] 5007	100
[OIII] 4959	240 ± 49	[NII] 6584	318
Hα 6563	1093 ± 210	[SII] 6717	17
[NII] 6584	833 ± 167	[SII] 6731	19

Abell 53 is bright at optical wavelengths, as evident in the photometry. PNe have strong permitted and forbidden emission lines in the optical region (around 400 to 700 nm), and ratios of these lines can give information about the temperature and density in the nebula; therefore, obtaining
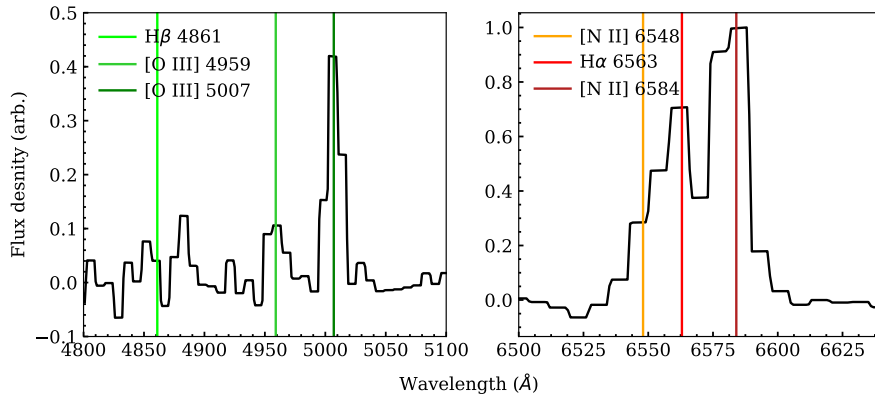
FIGURE 3.8: Low resolution optical spectrum of Abell 53 (Stenholm and Acker, 1987). Left: the [OIII] 4959+5007 doublet, and the Hβ line, if it were detected. The faint emission line at ∼ 4880 Å does not coincide with standard PNe emission lines, and therefore likely to be erroneous. Right: the Hα 6563 and [NII] 6548+6583 triplet. The locations of these emission lines are represented by the coloured vertical lines.

optical spectra is an extremely useful tool for learning about the physical processes within PNe. The first measurement of optical emission lines fluxes for Abell 53 was part of a spectrophotometry campaign using the University of Illinois 1m reflector at Prarie Observatory (Kaler, 1983). Additional measurements of optical lines are given in the Strasbourg-ESO catalogue of Galactic Planetary Nebulae (Acker et al., 1992), both of which are given in Table 3.6.

After extensively searching the literature, the only optical spectrum that could be found for Abell 53 was from Stenholm and Acker (1987). From a FITS file on the HASHPN platform, two sections of the spectrum have been reproduced here as Figure 3.8. It is immediately obvious that wavelength resolution is poor, causing lines to become blended (e.g. the [NII] 6548, Hα and [NII] 6583 triplet), and that signal to noise is low, so that only a few lines have been captured. For this reason, and with only a few previous measurements of line fluxes of Abell 53 with questionable accuracy, we decided to apply for our own optical spectroscopic observations. On the 8th August, 2019, we obtained data using the Intermediate-dispersion Spectrograph and Imaging System (ISIS) on the William Herschel Telescope (WHT). ISIS has 2 arms (blue and red), each with their own spectrograph, meaning that they can be used simultaneously. The blue grating, R300B, covers the range 3700 - 5300 Å, with a spectral resolution, $\Delta\lambda/\lambda$ at 4000 Å = 976 for a 1 arcsec slit width, resulting in a dispersion of 0.86 Å/pix. The plate scale is 0.20 arcsec / pixel. The red grating, R316R, covered 5700 - 8000 Å, with $\Delta\lambda/\lambda$ at 7000 Å = 1842 for a 1 arcsec slit width, giving a dispersion of 0.93 Å/pix. The plate scale is 0.22 arcsec / pixel. A slit width of 1 arcsec is used throughout. Observing conditions were generally good, with the seeing varying between 0.5 and 0.8 arcsec over the night. Images obtained for each of the blue

and red arms of ISIS included: 2×1200 s exposures of the target, 1×5 s standard exposures (for correcting atmospheric effects and flux calibration), 2 arc frames at the location of the target and standard (for wavelength calibration), 7 bias frames (for bias subtraction) and 5 flat frames (for flat-fielding).

3.2.2.2 LIRIS

As one of the main purposes of this work is to model the molecular hydrogen component of Abell 53, we applied for K-band spectroscopy, due to many ro-vibrational lines of H_2 located in this region. The service observations were acquired on the 29th June, 2018, using LIRIS. Flat-field and arc frames, along with observations of a spectroscopic standard, were also taken. We used a slit width of 1 arcsec; positioned at the same location as that used in the ISIS spectra (Figure 3.9), so that direct comparisons could be made. Observing conditions were generally good.
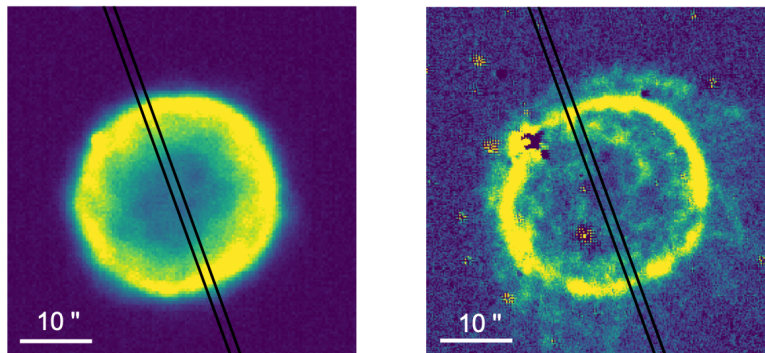
FIGURE 3.9: Approximate positions of the slits used for ISIS and LIRIS spectroscopy, overlaid onto IPHAS Hα image (left) and UWISH2 H_2-K image (right). Scale bars indicate 10 arcsec.

3.2.2.3 The spectra

The data reduction for ISIS and LIRIS data are similar, the latter of which was explained in detail in Chapter 2. Therefore, only a brief description of the process to create the calibrated ISIS spectra, and the IRAF packages used, is provided. The flowchart in Figure 3.10 shows this process, and also includes the steps required to create surface brightness profiles for various emission lines (see Sect 3.2.2.4). The raw target exposures for the blue and red filters are shown in Figure 3.11a.

FIGURE 3.10: A flowchart demonstrating the steps needed to transform the raw data from ISIS into fully-calibrated spectra and surface brightness profiles.

(A)   (B)

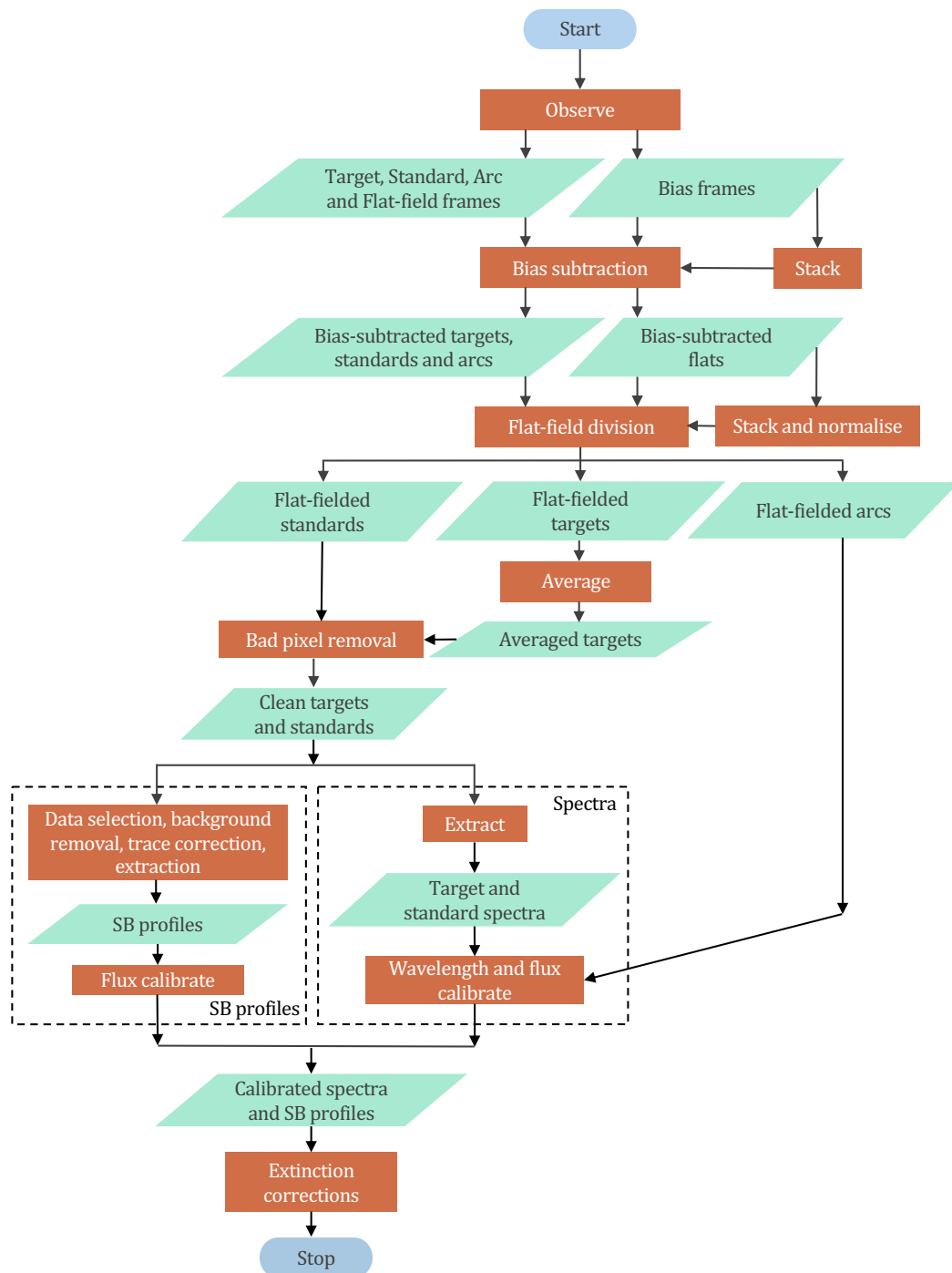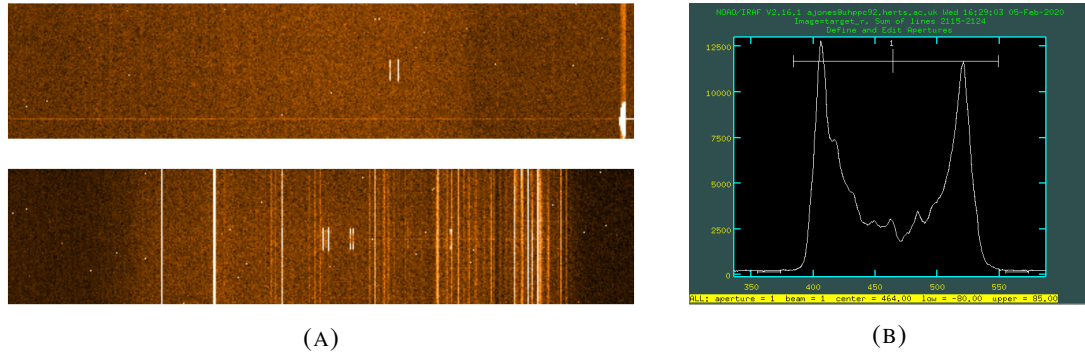FIGURE 3.11: (A) Raw ISIS spectra for Abel 53 in blue (top) and red (bottom). Dispersion axis in x direction, spatial axis in y direction. (B) A snapshot of the APALL routine, used to define the target and background regions for spectra extraction.

Getting the images ready   After downloading and organising the raw data from the INT server, the first step was bias subtraction - a step which was handled automatically for LIRIS data. A bias frame is a zero second exposure image, containing the signal due to the internal electronics. The bias frames were median stacked using IRAF: ZEROCOMBINE, and subtracted from the images of the target, standard, flat-fields and arcs using IRAF: IMARITH. After flat-fielding, the 2 target frames were averaged together to increase the signal to noise ratio, and bad pixels were removed from the target and standard images.

Extraction and calibration   Unlike LIRIS data, that were extracted using Python, for ISIS we used the IRAF: APALL package. We decided to use this package as it is designed to be used for extracting stellar spectra, i.e. a bright continuum, where in this case we could use the faint but detectable continuum from the proposed central star. APALL is split into 4 stages:

1. Finding the spectrum. This is a fairly simple step, as the location of the bright emission lines are easily visible, as in Figure 3.11a.

2. Define the target and background regions. All the flux from all the nebula emission lines must be extracted, so we decided to use the brighter, most extended lines to define the regions. In Figure 3.11b, a snapshot of the window used to define the target and background regions using APALL is given for the [NII] 6583 line. The x-axis is position along the slit, and the y-axis is the counts. We decided on a target extraction region of around 35 arcsec, and 2 background regions either side with a few arcsec width.
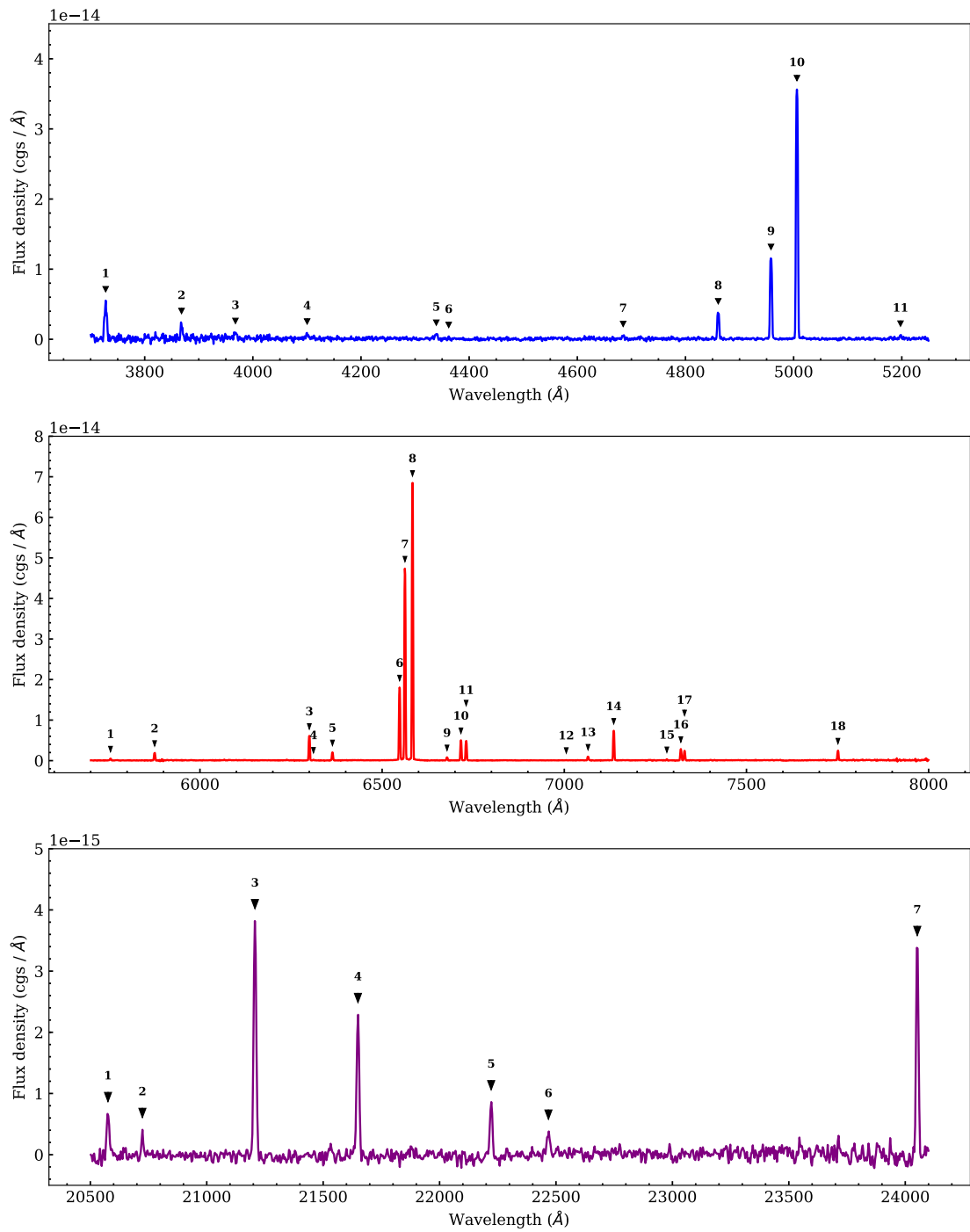
FIGURE 3.12: One dimensional fully-calibrated optical and near-IR spectra: blue (top), red (middle), K-band (bottom). Information about the numbered emission lines is given in Table 3.7. Note spectra have not been corrected for extinction at this stage.

3. Tracing the spatial profile along the dispersion axis. The dispersion axis will usually be slightly offset to the columns of pixels due to 3 main reasons: 1) distortions from the camera optics 2) misalignment between the grating and the chip 3) differential atmospheric refraction, causing the blue and red ends of the spectrum to be shifted by different amounts. The offset was negligible with LIRIS data, but more obvious in ISIS, and needed to be corrected.

4. Extracting the spectrum. At every point along the dispersion axis, the pixels within the target region are summed, and the background removed using the pixels from the background region.

The extracted spectra were then wavelength and flux calibrated as explained in Chapter 2, and are given in Figure 3.12 for ISIS and LIRIS. We attempted to extract the spectrum of the proposed central star, however the SNR was too low. This was unfortunate, as spectra of the central star would have been very useful for determining its temperature and luminosity for the modelling stage.

A large number of emission lines are identified in the spectra, by comparing wavelengths in spectra to those of typical nebula emission lines. We identified 36 lines: 11 in the blue, 18 in the red and 7 in the K-band; a mix of recombination, forbidden and molecular lines. In order to measure the flux of the emission lines, Gaussians are fitted, shown in Figures B.1 and B.2 for ISIS, and B.3 for LIRIS. Fluxes are given in Table 3.7, along with the rest wavelength in vacuum for each line.

3.2.2.4 The surface brightness profiles

With long slit spectroscopy, spatial information is also available, which means that the variation of the flux of emission lines along the axis of the slit is recorded - known as a surface brightness (SB) profile. This information will be extremely useful in the modelling stage, but also as an indicator of how physical properties such as shocks and excitation level vary across the nebula (see Sect 3.3). Sections from the cleaned images of the target in the 3 bands are given in Figure 3.13, and it is from these images that the SB profiles are generated; the steps required are given below.

TABLE 3.7: Fluxes of emission lines before correcting for extinction. F(rel.) are the fluxes given relative to Hβ.

| No.	Line ID	λ	F (erg cm^{-2} s^{-1})	F (rel.)
		ISIS: Blue		
1	[OII]	3728	$2.81(\pm0.18)\times10^{-14}$	1.688 ± 0.136
2	[NeIII]	3868	$8.46(\pm1.35)\times10^{-15}$	0.508 ± 0.085
3	[NeIII]	3968	$4.31(\pm1.21)\times10^{-15}$	0.259 ± 0.074
4	Hδ	4101	$2.32(\pm0.83)\times10^{-15}$	0.139 ± 0.051
5	Hγ	4339	$3.66(\pm0.76)\times10^{-15}$	0.219 ± 0.047
6	[OIII]	4362	$8.48(\pm3.35)\times10^{-16}$	0.051 ± 0.020
7	HeII	4685	$2.35(\pm0.55)\times10^{-15}$	0.141 ± 0.034
8	Hβ	4861	$1.67(\pm0.08)\times10^{-14}$	1.000 ± 0.000
9	[OIII]	4958	$5.22(\pm0.17)\times10^{-14}$	3.136 ± 0.186
10	[OIII]	5006	$1.60(\pm0.05)\times10^{-13}$	9.605 ± 0.569
11	[NI]	5198	$1.76(\pm0.48)\times10^{-15}$	0.106 ± 0.029
		ISIS: Red		
1	[NII]	5754	$1.79(\pm0.14)\times10^{-15}$	0.108 ± 0.010
2	HeI	5876	$7.74(\pm0.41)\times10^{-15}$	0.465 ± 0.034
3	[OI]	6300	$2.50(\pm0.09)\times10^{-14}$	1.502 ± 0.091
4	[SIII]	6312	$5.13(\pm1.12)\times10^{-16}$	0.031 ± 0.007
5	[OI]	6364	$8.25(\pm0.29)\times10^{-15}$	0.495 ± 0.030
6	[NII]	6548	$7.58(\pm0.26)\times10^{-14}$	4.551 ± 0.275
7	Hα	6563	$2.00(\pm0.07)\times10^{-13}$	11.983 ± 0.732
8	[NII]	6583	$2.81(\pm0.09)\times10^{-13}$	16.869 ± 0.974
9	HeI	6678	$3.10(\pm0.16)\times10^{-15}$	0.187 ± 0.013
10	[SII]	6716	$2.03(\pm0.07)\times10^{-14}$	1.221 ± 0.074
11	[SII]	6731	$1.99(\pm0.07)\times10^{-14}$	1.197 ± 0.073
12	[ArV]	7005	$1.95(\pm0.70)\times10^{-16}$	0.012 ± 0.004
13	HeI	7065	$3.82(\pm0.18)\times10^{-15}$	0.230 ± 0.016
14	[ArIII]	7136	$3.03(\pm0.10)\times10^{-14}$	1.817 ± 0.108
15	HeI	7281	$8.82(\pm1.55)\times10^{-16}$	0.053 ± 0.010
16	[OII]	7320	$1.17(\pm0.04)\times10^{-14}$	0.704 ± 0.042
17	[OII]	7330	$9.79(\pm0.31)\times10^{-15}$	0.588 ± 0.034
18	[ArIII]	7751	$9.42(\pm0.36)\times10^{-15}$	0.566 ± 0.035
		LIRIS		
1	HeI	20580	$1.00(\pm0.11)\times10^{-14}$	0.603 ± 0.075
2	H$_2$ 2-1 S(3)	20720	$3.39(\pm0.60)\times10^{-15}$	0.203 ± 0.037
3	H$_2$ 1-0 S(1)	21210	$5.40(\pm0.09)\times10^{-14}$	3.244 ± 0.169
4	Brγ	21650	$3.12(\pm0.12)\times10^{-14}$	1.873 ± 0.116
5	H$_2$ 1-0 S(0)	22220	$1.24(\pm0.08)\times10^{-14}$	0.746 ± 0.063
6	H$_2$ 2-1 S(1)	22470	$5.09(\pm1.03)\times10^{-15}$	0.306 ± 0.064
7	H$_2$ 1-0 Q(1)	24050	$4.42(\pm0.15)\times10^{-14}$	2.653 ± 0.157
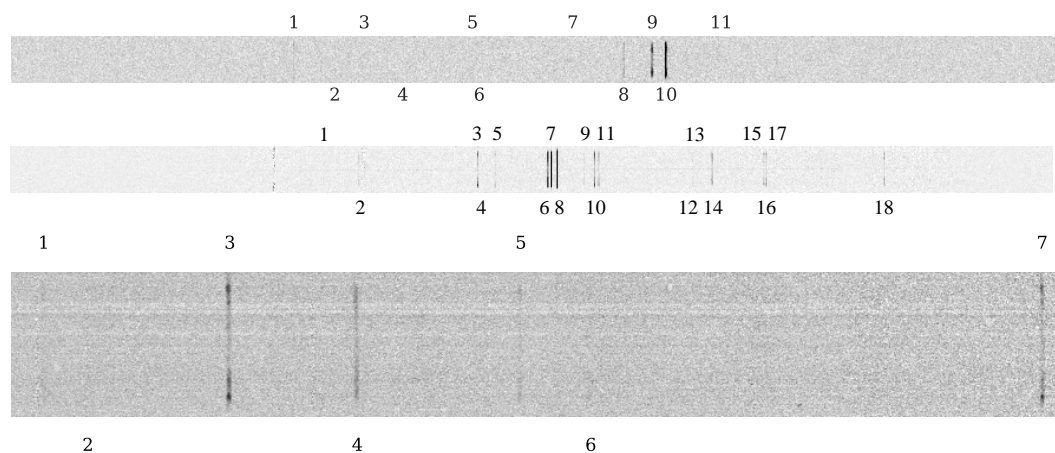
FIGURE 3.13: Regions used to extract the nebula spectra and surface brightness profiles, for the 3 filters: blue (top), red (middle) and K-band (bottom). The x-axis represents wavelength and the y-axis represents position along the slit. Each emission line is numbered according to Table 3.7.

1. Select the data. Similarly to extracting the spectra, the target and background regions were selected to ensure all the flux was accounted for. SB profiles would be made for all the emission lines identified from the spectra.

2. Remove the background. Unlike with the spectra, where APALL does this automatically, removal of the background needs to be done manually. The mean and standard deviation of the background regions either side of the target region are calculated. These are then used to create a synthetic background region, with normally distributed counts with mean and standard deviation as given, with the same dimensions as the target region. This is then subtracted from the data, and checks are made to ensure the background level is as close to zero as possible.

3. Trace correction. The standard star spectra were used, as they had much higher SNR than the faint central star. We therefore assume that the trace correction for the standard star spectra is also representative of the target spectra. The plots in Figure 3.14 show how the position of the standard star continua varies along the dispersion axis for the blue and red filters. Polynomial fits are made to the data (cubic for blue, quadratic for red) so that the pixel shift can be determined for any position along the axis. The centre of the region used to extract the SB profile for each emission line is then adjusted by this amount.

4. Extraction. The counts for each emission line could then be summed across the width of the slit, but preserved along the spatial direction, meaning that a profile which varies as a

function of radius was created. These profiles are given in Figures B.4, B.5 and B.6 for the blue, red and K-band filters respectively.

5. Flux calibration. To put a physical surface brightness unit on the y-axes of these profiles, e.g. erg cm^{-2} s^{-1} arcsec^{-2}, the total flux contained within each profile is used. However, rather than using the fluxes found from the spectra, we will instead use the IPHAS Hα+[NII] photometry, which will provide a more consistent comparison when comparing the Cloudy models to the observations.

- Firstly, we need to separate the Hα flux, F(Hα), and the [NII] flux from the total flux in the IPHAS image, F(Hα + [NII]), using the following equation:

$$F(H\alpha) = \frac{F(H\alpha + [NII])}{R + 1} \tag{3.3}$$

where R is the [NII] ($\lambda\lambda 6548+6584$) to Hα ratio measured from the spectra. This equation assumes that the transmission of the IPHAS Hα filter is consistent across the 3 emission lines[3]. The transmission of the filter is given in Figure 3.15, along with the corresponding portion of our red spectrum of Abell 53. R is found to be 1.78, and combining this with F(Hα + [NII]) = 7.32×10^{-12} erg cm^{-2} s^{-1}, gives a total Hα flux, F(Hα) = 2.63×10^{-12} erg cm^{-2} s^{-1}.

- The average of the North and South portions of the Hα surface brightness profile (Figure 3.16, left) is interpolated to create a synthetic 2D image, and scaled so that its total flux is equal to F(Hα) - Figure 3.16, middle. The flux is extracted from a 1 arcsec width region, which should be comparable to the Hα flux measured directly from the spectra. This value is found to be 1.21×10^{-13} erg cm^{-2} s^{-1}.

- The Hα SB profile along the whole slit is then scaled so that the integral of the profile equals this value. The units of the profile will now be in erg cm^{-2} s^{-1} arcsec^{-2}, as in Figure 3.16, right.

- SB profiles for other lines could then be calibrated, instead setting the integral to equal the line flux relative to the calculated Hα flux in the slit.
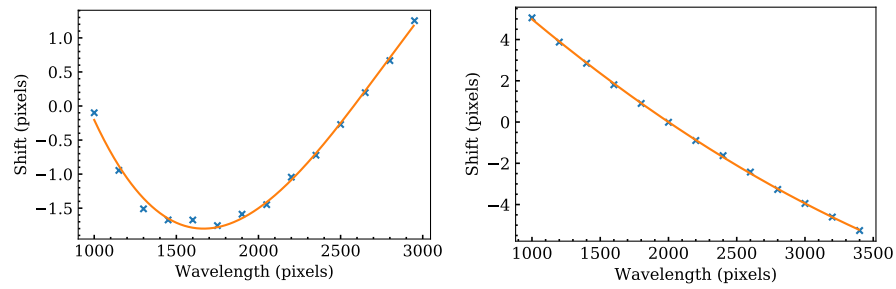
FIGURE 3.14: Determining the trace correction for the blue (left) and red (right) spectra. At select points along the dispersion axis, Gaussians are fitted to cross sections of the standard star spectra, and the mean position relative to a reference point is given by the blue crosses. The orange line is the best polynomial fit to the data points (cubic for blue, quadratic for red).
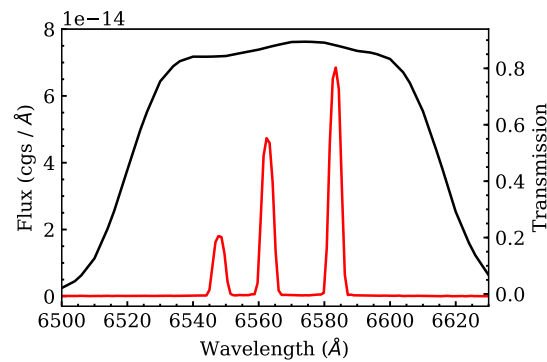
FIGURE 3.15: A close up of the red spectrum of Abell 53 showing the Hα and [N II] triplet (red line) along with the transmission profile for the IPHAS Hα filter (black line)
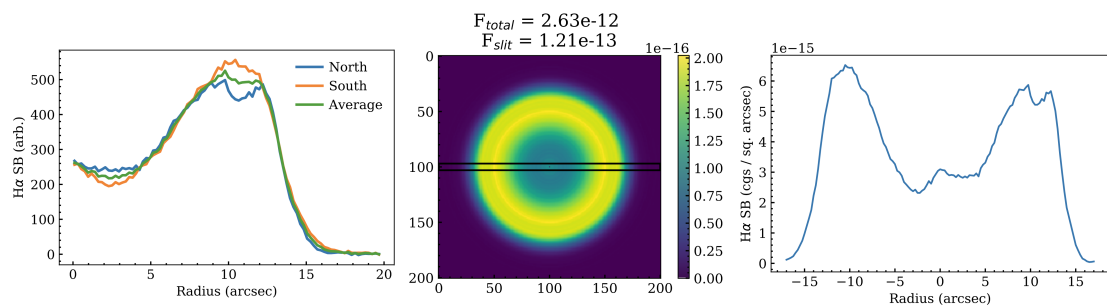
FIGURE 3.16: SB profile flux calibration. The average Hα profile (left) is used to generate a synthetic Hα image (middle) with a total flux equal to that measured from photometry. The flux in a slit with same dimensions as used for ISIS spectroscopy (black box) is measured and used to calibrate either the Hα SB profile (right) or other profiles using line ratios relative to Hα.
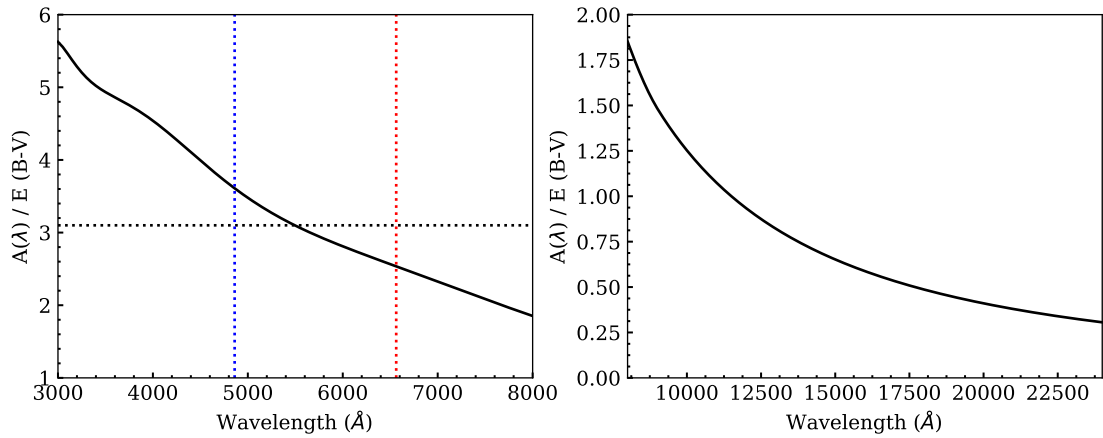
FIGURE 3.17: The extinction law of Cardelli et al. (1989), for $R_v = 3.1$, for optical (left) and near-infrared (right). The black horizontal dotted line represents $A(\lambda) / E(B-V) = 3.1$. The blue and red vertical dotted lines are the locations of $H\beta$ and $H\alpha$ respectively.

3.2.3 Extinction

Extinction is the decrease in the measured flux of an object due to interstellar dust absorbing and scattering the radiation as it passes through. It is highly dependent on wavelength, with observations at ultraviolet wavelengths being much more affected than those at infrared. An extinction law describes this dependence, and a commonly used law is that of Cardelli et al. (1989), which is shown in Figure 3.17. This extinction law is for a normalised extinction, $R_v = 3.1$, which is used for the diffuse ISM.

As Abell 53 lies very close to the plane of the Milky Way, where dust and gas is highly concentrated, the effect of extinction on the measured fluxes from the photometry and spectroscopy must be accounted for [4]. The method we use to correct for extinction is known as the Balmer Decrement, using the $H\alpha$ and $H\beta$ line fluxes from the ISIS spectroscopy. We compare the results to those using similar methods, relying on the same basic physical principles however using different observations, including other optical line ratios, optical and radio photometric fluxes, or a combination of both.

---

[3]In reality, we took into account the varying transmission at the positions of the 3 emission lines, however the difference is minimal.

[4]As extinction weakens with increasing wavelength, we do not correct for it at wavelengths greater than the near-IR K-band

3.2.3.1 The Balmer decrement using spectra

One of the most common methods for extinction determination is known as the Balmer Decrement. Assuming Case B of recombination, in a low density environment and an electron temperature of 10^4 K, the ratio of Hα (6563 Å) to Hβ (4861 Å) = 2.87 (Osterbrock and Ferland (2006), table 4.2). This is because both lines are members of the Balmer series, i.e. transitions to the $n = 2$ level in the hydrogen atom. Any difference between this value and the observed ratio will be due to extinction. The extinction at Hα and Hβ are given by the following equations:

$$\begin{aligned}
A(H\alpha) &= -2.5 \log \left[\frac{F(H\alpha)}{F_0(H\alpha)} \right] \\
A(H\beta) &= -2.5 \log \left[\frac{F(H\beta)}{F_0(H\beta)} \right]
\end{aligned} \tag{3.4}$$

where F and F_0 are the observed and intrinsic fluxes. $A(\lambda)$ is a measure of how much fainter an emission line flux appears at a particular wavelength, λ, due to extinction via intervening gas and dust. Colour, or colour index, is defined as the difference between two magnitudes at different wavelengths, e.g. $(B - V)$ (Evans, 1994). Colour excess, e.g. E $(B - V)$, is the difference in magnitudes between the intrinsic flux of an object, and the measured one. The colour excess between Hα and Hβ is given by

$$E(\beta - \alpha) = A(H\beta) - A(H\alpha) = 2.5 \log \left[\frac{F(H\alpha)}{2.87 \, F(H\beta)} \right] \tag{3.5}$$

where 2.87 is the ratio of the theoretical extinction-free fluxes of Hα to Hβ ($F_0(H\alpha)/F_0(H\beta)$). Using the extinction law described in equations 2a to 3b of Cardelli et al. (1989), with $R_v = 3.1$, the extinction coefficients for Hα and Hβ are given by

$$\begin{aligned}
k_{H\alpha} &= \frac{A(H\alpha)}{E(B-V)} = 2.533 \\
k_{H\beta} &= \frac{A(H\beta)}{E(B-V)} = 3.609
\end{aligned} \tag{3.6}$$

and in general:

$$k_\lambda = \frac{A(\lambda)}{E(B-V)} \tag{3.7}$$

where E $(B-V)$ is the standard colour excess. The Hα / Hβ colour excess can therefore also be written as

$$E(\beta - \alpha) = A(H\beta) - A(H\alpha) = E(B-V)[k_{H\beta} - k_{H\alpha}] \tag{3.8}$$

and an equation for the general colour excess is given by

$$E(B-V) = \frac{E(\beta - \alpha)}{k_{H\beta} - k_{H\alpha}} = \frac{2.5}{k_{H\beta} - k_{H\alpha}} \log\left[\frac{F(H\alpha)}{2.87\,F(H\beta)}\right] \tag{3.9}$$

The larger this value is, the greater the extinction to the object. Substituting F(Hα) and F(Hβ) with the fluxes we measure from our ISIS optical spectra, given by 2.00×10^{-13} erg cm^{-2} s^{-1} and 1.67×10^{-14} erg cm^{-2} s^{-1} respectively, we calculate an E$(B-V) = 1.44 \pm 0.061$. Similarly, the Hγ line can be used to determine extinction. The theoretical ratio of Hγ to Hβ is 0.466 under the same conditions (Osterbrock and Ferland, 2006). Using the measure line flux of Hγ, 3.66×10^{-15} erg cm^{-2} s^{-1}, and the extinction coefficient, 4.147, the colour excess, E$(B-V) = 1.45^{+0.455}_{-0.367}$, which is very close to the value found from Hα and Hβ. From our LIRIS spectra, we can also compare another recombination line of hydrogen, Brγ, to Hβ, which gives an E$(B-V)$ $= 1.40 \pm 0.02$.

3.2.3.2 Comparison to other methods

As well as spectroscopy, data from photometric observations can be used, and offer a bigger picture as flux is measured over the whole object rather than just a slit. Using the Balmer decrement, we can substitute our measurement of the total Hα flux, F(Hα) $= 2.63 \times 10^{-12}$, and the total Hβ flux, F(Hβ) $= 2.45 \times 10^{-13}$ (Kaler, 1983) into equation 3.9, to give an E$(B-V) = 1.33^{+0.13}_{-0.12}$.

Another method for extinction relies on the relation between radio and the Balmer series, as much of the radio continuum emission in PNe comes from the H\textsc{ii} region. From Pottasch (1984), the ratio of the radio to Hβ flux is

$$S_v/F(\mathrm{H}\beta) = 2.51 \times 10^7 T_e^{0.53} v^{-0.1} Y \,[\mathrm{Jy\ mW^{-1} m^2}] \tag{3.10}$$

where T_e is the electron temperature in Kelvin, v is the radio frequency in GHz and Y incorporates the HeII/HII ratio[5]. As in Ruffle et al. (2004), setting $T_e = 10^4$K, $v = 5$GHz, $Y = 1.1$ and converting to mJy gives

$$S_v(6\mathrm{cm})/F(\mathrm{H}\beta)_0 = 3.10 \times 10^{12} \,[\mathrm{mJy\ mW^{-1} m^2}] \tag{3.11}$$

Substituting $S_v = 59.7 \pm 0.5$ mJy (Ingallinera et al., 2014a) and $F(\mathrm{H}\beta) = 2.45 \times 10^{-13}$ (Kaler, 1983) into

$$\mathrm{E}(B-V) = \frac{2.5}{k_{\mathrm{H}\beta}} \log\left[\frac{S_v(6\mathrm{cm})/3.10 \times 10^{12}}{\mathrm{F}(\mathrm{H}\beta)}\right] \tag{3.12}$$

gives an E $(B-V)$ = 1.313 ± 0.035. Replacing $F_0(\mathrm{H}\beta)$ with $F_0(\mathrm{H}\alpha)/2.87$ using our calculated value of 2.63×10^{-12}, E $(B-V)$ = 1.305 ± 0.017.

All the values used to estimate the extinctions to Abell 53 are given in Table 3.8. Extinctions found using the spectra alone are higher than those also using radio observations.

3.2.3.3 Applying the correction

We decide to use the colour excess estimated from the Hα and Hβ emission lines, i.e. E$(B-V)$ = 1.44, as this method is the most commonly used, and has good agreement with the value calculated using the Hγ line. Also, using contemporaneous measurements, rather than combining spectra and photometry taken at different times under different conditions, is likely to yield more accurate results. We can find the extinction-free flux at any wavelength, given an extinction law, using the following:

$$\begin{aligned}
\mathrm{F}_0(\lambda) &= \mathrm{F}(\lambda) \cdot 10^{\mathrm{A}(\lambda)/2.5} \\
&= \mathrm{F}(\lambda) \cdot 10^{\mathrm{E}(B-V)k_\lambda/2.5} \\
&= \mathrm{F}(\lambda) \cdot \left[\frac{\mathrm{F}(H\alpha)}{2.87 \cdot \mathrm{F}(H\beta)}\right]^{\left[k_\lambda/(k_{\mathrm{H}\beta} - k_{\mathrm{H}\alpha})\right]}
\end{aligned} \tag{3.13}$$

---

[5]Note that 1 Wm^{-2} = 10^3 erg cm^{-2} s^{-1}

TABLE 3.8: Measurements and values used to calculate the interstellar extinction to Abell 53. The first section lists some H recombination lines and their fluxes relative to Hβ from ISIS and LIRIS. The fluxes of the 2 [N$_{II}$] lines that lie within the IPHAS Hα filter are also given, used to remove their contribution from the photometry. The second section gives the fluxes measured from the IPHAS photometry (with and without the NII contribution) and those from the literature: Hβ (Kaler, 1983) and S_v (Ingallinera et al., 2014a). The third section gives the extinction coefficients at the wavelengths of the 4 emission lines used taken from (Cardelli et al., 1989). The fourth section gives the theoretical values of the H recombination lines relative to Hβ, taken from (Osterbrock and Ferland, 2006). The fifth section gives the colour excesses calculated using 6 sets of measurements. The final section is the total extinction-free Hα and Hβ fluxes calculated using the ISIS spectra.

Spectroscopy	
ID	Flux (rel. to Hβ)
Hα	11.98 ± 0.73
Hβ	1.00 ± 0.00
Hγ	0.22 ± 0.05
Brγ	1.87 ± 0.12
[N$_{II}$] 6548	4.55 ± 0.27
[N$_{II}$] 6583	16.87 ± 0.97
Photometry	
ID	Flux (erg cm^{-2} s^{-1})
IPHAS (Hα + [N$_{II}$])	$7.32(\pm 0.20) \times 10^{-12}$
Hα	$2.63(\pm 0.10) \times 10^{-12}$
Hβ	$2.45(\pm 0.29) \times 10^{-13}$
S$_v$ 5 GHz	59.7 ± 0.5 mJy
Extinction coefficients (k)	
Hα	2.535
Hβ	3.609
Hγ	4.175
Brγ	0.361
Theoretical ratios (rel. to Hβ)	
Hα	2.87
Hγ	0.466
Brγ	0.0281
Colour excess, E($B-V$)	
ISIS: Hα and Hβ	$1.444^{+0.063}_{-0.059}$
ISIS: Hγ and Hβ	$1.446^{+0.444}_{-0.380}$
ISIS + LIRIS: Hβ and Brγ	$1.404^{+0.021}_{-0.020}$
Phot: Hα and Hβ	$1.333^{+0.131}_{-0.118}$
Phot: S$_v$ 5 GHz and Hα	$1.305^{+0.017}_{-0.017}$
Phot: S$_v$ 5 GHz and Hβ	$1.313^{+0.036}_{-0.033}$
Extinction-free total fluxes, F$_0$ (erg cm^{-2} s^{-1})	
Hα	$7.66^{+1.37}_{-1.10} \times 10^{-11}$
Hβ	$2.67^{+0.48}_{-0.38} \times 10^{-11}$

TABLE 3.9: Photometry after extinction correction, for the nebula and the proposed central star. Columns are: Band (survey and filter); k (extinction coefficients from Cardelli et al. (1989)); $F_{0,\lambda}$ (extinction-free photometry flux densities) and F_0 (extinction-free photometry fluxes, i.e. $F_{0,\lambda} \cdot W_{eff}$).

Band	k	$F_{0,\lambda}$ (erg cm^{-2} s^{-1} Å^{-1})	F_0 (erg cm^{-2} s^{-1})
Nebula + Central Star			
UVEX U	4.839	$2.91(\pm0.81) \times 10^{-13}$	$1.80(\pm0.50) \times 10^{-10}$
UVEX G	3.689	$3.13(\pm0.66) \times 10^{-13}$	$3.77(\pm0.79) \times 10^{-10}$
UVEX R	2.733	$3.03(\pm0.47) \times 10^{-13}$	$3.69(\pm0.58) \times 10^{-10}$
IPHAS Hα+[NII]	2.533	$2.27(\pm0.33) \times 10^{-12}$	$2.13(\pm0.31) \times 10^{-10}$
IPHAS r	2.733	$2.92(\pm0.46) \times 10^{-13}$	$3.57(\pm0.56) \times 10^{-10}$
IPHAS i	2.007	$3.94(\pm0.46) \times 10^{-14}$	$5.79(\pm0.68) \times 10^{-11}$
PS1 G	3.695	$3.12(\pm0.65) \times 10^{-13}$	$3.63(\pm0.76) \times 10^{-10}$
PS1 R	2.745	$3.13(\pm0.48) \times 10^{-13}$	$4.12(\pm0.64) \times 10^{-10}$
PS1 I	2.092	$2.13(\pm0.26) \times 10^{-14}$	$2.65(\pm0.32) \times 10^{-11}$
PS1 Z	1.589	$1.20(\pm0.11) \times 10^{-14}$	$1.16(\pm0.11) \times 10^{-11}$
PS1 Y	1.337	$1.96(\pm0.15) \times 10^{-14}$	$1.20(\pm0.09) \times 10^{-11}$
UKIDSS J	0.876	$5.38(\pm0.67) \times 10^{-15}$	$8.55(\pm1.06) \times 10^{-12}$
UKIDSS H	0.570	$9.24(\pm0.64) \times 10^{-15}$	$2.70(\pm0.19) \times 10^{-11}$
UKIDSS K	0.352	$1.42(\pm0.15) \times 10^{-15}$	$5.00(\pm0.51) \times 10^{-12}$
UWISH2 H$_2$-K	0.373	$6.37(\pm0.32) \times 10^{-16}$	$1.67(\pm0.08) \times 10^{-12}$
Central Star			
UVEX U	4.839	$1.78(\pm1.03) \times 10^{-15}$	$1.10(\pm0.63) \times 10^{-12}$
UVEX G	3.689	$6.70(\pm2.00) \times 10^{-16}$	$8.05(\pm2.41) \times 10^{-13}$
UVEX R	2.733	$5.52(\pm0.97) \times 10^{-16}$	$6.74(\pm1.18) \times 10^{-13}$
PS1 G	3.695	$8.01(\pm1.73) \times 10^{-16}$	$9.34(\pm2.01) \times 10^{-13}$
PS1 R	2.745	$4.20(\pm0.66) \times 10^{-16}$	$5.53(\pm0.88) \times 10^{-13}$
PS1 I	2.092	$1.55(\pm0.19) \times 10^{-16}$	$1.93(\pm0.23) \times 10^{-13}$
PS1 Z	1.589	$9.24(\pm0.86) \times 10^{-17}$	$8.93(\pm0.83) \times 10^{-14}$
PS1 Y	1.337	$5.17(\pm0.58) \times 10^{-17}$	$3.18(\pm0.35) \times 10^{-14}$
UKIDSS J	0.876	$2.86(\pm0.59) \times 10^{-17}$	$4.55(\pm0.94) \times 10^{-14}$
UKIDSS H	0.570	$1.04(\pm0.31) \times 10^{-17}$	$3.03(\pm0.91) \times 10^{-14}$
UKIDSS K	0.352	$1.76(\pm2.19) \times 10^{-18}$	$6.19(\pm7.68) \times 10^{-15}$

TABLE 3.10: Line fluxes after extinction correction. Columns are: No. (emission line number in band); Line ID; λ (rest wavelength of emission line); k (extinction coefficient from (Cardelli et al., 1989)); F_0 (extinction-free emission line flux) and F_0 (rel.) (extinction-free emission line flux relative to Hβ).

No.	Line ID	λ (Å)	k	F_0 (erg cm^{-2} s^{-1})	F_0 (rel.)
			ISIS: Blue		
1	[OII]	3728	4.771	$1.60^{+0.52}_{-0.38} \times 10^{-11}$	$7.889^{+1.079}_{-0.890}$
2	[NeIII]	3868	4.660	$4.14^{+1.49}_{-1.08} \times 10^{-12}$	$2.050^{+0.412}_{-0.365}$
3	[NeIII]	3968	4.571	$1.86^{+0.83}_{-0.62} \times 10^{-12}$	$0.931^{+0.283}_{-0.266}$
4	Hδ	4101	4.438	$8.34^{+4.27}_{-3.31} \times 10^{-13}$	$0.417^{+0.162}_{-0.149}$
5	Hγ	4339	4.175	$9.36^{+3.43}_{-2.60} \times 10^{-13}$	$0.465^{+0.109}_{-0.098}$
6	[OIII]	4362	4.149	$2.08^{+1.07}_{-0.87} \times 10^{-13}$	$0.104^{+0.043}_{-0.041}$
7	HeII	4685	3.789	$3.60^{+1.28}_{-1.02} \times 10^{-13}$	$0.179^{+0.044}_{-0.043}$
8	Hβ	4861	3.609	$2.03^{+0.38}_{-0.30} \times 10^{-12}$	$1.000^{+0.000}_{-0.000}$
9	[OIII]	4958	3.517	$5.62^{+1.28}_{-0.99} \times 10^{-12}$	$2.774^{+0.157}_{-0.153}$
10	[OIII]	5006	3.474	$1.63^{+0.36}_{-0.29} \times 10^{-11}$	$8.019^{+0.449}_{-0.419}$
11	[NI]	5198	3.312	$1.43^{+0.53}_{-0.43} \times 10^{-13}$	$0.071^{+0.020}_{-0.019}$
			ISIS: Red		
1	[NII]	5754	2.943	$8.99^{+1.83}_{-1.48} \times 10^{-14}$	$0.044^{+0.004}_{-0.004}$
2	HeI	5876	2.876	$3.55^{+0.68}_{-0.54} \times 10^{-13}$	$0.175^{+0.011}_{-0.010}$
3	[OI]	6300	2.661	$8.63^{+1.47}_{-1.19} \times 10^{-13}$	$0.426^{+0.021}_{-0.020}$
4	[SIII]	6312	2.656	$1.75^{+0.50}_{-0.43} \times 10^{-14}$	$0.009^{+0.002}_{-0.002}$
5	[OI]	6364	2.630	$2.73^{+0.46}_{-0.38} \times 10^{-13}$	$0.135^{+0.007}_{-0.007}$
6	[NII]	6548	2.542	$2.23^{+0.36}_{-0.30} \times 10^{-12}$	$1.100^{+0.057}_{-0.053}$
7	Hα	6563	2.535	$5.83^{+1.08}_{-0.87} \times 10^{-12}$	$2.870^{+0.000}_{-0.000}$
8	[NII]	6583	2.525	$8.08^{+1.31}_{-1.06} \times 10^{-12}$	$3.987^{+0.196}_{-0.186}$
9	HeI	6678	2.480	$8.41^{+1.36}_{-1.13} \times 10^{-14}$	$0.041^{+0.003}_{-0.002}$
10	[SII]	6716	2.462	$5.38^{+0.84}_{-0.70} \times 10^{-13}$	$0.265^{+0.014}_{-0.014}$
11	[SII]	6731	2.455	$5.22^{+0.83}_{-0.68} \times 10^{-13}$	$0.257^{+0.014}_{-0.013}$
12	[ArV]	7005	2.323	$4.26^{+1.72}_{-1.54} \times 10^{-15}$	$0.002^{+0.001}_{-0.001}$
13	HeI	7065	2.294	$8.09^{+1.22}_{-1.04} \times 10^{-14}$	$0.040^{+0.003}_{-0.003}$
14	[ArIII]	7136	2.260	$6.12^{+0.88}_{-0.73} \times 10^{-13}$	$0.302^{+0.018}_{-0.017}$
15	HeI	7281	2.190	$1.62^{+0.37}_{-0.33} \times 10^{-14}$	$0.008^{+0.001}_{-0.001}$
16	[OII]	7320	2.171	$2.11^{+0.29}_{-0.24} \times 10^{-13}$	$0.104^{+0.007}_{-0.006}$
17	[OII]	7330	2.166	$1.75^{+0.24}_{-0.20} \times 10^{-13}$	$0.086^{+0.005}_{-0.005}$
18	[ArIII]	7751	1.966	$1.29^{+0.16}_{-0.14} \times 10^{-13}$	$0.063^{+0.005}_{-0.004}$
			LIRIS		
1	HeI	20580	0.392	$1.69^{+0.19}_{-0.19} \times 10^{-14}$	$0.008^{+0.002}_{-0.001}$
2	H$_2$ 2-1 S(3)	20720	0.388	$5.68^{+1.02}_{-1.01} \times 10^{-15}$	$0.003^{+0.001}_{-0.001}$
3	H$_2$ 1-0 S(1)	21210	0.373	$8.87^{+0.25}_{-0.24} \times 10^{-14}$	$0.044^{+0.007}_{-0.006}$
4	Brγ	21650	0.361	$5.04^{+0.21}_{-0.21} \times 10^{-14}$	$0.025^{+0.004}_{-0.004}$
5	H$_2$ 1-0 S(0)	22220	0.346	$1.97^{+0.14}_{-0.14} \times 10^{-14}$	$0.010^{+0.002}_{-0.001}$
6	H$_2$ 2-1 S(1)	22470	0.340	$8.02^{+1.62}_{-1.62} \times 10^{-15}$	$0.004^{+0.001}_{-0.001}$
7	H$_2$ 1-0 Q(1)	24050	0.305	$6.63^{+0.25}_{-0.24} \times 10^{-14}$	$0.033^{+0.005}_{-0.005}$

where F(λ) is the measured flux at wavelength λ, and k_λ is the corresponding extinction coefficient. This equation is used to find the extinction-free photometry (at wavelengths shorter than the K-band), emission line fluxes from ISIS and LIRIS, and select surface brightness profiles. The corrected photometry and line fluxes are given in Tables 3.9 and 3.10 respectively.

3.3 Physical properties

In this section, the multi-wavelength observations will be used to infer some of the physical characteristics of Abell 53, some of which will be used to constrain the models in Chapter 4.

3.3.1 Photometry
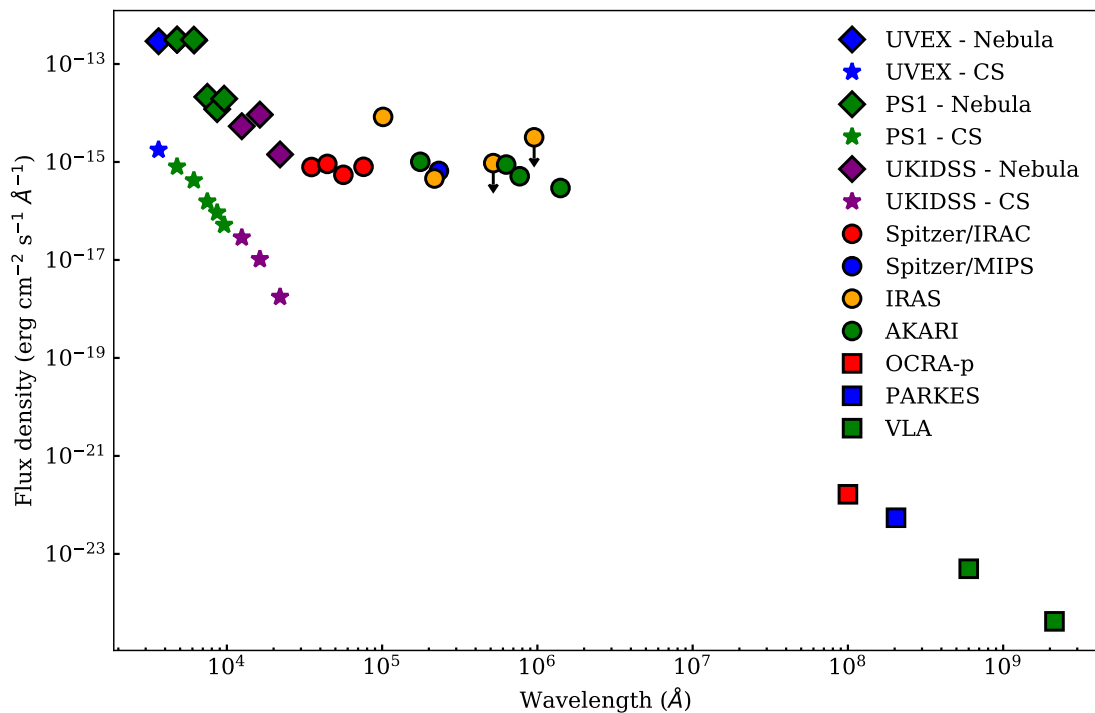
FIGURE 3.18: SED of the main nebula, and proposed central star of Abell 53, showing all the photometry calculated from images in this work, and those found in the literature.

The broadband photometric measurements of Abell 53, given in Tables 3.5 and 3.9, are brought together to create an SED (Figure 3.18), which also displays the proposed central star photometry. From the near-UV to near-IR, the largest contribution to the flux is from the recombination and forbidden emission lines, as there is little evidence of a strong continuum in the spectra. At longer wavelengths, continuum emission can start to dominate the filters. Some PNe are

observed to have a bump in the SED at around 30 μm, which can be explained by the presence of a large mass of dust, radiating as a blackbody with $T_{eff} = 100$ K. Continuum emission at radio wavelengths in PNe is either due to thermal free-free emission of electrons (Bremsstrahlung radiation) or relativistic electrons accelerated by magnetic fields (synchrotron radiation). The spectral index is a measure of the slope of the SED at radio wavelengths, and is often used to distinguish between these two types of radiation. In general, positive or slightly negative spectral indices signal Bremsstrahlung radiation, while strongly negative values indicate synchrotron radiation. As mentioned in the introduction, Ingallinera et al. (2014b) measured a flat spectral index of $\alpha = -0.06 \pm 0.01$ for Abell 53, suggesting Bremsstrahlung radiation dominates.

3.3.2 Spectroscopy

We obtained 3 portions of spectra for Abell 53 (ISIS: blue and red, LIRIS: K-band) and have identified 36 emission lines in them, originating from 6 elements: hydrogen, helium, nitrogen, oxygen, neon and argon; with various degrees of ionisation. The 5 brightest lines are [OIII] ($\lambda 5007$), [OII] ($\lambda 3728$), [NII] ($\lambda 6583$), Hα ($\lambda 6563$) and [OIII] ($\lambda 4958$). In the K-band, 5 H$_2$ lines are observed, along with Brγ and HeI. As discussed in Chapter 2, ratios of certain emission lines of H$_2$ can reveal how it is being excited. We find H$_2$ 1-0 S(1) / 2-1 S(1) = 11.1, which implies that the H$_2$ is dominated by thermal excitation, possibly due to propagating shock-waves (see Section 3.3.6).
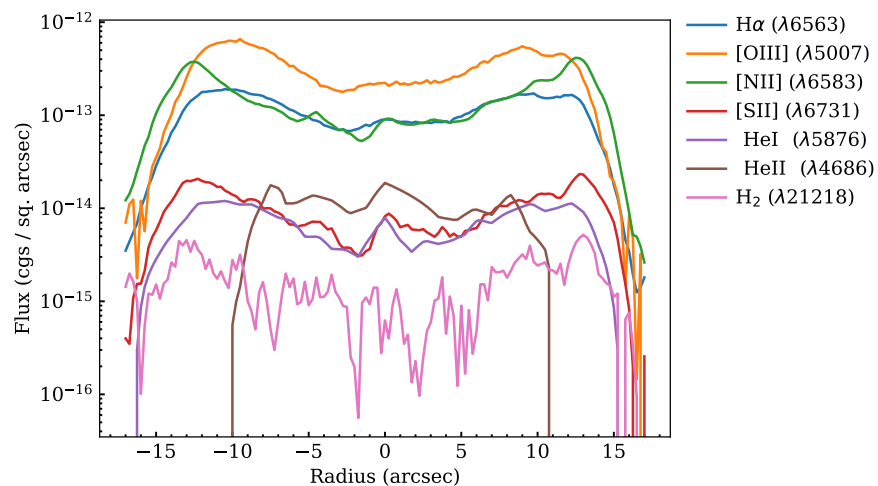
3.3.3 Surface brightness profiles

FIGURE 3.19: Surface brightness profiles of Abell 53 for select lines (log scale).
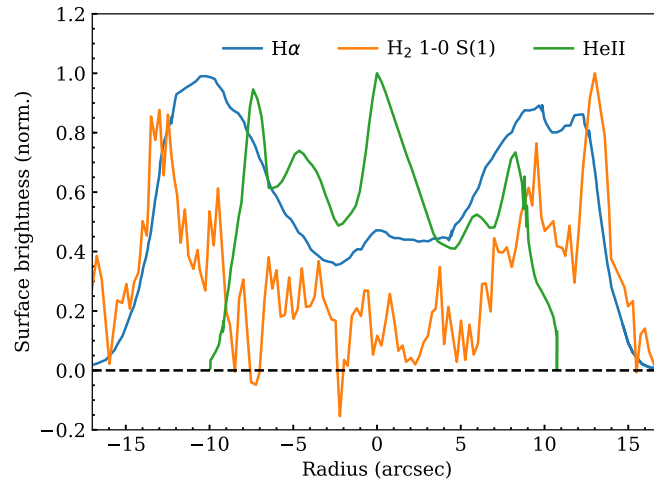
FIGURE 3.20: Surface brightness profiles of Hα, H$_2$ 1-0 S(1) and HeII (4686 Å) on a normalised linear scale (i.e. SB$_{max}$ = 1.0). These profiles are those extracted from spectroscopy rather than photometry.

TABLE 3.11: The peak surface brightnesses and positions, and outer radii of select emission lines of Abell 53. The peak position is simply the radius at which the maximum surface brightness is observed. The outer radius is defined as the radius at which the surface brightness reaches 10% of the maximum value. The average of the North and South lobes are taken in both cases.

Line	Wavelength (Å)	Peak SB (erg cm^{-2} s^{-1} arcsec^{-2})	Peak position (arcsec)	Outer radius (arcsec)
HeII	4686	1.83×10^{-14}	7.81	10.11
[OIII]	5007	6.42×10^{-14}	10.01	14.31
HeI	5876	1.20×10^{-14}	10.74	15.36
Hα	6563	1.91×10^{-13}	10.90	15.25
[NII]	6583	4.15×10^{-13}	12.53	15.55
[SII]	6731	2.32×10^{-14}	12.55	15.64
H$_2$ 1-0 S(1)	21218	5.19×10^{-15}	13.03	15.58

The surface brightness (SB) profiles for 7 emission lines of Abell 53 are given in Figure 3.19, and some details given in Table 3.11. These lines are some of the most commonly observed in PNe, and represent different excitation classes. Figure 3.20 shows the Hα and H$_2$ 1-0 S(1) SB profiles normalised so their maximum value is 1. The HeII (λ4686) line peaks at the smallest radius (7.8 arcsec) and is not observed beyond 10.1 arcsec. This is expected, as we would expect ionised helium to be located deep inside the nebula near the CS, where the flux of ionising photons is greatest. [OIII] (λ5007) peaks at the next shortest radius (10.0 arcsec), followed by HeI and then Hα. Located furthest out is the H$_2$ 1-0 S(1) line, which is closely traced by the [NII] and [SII] lines. We would expect the molecular material to be located at the largest radii, where the ionising photon flux from the CS is lower, and so a photodissociation region (PDR) can form. SB profiles for various lines are utilised in the following sections to shed some light on various properties.
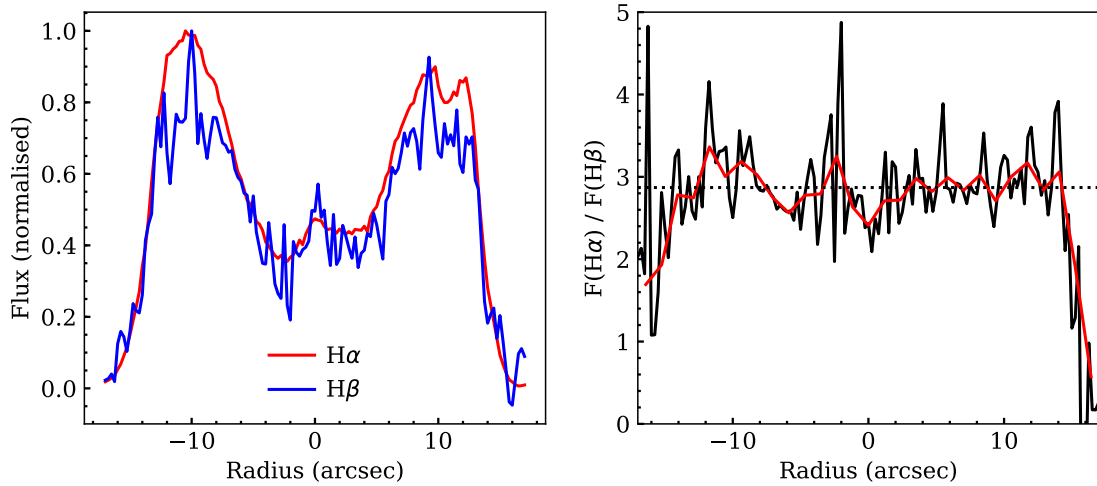
3.3.4 Internal extinction

FIGURE 3.21: SB profiles of normalised Hα and Hβ (left), and the ratio of these fluxes (right), where the red line is a moving average. The horizontal dotted line represents the average ratio of 2.87.

It was shown in Section 3.2.3 that the interstellar dust between Abell 53 and us will cause some observations to look fainter than they truly are. However, it is likely that there are dust grains produced within Abell 53, and these grains can also obscure the light that reaches us - this is known as internal extinction. In order to test whether this is the case, we make use of the Hα and Hβ SB profiles, which are given in Figure 3.21. The right panel gives the ratio of the profiles along the slit, and as they have already been corrected for line of sight extinction using the Balmer decrement, the average ratio is 2.87. There may be a slight increase in the Hα/Hβ ratio towards the edges of the nebula, peaking at roughly 12 arcsec, before dropping off with the decrease in SNR. This would imply a larger internal extinction in this region, and therefore a higher dust grain abundance. However, the variation is small enough that we choose to ignore its effects.

3.3.5 Density and temperature

Various emission line ratios will have different dependencies on the temperature and density within the ionised nebula. Notable examples include lines of [OIII] ($\lambda4363,4959,5007$), [NII] ($\lambda5754,6548,6583$), [NeIII] ($\lambda3869,3968,3343$) and [SIII] ($\lambda9532,9069,6312$) for temperature, and [OII] ($\lambda3726,3729$) and [SII] ($\lambda6716,6731$) for density.
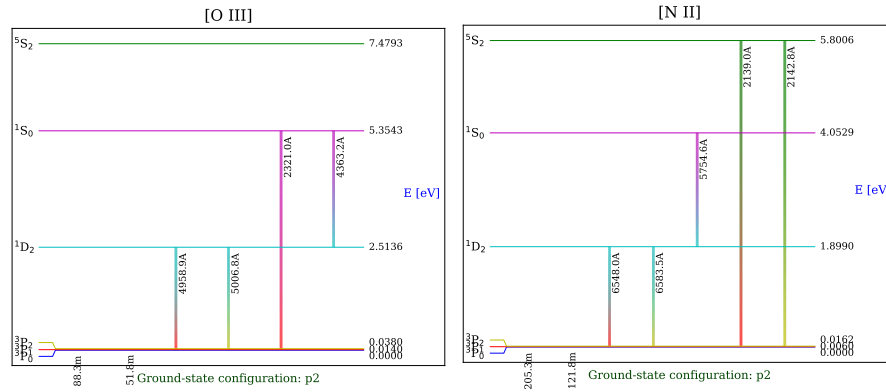
3.3.5.1 Temperature

FIGURE 3.22: Grotrian diagrams showing some of the energy levels for [OIII] and [NII]. These were made using the PYNEB Python package (Luridiana et al., 2015).
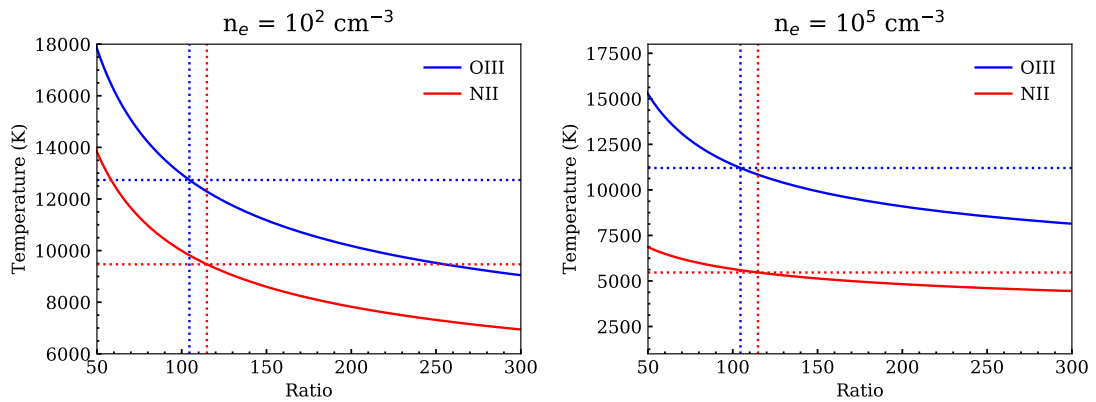
FIGURE 3.23: Plots showing how the [OIII] $(4959 + 5007)/4363$ ratio and [NII] $(6548 + 6583)/5754$ ratio scale with temperature for a low density regime (left) and high density (right). Dotted lines represent observations.

Emission lines of O2+ are probably the most commonly used to estimate nebula temperatures. This is because this ion has lines from two different energy levels with noticeably different excitation energies, while lying within the observable optical region (Osterbrock and Ferland, 2006). The Grotrian diagram for this ion, which shows the allowed electronic transitions between energy levels, is given in Figure 3.22 (left). Collisions with higher energy (and therefore higher temperature) free electrons are needed to excite bound electrons in the O2+ ion to the $^1S_0$ energy level, in order for the $\lambda 4363$ photon to be emitted. However, less energetic free electrons are required to populate the lower levels which produce the $\lambda 4959,5007$ lines. Hence, the ratio of these lines tells us the temperature of the free electrons in the gas. A similar argument is applicable to the [NII] ion.

Equations 5.4 and 5.5 in Osterbrock and Ferland (2006) relate the temperature (T) and electron density (n_e) to the [OIII] and [NII] line ratios respectively[6]:

$$[\text{OIII}]\frac{4959+5007}{4363} = \frac{7.90e^{3.29\times10^4/T}}{1+4.5\times10^{-4}n_e/T^{0.5}} \tag{3.14}$$

$$[\text{NII}]\frac{6548+6583}{5755} = \frac{8.23e^{2.50\times10^4/T}}{1+4.4\times10^{-3}n_e/T^{0.5}} \tag{3.15}$$

In Figure 3.23, we show these dependencies for a low and high density case, and use the plots with our observations of the line ratios to estimate the temperature. For the low density case, we find T = 12736 and 9468 K for [OIII] and [NII] respectively, and for the high density limit, we find T = 11202 and 5465 K.

3.3.5.2 Density
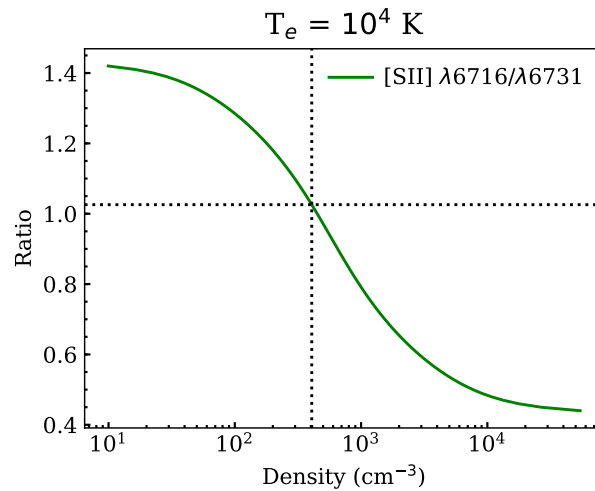
FIGURE 3.24: Plot showing how the [SII] 6716/6731 ratio scales with electron density for a 10^4 K nebula. Dotted lines represent observations.

A commonly used indicator of electron density is the ratio of the [SII](λ6716,6731) lines. These lines have similar transition energy differences (as their wavelengths are close), meaning that a collision with a free electron has an equal chance of exciting bound electrons from the ground state to either one of these levels. When the density is low ($\leq 100\,\text{cm}^{-3}$), the chance of a collision is rare, and so electrons in these excited levels can emit photons as they de-excite to the ground

---

[6]These equations become less applicable as the density increases beyond 10^5 cm^{-3}, as collisional excitation becomes more significant.
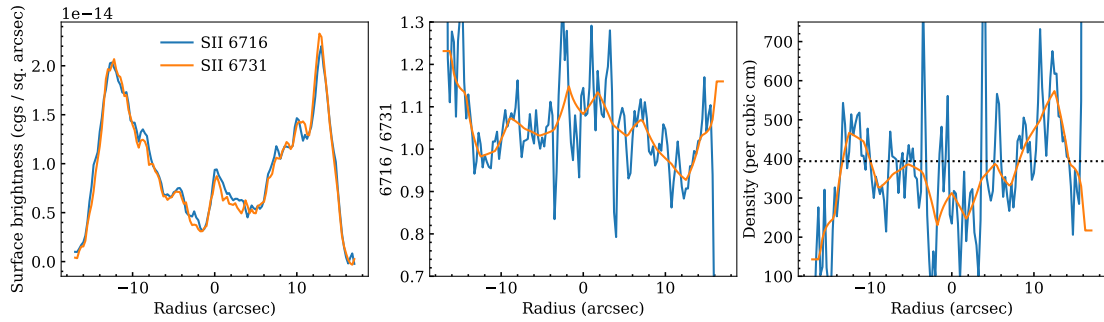
FIGURE 3.25: Using the [SII] emission lines to search for electron density variation with radius. From left to right, the three plots show the observed SB profiles, their ratio and calculated density. In the middle and right plots, the orange line is a moving average. There is some tentative evidence for a slight density increase with increasing radius, followed by a sharp density decrease at the edge where the signal to noise drops significantly.

state. In this case, the $\lambda 6716/\lambda 6731$ ratio is given by the ratio of their statistical weights (i.e. the number of electrons a level can hold), equal to 1.5. However, at high densities, the probability of a collisional de-excitation occurring is greater, meaning that the electron will drop to the ground state before it can radiate a photon. In this case, the $\lambda 6716/\lambda 6731$ ratio will also depend on the relative lifetimes of the levels, as a shorter lifetime means a greater chance of a spontaneous emission, and so a stronger line. The ratio at densities $\geq 10^4$ cm^{-3} is around 0.44.

We use an empirical fit from Proxauf et al. (2014) (their equation 3) to estimate the electron density using our measured total [SII]($\lambda 6716,6731$) ratio. This gives a density of 402 cm^{-3} for a nebula temperature of 10^4K. The fit is shown in Figure 3.24, which clearly demonstrates the plateauing of the line ratio at the two density extremes[7].

Rather than using the total line fluxes, we can also use the SB profiles to measure how the density varies as a function of radius, by calculating the [SII]($\lambda 6716,6731$) ratio at each point along the slit[8]. The results are given in Figure 3.25, and it can be seen that there is evidence for a density increase moving radially outwards, and then a sharp decrease as the edge of the nebula is reached, and the signal becomes too weak to be meaningful. The density in the central region is roughly 300 cm^{-3}, and increases to 400-500 cm^{-3} in the bright rim.
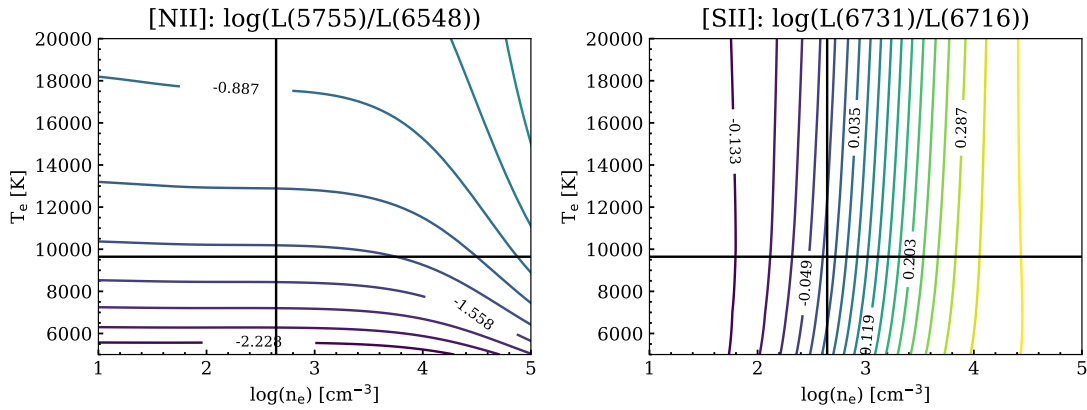
FIGURE 3.26: Temperature-density diagnostic diagrams for [NII] (left) and [SII] (right). The coloured contours are theoretical line ratios, and the point of intersection of the horizontal and vertical lines mark the observed ratios.

3.3.5.3 Combined

It would be ideal if we could estimate as many temperatures and densities as possible, and take an average. However, we only have observations of 3 sets of ionic lines ([NII], [SII] and [OIII]); the latter of these, specifically the $\lambda 4363$ line, has a very low SNR, as it is a weak line compared to the $\lambda 4959$ and $\lambda 5007$ lines, but also as its wavelength lies very close to a strong sky emission line from light pollution[9]. We therefore use the [NII] and [SII] line ratios to determine the best T_e-n_e pair using the GETCROSSTEMDEN method from the PYNEB package (Luridiana et al., 2015), which works by cross-converging the temperature and density from the two sensitive line ratios though iteration. The best values found are $T_e = 9653$ K and $n_e = 435$ cm^{-3}, and are demonstrated in Figure 3.26.

3.3.6 Shocks

Ratios of Hα to lines of [SII] and [NII] have been shown to help distinguish photoionised plasma from shocked gas in PNe (Garcia Lario et al. 1991; Magrini et al. 2003). Here we adopt a similar method to that described in section 5.3 of Öttl et al. (2014), using the SB profiles of these lines to investigate how the ratios vary across the nebula. In Figure 3.27 (top left), we show the ratio of Hα to [SII] $(6716+6731)$ and [NII] $(6548+6583)$ as the blue and orange lines respectively.

---

[7]The [OII] ($\lambda 3726,3729$) ratio could also be used as a density tracer, however as evident in Figure B.1, the wavelength resolution of the ISIS spectra is insufficient to resolve the lines.

[8]We attempted a similar analysis to measure the temperature variation along the slit using the [NII] line ratio, however the SNR of the $\lambda 5754$ line was too weak.

[9]Different values of temperature and density will be found depending on the choice of emission lines. For example if a better detection of the $\lambda 4363$ [OIII] line was obtained, it is likely that the temperature estimated using the oxygen lines would be higher, as they peak at lower radii, closer to the central star.
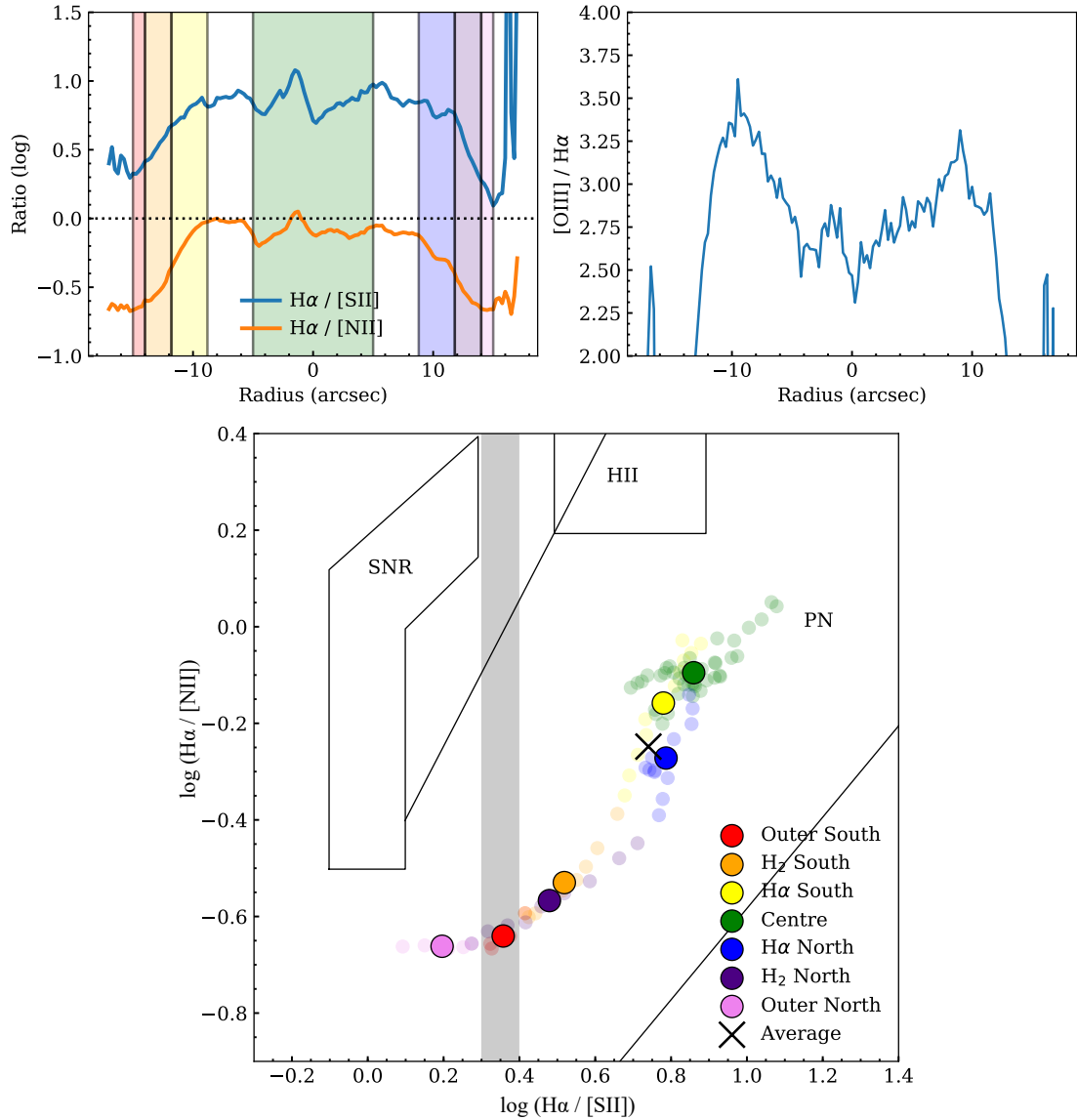
FIGURE 3.27: Searching for shock signatures. Top left: Hα / [SII] (6716 + 6731) and Hα / [NII] (6548 + 6583) variation with radius. Coloured regions are defined in the legend of the bottom figure. Top right: [OIII] λ5007 / Hα variation with radius. Bottom: diagnostic diagram at various points along slit. Data has been separated into 7 regions, whose locations are shown in the top left figure. The larger circles with black outlines are the mean values for that region. Points that lie to the left of the grey region are more likely to be associated with shocks (Bohigas, 2008). The two diagonal lines mark the region where PNe should lie, the upper rectangle marks where HII regions are, and the region to the left is for supernova remnants.

Overlaid are 7 regions, which we label as Outer South (red), H_2 South (orange), $H\alpha$ South (yellow), Centre (green), $H\alpha$ North (blue), H_2 North (indigo) and Outer North (violet). Centre is defined as the region where the $H\alpha$ SB is roughly constant in the central region (5 arcsec radius). The $H\alpha$ and H_2 regions are where the surface brightnesses of $H\alpha$ and H_2 respectively reach their maximum values. The two Outer regions are where the H_2 SB quickly drops off, but where the signal to noise in all lines is still significant (14 to 15 arcsec radius). In Figure 3.27 (bottom) we give the diagnostic diagram, separated into these 7 regions. The central region, and regions where the bulk of $H\alpha$ emission is observed, are clearly associated with photoionised plasma. Moving radially outwards, the $H\alpha$ to [SII] ratio decreases, and at the very edge of the nebula, line ratios that may start to be associated with shocks are observed. Guerrero et al. (2013) investigated using the [OIII] to $H\alpha$ ratio to unveil shocks in PNe. Using the way this ratio changes with radius, they found PNe can be divided into 4 types. Our observations of Abell 53 would place it in their type C (not to be confused with C-type continuous shocks) - those that display a [OIII] to $H\alpha$ ratio that decreases at the outer edge of the nebula (see Figure 3.27; top right). This can be explained with a decrease in the O2+ / H+ in the outermost layers of the nebula. Either a low stellar temperature for a young PN, or a low luminosity of an evolved PN, might be responsible for the low degree of ionisation.

3.3.7   Abundances

The abundance of an ion measures its amount (by number density or mass) relative to that of hydrogen. The relative amounts of ions and subsequent elements determine much of the chemistry of the nebula. The intensities of most emission lines from ionised nebulae are proportional to the abundance of that ion, as the lines tend to be optically thin (i.e. escape the nebulae with relative ease). In an ideal situation, we would need accurate information on the density and temperature of each ion in order to calculate the ionic abundances. However, the availability of this information is often limited by the number of emission lines observed. To estimated the ionic abundances in Abell 53, we make use of the PYNEB package in PYTHON, along with the average temperature and density calculated in Section 3.3.5.

Ionic abundances can be determined from either recombination (RLs) or collisionally-excited (CELs) lines. For recombination lines, the intensity of a line is usually proportional to $n_e \times n(X^{+i})$, where n_e is the electron density, and $n(X^{+i})$ is the ion density, and inversely proportional to the electron temperature, T_e. This means that the only intense RLs are those that originate

from the most abundant ions, i.e. from H and He. The intensities of CELs are highly dependent on T_e. Their intensities relative to Hβ can be expressed as

$$\frac{I(\lambda)}{I(\text{H}\beta)} = \frac{X^{+i}}{\text{H}^+} \frac{\nu_\lambda}{\nu_{\text{H}\beta}} \frac{A_{nn'} f_k}{n_e \alpha_{\text{H}\beta}^{eff}} \tag{3.16}$$

where ν is the frequency, $A_{nn'}$ is the spontaneous transition probability, f_k is the fraction of ions in the upper level and $\alpha_{\text{H}\beta}^{eff}$ is the recombination coefficient. PYNEB uses all available observed line intensities with the average temperature and density in order to estimate the ionic abundances by solving the equations to obtain the level populations (Peimbert et al., 2017).

Elemental abundances are estimated using an average of the available ionisation correction factors (ICFs), which account for the fact that not all ions are observed. The elemental abundance can therefore be expressed as

$$\frac{X}{\text{H}} = \Sigma_{\text{obs}} \frac{X^{+i}}{\text{H}^+} \times ICF \tag{3.17}$$

As lines for only 7 elements are observed (hydrogen, helium, nitrogen, oxygen, sulphur, argon and neon), abundances can only be calculated for these elements. All values are given in Table 3.12. These values are very much estimations, with large associated uncertainties, due to only a small number of emission lines being observed for many of the ions, however are reasonable when compared to abundances of PNe in general. We attempt to improve these abundance estimations in the modelling stage.

3.3.8 Radius and distance

Many estimations of distance have been made of Abell 53, most of which rely on relations between surface brightness and radius. For example, Abell (1966) state that the luminosity of the ionised region is proportional to the square of its density and the volume, while also proportional to the product of the observed flux of a given line and the square of the distance. Based on this, and assuming an ionised mass of 0.2 M$_\odot$, they estimate a nebular density of 853 cm^{-3}, a diameter of 0.25 pc, and a distance between 1.69 kpc and 2.44 kpc, depending on whether an extinction correction was applied. Other estimates of distance include Cahn and Kaler (1971) (between 1.61 kpc and 2.01 kpc); Zhang (1995) (2.38 kpc); Phillips (2004) (1.68

TABLE 3.12: Ionic and elemental abundances of Abell 53, relative to hydrogen, calculated using the PYNEB package in PYTHON.

Ion	Degree	Wavelength (Å)	Ionic abundances	Mean ionic abundances	Elemental abundances
He	I	5876	0.125	0.120	0.152
		6678	0.104		
		7065	0.146		
		7281	0.105		
	II	4686	0.0146	0.0146	
N	I	5198	1.14×10^{-5}	1.14×10^{-5}	1.82×10^{-4}
	II	5755	7.31×10^{-5}	7.87×10^{-5}	
		6548	7.30×10^{-5}		
		6583	8.99×10^{-5}		
O	I	6300	9.26×10^{-5}	9.22×10^{-5}	5.40×10^{-4}
		6364	9.17×10^{-5}		
	II	3727	3.57×10^{-4}	3.85×10^{-4}	
		7319	4.05×10^{-4}		
		7330	3.94×10^{-4}		
	III	4363	7.13×10^{-4}	4.53×10^{-4}	
		4959	3.28×10^{-4}		
		5007	3.18×10^{-4}		
S	II	6716	1.56×10^{-6}	1.56×10^{-6}	3.83×10^{-6}
		6731	1.56×10^{-6}		
	III	6312	2.28×10^{-6}	2.28×10^{-6}	
Ne	III	3869	2.59×10^{-4}	3.23×10^{-4}	8.85×10^{-4}
		3968	3.88×10^{-4}		
Ar	III	7136	2.71×10^{-6}	2.54×10^{-6}	3.24×10^{-6}
		7751	2.37×10^{-6}		
	V	7005	4.58×10^{-8}	4.58×10^{-8}	

kpc) and Ingallinera et al. (2014a) (2.1 kpc). The distribution of these values demonstrates that distances to PNe are difficult to estimate, and depend on the methods used and the observations available.

We attempt to measure the radius and distance to Abell 53 making use of the Hα surface brightness-radius relation (Frew et al., 2016), using our calculated Hα flux from photometry of the IPHAS image. The Hα surface brightness is found using

$$S_0(H\alpha) = \frac{F_0(H\alpha) \cdot 10^{10.629}}{\pi \cdot \theta^2} [\text{erg cm}^{-2}\text{s}^{-1}\text{sr}^{-1}] \tag{3.18}$$

where $F_0(H\alpha)$ is the extinction-free Hα flux, θ is the angular radius in arcsec, and the $10^{10.629}$ factor converts square arcseconds to steradians. For θ, we use the mean radius at which the flux reaches 10% of its maximum value, i.e. 15.25 arcsec. $S_0(H\alpha)$ is found to be $4.48(\pm0.80)\times10^{-3}$

TABLE 3.13: Temperatures and luminosities of the central star of Abell 53 from the literature using the Zanstra method.

Reference	log T (K)	log L (L$_\odot$)
Abell (1966)	5.14	2.34
Piliugin and Khromov (1979)	5.235	
Kaler (1983)	4.839 (H), 5.033 (HeII)	2.322 (H), 2.872 (HeII)
Stanghellini et al. (1993)	5.167 (HeII)	3.198
Stanghellini et al. (2002)	5.212 (HeII)	2.356
Phillips (2003)	4.839 (H), 5.106 (HeII)	

erg cm^{-2}s^{-1}sr^{-1}, assuming an uncertainty on θ of 0.5 arcsec. The Hα surface brightness-radius relation, equation 17 from Frew et al. (2016), is given by

$$\log S_0(H\alpha) = -3.63(\pm0.06)\log r - 5.34(\pm0.05) \quad (3.19)$$

which gives a radius of 0.15 $\pm$ 0.01 pc. The distance can then be found using simple trigonometry:

$$d = \frac{r}{\tan(\theta)} \approx \frac{r}{\theta} \cdot 10^{5.314} \text{ [pc]} \quad (3.20)$$

where the $10^{5.314}$ factor converts arcseconds to radians. This gives a distance of 2.03 $\pm$ 0.13 kpc, similar to previous estimates. Frew et al. (2016) also estimated the radius and distance of Abell 53 using a Hα surface brightness measured from the SuperCOSMOS Hα Survey (SHS) survey. They found a radius of 0.18 pc, and a distance of 2.32 kpc; these are higher than what we found, however this can be explained by the fact that we used a larger value of extinction.

3.3.9 The central star

One of the most common ways of estimating the temperature of the central star of a PN is by using the Zanstra method (Zanstra, 1927). The basic principle relies on comparing the nebular recombination flux with the magnitude of the stellar continuum, and assuming that the nebular is optically thick in the Lyman continuum (i.e. no ionising photons can escape the nebula). This means that observations of the nebula (e.g. a Hβ line flux) and of the central star (e.g. V-band) are needed - the latter of these often being difficult to measure as the nebula continuum is usually brighter that the stellar continuum (Kwok, 2000). Also, using different hydrogen or
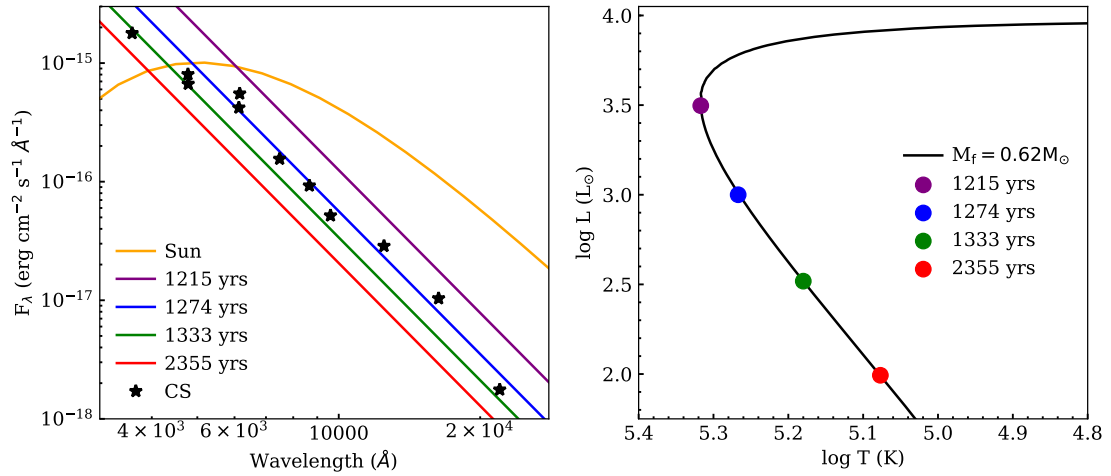
FIGURE 3.28: Left: SED of proposed central star of Abell 53 (black stars, observed). We overlay the blackbody curve of the Sun (orange line), and 4 Rayleigh-Jeans tails representing a CSPN at different stages on the white dwarf cooling track (right figure). We use the track of a 0.6 $M_\odot$ core star, with Z = 0.01, taken from Miller Bertolami (2016), at the following times: 1215 years (purple), 1274 years (blue), 1333 years (green) and 2355 years (red).

helium lines can yield different values. Nonetheless, estimates of the temperature and luminosity of the central star of Abell 53 have appeared in the literature, and can be found in Table 3.13. Estimates of the CS temperature range from as low as 69 kK to as high as 172 kK, bringing a degree of uncertainty to the reliability of the observations used.

In Figure 3.28 (left), we have plotted our photometry of the proposed central star, from the near-UV to the near-IR. We also plot a blackbody curve representing the Sun (T = 5778 K, L = 1 $L_\odot$), and Rayleigh-Jeans tails for a CSPN (M_{core} = 0.6 $M_\odot$, Z = 0.01, Miller Bertolami 2016) at different stages on the white dwarf cooling track, shown in Figure 3.28 (right). Cooling tracks, rather than the horizontal branch, were chosen due to the required luminosity. The SED of a blackbody is defined by Planck's law:

$$B(\lambda, T) = \frac{2hc^2}{\lambda^5} \frac{1}{e^{\frac{hc}{\lambda kT}} - 1} [\text{Wm}^{-2}\text{sr}^{-1}\text{m}^{-1}] \tag{3.21}$$

where $B(\lambda, T)$ is the spectral radiance, h is the Planck constant, c is the speed of light, λ is the wavelength, k is the Boltzmann constant and T is the effective temperature. This can be converted into the same units as those of the central star SED (erg cm^{-2}s^{-1}Å^{-1}) by multiplying by $10^3 \cdot 10^{-10}$ (π R^2/D^2), where the first two terms are the conversions from Wm^{-2} to erg cm^{-2}s^{-1}, and m to Å respectively, and the final term removes the solid angle units; this uses the

distance (D) to the star (found in Section 3.3.8), and the radius (R) of a blackbody. The radius is found by applying the Stefan-Boltzmann law to a blackbody:

$$L = 4\pi R^2 \sigma T^4 \tag{3.22}$$

where L is the luminosity and sigma is the Stefan-Boltzmann constant. The Rayleigh-Jeans law is an approximation to Planck's law, which can be applied at large wavelengths:

$$B(\lambda, T) = \frac{2ckT}{\lambda^4} \tag{3.23}$$

It can be seen that our measurements of the proposed central star are in agreement with theoretical SEDs for a cooling white dwarf, and are unlike the SED from a solar-type star. This, combined with its central proximity to the nebula, is further evidence that this is likely to be the central star of Abell 53. However, large uncertainties in the photometry at the short and long wavelength ends, along with only an estimate on the distance to the star, means that it would be very difficult to try to determine the temperature and luminosity of the central star based on this information alone.

3.4 Summary

This chapter began by describing the methods used to obtain both photometric and spectroscopic measurements of Abell 53. The photometry made use of broad and narrow-band images from various surveys - some of which fluxes were extracted from, while others were taken from the literature. As no sufficient quality spectra of Abell 53 were available, applications for ISIS and LIRIS long-slit spectroscopy using the William Herschel Telescope were made. The advantage of this was that spatial information in the form of surface brightness profiles was also obtained. Using ratios of optical lines meant that extinction could be estimated and corrected for, to allow for these observations to be compared directly to an extinction-free model. However, some discrepancies between colour excesses calculated using different observations is slightly concerning, especially given Abell 53's proximity to the dusty galactic plane.

It was then discussed how these observations could be used in estimating some physical conditions within Abell 53. The small variation of the Hα to Hβ ratio with radius implied low levels

of internal extinction. Emission lines of [NII] and [SII] gave some insight into the temperature and density in the gas, and when combined with Hα, gave evidence of shock heating at the edges of the nebula. The entire set of optical emission lines were used to estimate the abundances of the most common elements. Importantly, a conversion from angular to physical sizes could be found making use of the well-established Hα surface brightness-radius relation. Future, more accurate measurements of distance to the nebula would require this conversion to be updated. It was also shown that the photometric measurements of a point source located at the centre of Abell 53 could be used to distinguish it from a solar-type star, and so increase the likelihood of it in fact be the nebula's central star.

This analysis has showed that a wealth of useful information can be obtained from a fairly small set of observations. This information will be used in the next chapter to develop a photoionisation model of Abell 53.

Chapter 4

Simulation of optical and molecular emission lines of Abell 53

In this chapter, the process behind finding the best set of parameters that describe a simple photoionisation model of Abell 53 using Cloudy is described. We fit to observations of both optical line ratios and surface brightness profiles using a Markov-Chain Monte Carlo (MCMC) process, and present results from two runs: the first using a blackbody as the incident radiation field, and the second using a more realistic stellar atmosphere. We then take the best fit, and generate a grid of models with different parameters that describe the properties of the PDR, in order to fit to H_2 observations. We hope that the parameters of the model will help shed some light on the evolutionary stage of Abell 53, and to offer an explanation of the conditions for H_2 formation and excitation.

4.1   Cloudy: a photoionisation code

Cloudy is a one-dimensional photoionisation code widely used to simulate various astrophysical environments, from AGN to HII regions[1]. The version used in this work is C17.01, and is described in Ferland et al. (2017). The code has been used extensively to model PNe - some examples include NGC 6781 (Otsuka et al., 2017); Tc 1 (Aleman et al., 2019); NGC 2438 (Öttl et al., 2014); NGC 3242, NGC 6826, and NGC 7662 (Barría and Kimeswenger, 2018); IC 4663 (Puspitaningrum and Malasan, 2019) and NGC 6210 (Bohigas et al., 2015). In this section,

---

[1]See `https://www.nublado.org/` for more information.

some of the basic principles used by Cloudy are described, along with the main inputs required to run a model. Also discussed is pyCloudy (Morisset, 2013), a Python library dedicated to streamlining handling of the output data, but also allowing the creation of pseudo-3D models.

4.1.1   How it works

Cloudy works by simultaneously solving the equations of statistical and thermal equilibrium, those that balance ionisation-neutralisation processes, and heating-cooling processes, in order to predict the distribution of ionisation, density, and temperature across a cloud, and its resulting spectrum. With huge databases of atomic and molecular data, a large number of observables can be reproduced from only a few input parameters. The following must be specified for a model to run (however many more options are available):

- The shape and intensity of incident radiation field. For example, the shape could be described by a blackbody approximation, defined with an effective temperature, or a stellar atmosphere file describing a white dwarf, requiring also a surface gravity. The total luminosity of the incident field can be given in solar luminosities.

- The total hydrogen density - i.e. the sum of ionised, neutral and molecular states. This can either be constant, or varying with radius, either as a power law, or custom.

- Composition of the gas - i.e. the abundances of elements. Cloudy handles the first 30 elements, which can be specified relative to hydrogen, or switched off completely.

- Thickness of the cloud - the distance from the radiation source to the inner edge of the cloud needs to be defined, so that Cloudy can calculate the incident photon flux. Also, the outer edge of the cloud must be specified to prevent the simulation from running indefinitely. This stopping condition can take the form of a radius, gas temperature, shell mass, observed line ratio etc.

- Geometry - this can be either open or closed. For the open case, the covering factor (fraction of 4π sr covered by gas) is small (e.g. a slab of material irradiated on one side). In the closed case, the covering factor is a maximum, so that the source of radiation is completely surrounded by gas (e.g. a spherical PN). The closed spherical case is used in all our models.

The desired parameters are entered into an input file which is read by Cloudy; an example of which can be found in Figure C.1. When the simulation starts, the cloud is divided up into thin concentric rings, called zones. The thicknesses of the zones are constantly adjusted to ensure the physical conditions across them are unchanged. The number of zones is normally no more than a few hundred, and the outer zone will be specified by the choice of stopping condition. The simulation is normally re-ran by using the 'iterate' command, which checks that the total optical depth scale is correct. The main output is the SED transmitted by the nebula, along with various parameters saved at each zone. These include gas temperature, ionic fractions, column densities, line emissivities, various reaction rates and many more. Detailed documentation describing Cloudy can be found in the *Hazy* manuals; which are acquired upon installation of the code.
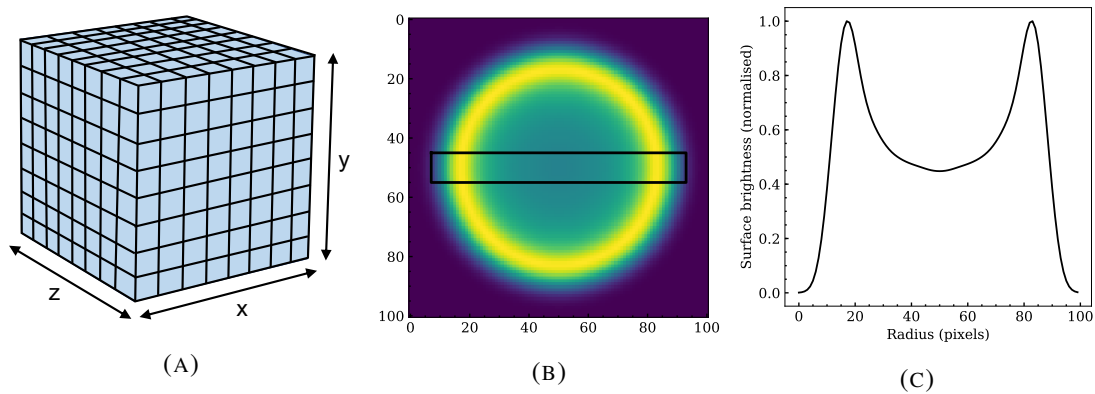
4.1.2 pyCloudy

FIGURE 4.1: Steps for creating a synthetic surface brightness profile from a pseudo-3D py-Cloudy model of a PN (see text for details). The black rectangle in (B) marks the location of the slit used in the long-slit spectroscopy to be compared to.

pyCloudy is a Python library that allows the defining and writing of Cloudy input files, reading of the output files from multiple models, and the building of pseudo-3D models[2]. The latter of these is done by performing a 3D reconstruction in a coordinate cube by interpolation between various 1D runs. In the case of a spherical model, such as those used in this work, only a single model needs to be run. The results can then be interpolated onto a grid by rotating around 4π sr. pyCloudy is therefore not a full 3D code, as it only considers radial radiation. However, the fact that models can be run in a few minutes, rather than hours or even days for full 3D codes such as MOCASSIN (Ercolano et al., 2003), makes it an extremely useful tool for modelling PNe quickly.

---

[2]See `https://sites.google.com/site/pycloudy/` for more information.

The generation of pseudo-3D models meant that the one-dimensional emissivity profiles from Cloudy could be converted into two-dimensional surface brightness profiles, which could be compared to long-slit spectroscopic observations (see Figure 4.5 for Abell 53). The steps for this process are shown in Figure 4.1. A cube of emissivities of a particular emission line (or portion of the SED) created through the interpolation process (Figure 4.1a) is summed in one direction to create a 2D image (Figure 4.1b). The image can be convolved with a Gaussian profile with a FWHM (full width at half maximum) equivalent to the atmospheric conditions when the spectra were observed. The flux within a rectangular region is extracted, with the same dimensions as the slit used in the spectra. The region can then be summed along each column to create a 1D surface brightness profile (Figure 4.1c). A conversion can be made using the physical and angular radius of Abell 53, along with the dimensions of the 3D model, to convert surface brightness from pc^{-2} to $arcsec^{-2}$.

4.1.3 Synthetic photometry

Using the output SED from a PN model, along with the transmission profile of a particular filter, narrow and broad-band synthetic photometry can be reproduced, which can be compared to observations. The flux density through a filter is given by

$$F_\lambda = \frac{\int f_\lambda \cdot T(\lambda)\, d\lambda}{\int T(\lambda)\, d\lambda} \tag{4.1}$$

where f_λ is a point on the SED at a particular wavelength λ, and $T(\lambda)$ is the transmission of the filter at that wavelength. This equation assumes there is no line of sight extinction, or atmosphere to distort the signal.

In order to calculate a photometric colour, i.e. the difference in magnitudes between two filters, the following can be used

$$\begin{aligned}
colour = m_1 - m_2 &= -2.5\log\left(\frac{F_{\lambda,1}}{F_{zp,1}}\right) + 2.5\log\left(\frac{F_{\lambda,2}}{F_{zp,2}}\right) \\
&= -2.5\log\left(\frac{F_{\lambda,1}}{F_{\lambda,2}} \cdot \frac{F_{zp,2}}{F_{zp,1}}\right)
\end{aligned} \tag{4.2}$$

where $F_{\lambda,i}$ are the flux densities and $F_{zp,i}$ are the corresponding zero points.

4.2 Photoionisation models of Abell 53

Abell 53 was thought to be a good candidate for modelling mainly due to its morphology, but also on the availability of multi-wavelength imaging from which surface brightness profiles and photometry can be extracted. Its almost round shape suggests that, to a first approximation, spherical symmetry may be assumed, so that complex hydrodynamical models need not be applied. Also, it is bright in both ionised and molecular hydrogen emission, both having similar profiles with radius. Cloudy, being a one dimensional code, would therefore be a good choice in this case. The main aim of this chapter is to fit the observed spatial profiles of the ionised and molecular hydrogen emission simultaneously, with as simple a model as possible. To our knowledge, this has never been attempted before for this PN.

4.2.1 The input
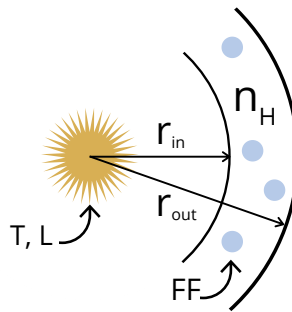
FIGURE 4.2: Sketch of the photoionisation model, showing the 5 parameters (T_*, L_*, r_{in}, n_H and FF) to be found. r_{out} is fixed at 0.167 pc.

In our model of Abell 53, we assume a spherical shell, located at a distance of 2.03 kpc. We use an outer radius as a stopping condition, set to be 0.167 pc (17 arcsec). This is chosen as we are confident that no significant emission lies outside of this radius. Dust grains are included in our simulations, consisting of a mixture of graphites and silicates. We use the default ISM grain parameters, which uses a power-law size distribution, resolved into ten size bins each for graphites and silicates. Gas to dust ratios vary significantly for PNe - we use the default Cloudy ISM value of 174. The number of grains per hydrogen for graphites and silicates were 1.545×10^{-10} and 1.786×10^{-10} respectively. The 'cosmic rays background' command subjects the nebula to a cosmic ray flux suitable to that of an object in the Milky Way. We also make use of the 'iterate' command in Cloudy[3].

---

[3]The commands are described in detail in the Hazy 1 document for Cloudy

TABLE 4.1: Input parameters for our MCMC fit. The first section gives the lower and upper limits of the parameter space to be explored (log units). The second section are the fixed parameters. The third section gives the observations, i.e. what we use to constrain the parameters.

Variable		
Parameter	Limits	
T_* (K)	4.70	5.30
L_* ($L_\odot$)	1.0	3.0
r_{in} (cm)	16.489	17.694
n_H (cm^{-3})	2.0	4.0
FF	-2.0	0.0
Fixed		
Parameter	Value	
Abundances	He	0.13
	C	6.49×10^{-4}
	N	1.76×10^{-4}
	O	8.03×10^{-4}
	Ne	4.39×10^{-4}
	Mg	1.30×10^{-7}
	Si	2.00×10^{-7}
	S	4.71×10^{-6}
	Cl	1.60×10^{-7}
	Ar	3.39×10^{-6}
	Fe	8.00×10^{-8}
Distance (kpc)	2.029	
Outer radius (pc)	0.167	
Dust	ISM (D/G = 5.759e-03)	
Observations		
Parameter	Value	
Total Hα flux (cgs)	7.66×10^{-11}	
Optical line ratios	All apart from Hδ, Hβ, [OIII](λ4363) and [Arv](λ7006)	
Surface brightness profiles	Hα (λ6563), [OIII] (λ5007), [NII] (λ6583), [SII] (λ6731), HeI (λ5876) and HeII (λ4686)	

Abundances are difficult to determine for PNe without an extensive dataset. In Section 3.3.7, we used a fairly simple routine to find rough estimations of some of the abundances of Abell 53 based on our optical spectra. To hopefully improve the accuracy of these estimations, we ran a preliminary fit using Cloudy's built-in optimizer, where we allowed the 6 elemental abundances (He, N, O, S, Ar and Ne) to vary[4], using the values from Table 3.12 as starting values, in order to fit the ISIS spectral emission lines. The total number of iterations was 2000, and a tolerance (desired fractional accuracy of the parameters) of 0.05 was used. The best values found for the 6 abundances were then fixed in the MCMC run. For other elemental abundances (C, Si, Cl,

---

[4]We also allowed the central star temperature and luminosity, inner radius and density to vary. ISM grains, a filling factor of 1.0 and a stopping radius condition were applied.

Mg and Fe), we use the same abundances as used in Aleman and Gruenwald (2011), which are taken from Kingsburgh and Barlow (1994) or Stasińska and Tylenda (1986). All other elements are switched off.

The observations we decided to fit for are the total Hα flux, most of the optical emission lines[5], relative to Hα (see Table 4.3) and the southern portions of 6 surface brightness profiles (Hα λ6563, [O III] λ5007, [N II] λ6583, [S II] λ6731, He I λ5876 and He II λ4686)[6]. Uncertainties on the SB profiles were estimated by using the upper and lower limits of the line fluxes when flux-calibrating the profiles.

In order to fit the observations of Abell 53, we first allow 5 parameters to vary: the temperature (T_*) and luminosity (L_*) of the incident radiation field (assuming a blackbody approximation for the central star); the inner radius (i.e. the distance between the central star and the start of the nebula, r_{in}); the total hydrogen density (assumed to be constant throughout the nebula, n_{H}) and the filling factor (FF), which describes the clumpiness of the model. We name this model Model 1. The variable and fixed parameters are given in Table 4.1. A simple sketch of the model is given in Figure 4.2.

4.2.2 The fitting procedure

4.2.2.1 The Bayesian approach

The classical approach to parameter estimation usually involves trying to minimise the χ^2 statistic, defined as

$$\chi^2 = \frac{(O - M)^2}{\sigma^2} \tag{4.3}$$

where O represents the observations, M the model values and σ the uncertainty on the observations. However, there is no reason to assume this is the best statistic to use. Rather than thinking of the desired parameters of the model as perfect values, it is better to think of them as probability distributions. This is where Bayes' theorem comes in:

---

[5]We exclude 4 emission lines from our fit, including Hδ, Hβ, [O III](λ4363) and [Ar V](λ7006). Hβ is excluded as it was used to find the extinction, under the assumption that F(H$\alpha)_0$ / F(H$\beta)_0$ must equal 2.86. The other 3 lines were excluded due to low SNR.

[6]These were generated as explained in Section 4.1.2, and convolved with a Gaussian profile with FWHM = 0.65 arcsec, which corresponds to the average seeing for the ISIS spectra over the observing night.

$$P(A|B) = \frac{P(B|A) \cdot P(A)}{P(B)} \tag{4.4}$$

Mathematically, this says that the probability of an event A occurring, given that we know B is true, is equal to the probability of B occurring, given that A is true, multiplied by the probability of A occurring, all divided by the probability of B occurring. In Bayesian inference, if we let A represent a model hypothesis and B represent some data, then $P(A|B)$ is the posterior (the probability of the model being correct, given the data); $P(B|A)$ is the likelihood (the probability of observing the data, given the model); $P(A)$ is the prior probability (i.e. an estimate of the model hypothesis without any data); and $P(B)$ is the global likelihood (this is usually just a normalisation constant, as the sum of the posterior probabilities must always equal 1). Bayes' theorem can therefore be recast as

$$P(model|data) \propto P(data|model) \cdot P(model) \tag{4.5}$$

Therefore, the two terms that need to be found are the likelihood and the prior. To simplify matters, we will assume that the priors are flat near the peak of the likelihood function. This means that the prior has little effect on the shape of the peak of the likelihood function, and can effectively be ignored. Applying this to our situation, Equation 4.5 reduces to

$$P([T_*, L_*, r_{in}, n_H, FF] \mid data) \propto P(data \mid [T_*, L_*, r_{in}, n_H, FF]) \tag{4.6}$$

where *model* has been replaced by the parameters we wish to constrain. We now only need to find the likelihood function. Assuming that the probability of obtaining a data point (x_i, y_i, σ_i) is independent of all the other data points:

$$
\begin{aligned}
P(data \mid [T_*, L_*, r_{in}, n_H, FF]) &= P(\{x_i, y_i, \sigma_i\}^N \mid [T_*, L_*, r_{in}, n_H, FF]) \\
&= P([x_1, y_1, \sigma_1] \mid [T_*, L_*, r_{in}, n_H, FF]) \times \\
&\quad P([x_2, y_2, \sigma_2] \mid [T_*, L_*, r_{in}, n_H, FF]) \times ... \\
&\quad P([x_N, y_N, \sigma_N] \mid [T_*, L_*, r_{in}, n_H, FF]) \\
&= \prod_{i=1}^{N} P(x_i, y_i, \sigma_i \mid [T_*, L_*, r_{in}, n_H, FF])
\end{aligned} \tag{4.7}
$$

Assuming Gaussian uncertainties, the likelihood function, $\mathscr{L}$, becomes:

$$\mathscr{L} = \prod_{i=1}^{N} \frac{1}{\sqrt{2\pi}\sigma_i} \exp\left(\frac{-(O_i - M_i)^2}{2\sigma_i^2}\right) \tag{4.8}$$

and taking natural logs gives

$$\begin{aligned} \ln(\mathscr{L}) &= K^2 - \sum_{i=1}^{N} \frac{(O_i - M_i)^2}{2\sigma_i^2} \\ &= K^2 - 0.5\chi^2 \end{aligned} \tag{4.9}$$

where K is a constant. This shows that maximising the log of the likelihood function is equivalent to minimising χ^2. We now need a tool in order to find the best distribution of parameter values that maximise the likelihood.

4.2.2.2   Markov Chain Monte-Carlo (MCMC)

A Markov-Chain is a mathematical process in which a series of steps are taken through a parameter space, where each step depends only on the current location in the space. After each step, the ratio of the posterior at the current and previous positions, a, is calculated, along with a random number, r, between 0 and 1. If $r < a$, the step is accepted, and the process repeated. Using this algorithm, known as a Metropolis-Hastings algorithm (Metropolis et al. 1953; Hastings 1970), means that after some time, the walkers that take these steps are likely to be found in a region where the posterior probability is high, and so corresponds to the region where the best-fit parameters can be found.

The burn-in phase corresponds to the initial period of time where the walkers search for the regions of high posterior probability. To ensure that the burn-in phase is completed, meaning the desired parameter distributions are eventually found, the algorithm needs to be repeated many times. To save on time and resources, we were able to simultaneously run multiple Cloudy models using the multi-threaded version of the Metropolis-Hastings algorithm, described in Mullin and Hardcastle (2009). We ran our simulation for 168 hours on 128 cores, using the University of Hertfordshire's high performance computing (HPC) facility, resulting in a total number of models of 32407.

4.2.2.3 The priors

Choosing good prior information ensures the MCMC routine samples the whole possible parameter space, while not wasting resources by testing unphysical parameters. We use flat priors, defined by a lower and upper limit. The choice of priors are described below:

- The central star parameters: effective temperature (T_*) and total luminosity (L_*). These are allowed to vary from 4.70 to 5.30 (log K), and 1.0 to 3.0 (log $L_\odot$) respectively. These were chosen to represent the parameter space where models of different mass central stars on their respective cooling tracks pass through (Miller Bertolami, 2016).

- The inner radius (r_{in}), varied from 0.01 to 0.16 pc. This range ensures that we allow both thick and thin shells, while not making models that extend beyond the observed estimated radius.

- The total hydrogen density (n_H), varied from 100 to 10000 cm^{-3}, which lies within the range of typical PN electron densities (Frew and Parker, 2010).

- The filling factor (FF), varied from 0.01 to 1.0. The smaller the number, the clumpier the model, which Cloudy accounts for by replacing regions of the nebula with vacuum.

4.2.3 Results of the fit

The best-fit parameters are given in Table 4.2, with the best fit optical line ratios and surface brightness profiles in Table 4.3 (Model 1) and Figure 4.5 respectively. It is worth emphasising that only a few studies have attempted to fit to SB profiles of PNe (e.g. Öttl et al., 2014; Barría and Kimeswenger, 2018), and to our knowledge, this is the first to perform the fit using MCMC methods. The best-fit parameters are determined from the median of the values where the burn-in phase has completed, while the uncertainties are given by the 3σ (0.135 and 99.865th percentile) confidence levels. In Figure 4.3, we display the results from the fitting procedure. The top plot shows the progress made by the fitting routine over the run, and how the best-fit values for the five parameters are reached. The bottom corner plot shows the various parameter spaces. Any skewness in these distributions suggests a covariance between two parameters, where a positive covariance means that larger values of one parameter correspond to larger values of another. It can be seen that a fairly weak positive covariance exists between the inner radius and the filling
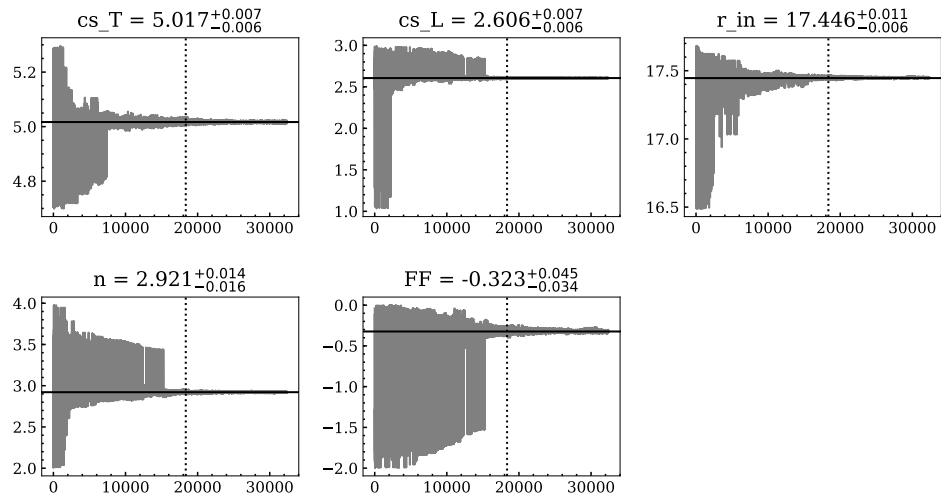
(A)
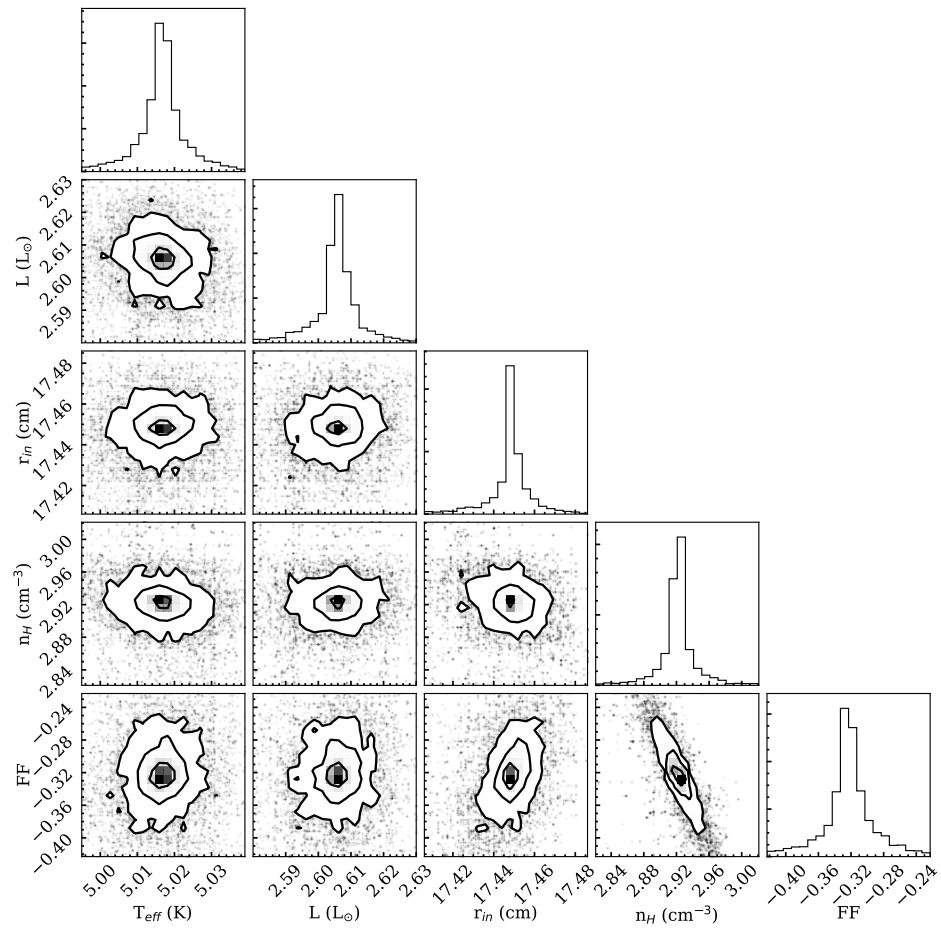
(B)

FIGURE 4.3: Plots from the MCMC run for Model 1. (A) convergence plots, with model number on the x-axis (effectively time), and the parameter value on the y-axis. The vertical black line indicates the end of the burn-in phase, while the horizontal black line is the median value after the burn-in phase has ended. (B) corner plots, demonstrating the various parameter spaces.
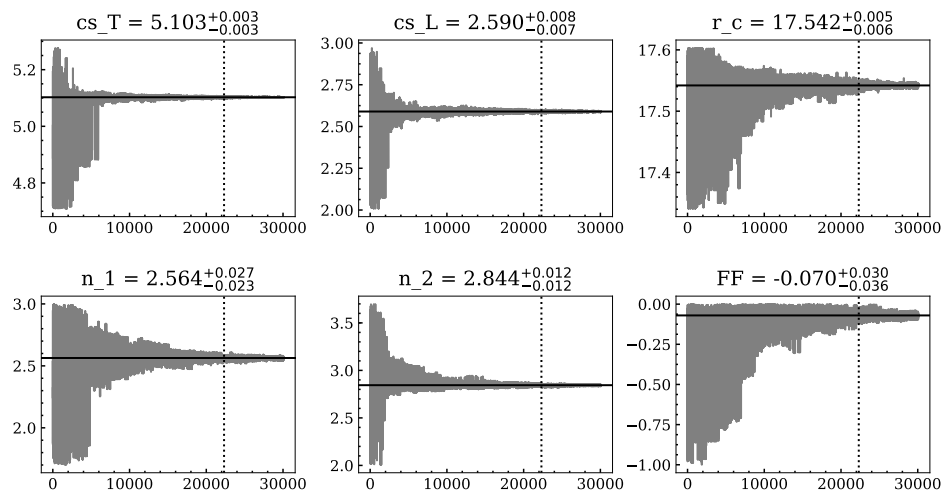
(A)
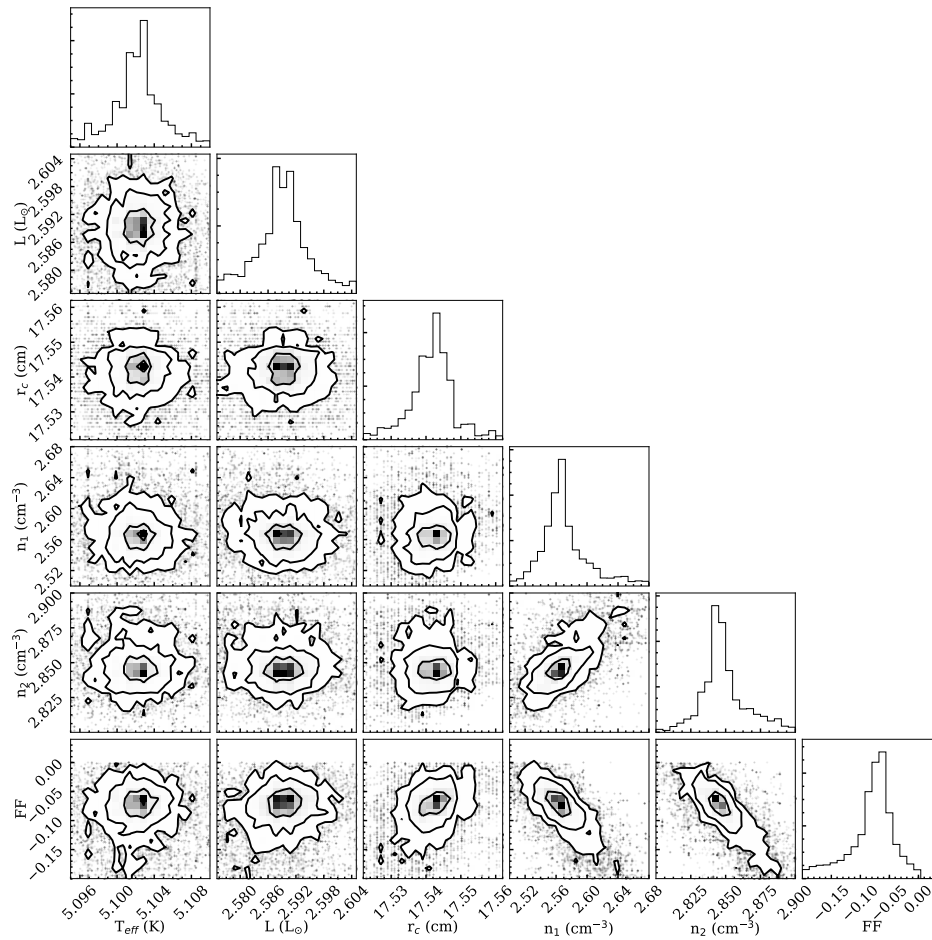
(B)

FIGURE 4.4: Same as Figure 4.3, but for Model 2.

TABLE 4.2: Best-fit parameters for Models 1 and 2 with 3σ uncertainties (log units).

Model 1		Model 2	
Parameter	Value (log)	Parameter	Value (log)
T_* (K)	$5.017^{+0.007}_{-0.006}$	T_* (K)	$5.103^{+0.003}_{-0.003}$
L_* ($L_\odot$)	$2.606^{+0.007}_{-0.006}$	L_* ($L_\odot$)	$2.590^{+0.008}_{-0.007}$
r_{in} (cm)	$17.446^{+0.011}_{-0.006}$	r_c (cm)	$17.542^{+0.005}_{-0.006}$
n_H (cm^{-3})	$2.921^{+0.014}_{-0.016}$	$n_{H,1}$ (cm^{-3})	$2.564^{+0.027}_{-0.023}$
FF	$-0.323^{+0.045}_{-0.034}$	$n_{H,2}$ (cm^{-3})	$2.844^{+0.012}_{-0.012}$
		FF	$-0.070^{+0.030}_{-0.036}$

factor, and a strong negative covariance exists between the density and the filling factor. In other words, clumpier models require thicker and denser nebula shells.

For a fairly straightforward model, the overall fit to the observations is quite good. Many of the line ratios agree to within 10%, and the surface brightness profiles (Figure 4.5) are generally reproduced[7], with the exception of the HeII ($\lambda 4686$) line, which has a profile that peaks 2 to 3 arcsec beyond what is observed (corresponding to the inner radius of the model). A radius of 0.09 pc combined with an outer radius of 0.167 pc gives a shell thickness of 0.077 pc. A higher than expected density is found (834 cm^{-3}, compared to our estimated value based on SII observations of 435 cm^{-3}), however lies within values for typical PNe. The average electron temperature in the model, 9123 K, is supported by our value of 9653 K estimated using [NII] lines. We also find that a filling factor of 0.475 means that a reasonable degree of clumpiness in the nebula is favoured, which is supported by the fact that images of Abell 53 show clear signs of clumps.

The best-fit central star parameters (temperature and luminosity) are displayed in Figure 4.6 along with evolutionary tracks of different masses for a single metallicity (Miller Bertolami, 2016). For Model 1, this point does not coincide with any of the tracks within the uncertainties, however lies closest to the lowest-mass track ($M_{\text{final}} = 0.532$ M$_\odot$).

4.2.4 A more realistic model

In Model 1 it was assumed that a blackbody is a reasonable approximation for the incident radiation field. However, the true spectra of central stars are observed to deviate from a blackbody, especially at energies greater than the ionisation energy of HeII (228 Å). Central stars evolve quickly around the HR diagram, and so too do their spectra, displaying a variety of emission

---

[7]Each SB profile consists of 69 data points, therefore the fitting procedure will be more constrained towards these than the line ratios.

TABLE 4.3: Best-fit total Hα flux (cgs units) and optical lines (relative to Hα) from Models 1 and 2. χ^2 values are also given to indicate how well each observation has been fit, where lower values correspond to better fits.

ID	λ(Å)	Observed	Uncertainty	Model 1		Model 2	
				Value	χ^2	Value	χ^2
Hα	6563	7.67×10^{-11}	1.28×10^{-11}	7.48×10^{-11}	2.20×10^{-2}	6.54×10^{-11}	7.85×10^{-1}
O$_{II}$	3727	2.75	3.52×10^{-1}	2.33	1.45	2.89	1.39×10^{-1}
Ne$_{III}$	3868	7.16×10^{-1}	1.38×10^{-1}	7.16×10^{-1}	5.32×10^{-6}	1.03	5.10
Ne$_{III}$	3969	3.24×10^{-1}	9.79×10^{-2}	2.17×10^{-1}	1.18	3.12×10^{-1}	1.41×10^{-2}
Hγ	4340	1.63×10^{-1}	3.61×10^{-2}	1.68×10^{-1}	2.46×10^{-2}	1.69×10^{-1}	2.68×10^{-2}
He$_{II}$	4686	6.24×10^{-2}	1.52×10^{-2}	4.44×10^{-2}	1.40	5.37×10^{-2}	3.24×10^{-1}
O$_{III}$	4959	9.66×10^{-1}	5.37×10^{-2}	9.48×10^{-1}	1.05×10^{-1}	1.29	3.55×10^{1}
O$_{III}$	5007	2.79	1.52×10^{-1}	2.83	5.55×10^{-2}	3.84	4.71×10^{1}
N$_{I}$	5199	2.48×10^{-2}	6.86×10^{-3}	2.66×10^{-2}	6.42×10^{-2}	3.16×10^{-2}	9.85×10^{-1}
N$_{II}$	5754	1.55×10^{-2}	1.32×10^{-3}	1.73×10^{-2}	1.87	2.28×10^{-2}	3.10×10^{1}
He$_{I}$	5876	6.11×10^{-2}	3.70×10^{-3}	5.68×10^{-2}	1.35	5.60×10^{-2}	1.87
O$_{I}$	6300	1.48×10^{-1}	7.18×10^{-3}	1.37×10^{-1}	2.55	1.75×10^{-1}	1.42×10^{1}
S$_{III}$	6312	3.02×10^{-3}	6.70×10^{-4}	2.89×10^{-3}	3.71×10^{-2}	3.74×10^{-3}	1.17
O$_{I}$	6364	4.70×10^{-2}	2.33×10^{-3}	4.37×10^{-2}	1.97	5.60×10^{-2}	1.50×10^{1}
N$_{II}$	6548	3.83×10^{-1}	1.93×10^{-2}	4.49×10^{-1}	1.15×10^{1}	5.15×10^{-1}	4.66×10^{1}
N$_{II}$	6583	1.39	6.65×10^{-2}	1.32	9.62×10^{-1}	1.52	3.80
He$_{I}$	6678	1.44×10^{-2}	9.10×10^{-4}	1.58×10^{-2}	2.23	1.56×10^{-2}	1.55
S$_{II}$	6716	9.22×10^{-2}	4.96×10^{-3}	8.82×10^{-2}	6.78×10^{-1}	1.08×10^{-1}	1.02×10^{1}
S$_{II}$	6731	8.97×10^{-2}	4.83×10^{-3}	9.31×10^{-2}	4.83×10^{-1}	1.09×10^{-1}	1.52×10^{1}
He$_{I}$	7065	1.39×10^{-2}	9.30×10^{-4}	1.45×10^{-2}	4.17×10^{-1}	1.43×10^{-2}	1.75×10^{-1}
Ar$_{III}$	7136	1.05×10^{-1}	6.17×10^{-3}	1.03×10^{-1}	9.04×10^{-2}	1.15×10^{-1}	2.58
He$_{I}$	7281	2.79×10^{-3}	5.10×10^{-4}	3.24×10^{-3}	7.80×10^{-1}	3.25×10^{-3}	8.00×10^{-1}
O$_{II}$	7320	3.61×10^{-2}	2.23×10^{-3}	3.42×10^{-2}	7.24×10^{-1}	4.31×10^{-2}	9.89
O$_{II}$	7330	3.00×10^{-2}	1.85×10^{-3}	2.80×10^{-2}	1.20	3.53×10^{-2}	8.16
Ar$_{III}$	7751	2.21×10^{-2}	1.60×10^{-3}	2.45×10^{-2}	2.16	2.73×10^{-2}	1.03×10^{1}

TABLE 4.4: χ^2 values for Models 1 and 2, including those for the optical line fluxes (including total Hα flux), surface brightness profiles and the totals. $\chi^2_v = \chi^2/(n-m)$ is the reduced chi squared statistic, where n is the number of observations, and m is the number of fitted parameters. Each SB profile consists of 69 data points, and there were 25 line fluxes to be fitted to. Hence, $n = (69 \times 6) + 25 = 439$.

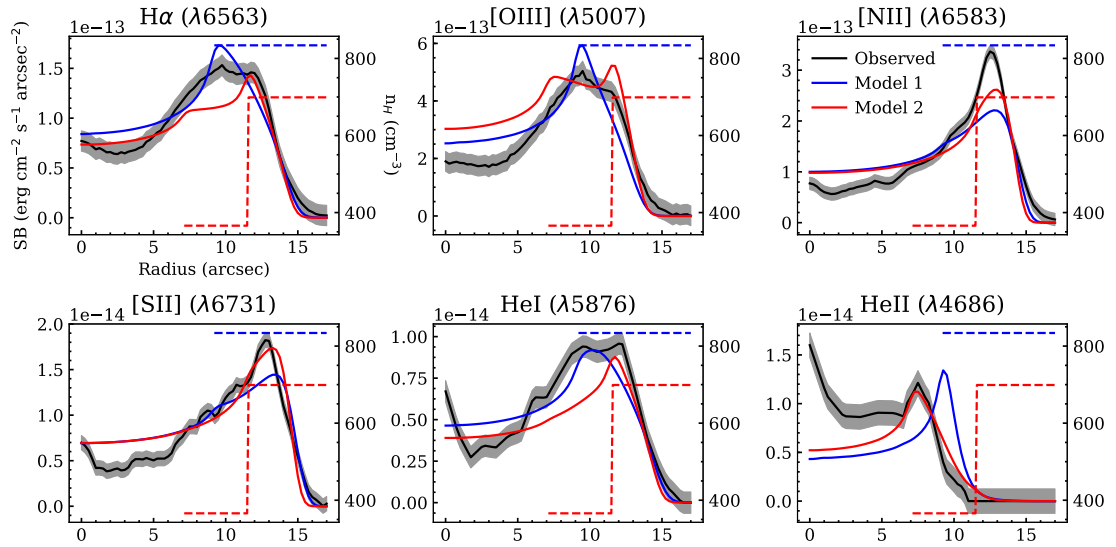|	χ^2	
	Model 1	Model 2
Line fluxes	33.3	263
SB profiles:		
Hα	132	181
O$_{III}$	232	456
N$_{II}$	718	489
S$_{II}$	429	382
He$_{I}$	194	392
He$_{II}$	881	401
Total χ^2	2619	2564
Total χ^2_v	6.04	5.92

FIGURE 4.5: Surface brightness profiles for best-fit models (solid lines). Blue and red lines are for Models 1 and 2 respectively; observed profiles are given by the solid black lines, with estimated uncertainties given by the grey region. The dashed lines gives the total hydrogen density profiles, with values given on the right-hand axis.
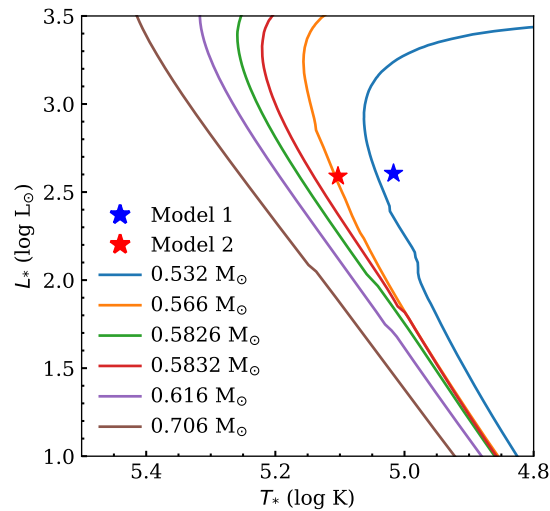

FIGURE 4.6: CS tracks of different core masses from Miller Bertolami (2016) for Z=0.01, with the best-fit values of temperature and luminosity for Models 1 and 2 overlaid. Uncertainties fall within the size of the marker. There is no significant change in the tracks for similar mass stars of lower metallicities.

and absorption lines, along with varying levels of continuous absorption. The majority of CSPN can be split into two groups: those that contain stellar H features (H-rich), and those that do not (H-poor) (Mendez, 1991).

To see what effect using a more realistic input SED would have on the fit, the blackbody is replaced with a stellar atmosphere model of a H-Ni PN nucleus, taken from Rauch (2003), defined by a temperature and surface gravity, or log g. Without better observations of the CS of Abell 53, a value of log g is assumed throughout the fit. As the results of Model 1 suggest that a lower mass CS is preferable, and the fact that higher mass central stars tend to be associated with bipolar PNe (whereas Abell 53 is round), we set log $g = 7$. This value roughly corresponds to the average surface gravities of the lower mass stars on their respective cooling tracks, taken from Miller Bertolami (2016).

As mentioned in the previous section, the position of the peak of the simulated HeII SB profile was beyond what is observed. In order to push this profile inwards, there needs to be nebula material at smaller radii than the best-fit value of r_{in}. We therefore adapt our model slightly to include a lower-density region, with density $n_{H,1}$ that begins at 0.07 pc, which then joins the rest of the nebula, with density $n_{H,2}$, at some radius, r_c. There are now 6 parameters to be determined from the fit: T_*, L_*, r_c, $n_{H,1}$, $n_{H,2}$ and FF. r_c is allowed to vary between 0.071 and 0.13 pc. $n_{H,1}$ and $n_{H,2}$ are varied from 50 to 1000 cm^{-3}, and 100 to 5000 cm^{-3} respectively. All other parameters are as described for Model 1. This model is named Model 2.

The results of the MCMC fit are given in Figure 4.4. Key differences between the best fit parameters of Models 1 and 2 include the latter requiring lower densities (a mean density of 613 cm^{-3} weighted over volume brings it closer to what was estimated using [SII] lines) and filling factor, but also a higher CS temperature (see Table 4.2). Figure 4.6 shows that this higher temperature results in the CS lying very close to the cooling track of a 0.566 M$_\odot$ core mass star. The closest point on this track to our best-fit parameters gives a CS age of $\sim$ 18000 years. Improvements to the SB profiles of [NII], [SII] and HeII are found with Model 2; the latter of these now having its peak position coincident with what is observed (Figure 4.5). However, the inclusion of the inner lower density region has distorted the shapes of the Hα and [OIII] profiles. The total Hα flux has been reduced to the lower limit of what is observed, and the quality of the fit to the optical line ratios have been reduced (apart from minor improvements to 5 lines). The total chi squared values for Models 1 and 2 are fairly similar, however these are heavily influenced by the SB profiles.

TABLE 4.5: Best-fit parameters (density, thickness and temperature floor) for the H_2 observations, for models where PAHs aren't and are included.

| PAHs | Best values | | | H_2 1-0 S(1) / Hα | | H_2 1-0 S(1) / 2-1 S(1) | |
	n (cm^{-3})	t (pc)	T_f (K)	Obs.	Mod.	Obs.	Mod.
No	15750	0.010	2100	0.01522 ± 0.00229	0.015236	11.06 ± 2.26	11.048499
Yes	14750	0.009	2100		0.015223		11.050926

Even though this scenario was intended to represent a more realistic model of Abell 53, from this point the best-fit model using a blackbody (Model 1) will be considered, as the fit to the optical line ratios, as well as the total Hα flux, was much better, even though the lack of an inner, lower density region meant that the fit to the He II was worse.

4.2.5 Simulating the H_2 emission

Up to this point, only the ionised region of Abell 53 has been modelled, where the majority of the strong optical lines originate from. However, one of the main purposes of this work is to simultaneously recover both the optical and near-IR H_2 observations using a single model. It is known that H_2 is seen to form in clumps of high density material within PNe, and we believe Abell 53 to be no exception. To re-create this in our models, we take the geometry of Model 1 and add to the outer nebula a much higher density region, of which the thickness (t) and density (n) are to be determined. The outer radius is kept fixed at 0.167 pc, while the position of the beginning of the high-density region is adjusted. To simulate the extra heating which would occur in a shock, we make use of the 'temperature floor' command, which sets a minimum electron temperature that can be reached[8]. A grid of models was made by varying the thickness (t), density (n) and temperature floor (T_f) of the region, while keeping everything else fixed, in order to fit both the H_2 1-0 S(1) flux (rel. to Hα), and the H_2 1-0 S(1) / 2-1 S(1) ratio[9].

The parameters and results of the best model are given in Table 4.5. The inclusion of this high density region with a temperature floor increases the intensity of the H_2 1-0 S(1) line by a factor close to 2000. The observed brightness of the 1-0 S(1) line is degenerate to the thickness of the region, and its density - thinner regions require a larger density, and vice versa (see Figure 4.7a. The H_2 1-0 S(1) / 2-1 S(1) ratio is strongly dependent on the choice of temperature floor. To achieve the observed value, while maintaining the observed flux of the 1-0 S(1) line, this should

---

[8]This is similar to the method adopted by Otsuka et al. (2017).

[9]As the parameters are manually chosen, the entire continuous parameter space cannot be explored. This method was only utilised as it is quicker and simpler to implement, and we were only interested in determining a reasonable estimation of the best-fit parameters.
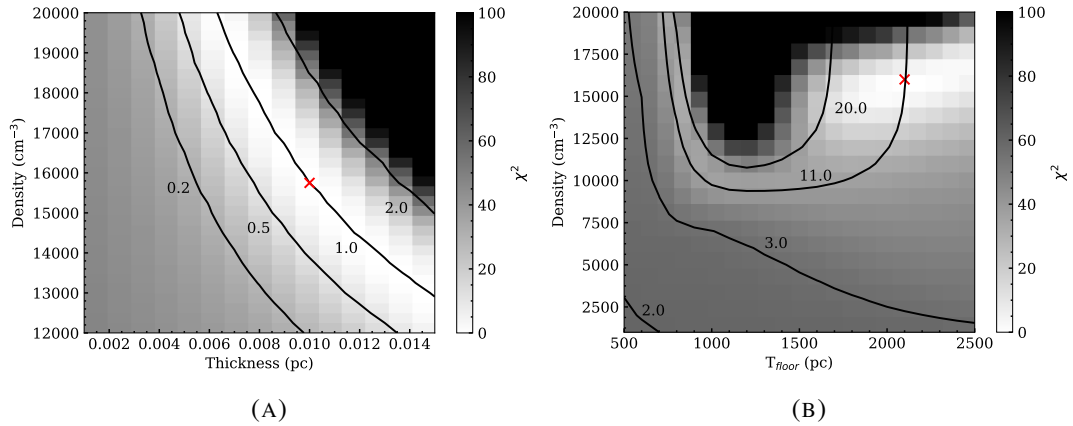
FIGURE 4.7: Searching for the best H$_2$ parameters (with PAHs off). Both images display the combined χ^2 for the H$_2$ 1-0 S(1) / Hα and H$_2$ 1-0 S(1) / 2-1 S(1) ratios. (A) Variation of χ^2 with density and thickness, for T_f = 2100 K. Contours represent four factors that the observed H$_2$ 1-0 S(1) / Hα ratio is multiplied by (i.e. 1.0 is the observed H$_2$ 1-0 S(1) flux, 2.0 is double etc.). (B) Variation of χ^2 with density and temperature floor, for thickness = 0.010 pc. Overlaid are 4 contours which give different values of the H$_2$ 1-0 S(1) / 2-1 S(1) ratio. In both plots, the red cross marks the location of minimum χ^2.

be close to 2100 K (Figure 4.7b). The bright IRAC 8μm image likely shows that polycyclic aromatic hydrocarbons (PAHs) are present in Abell 53. To test what effect the presence of PAHs has on the intensity of the 1-0 S(1) line, we re-ran the grid of models with them included. The results in Table 4.5 show that a region with lower density (and slightly thinner) can reproduce the same results.

The default parameters describing the PAH properties in Cloudy give a power-law distribution of sizes with 10 size bins (as described in Abel et al. (2008)), along with two single-sized PAHs. PNe are usually divided into those which are carbon-rich (C/O abundance > 1) and those which are oxygen-rich (C/O < 1). Oxygen-rich AGB stars are concentrated towards the galactic centre, while carbon-rich AGB stars are distributed more evenly with distance from the centre (e.g. Ishihara et al. 2011). The C/O value in the atmospheres of AGB stars will determine the type of dust grains that form in the PNe. PAHs are often, but not exclusively, found in carbon-rich PNe. If the bright IRAC 8μm image of Abell 53 suggests that PAHs may be present, then it may be likely that Abell 53 is carbon-rich. However, without access to high resolution spectra at mid-IR wavelengths, it is not possible to say conclusively whether Abell 53 is oxygen-rich or carbon-rich.

Unfortunately, the H$_2$ 1-0 S(1) SB profile could not be reproduced using the current geometrical assumptions, without drastically changing the optical SB profiles (see Figure 4.8a). This is because, as seen in Figure 3.20, the H$_2$ 1-0 S(1) profile peak position lies just beyond of the SB
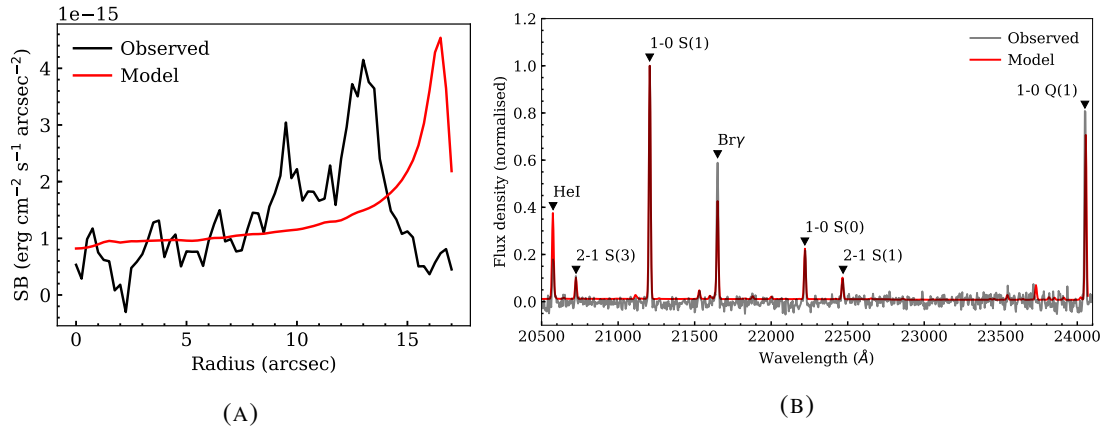
FIGURE 4.8: (A) Observed and model H_2 1-0 S(1) SB profiles. (B) Observed and model K-band spectra, with emission lines labelled. As Cloudy can only generate an SED for the whole nebula, we show here the spectra normalised so that the peak of the H_2 1-0 S(1) line is 1.0. The synthetic K-band spectrum is convolved to match observations.

profile of Hα, and their close proximity makes it very difficult to fit both simultaneously. This is why the high density region is not placed at radii less than 0.15 pc - any closer than this will alter the optical SB profiles.

The observed and synthetic K-band spectra (normalised) of Abell 53 are shown in Figure 4.8b. It can be seen that good fits are obtained for the H_2 lines. The observed H_2 1-0 S(1) / Brγ ratio was 1.76, compared to the modelled value of 1.59. The fit looks worse than reality for the Brγ line in Figure 4.8b, as the model spectrum is that of the whole nebula, rather than that through a 1 arcsec-width slit (as in the LIRIS observations). As H_2 emission is brightest in the outer regions, the spectrum of the whole nebula would therefore contain more H_2 1-0 S(1) relative to Brγ, than that through a slit positioned at the centre. The 20580 $\mathring{A}$ HeI line intensity is overestimated in the model.

4.2.6 IRAC profiles

As mentioned in the introduction of this chapter, Phillips and Ramos-Larios (2008) measured the surface brightness profiles of Abell 53 in the 4 IRAC bands. In Figure 4.9, we have re-plotted portions of these profiles, and compared them to the profiles from our best-fit model (including the high-density outer region)[10]. Many emission lines of H_2 lie within the IRAC passbands, as well as broad PAH features, while smooth emission from dust grains is responsible for the continua. Throughout the modelling, a dust to gas ratio representative of the ISM is adopted. We

[10]The model SB profiles for the IRAC bands simply sum the flux of the SED between an upper and lower wavelength limit for each filter (rather than taking into account filter transmission profiles.)

show the profiles for the two models described in Table 4.5 - those where PAHs are and are not included. The most significant effect of the inclusion of PAHs is an increase to the 8μm IRAC band, within which lies the 7.7 μm PAH feature. Without sufficient mid-IR observations, we make no attempt to fit the dust and PAH components of Abell 53. Nonetheless, the reasonable closeness of the observed and simulated IRAC SB profiles is a fair indication that the grain and PAH abundances are reasonable.
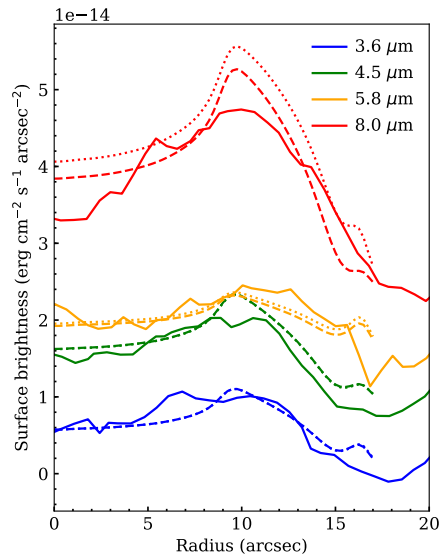

FIGURE 4.9: IRAC SB profiles for best-fit models. Observed values (solid lines) are taken from the left portion of figure 4 from Phillips and Ramos-Larios (2008). The model profiles without (dashed lines) and with PAHs (dotted lines) are taken from the best-fit models described in the previous section. All lines are vertically shifted by the same values as in Phillips and Ramos-Larios (2008), which are 0, 2.5, 5.0 and 7.5 MJy/sr for the 3.6, 4.5, 5.8 and 8.0 μm bands respectively.

4.2.7 The SED

The best-fit SED is shown in Figure 4.10, where we also show the SED of the input radiation field (blackbody) and overlay our photometry. While we did not use the broadband photometry fluxes to constrain the fit, it can be seen that there are no huge discrepancies between the observations and the synthetic nebula SED. There is a discrepancy between the incident SED and the CS photometry. If the CS photometry is accurate, this would imply that a hotter CS would be preferable, which would shift the SED to the left - this is what was found for the stellar atmosphere fit. However it was decided not to fit to the CS photometry due to the relatively large uncertainties and the remaining doubt as to whether the faint star observed close to the centre of the nebula is in fact the central star of Abell 53.
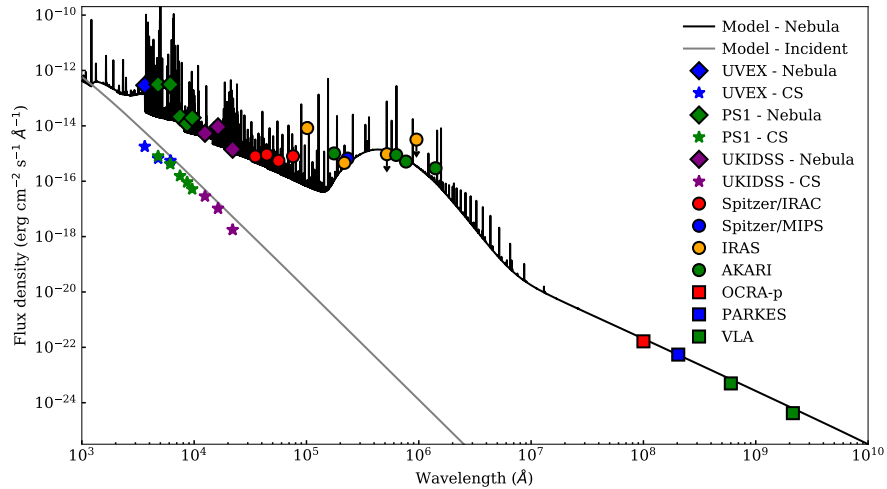
FIGURE 4.10: Best-fit SEDs for the nebula and central star, with photometry overlaid.
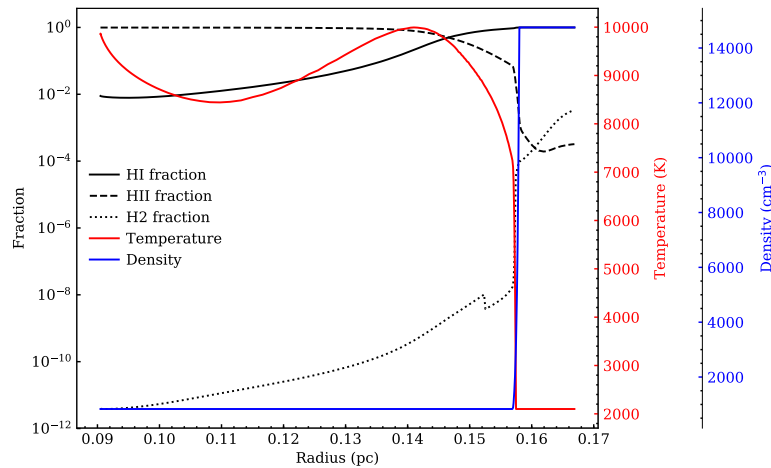
4.2.8 Nebula structure

FIGURE 4.11: Variation of H density (blue), electron temperature (red) and fractional abundances relative to total (black) as a function of radius within the nebula.

Some parameters as a function of radius within the nebula are given in Figure 4.11. The electron kinetic temperature varies between 10000 K and 8000 K out to 0.14 pc, consistent with our initial estimate based on observations of [NII] (9653 K). At 0.155 pc, the temperature drops sharply, coinciding with a sharp increase in the H density. Hydrogen in the nebula is entirely ionised out to around 0.14 pc. From here to 0.15 pc, it transitions into a predominantly neutral region, at which point it can be said that a PDR begins. H_2 starts to build up significantly where the density increases. Our model of Abell 53 would be described as radiation-bounded - that is, a model where the ionised-neutral boundary lies within the nebula, therefore consisting of an inner ionised region, responsible for the optical line intensities, and an outer neutral region, where the H_2 lines are produced.

4.3 Discussion and summary

To our knowledge, this was the first attempt at creating a photoionisation model of Abell 53 - a largely unstudied planetary nebula. Due to its nearly round shape, it was thought to make a good candidate for attempting to fit a simple spherical model to observations of emission lines. In general, one could say that this objective was largely achieved, however some issues still remain to be discussed, while others are left as future work.

In this Chapter, Cloudy, a well-known photoionisation code, has been used to try to replicate the observations of Abell 53. Using a blackbody to describe the incident radiation field, along with a nebula shell of a particular thickness, density and clumpiness (5 parameters in total), a good fit to the intensities of a large number of optical emission lines, relative to Hα, and the variation in intensity with radius of 6 emission lines, was obtained for Abell 53. The best-fit parameters included a star with an effective temperature and luminosity of 104 kK and 400 L$_\odot$ respectively, along with a shell spanning from 0.09 to 0.167 pc, with density 830 cm^{-3} and filling factor 0.48. Issues with reproducing the location of the He$_{II}$ 4686 line, and the desire to have a more realistic incident SED, led to running another fit utilising white dwarf stellar atmosphere files and a second, lower density inner region. While improvements to the SB profiles of some lines were found, along with a temperature-luminosity pair of 127 kK and 390 L$_\odot$, more in-line with theoretical cooling tracks, generally the fit to the optical line ratios was worse. This is unfortunate, as it seemed reasonable that including a physically sensible input radiation field would lead to an improved fit. An area of future work would be to explore the parameter space further, perhaps excluding the SB profiles from the fit, and even using different surface gravities.

Keeping with the theme of this thesis, it was of great interest to reproduce the large intensity of H$_2$ 1-0 S(1) in Abell 53, observed both in the UWISH2 survey and K-band spectra. Cloudy is a photoionisation code, and works by balancing the rate at which electrons are stripped from nuclei and the rate at which they recombine. While it has a large dataset of H$_2$ lines and sophisticated methods on calculating its rates of formation and destruction, it does not handle shock excitation, which may be at least partly responsible for the intensities of the H$_2$ 1-0 S(1) and 2-1 S(1) lines. Otsuka et al. (2017) found that using a temperature floor option can help to simulate the extra heating that would occur due to a propagating shock wave, and so reproduce observed H$_2$ intensities. However, Cloudy is not designed to be a replacement for a sophisticated shock code. Nonetheless, H$_2$ line fluxes in the K-band were reproduced in Abell 53, using a 2100 K temperature floor in an outer region of density $\sim$ 15000 cm^{-3} and thickness 0.010 pc. A much

higher density is needed, as it helps to prevent the entire shell from becoming ionised, and a higher density leads to a higher concentration of dust grains - the primary sites of H_2 formation.

A negative aspect of the inclusion of this high density region is its effect on the total mass of the shell - increasing it from a reasonable 0.25 $M_{\odot}$ to a rather large value of = 1.17 $M_{\odot}$. If the CS is located on a cooling track for a low-mass star, i.e. M_{ZAMS} = 1.0 or 1.25 $M_{\odot}$, M_f = 0.532 or 0.566 $M_{\odot}$ (Miller Bertolami, 2016), then a maximum possible mass available to form a PN would be around 0.47 or 0.68 $M_{\odot}$ - a shell mass of 1.17 $M_{\odot}$ is unlikely. Another issue is the inability to reproduce the SB profile of the 1-0 S(1) line in the model. This is likely a consequence of the idealistic assumptions of a spherical geometry, and an oversimplified density profile. Hydrodynamical models (e.g. Schönberner et al. 2005a) have shown that complex density profiles are produced when shock interactions are considered. Observations of PNe such as Fang et al. (2015) and Fang et al. (2018) demonstrated that H_2 emission can be bright in high density knots and clumps, where they are shielded from the high UV flux of the central star. Limited by a lack of options for a variable filling factor with radius, these conditions were difficult to reproduce in our models. In reference to the spherical geometry assumption, while reasonable to assume given the round shape of Abell 53, it is likely that a more complex geometry exists. This could be in the form of a toroidal shell, or even as a bipolar hour glass geometry, viewed edge on. pyCloudy can be used to generate SB profiles for non-spherical models of this type - another area for future work would be to explore these various geometries.

More accurate determinations of model parameters would require additional data sets. As shown in Otsuka et al. (2017), mid-IR spectra are a valuable tool in determining the properties of both H_2 and dust grains. Ideally, observations of IR fine-structure lines (e.g. [CII] 158μm, [OI] 65μm, [CI] 609 μm) are needed to accurately determine the physical structure of the PDR. Deeper and increased resolution spectra in the optical region would reveal many more emission lines - especially those of higher excitation classes. This would allow for better abundance determinations and constraints to the ionised region. While we chose to use Cloudy due to its accessibility and extensive data set, other codes are available. Two examples are MAPPINGS (Sutherland et al., 2018), which can handle photoionisation and ionisation by shock waves; and MOCASSIN (Ercolano et al., 2003), a 3D radiative-transfer code using Monte-Carlo techniques.

In summary, the purpose of this Chapter was to re-create observations of a planetary nebula using a photoionisation code, and in particular, simultaneously fit to both the ionised and neutral components. Observations of both the optical and near-infrared regions were utilised, and

realistic optimum parameters were found. To our knowledge, this was the first attempt at fitting surface brightness profiles of atomic lines, along with line fluxes of H_2, for a planetary nebula. The work presented in Chapters 3 and 4 are in the process of becoming a paper (Jones and Gledhill (in prep.)).

Chapter 5

Photoionisation models of evolving PNe

5.1 Introduction

5.1.1 Models of evolving PNe in the literature

Mass loss during the AGB phase, and in the post-AGB phase, where the star heats up and evolves to the left of the HR diagram, is responsible for the formation of the PN and the star's subsequent evolution to the white dwarf stage. The slow and dense AGB wind is heated and ionised by the radiation field of the CS. A shock wave is generated which becomes compressed on its inner edge by the much faster CS wind (Schönberner, 2016). This scenario can describe observations of round and elliptical PNe, many of which consist of an inner bright rim and a fainter outer shell, which in turn is surrounded by the previously ejected halo. The interacting stellar winds (ISW) model (Kwok et al., 1978) was the first to develop this idea, by suggesting that a fast ($>$1000 kms^{-1}) wind from the CS can sweep-up and overtake the slower ($\sim$ 15 kms^{-1}), denser AGB material, shaping it in the process. Refinements to their work (Kwok 1982; Volk and Kwok 1985) meant that reasonable PN expansion velocities ($\sim$ 20 kms^{-1}) could be produced. However, the ISW model could not explain the growing number of observations of multiple-shell PNe.

This issue was confronted by the first radiation-hydrodynamics models (Schmidt-Voigt and Koeppen 1987a; Schmidt-Voigt and Koeppen 1987b), and ever since, there have been more and more sophisticated codes developed to improve the models. Radiation-hydrodynamics models of PNe look at the interplay between the heating and subsequent ionisation of the gas, with

the changing momentum of the gas due to dynamic evolution of the stellar and AGB winds. In general, they find that the main PN is confined between two shock fronts, where there are sudden changes in density. The outer front is formed as the shock moves into the previously ejected, slow, dense AGB wind, while the inner front is due to the PN being heated and ionised by the newer, fast stellar wind. Steffen et al. (1998) used one of the first time-dependent models, concentrating on the momentum transfer from collisions between dust grains and the gas in a stellar wind, and found that the final thermal pulses on the AGB were largely responsible for the density structure and energy distribution in the subsequent planetary nebula. The parameter study of Perinotto et al. (2004) made use of the central star evolutionary models of Bloecker (1995) and Schoenberner (1983), which have since been updated (Miller Bertolami, 2016), with higher luminosities and faster post-AGB timescales. Like other models, they confirmed that the ionisation front travels outwards from the CS and sets up a shock wave which disturbs the density and velocity structure. At early PN phases, while the wind power is low, the PN structure is dominated by the effects of ionisation. As the CS wind increases, it forms a double-shell structure, which can in turn become a single shell structure as the main PN overtakes the outer shell. Jacob et al. (2013) made efforts to clarify the definition of the 'true' expansion velocity of PNe - i.e. the velocity of the shell's leading shock, defining the outer radius of the PN. This is something that cannot be measured spectroscopically (i.e. through the shifting and splitting of certain emission lines). They found a value of $42 \, \mathrm{kms}^{-1}$, nearly double the value commonly used.

5.1.2 Models of the evolving neutral component

In response to the growing number of observations of the neutral component of planetary nebulae (see Sect. 1.1.4), Natta and Hollenbach (1998) was one of the first works to theoretically model this emission, in order to investigate whether these observations can be a useful indicator of age. They follow the time-dependent chemistry and excitation of H_2 to look at the effects that shocks, FUV photons and soft X-rays from an evolving central star have on the neutral region of an expanding shell. They emphasise that time-dependent H_2 chemistry is needed for producing strong H_2 emission in old PNe with high mass cores. However, the importance of this dependency is reduced at higher densities. They find that their models split into 3 layers: an inner ionised region, a central neutral region and an outer molecular region; and 3 phases of evolution. The early evolution, where the FUV photon flux and density is high, has the brightest H_2 lines, specifically the 1-0 S(1) line. The H_2 is excited via UV-pumping, but the high densities

ensure that levels are de-excited via collisions, hence the 1-0 S(1) and 2-1 S(1) lines have ratios typical of thermalised gas. At later times, the FUV flux and density fall. As a result, the H_2 line intensities decrease, and as the molecular gas cools, the significance of collisions on H_2 falls - its excitation is now dominated by fluorescence. At even later times, where the central star temperature reaches its maximum, the soft X-rays come into play, heating and ionising the neutral gas. Once again, thermal emission starts to dominate the H_2 excitation. The lengths of these stages depend strongly on the central star mass, which controls the evolution of the incident SED and expansion properties.

Aleman and Gruenwald (2004) and Aleman and Gruenwald (2011) investigated the viability of H_2 molecules surviving in the ionised region of PNe. Using a photoionisation code, they found the density of H_2 can remain sufficiently high in the ionised region, as long as the temperature is not too high. For high temperature central stars, the contribution to the H_2 line intensities from the ionised region can be significant in some PNe, especially in the transition region from ionised to neutral material. The relative importance of the mechanism exciting the H_2, either via collisions or UV pumping, depends on the nebula density and central star temperature - the former mechanism dominates when these are high.

Many PNe are observed to have bright H_2 emission embedded in knots and clumps, where the optical depth is sufficient to shield from the UV flux of the central star. One of the best examples of a PN with knots of bright H_2 emission is the Helix nebula (e.g. Matsuura et al. 2009; Meixner et al. 2005) and various models have been used to try to reproduce the observations; for example Aleman et al. (2011). They found that the knots need to be located close to the ionised region in order for the radiation to be significant enough to excite the H_2 and produce a bright 1-0 S(1) line. Priestley and Barlow (2018) modelled the emission from knots in PNe, represented by a large density jump at a certain distance from the star, and a combination of photoionisation and PDR codes. Their main findings were that H_2 surface brightnesses comparable to observations could be obtained for very hot central stars ~ 150000 K, however with the inclusion of extreme-UV photons, lower temperatures can be sufficient to start to approach the lower limit of observations.

5.1.3 PN evolution using Cloudy

To build on the works described above, it is the aim of this chapter to investigate the processes responsible for the formation and destruction of H_2 in PNe at various stages of evolution, and the mechanisms contributing to the intensity of the 1-0 S(1) line, and its intensity relative to 2-1

S(1). However, rather than applying time-dependent and hydrodynamical models, such as those described above, which are computer-expensive and complex to set up, we want to explore how applicable a sequence of static Cloudy models at different ages can be in attempting to reproduce surface brightnesses of observations of H_2 from the UWISH2 survey. For this to work, the timescales for various reactions need to be carefully monitored, to ensure they do not significantly exceed the time period between successive models. Under idealistic assumptions, we hope to be able to replicate and explain some of the results found in the K-band spectroscopy study of Chapter 2.

This chapter begins by describing the results of a model sequence with simplified but realistic PN conditions, to make sure the evolution of the photoionised region behaves as expected. I then introduce some ideas on H_2 formation and destruction timescales, and investigate the effect of density on the rates of reactions involving the H_2 molecule. H_2 surface brightnesses and line ratios are then presented for particular model sequences, and compared to my findings in Chapters 2 to 4.

5.2 A sequence of simple photoionisation models

To begin with, a sequence of static models is generated, with straightforward conditions that are fairly representative of a real PN. This method is similar to that of Vejar et al. (2019), who looked at the usefulness of photoionisation models as a means of simulating observations of evolving PNe for the Large Synoptic Survey Telescope (LSST).

5.2.1 Input parameters

The input parameters for this model are displayed in Table 5.1, with 25 separate Cloudy models at different ages making up the sequence. The incident SED for each model is described by a stellar atmosphere file (Rauch, 2003), with a temperature, surface gravity and luminosity, all of which vary as a function of age. These stellar atmosphere models only exist where $50 < T_* < 190$ kK, and $5.0 < \log g < 8.0$. Hence, blackbody approximations are used for the first 3 models of the sequence. The parameters correspond to a stellar track with a zero age main sequence (ZAMS) mass of 2.00 $M_\odot$, and a final mass (end of AGB) of 0.5826 $M_\odot$, with metallicity, Z = 0.01 (Miller Bertolami, 2016). The central stars calculated in this work evolve much faster and reach higher luminosities than older tracks of Bloecker (1995). We select values of T, L and $\log g$

TABLE 5.1: Inputs for the model sequence. From left to right: model number, age, CS temperature, CS luminosity, surface gravity, inner radius, hydrogen density, outer radius and thickness.

N	t (years)	T_* (log K)	L_* (log $L_\odot$)	log g (cm s^{-2})	r_{in} (pc)	log n_H (cm^{-3})	r_{out} (pc)	Thickness (pc)
1	308.2748	4.479114	3.870924	3.201506	0.007878	5.602796	0.008590	0.000713
2	502.7470	4.658860	3.864369	3.927046	0.012847	5.177976	0.013897	0.001050
3	751.3883	4.812929	3.852927	4.554758	0.019201	4.828948	0.022092	0.002891
4	1009.4060	4.928480	3.835979	5.033907	0.025794	4.572546	0.031756	0.005962
5	1256.4005	5.018354	3.813033	5.416343	0.032106	4.382422	0.041424	0.009318
6	1649.7777	5.133905	3.752833	5.938746	0.042158	4.145828	0.056434	0.014276
7	1992.2561	5.210267	3.658513	6.338509	0.050910	3.981989	0.069731	0.018821
8	2198.8010	5.242475	3.564194	6.561658	0.056188	3.896307	0.078102	0.021914
9	2404.3056	5.258844	3.390065	6.801262	0.061439	3.818700	0.081892	0.020453
10	2492.8963	5.245592	3.152760	6.985559	0.063703	3.787271	0.078095	0.014392
11	2520.7742	5.220809	2.949357	7.089831	0.064415	3.777611	0.074776	0.010361
12	2551.0903	5.183947	2.712052	7.179690	0.065190	3.767228	0.072493	0.007303
13	2655.8415	5.117016	2.339145	7.284871	0.067867	3.732275	0.071704	0.003838
14	3010.0728	5.065176	2.067940	7.348716	0.076919	3.623526	0.079615	0.002697
15	3253.8668	5.041228	1.966238	7.354629	0.083148	3.555880	0.085857	0.002708
16	3626.9467	5.027901	1.898436	7.369122	0.092682	3.461597	0.095747	0.003065
17	3934.0930	5.021309	1.864536	7.376653	0.100531	3.390991	0.103973	0.003442
18	4352.2719	5.014736	1.830635	7.384261	0.111217	3.303248	0.115234	0.004017
19	4934.3904	5.008192	1.796734	7.391985	0.126092	3.194213	0.131011	0.004919
20	5761.1560	5.001689	1.762834	7.399875	0.147219	3.059661	0.153589	0.006370
21	6952.3113	4.995252	1.728933	7.408030	0.177657	2.896422	0.186426	0.008768
22	8659.1940	4.988887	1.695032	7.416470	0.221275	2.705725	0.234072	0.012797
23	11025.7770	4.982600	1.661132	7.425219	0.281750	2.495862	0.301206	0.019456
24	14155.2695	4.976380	1.627231	7.434241	0.361720	2.278844	0.391789	0.030070
25	18100.6937	4.970205	1.593331	7.443443	0.462540	2.065290	0.508775	0.046234

corresponding to ages which span from 500 years to nearly 20000 years after the end of the ABG phase, encompassing the lifetime of a typical PN.

To take into account an expanding nebula envelope, the inner radius, r_{in}, is increased at each step, dependent on an expansion velocity, v_{sh}, which we set to equal 25 km/s, the same used in Natta and Hollenbach (1998). We assume a constant expansion, hence, $r_{in} = v_{sh} \times t$, where t is the age used to define the incident SED as described above. As in Miller Bertolami (2016), $t = 0$ is the point when $\log(T_*) = 3.85$. The outer radius, and therefore the thickness, for each model, is determined by a stopping condition. As we are only interested in the ionised region in this section, the models are set to stop when the electron temperature falls to 4000 K.

As PNe expand into the ISM, their material will become more disperse. The hydrogen density will decrease as a function of time, as well as decreasing with radius within each individual shell. The hydrogen density at the inner edge of each model in the sequence, n_H, varies with r_{in} defined above, under the following power law:

$$n_H = n_0(r_0/r)^\alpha \tag{5.1}$$

TABLE 5.2: Model abundances relative to hydrogen

Element	log(X/H)	Element	log(X/H)
He	-1.0000	Si	-5.0000
C	-3.1079	P	-6.6990
N	-3.7447	S	-5.0000
O	-3.3565	Cl	-6.7696
F	-6.5229	Ar	-5.5686
Ne	-3.9586	K	-6.9208
Na	-5.7212	Ca	-7.9208
Mg	-5.7959	Fe	-6.3010
Al	-6.5686	Ni	-7.7447

The densities of PNe are spread over a large range, and typical electron densities can be anywhere from 10^0 to 10^5 cm^{-3} (Frew and Parker, 2010). As the purpose of the model sequence is to represent a simple evolving PN, the parameters of this equation are set to coincide with the densities found in the PhD thesis of Frew (2008), who determined the densities of ~ 240 Galactic and Magellanic PNe. They found that those densities scale with radius: $\log(n_e) = -2.31(\pm 0.04)\log(r) + 1.02$, where n_e is the electron density of the nebulae. We assume that the total hydrogen density equals the electron density at the inner edge of the nebula, where all the hydrogen will be in its ionised form. We set $n_0 = 10^{3.819}$ cm^{-3} at $r_0 = 0.0614$ pc, so that at the point of maximum CS temperature (2404 years), the nebula hydrogen density is the value found from the relation. α is set to 2, representing a constant rate of mass outflow. In hydrodynamical models, values of α less than 1.5 would result in the ionisation front becoming trapped behind the shock front. A value of 3 implies a freely-expanding shell, with the expansion velocity increasing with time as α is increased beyond 3 (Schönberner et al., 2005b). The density within each individual shell also varies as the inverse square of radius.

Abundances of the elements included in the models are taken from Aller and Czyzak (1983) and Khromov (1989), and are displayed in Table 5.2. Many other parameters can be specified within Cloudy (see Chapter 4), including a filling factor, dust to gas ratio, PAH abundance and a temperature floor. For our model sequence, the filling factor is set to unity, the dust to gas mass ratio set to the ISM value of ~ 0.006 (the default value for Cloudy), a default PAH distribution as described in Abel et al. (2008), and no temperature floor is applied. The distance to the PN need not be specified, and so line emission is measured as luminosities (erg s^{-1}) rather than fluxes (erg cm^{-2}s^{-1}). In Figure 5.1, plots describing the main model inputs as a function of age are given.
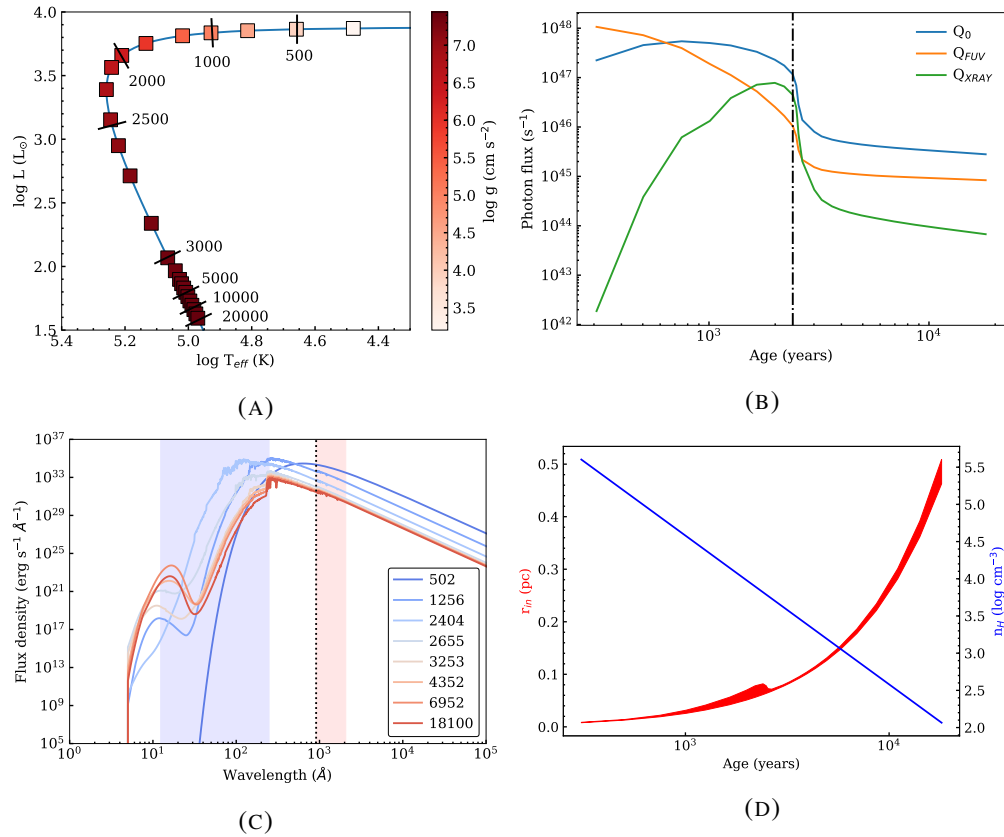
FIGURE 5.1: Input parameters. (A) HR diagram for a 0.5826 M$_\odot$ star taken from Miller Bertolami (2016), showing its temperature, luminosity and surface gravity as a function of age (given by the tick labels in years). (B) Incident fluxes for various photon energies: H-ionising (Q$_0$), i.e. <911 Å; FUV (Q$_{FUV}$), defined as 911 to 2066 Å and soft X-rays (Q$_{XRAY}$), defined as 12.4 to 248 Å. The vertical dashed and dotted line marks the position of maximum CS temperature. (C) Incident SEDs at select ages. The vertical dotted line represents the ionisation energy of H, while the blue and red regions represent the soft X-ray and FUV photon regions respectively. (D) Variation of radii and densities with age. The red region represents the thickness of each nebula shell.

5.2.2 Results

Snapshots of the PN structure at 4 ages are given in Figure 5.2. The fraction of H mass in either its ionised or neutral state as a function of age is given in Figure 5.3a. At 502 years, the density is high ($10^{5.18}$ cm^{-3}) while T_* is relatively cool (45000 K). There is a clear ionisation front located at a depth of 0.0009 pc, where the HII fraction and electron temperature drop significantly. Beyond this depth, the hydrogen will predominantly be neutral. The temperature of the star increases as the PN evolves, reaching its maximum value (180000 K) at 2404 years. While T_* is increasing, the majority of H is found in its ionised form. At 1992 years, the ionisation front reaches its maximum radius (~ 0.015 pc), after which point it begins to recede. While on the cooling track, the majority of H is found in its neutral form. From around 2000 to 3000 years, the luminosity of the central star quickly decreases by over an order of magnitude. The
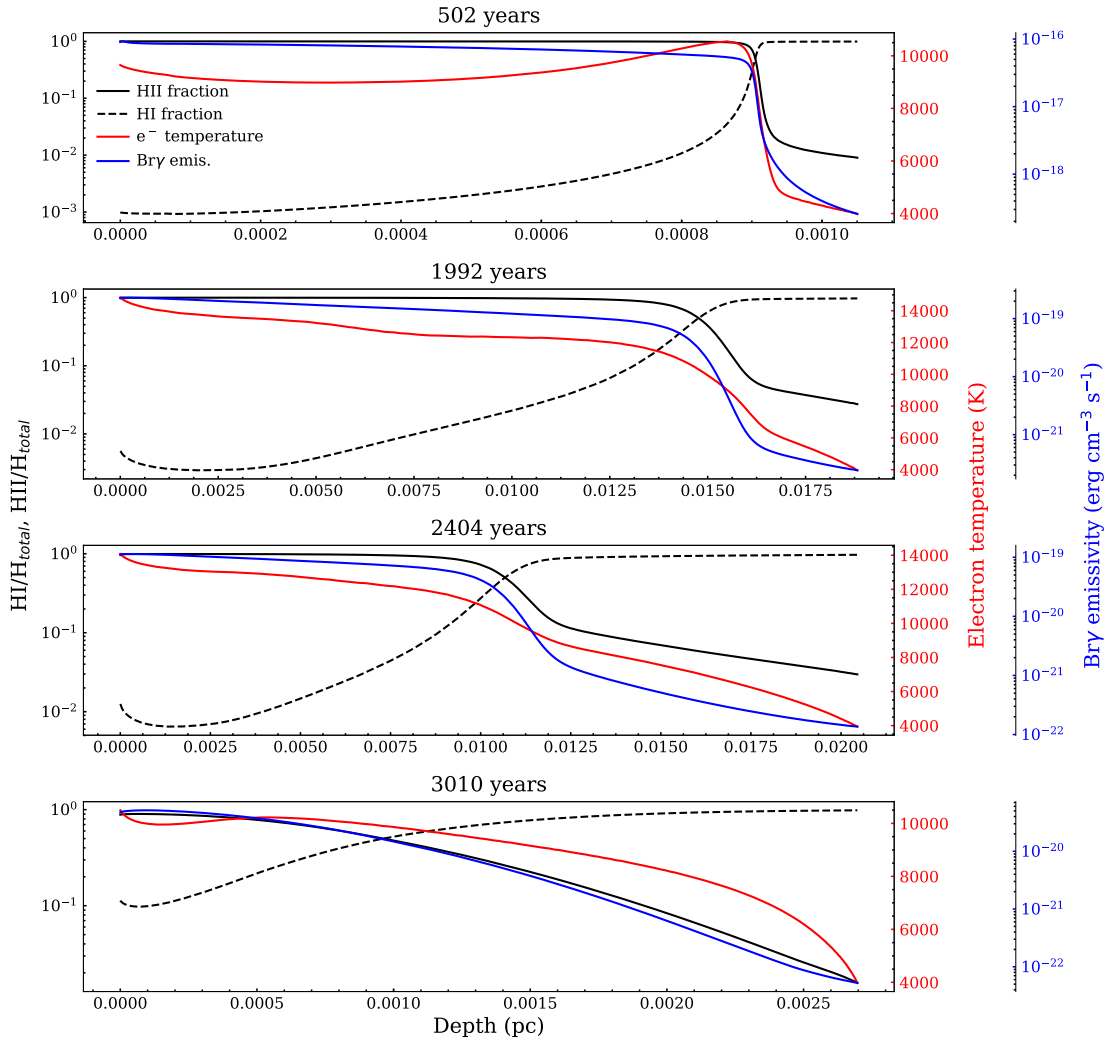
FIGURE 5.2: Views of the shell structure at 4 ages: 502, 1992, 2404 and 3010 years. The x-axis gives the depth into the shell, where depth = 0 pc represents the inner edge of the shell, closest to the CS. The black lines give the fractions of ionised (solid) and neutral (dashed) hydrogen relative to the total amount. The red line is the electron temperature in K. The blue line is the emissivity of the Brγ line.

Brγ emissivity falls with the decrease in CS luminosity and nebula density. Beyond 3000 years, no obvious ionisation front is set up. The change in thickness of the PN shell, as shown in Figure 5.1d, is a consequence of the stopping condition. The PN is thicker at around the point of maximum T_*, as the electron temperature within the shell is higher, and so the 4000 K stopping condition is reached at larger radii.

In Figure 5.3b, various Hα surface brightnesses[1] are displayed, as a function of the Hα radius. Model 1 Hα surface brightnesses are comparable to the Hα SB-radius relation calibrated by

---

[1] Surface brightness, $S = F/(\pi\theta^2)$, where F is the line flux in erg cm^{-2} s^{-1}, and θ is the angular radius in arcsec. Replacing F with $L/(4\pi D^2)$, where L is the line luminosity, and D is the distance to the PN, and $\theta = R/D$, where R is the PN radius, gives $S = L/(4\pi^2 R^2)$, in erg cm^{-2} s^{-1} sr^{-1}.
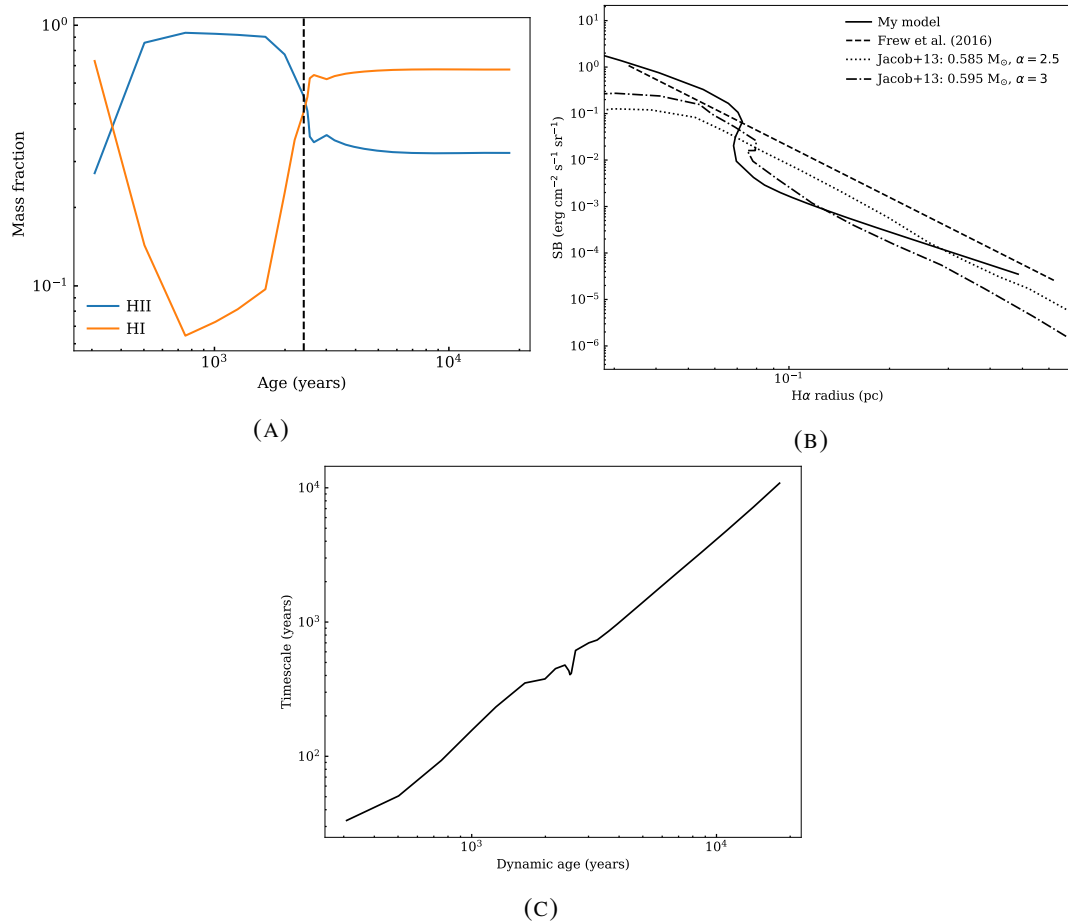
(A)

(B)

(C)

FIGURE 5.3: (A) Mass fractions of ionised (blue) and neutral (orange) hydrogen relative to total hydrogen, as a function of age. The vertical dashed line marks the position of maximum CS temperature. (B) Hα surface brightnesses as a function of Hα radius. The solid line is for the Cloudy model sequence, while the dashed line is the Hα SB-radius relation (Frew et al., 2016). The dotted and dashed+dotted lines are the Hα SB variations for simulations of a 0.585 M$_\odot$ star with α=2.5, and a 0.595 M$_\odot$ star with α=3.0 respectively, taken from Jacob et al. (2013). The Hα radii for my models are determined as the points where the Hα emissivity fell to 10% of its maximum value. (C) Hydrogen recombination timescale as a function of the dynamic age (i.e. that of the CSPN).

Frew et al. (2016) at small and large radii, however is lower than the relation at medium radii. The sharp drop in the brightness at 0.07 pc, and a decrease in Hα radius, correspond to around the position of maximum T_* (and a rapid decrease in luminosity). This is a trend that also appears in the hydrodynamical models of Jacob et al. (2013), where the tracks for comparable mass stars are shown. They attribute the behaviour to enhanced phases of recombination occurring in models with more massive nuclei.

In Figure 5.3c, the longest H recombination timescale (i.e. the timescale for all the ionised gas to recombine) computed by Cloudy is given as a function of the CSPN age. The timescale increases with age (i.e. reaction rates decrease) which follows the decrease in density. If the

timescales exceed the intervals between successive models in the sequence, the models do not have enough time to react to the changes in the recombination state. At later times (> 4000 years), where the density is lowest, the H recombination timescale exceed around 1000 years, and so these models become unreliable. This may result in the slight over-prediction of the Hα surface brightness at later times, as seen in Figure 5.3c. In general, the brightnesses computed by Cloudy compare favourably to the hydrodynamical models, and so we believe them to be an accurate representation of an evolving PN, however, one needs to be careful by checking the reaction rates to ensure the model's reliability.

5.3 H$_2$ formation and destruction timescales

Cloudy works by balancing the rate at which all ion species (including neutral and molecular) are created and destroyed, and finding the equilibrium number of each species depending on the reaction rates for creation and destruction. Therefore, there is no starting point - the code finds the equilibrium point for the given conditions (mainly gas density and incident radiation field), on the assumption that all reactions are allowed to run to equilibrium. Cloudy relies on a steady-state chemistry, which means that the rate of reactions that form a particular species is balanced by the rate of reactions that remove the species. For a steady-state chemistry to apply, dynamic changes in a system must occur on a longer timescale than the chemical reaction timescale. For the case of our sequence of Cloudy models, this means that the parameters that control the incident radiation field (i.e. the temperature and luminosity of the CS) must not change on a timescale faster than the formation and destruction rates of H$_2$, which are often the slowest steps.

One of the most important H$_2$ formation mechanisms is that which occurs on the surfaces of grains. Cloudy calculates the grain H$_2$ formation rate using the equation from (Cazaux and Tielens, 2002):

$$r_g = \sum 0.5 \, n(\text{H}^0) \, [n_g \sigma_g / n(\text{H})] \, u_\text{H} \, \varepsilon(\text{H}_2) \, S_\text{H}(T) \quad [\text{s}^{-1}] \tag{5.2}$$

where $n(\text{H}^0)$ is the atomic H density, $n(\text{H})$ is the total hydrogen density, $n_g \sigma_g$ is the total cross section of the grains, u_H is the average speed of the H atom, $\varepsilon(\text{H}_2)$ is the H to H$_2$ conversion efficiency, and $S_\text{H}(T)$ is the sticking probability, which has a temperature dependence on both

the gas and grains. As the main factor here is the density dependence, this equation can simply be recast as:

$$\frac{dn(H_2)}{dt} = \gamma_{gr}\, n\, n_H \quad [\mathrm{cm^{-3}s^{-1}}] \tag{5.3}$$

where n is the gas density, n_H is the atomic H density, and γ_{gr} is the rate coefficient. Using the value of $\gamma_{gr} = 3 \times 10^{17}\ \mathrm{cm^3\ s^{-1}}$ from Natta and Hollenbach (1998), this means that the timescale, τ, to form 1 H_2 molecule is $\sim 10^9\,/\,(n\, n_H)$ yr, or $\sim 10^9\,/\,n$ yr to convert all atomic H to molecular. This value should not exceed the $\sim$ 100 to 1000 yr timescale for changes in the FUV flux from the CS; if it does, then time-dependent calculations should be applied.

When a strong Lyman radiation field is present, H_2 molecules are primarily destroyed via the Solomon process. This occurs when electronic transitions to the Lyman and Werner bands are followed by radiative decays to high vibrational states of the ground electronic state, which can result in dissociation. The total destruction rate in Cloudy due to the Solomon process is given by

$$r_c = \frac{1}{n(H_2)} \sum_u n_u A_c \quad [\mathrm{s^{-1}}] \tag{5.4}$$

where n_u is the population of an electronic excited state, and A_c is the transition probability from the excited state into the ground state (Shaw et al., 2005).

5.4 Models of constant density knots

In this section, H_2 formation and destruction timescales of constant density models will be used to investigate how applicable Cloudy models can be for simulating the evolving molecular component. We look at densities toward the higher end of observations, in the range 10^4 to $10^8\ \mathrm{cm^{-3}}$, comparable to the densities observed in embedded knots. By keeping the density constant over time, we ensure high densities even for the oldest models. Instead of using a 4000 K temperature stopping condition, we now choose to stop each model in the sequence when the shell mass reaches 0.3 $M_\odot$ (the same shell mass used in the models of Natta and Hollenbach (1998)), ensuring that the models penetrate deep into the PDR and outer molecular regions. To keep the shell masses constant at 0.3 $M_\odot$, the volume of the shell must stay constant,

which means as the shells expand, they will become thinner. This simple scenario is equivalent to a constant thickness shell, with an increasing filling factor, or having a shell composed of clumps/knots of gas, and as the shell expands, the knots stay at the same density and get further apart.
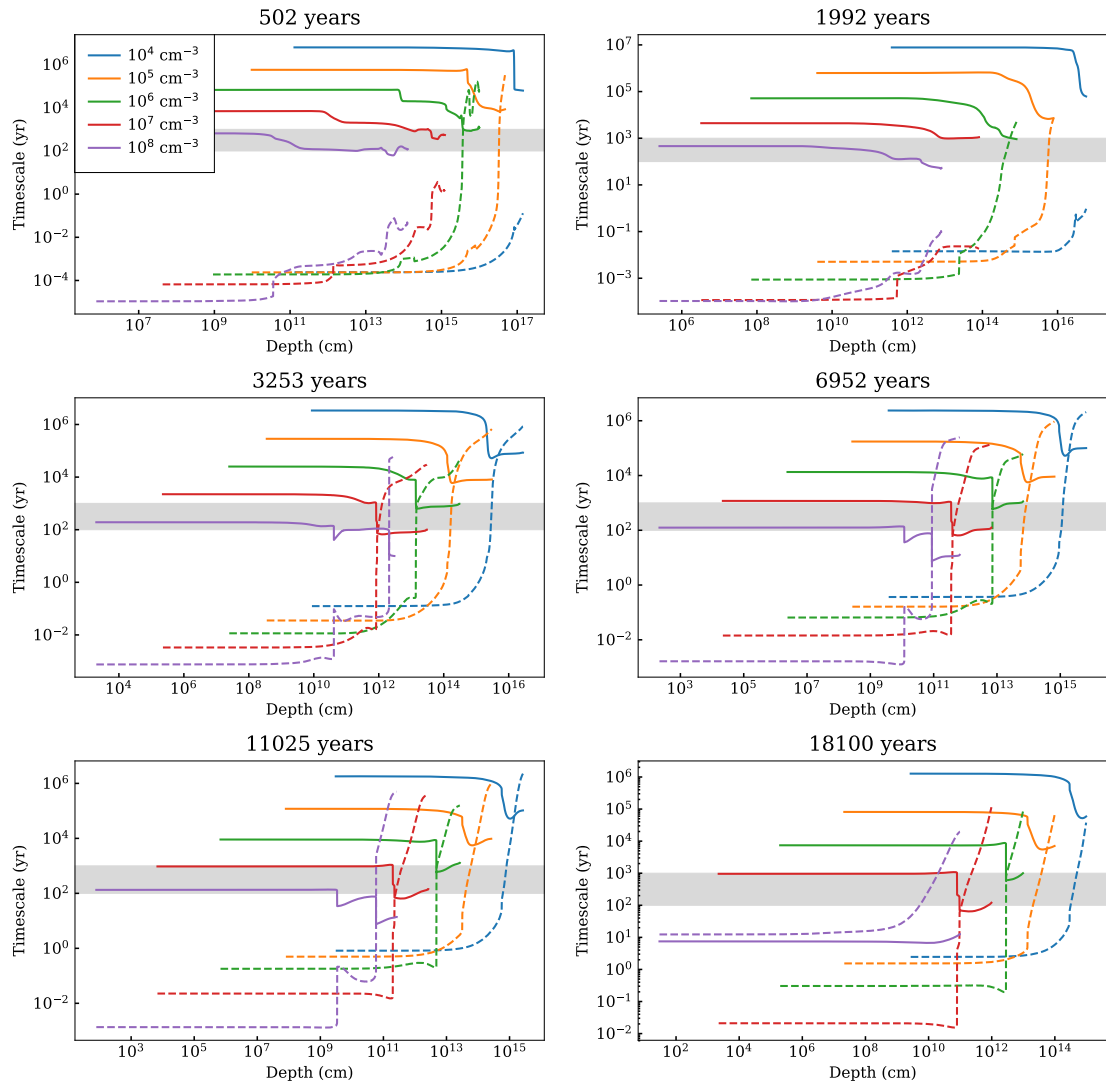
5.4.1 Timescales

FIGURE 5.4: H_2 formation on grains (solid) and total destruction (dashed) timescales as a function of depth for models of different densities at 6 ages. The different colours of the lines represent the density (see legend for details). The grey region spans from 100 to 1000 years, marking the region of the timescale of the varying CS radiation field.

The H_2 formation rate on grains and total destruction timescales as a function of depth for the 5 model sequences at select ages are given in Figure 5.4. As expected, increasing the nebula density increases the H_2 formation rate on grains (see Equation 5.3), which decreases the timescale

required for H_2 to form. We find the same trend when increasing the dust to gas ratio (not shown here) and presumably, while we did not explore different grain sizes and distributions, increasing the grain size (i.e. increasing the grain surface area), increases the probability that a H atom sticks to a grain surface, and so would also increase the reaction rate. The timescale over which H_2 formation on grains occurs decreases (i.e. slowest rate increases) at older times, as the nebula expands and the CSPN luminosity falls. More H_2 forms on grains at older times. Within each nebula, the H_2 formation rate on grains increases at the location of the ionisation front, where the electron temperature rapidly drops. Grain surface chemistry is more efficient at temperatures ≤ 500 K, and occurs with almost maximum efficiency at T ≤ 20 K (Cazaux and Tielens, 2004). At higher temperatures, H atoms struggle to stick well to the grains, making H_2 formation difficult. Only the densest models (10^7 and 10^8 cm^{-3}) have H_2 grain formation timescales within the 100 - 1000 year range, in line with changes to the CSPN flux. This means that for these models, H_2 has the ability to reform faster than the intervals between the models in the sequence. However, where the CSPN flux changes rapidly (i.e. when the star is heating up and reaching its maximum temperature), dense H_2 knots may not have formed, making these portions of the models unreliable. Therefore, we can only trust the handling of H_2 in the models where the density is high and the star is on the cooling track.

The total destruction rate of H_2 is highest in the inner nebula regions, and then decreases (i.e. the timescale increases) where the HII region stops and the electron temperature decreases. As the Solomon process is mainly responsible for destruction of H_2 molecules, the rate of destruction drops off in regions where ionising photons can not penetrate into the gas. Apart from at the edges of the nebulae, the total destruction rate far exceeds that of the H_2 grain formation rate. The fastest H_2 destruction rates occur where the CSPN temperature is increasing, and slowest at later times.

Dense knots as sites of H_2 emission tend to be observed in PNe with central stars on their respective cooling tracks. H_2 is formed in dense AGB winds, however the origin of H_2 after the onset of ionisation is still debated. Either the H_2 can survive in the ionised region (e.g. models of Aleman and Gruenwald (2004)), the H_2 survives in the knots which formed before the ionisation phase, or the H_2 was destroyed, but then reforms at a later stage when the knots form. With their models of knots in the Ring Nebula, van Hoof et al. (2010) argue that the latter of these scenarios is the most plausible explanation - the H_2 is most likely being formed on dust grains in high density knots which formed after the gas recombined as the CSPN entered the cooling track (O'Dell et al., 2007). These knots are likely to be dense enough for self-shielding

to be significant, and for the H_2 to reform on timescales of the order 100s of years. Therefore, Cloudy can be used to model evolution of PNe on the cooling track for these high density knots.
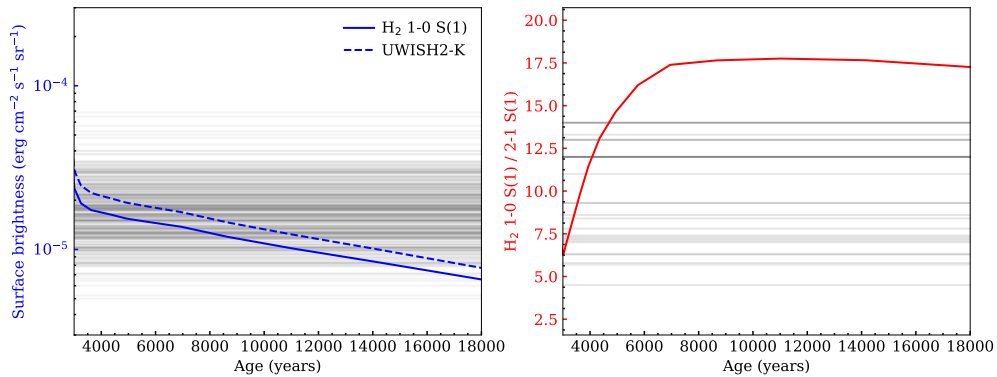
5.4.2 Dense knot models

FIGURE 5.5: Left: surface brightnesses (blue) of the H_2 1-0 S(1) line (solid) and through the UWISH2-K filter (dashed) for the constant 10^7 cm^{-3} model. Each grey horizontal line represents an observation of a PN surface brightness from the UWISH2 survey. Right: the H_2 1-0 S(1) / 2-1 S(1) ratio (red) for the constant 10^7 cm^{-3} model. The grey horizontal lines represent the observations of the bipolar PN sample from Chapter 2.

In Figure 5.5, we present some of the outputs for the 10^7 cm^{-3} knot model while on the cooling track, as these are the ones where reformation of H_2 can occur on short enough timescales. The H_2 1-0 S(1) surface brightness for the model shows a steady decrease over time, as the nebula expands and gets thinner. While on the cooling track, the SBs are comparable to those of the objects in the UWISH2 survey. This may suggest that the H_2 emission in these objects is compatible with the emission from dense knots. The surface brightness through the UWISH2-K filter[2] is also given, and the fact that it is only slightly higher than the 1-0 S(1) brightness means that the majority of the emission through the filter originates from this line. The H_2 1-0 S(1) / 2-1 S(1) line ratio shows a sharp increase when entering the cooling track, and then levels off at around a value of 17. Up to around 5000 years, the ratio is comparable to our observations of bipolar PNe found in Chapter 2, however at later stages, it becomes larger. Nonetheless, it is still indicative of thermal H_2 emission (10 - 20), and confirms the idea that evolved PNe show evidence of thermally excited H_2.

In Figure 5.6, a portion of the simulated K-band spectrum is shown for two different models at two ages. The first, at a time of 2200 years, is taken from the purely photoionised model sequence described in Section 5.2, at an age close to maximum T_*. The strongest lines contributing

---

[2]The surface brightness through the UWISH2 filter is found by first estimating and subtracting the K-band continuum level from the SED, then convolving it with the transmission filter used in the survey, as in Equation 4.1.
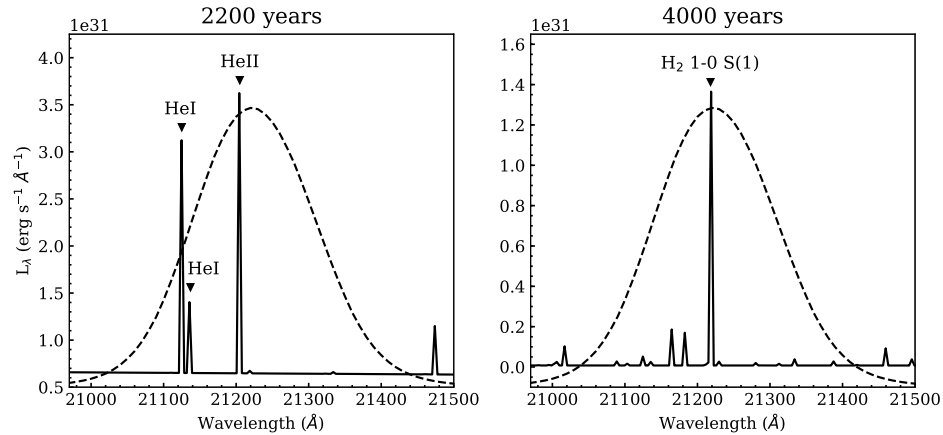
FIGURE 5.6: K-band spectra at the location of the UWISH2 H$_2$ filter, centred on the H$_2$ 1-0 S(1) line at 21218 $\mathring{A}$, at two ages from two different model sequences. The first is taken from the purely photoionised sequence described in Section 5.2, while the second is taken from the 10^7 cm^{-3} knot model. Some of the strongest emission lines within the wavelength range are labelled. The dashed line represents the transmission of the UWISH2 H$_2$ filter, which has maximum transmission of 0.8.

to the UWISH2 filter (dotted line) for this model are recombination lines of HeI and HeII. In the second figure, the spectrum is from the 10^7 cm^{-3} knot model while on the cooling track, where the dominant emission line within the filter is by far the H$_2$ 1-0 S(1) line. This means that, for young hot PNe, a significant contribution to the UWISH2 filter can be from sources other than H$_2$, and so it should not necessarily be assumed that all of the flux from UWISH2 survey images is due to H$_2$ emission for certain PNe.

5.5 Summary

Photoionisation models constructed using Cloudy have been shown to be capable of replicating observations of H$_2$ emission from PNe at particular points in their evolution. However, when the evolution of a PN with time is of interest, the go-to framework is radiation-hydrodynamic models, which can incorporate shock models as media of different density interact. The purpose of this chapter was to see whether a sequence of Cloudy models could be used to replicate the H$_2$ emission from an evolving PN. The main issue with using a sequence of static models rather than a single time-dependent model is that information describing the final state of each model is not passed on to the next one, and so the time it takes for reactions to occur must happen on timescales comparable to the intervals between successive models.

The model sequence used realistic conditions typical of a PN, including the changing SED from the ageing central star, a constant expansion velocity and the consequent density fall-off. We began by considering only the photoionised region, by using a lower limit on the electron temperature to stop the model at the edge of the ionised region. The static models gave Hα surface brightness comparable to observations and hydrodynamical models, leading us to believe that this method was reliable. However, the timescales required for H recombination became quite large at later times, as the density drops off. The nebula density is a key parameter affecting the reaction timescales.

In order to try to match the surface brightnesses in the UWISH2 survey, constant density models were developed with densities up to the highest observed in knots in PNe. We paid special attention to the reaction rates of H$_2$ formation on grain surfaces, and total H$_2$ destruction, which are highly dependent on density. Unless the density is at the highest end of possibilities ($\geq$ 10^7 cm^{-3}), the timescale required to reform H$_2$ on grains is much longer than the intervals between successive models, meaning that the CS flux changes before the models have time to react to the changes. Therefore, only models where the density $\geq 10^7$ cm^{-3} can be trusted to be representative of an evolving PN. The H$_2$ surface brightness for the 10^7 cm^{-3} density model while on the cooling track are of the same order as those in the UWISH2 survey, and so it is possible that dense knots are the predominant locations of H$_2$ formation and subsequent emission. Through inspection of the synthetic spectra from the models, we found that emission from lines other than the 2.122 μm H$_2$ 1-0 S(1) line, including those of HeI and HeII, can significantly contribute to the flux measured using the UWISH2 filter; this is especially true for young, hot PNe. Care must therefore be taken when assuming that all the flux using this filter comes from H$_2$ - the best way to ensure this is by obtaining spectroscopy alongside the photometry.

While they are no replacement for advanced radiation-hydrodynamical codes, our sequences of simple, static models, with future improvements, can be a quick (individual models take no longer than $\sim$ 20 minutes to run) and useful tool to explore the evolving neutral component of PNe. Areas of future work include investigating a larger parameter space, for example varying dust and PAH properties, or elemental abundances (e.g. C/O, which are known to influence the H$_2$). It is likely that the majority of PNe in the UWISH2 survey have non-spherical morphologies, and so utilising the 3D features of pyCloudy, it would be interesting to explore how the emissivity of 1-0 S(1) varies when spherical symmetry is not assumed. Cloudy has a time-dependent feature currently under development, where only the CS luminosity can be varied.

Once this is fully operational, and allows changes to the CS temperature, nebula density and size, comparisons can be drawn between time-dependent and Cloudy models, to ensure that H_2 can reform on sufficient timescales.

5.6 Final summary and conclusions

In this thesis, observations and simulations of planetary nebulae have been used to investigate the changing properties of molecular hydrogen with nebula shape and age. It was divided into 3 main sections:

Analysis of K-band spectra of a sample of PN candidates from the UWISH2 survey.

- This survey was the first blind H_2 1-0 S(1) (2.122 μm) survey of the Galactic Plane, which detected over 30000 individual extended H_2 features, including over 300 known and suspected PNe. One of the main advantages of searching for PNe at infrared rather than optical wavelengths, is that the effect of interstellar extinction is significantly reduced, meaning objects normally invisible at optical wavelengths can now clearly be seen.

- In order to help classify the suspected PNe as true PNe, K-band spectra were obtained for 29 objects, many of which with no previous observations. Through detection of the Brγ (2.166 μm) H recombination line, we found evidence for ionised emission in all but 4 of the objects. 13 candidate PNe had spectra with the Brγ line, but no signs of Hα emission in optical surveys, meaning they are part of the optically-obscured PN population (Jones et al., 2018). This reinforces the notion that many PNe could be missing from surveys that only look at optical wavelengths, as they are hidden behind dust.

- We measured ratios of H_2 line fluxes, which trace the H_2 excitation mechanism, and attempted to link them to the shape and age of the objects. The H_2 morphology was found to be bipolar for the majority of the objects, and these can be split into PNe with narrow waists (W-BPNe) or large equatorial rings (R-BPNe). Using the spatial extents of the ionised and molecular hydrogen as a tracer of evolutionary stage, we found that UV-fluorescence plays a greater role in W-BPNe, which are likely younger objects, while R-BPNe are predominantly thermally excited, and are likely more evolved.

- In order to better classify the candidate PNe in the UWISH2 survey as true PNe or something else, optical and K-band spectra of a much larger sample of objects are required.

The UWISH2 survey focussed only on the northern galactic plane, and a complementary campaign of the southern portion would no doubt lead to detections of new objects never seen before. While long-slit spectroscopy is a useful tool for measuring line ratios with the advantage of spatial information in one dimension, more detailed spatial information, especially for objects with small angular radii, can be achieved using integral field spectroscopy (IFS). This would allow excitation mechanisms to be inferred over the entire target, while comparing to the two-dimensional structure of the ionised region, and allow for better conclusions of morphology and evolutionary stage to be drawn (e.g. Gledhill and Forde 2015).

Using multi-wavelength observations to develop a photoionisation model of Abell 53

- Abell 53 is a PN with a round appearance, and has been known since 1955. It has a bright ring of ionised and molecular hydrogen, filled in with more disperse and clumpy material. With only a few exceptions, Abell 53 is a little-studied PN, and so, combined with its symmetric appearance, we thought it would make a good candidate for modelling.

- A range of observations were collected, including our own observations of optical and near-infrared spectroscopy, as well as photometry from the literature. The spectra were used to estimate some physical characteristics of Abell 53, including internal extinction, nebula temperature and density, and radius and distance.

- The motivation behind creating a model of Abell 53 was to find a small number of parameters describing the nebula and central star, in order to best re-create the current observations, and to provide an explanation of the ionised and molecular hydrogen structure, and to predict an evolutionary stage. The main input for the models were the optical surface brightness profiles, along with the ratio and flux of the H_2 emission lines.

- We found that the ionised structure can be fairly well reproduced with typical PN conditions. The best parameters of temperature and luminosity suggest that the central star of Abell 53 is on the cooling track. A dense, hot, outer region is required to reproduce observations of H_2, leading us to believe that thermal excitation, likely in the form of shocks, is mainly influencing the H_2.

- There are some issues with our models which would need to be resolved given more time. The assumption of spherical symmetry and a simplified density profile meant that the

intricacies of the emission line profiles could never be perfectly matched. It is rare that a PN is truly spherical, and a projection effect may only give the illusion of roundness. An exploration of the many possible bipolar symmetries was intended, however this could not be included in the scope of my work due to time constraints. Additional observations in the infrared, including high resolution imaging of the main dust and PAH bands, would allow calculations of the dust abundance and composition, providing valuable evidence of the primary formation sites and mechanisms of H_2.

Developing sequences of photoionisation models to explore the evolution of H_2 emission with age

- After creating a model which described fairly well the observations of a PN at a particular point in its evolution, we then wanted to see if we could develop a sequence of models, each one describing a PN at a different stage of evolution. Normally, time-dependent radiation hydrodynamics models are the go-to framework, however these can be complicated to implement and time-expensive. A sequence of static models is fast and simple to run, however the slow rates of certain reaction could limit their effectiveness.

- A simple evolving photoionised region was made, which could replicate observations and more advanced models of the $H\alpha$ surface brightness-radius relation. However, the rates of H recombination became slow at later stages, where the density was low.

- Models of various densities were tested to see how the timescales of H_2 grain formation and total destruction limited the models. Only the densest models had timescales short enough for this method to be feasible.

- A dense 10^7 cm^{-3} knot can reproduce H_2 surface brightnesses in the UWISH2 survey, and it seems plausible that the H_2 emission from PNe such as Abell 53 is largely occurring in dense knots, which form as the CSPN enters its cooling track.

- Clearly these models are no replacement for more sophisticated models, however we have shown that they can be a useful aid for exploring how the H_2 emission from PNe changes over time.

Appendix A

K-band spectra of UWISH2 PNe

K-band spectra for all targets observed in Chapter 2, excluding PN G050.5+00.0 and PN G059.7-00.8 (see Figures 2.5 and 2.6 respectively), in order of increasing Galactic longitude. This includes spectra extracted from different regions of the same target, which are given in the title. We label any emission lines present.
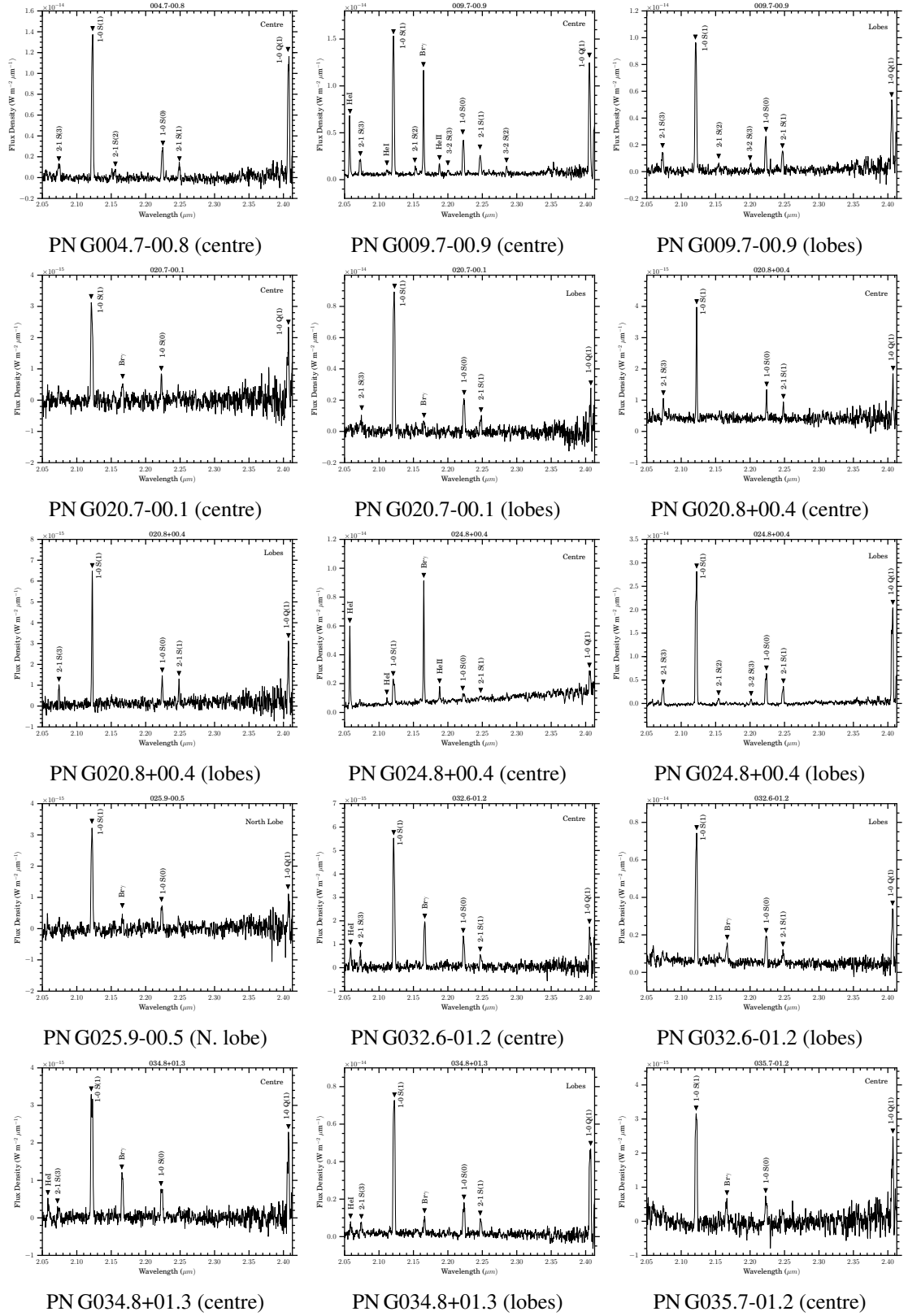
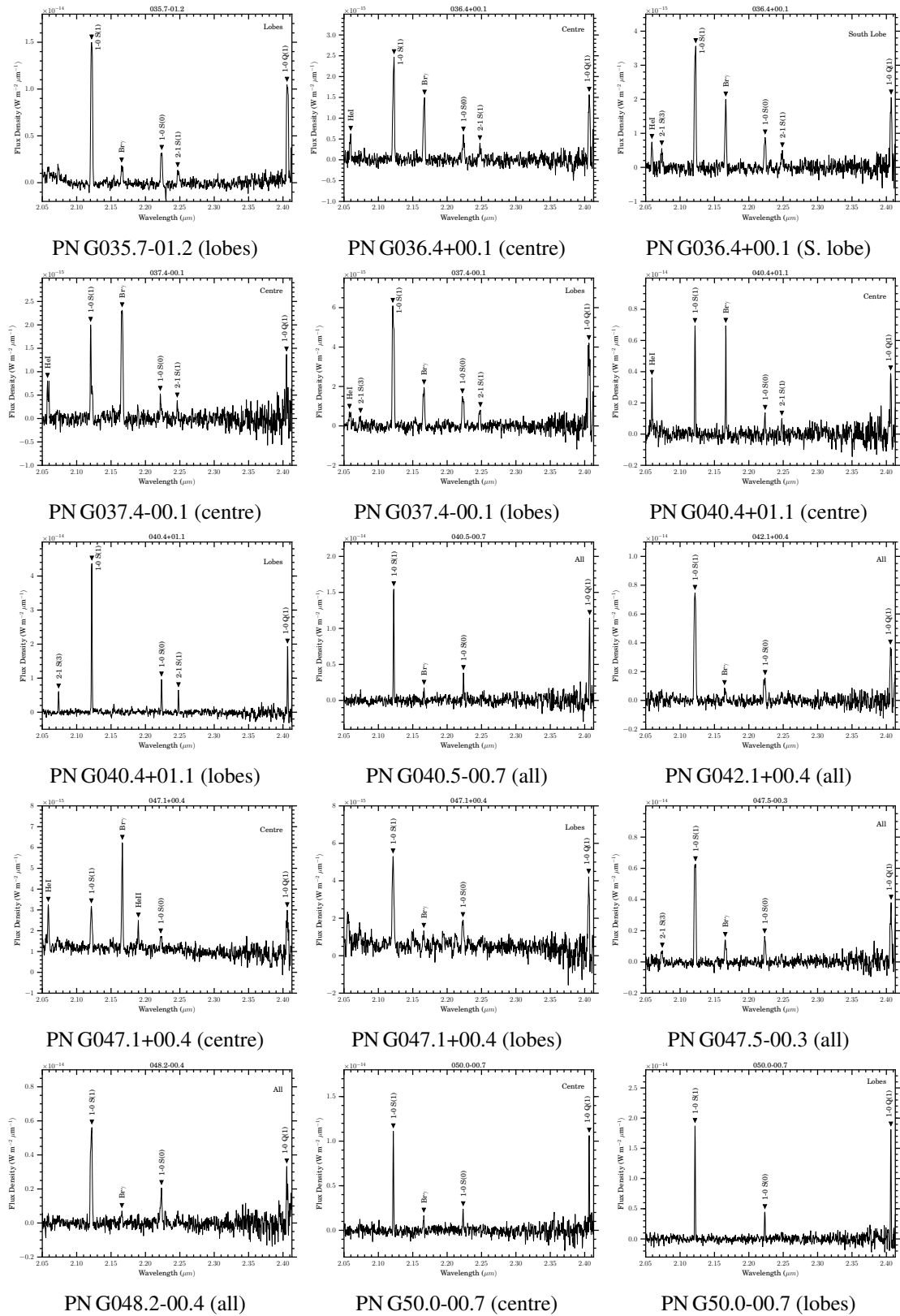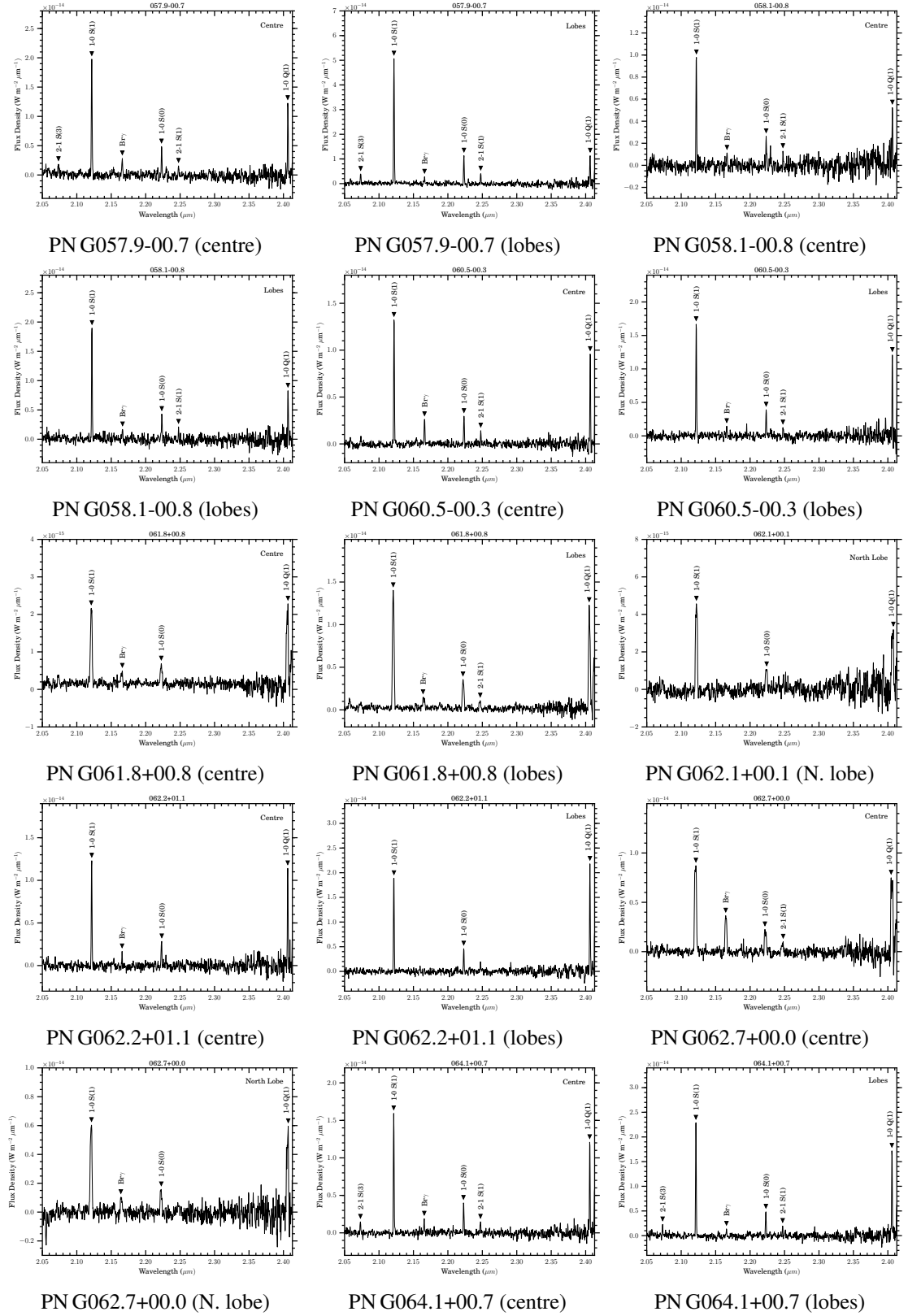FIGURE A.1: K-band spectra of UWISH2 sample

PN G035.7-01.2 (lobes)

PN G036.4+00.1 (centre)

PN G036.4+00.1 (S. lobe)

PN G037.4-00.1 (centre)

PN G037.4-00.1 (lobes)

PN G040.4+01.1 (centre)

PN G040.4+01.1 (lobes)

PN G040.5-00.7 (all)

PN G042.1+00.4 (all)

PN G047.1+00.4 (centre)

PN G047.1+00.4 (lobes)

PN G047.5-00.3 (all)

PN G048.2-00.4 (all)

PN G50.0-00.7 (centre)

PN G50.0-00.7 (lobes)

FIGURE A.1: continued

PN G057.9-00.7 (centre)

PN G057.9-00.7 (lobes)

PN G058.1-00.8 (centre)

PN G058.1-00.8 (lobes)

PN G060.5-00.3 (centre)

PN G060.5-00.3 (lobes)

PN G061.8+00.8 (centre)

PN G061.8+00.8 (lobes)

PN G062.1+00.1 (N. lobe)

PN G062.2+01.1 (centre)

PN G062.2+01.1 (lobes)

PN G062.7+00.0 (centre)

PN G062.7+00.0 (N. lobe)

PN G064.1+00.7 (centre)

PN G064.1+00.7 (lobes)

FIGURE A.1: continued

PN G064.9+00.7 (lobes)

FIGURE A.1: continued

Appendix B

Emission lines of Abell 53

Emission lines and SB profiles from spectra of Abell 53. Figures B.1, B.2 and B.3 are close-ups of the emission lines identified in the ISIS and LIRIS spectra, for the blue, red and K-bands respectively. Gaussian fits are given by the black lines. The central position of the Gaussian is indicated by the vertical dotted line. The flux and uncertainty are given for each line. Figures B.4, B.5 and B.6 are the corresponding SB profiles, given in raw data units.
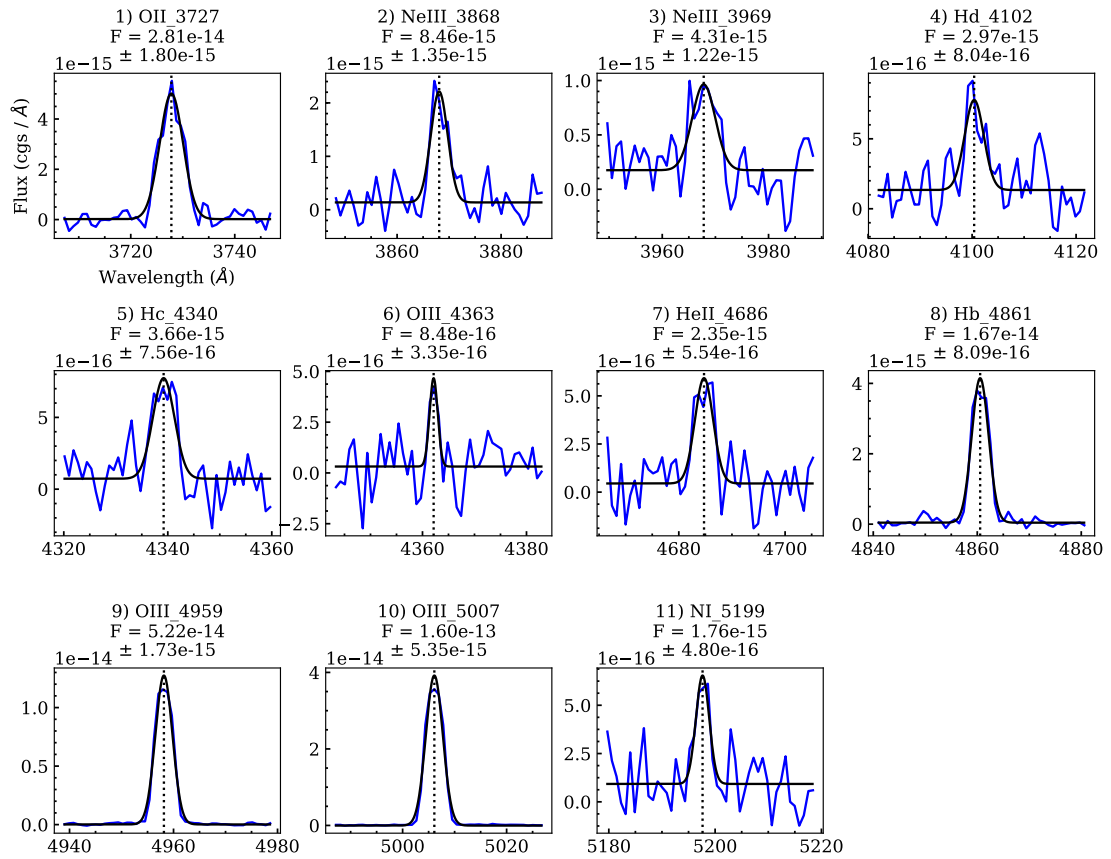
FIGURE B.1: Abell 53 emission line fits in blue
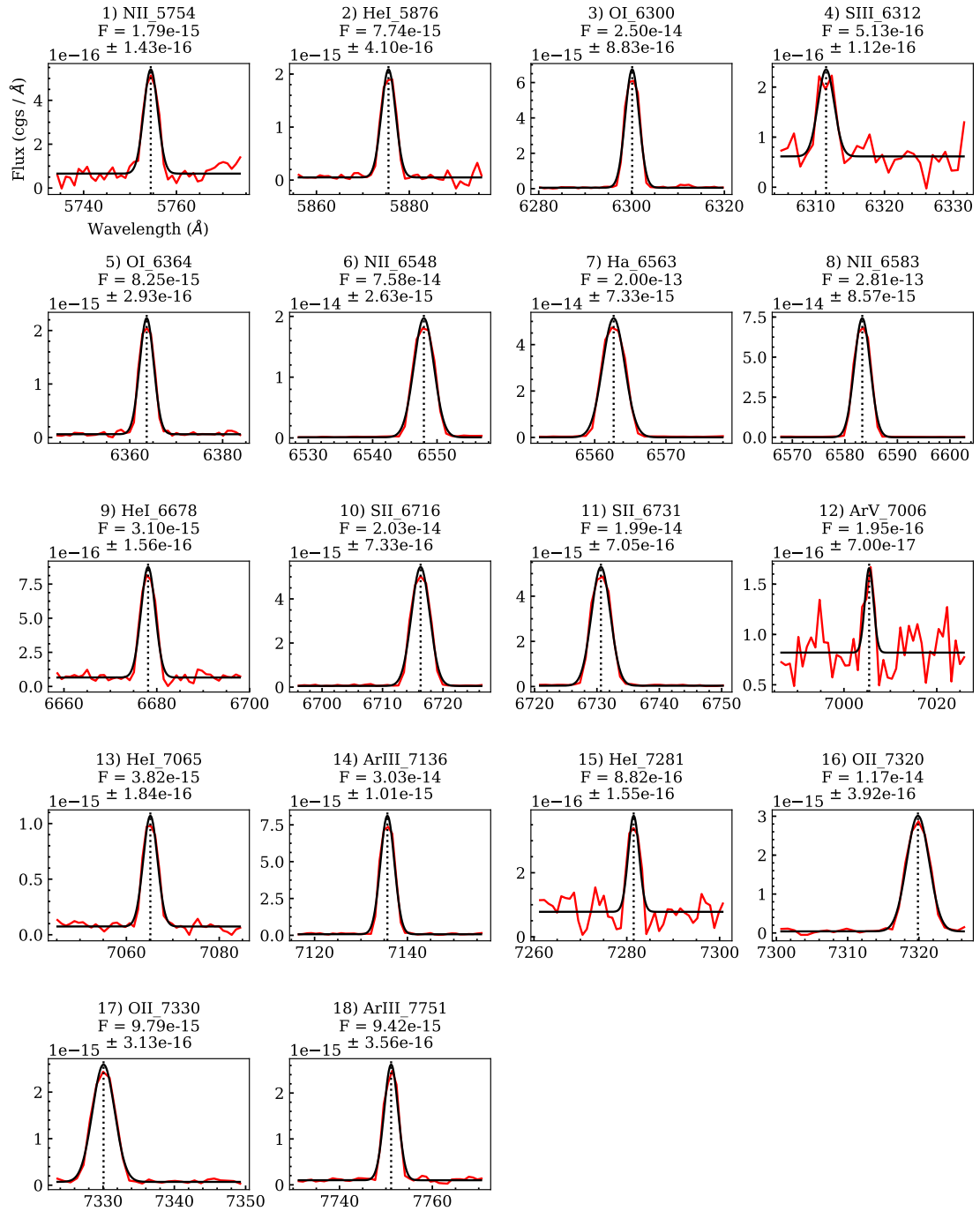
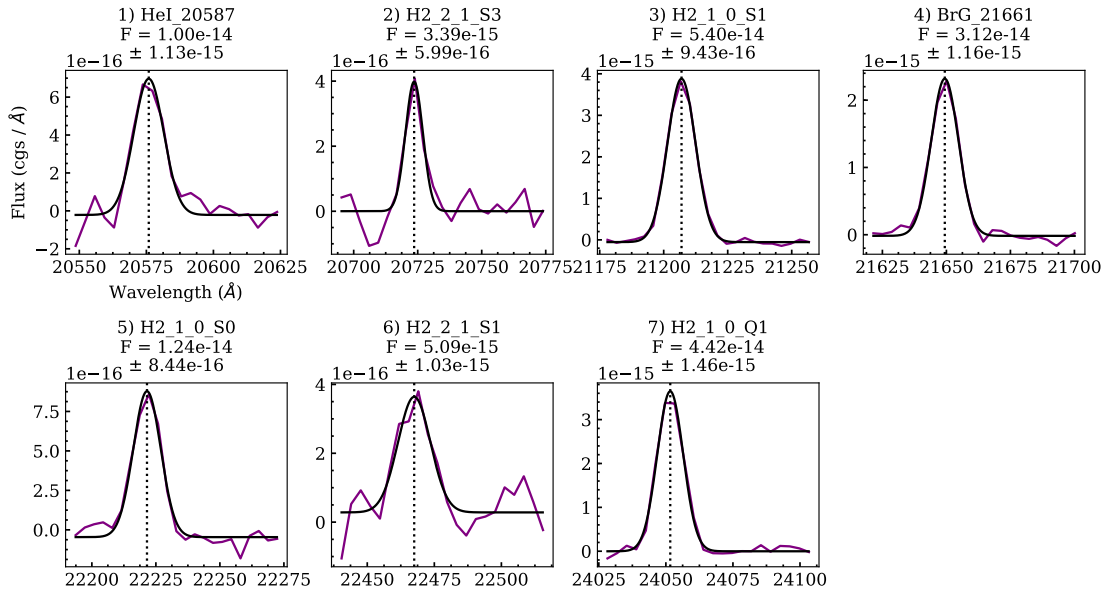FIGURE B.2: Abell 53 emission line fits in red

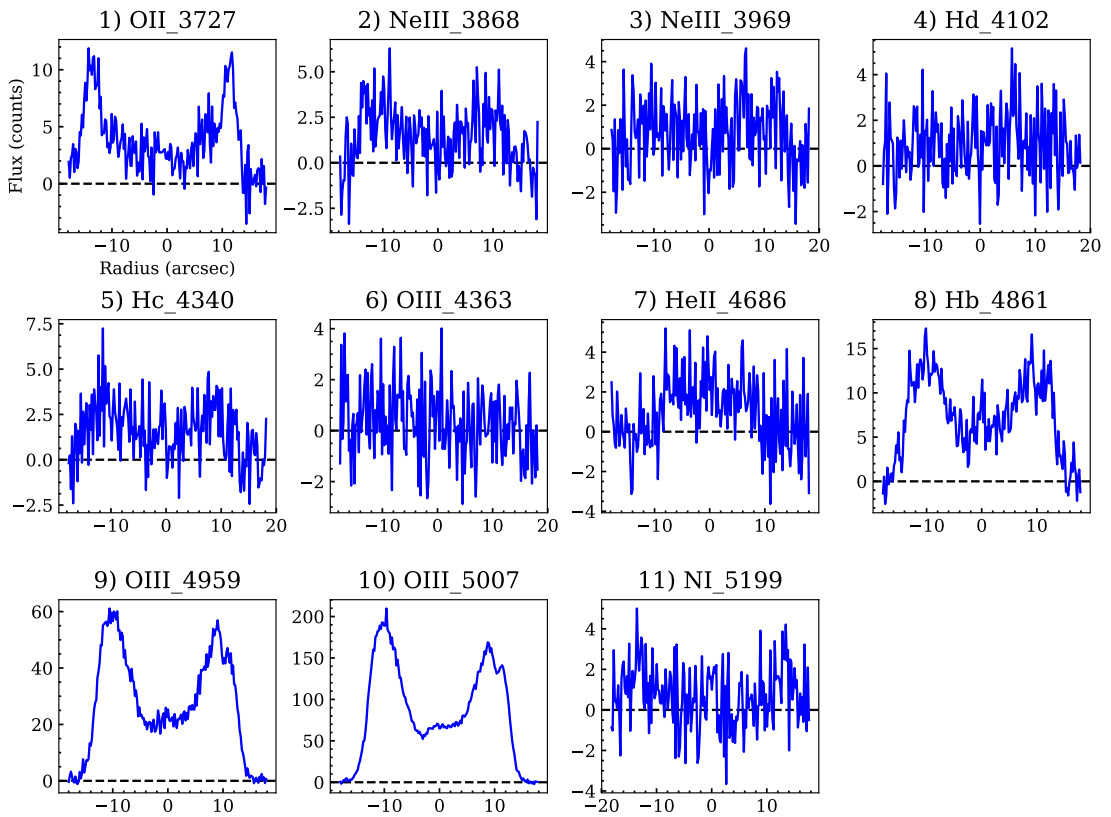FIGURE B.3: Abell 53 emission line fits in K-band

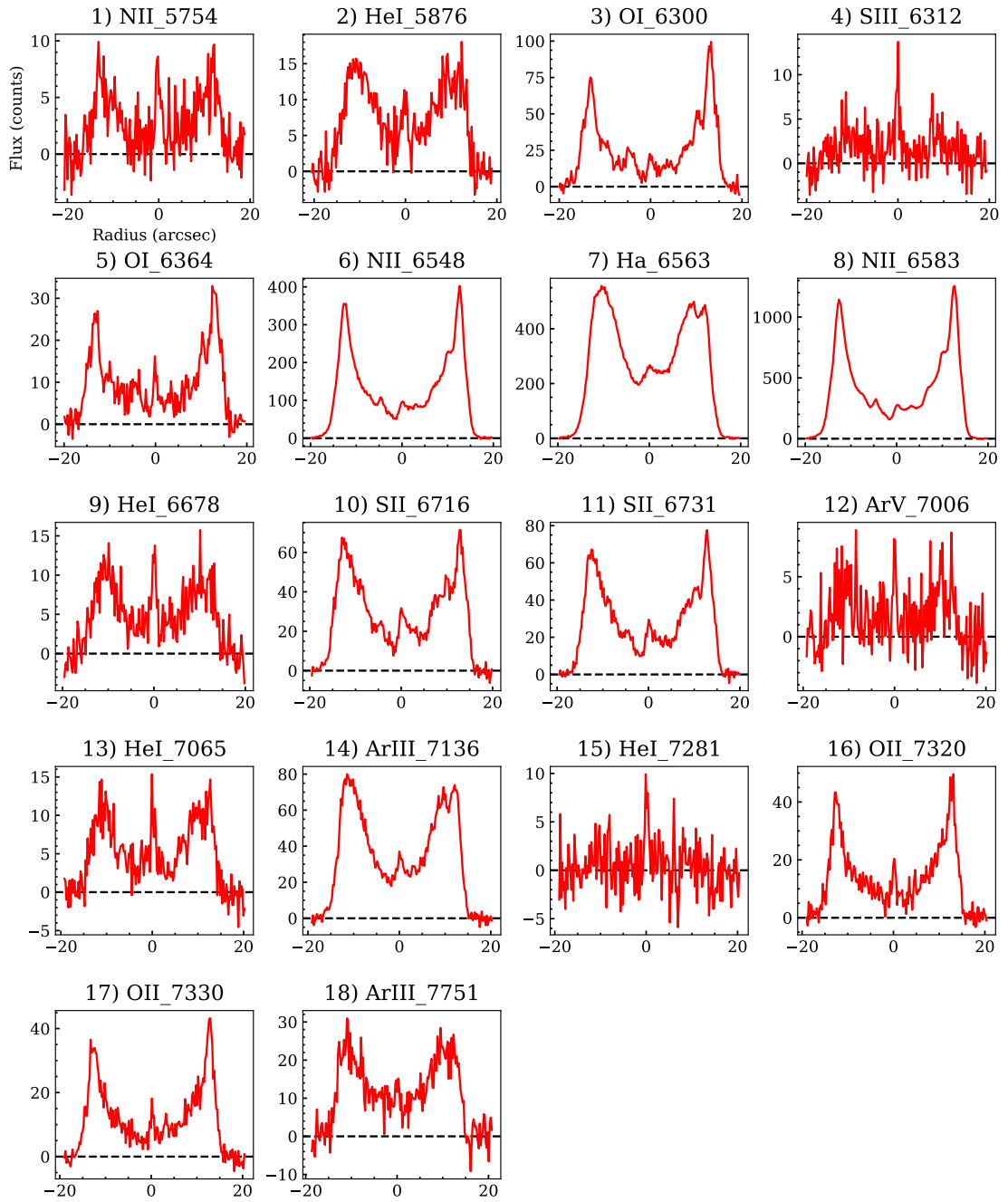FIGURE B.4: Abell 53 surface brightness profiles in blue

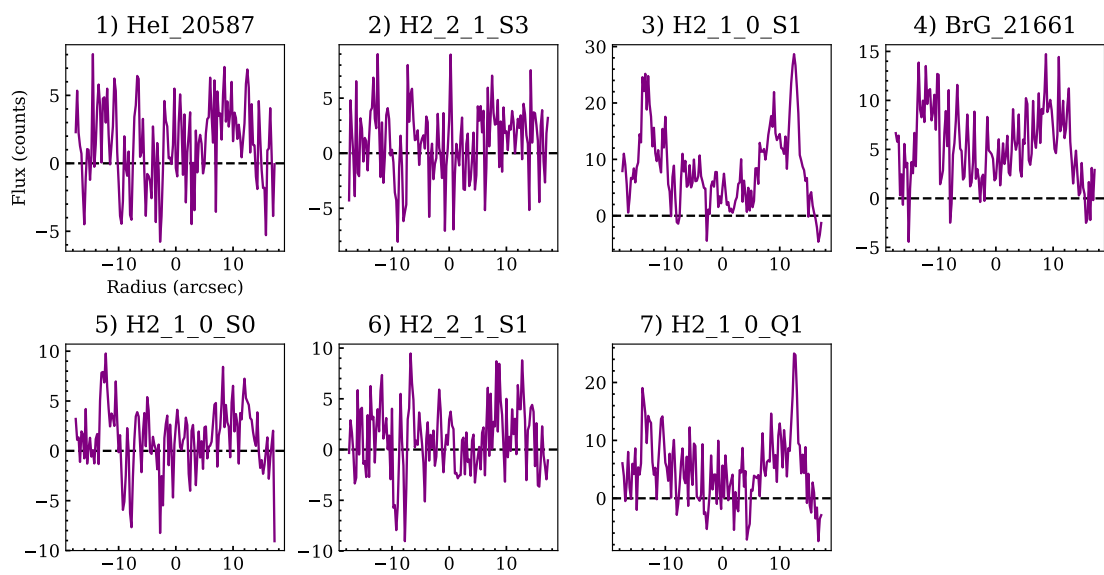FIGURE B.5: Abell 53 surface brightness profiles in red

FIGURE B.6: Abell 53 surface brightness profiles in K-band

Appendix C

Cloudy input file

Example of an input file used by Cloudy to create a photoionisation model of a PN. In this case, the incident SED is described by a blackbody with effective temperature of 10^5 K and a luminosity of 10^3 $L_\odot$. The inner radius (distance between source of radiation and inner edge of cloud) is 10^{17} cm, while the hydrogen density is a constant 10^3 cm^{-3} throughout the nebula. Abundances of some of the most important elements are given relative to hydrogen (log units), while all other elements are switched off. The geometry of the nebula is a sphere, and the iterate command is applied. The simulation will stop when a gas temperature of $10^{3.602}$ (4000) K is reached. 'Print' commands will save data to the main output file, while 'save' commands save data in separate files. See Sect 4.1.1 for more details.

```
blackbody 5.0
luminosity total solar 3.0
radius 17.0
hden 3.0
element abundance helium -0.885172
element abundance nitrogen -3.753978
element abundance oxygen -3.095145
element abundance neon -3.357303
element abundance sulphur -5.327289
element abundance argon -5.469643
element abundance carbon -3.188
element abundance silicon -6.699
element abundance chlorine -6.796
element abundance magnesium -6.886
element abundance iron -7.097
init file="ism.ini"
print lines sort wavelength
print last iteration
sphere
iterate
stop temperature 3.602
save last radius ".rad"
save last continuum ".cont"
save last overview ".ovr"
save last physical conditions ".phy"
save last lines emissivity ".emis"
H  1 4861.33A
O  3 5006.84A
N  2 6548.05A
H  1 6562.81A
N  2 6583.45A
S  2 6716.44A
S  2 6730.82A
end of lines
```

FIGURE C.1: Example of a Cloudy input file

Bibliography

Abel, N.P., van Hoof, P.A.M., Shaw, G., et al., 2008. Sensitivity of PDR Calculations to Micro-physical Details. *ApJ*, 686(2):1125.

Abell, G.O., 1955. Globular Clusters and Planetary Nebulae Discovered on the National Geographic Society-Palomar Observatory Sky Survey. *PASP*, 67(397):258.

Abell, G.O., 1966. Properties of Some Old Planetary Nebulae. *ApJ*, 144:259.

Acker, A., Marcout, J., Ochsenbein, F., et al., 1992. *The Strasbourg-ESO Catalogue of Galactic Planetary Nebulae. Parts I, II.*

Acosta Pulido, J.A., Ballesteros, E., Barreto, M., et al., 2003. First Commissioning of the IR Spectrograph LIRIS. *The Newsletter of the Isaac Newton Group of Telescopes*, 7:15.

Akras, S., Gonçalves, D.R., and Ramos-Larios, G., 2017. H_2 in low-ionization structures of planetary nebulae. *MNRAS*, 465(2):1289.

Akras, S., Gonçalves, D.R., Ramos-Larios, G., et al., 2020. H_2 emission in the low-ionization structures of the planetary nebulae NGC 7009 and NGC 6543. *MNRAS*, 493(3):3800.

Aleman, I. and Gruenwald, R., 2004. Molecular Hydrogen in the Ionized Region of Planetary Nebulae. *ApJ*, 607(2):865.

Aleman, I. and Gruenwald, R., 2011. H_2 infrared line emission from the ionized region of planetary nebulae. *Astronomy and Astrophysics*, 528:A74.

Aleman, I., Leal-Ferreira, M.L., Cami, J., et al., 2019. Characterization of the planetary nebula Tc 1 based on VLT X-shooter observations. *MNRAS*, 490(2):2475.

Aleman, I., Zijlstra, A.A., Matsuura, M., et al., 2011. Modelling the warm H_2 infrared emission of the Helix nebula cometary knots. *MNRAS*, 416(1):790.

Ali, A. and Dopita, M.A., 2019. IFU spectroscopy of southern PNe - VII. Photoionization modelling of intermediate excitation class objects. *MNRAS*, 484(3):3251.

Aller, L.H. and Czyzak, S.J., 1983. Chemical compositions of planetary nebulae. *ApJ*, 51:211.

Anderson, L.D., Bania, T.M., Balser, D.S., et al., 2011. The Green Bank Telescope H II Region Discovery Survey. II. The Source Catalog. *ApJ*, 194:32.

Astropy Collaboration, Robitaille, T.P., Tollerud, E.J., et al., 2013. Astropy: A community Python package for astronomy. *Astronomy and Astrophysics*, 558:A33.

Balick, B., 1987. The Evolution of Planetary Nebulae. I. Structures, Ionizations, and Morphological Sequences. *AJ*, 94:671.

Barría, D. and Kimeswenger, S., 2018. HST/WFPC2 imaging analysis and cloudy modelling of the multiple-shell planetary nebulae NGC 3242, NGC 6826, and NGC 7662. *MNRAS*, 480(2):1626.

Benjamin, R.A., Churchwell, E., Babler, B.L., et al., 2003. GLIMPSE. I. An SIRTF Legacy Project to Map the Inner Galaxy. *PASP*, 115(810):953.

Bensby, T. and Feltzing, S., 2006. The origin and chemical evolution of carbon in the Galactic thin and thick discs*. *Monthly Notices of the RAS*, 367:1181.

Black, J.H. and Dalgarno, A., 1976. Interstellar H2 - The population of excited rotational states and the infrared response to ultraviolet radiation. *The Astrophysical Journal*, 203:132.

Black, J.H. and van Dishoeck, E.F., 1987. Fluorescent excitation of interstellar H2. *ApJ*, 322:412.

Bloecker, T., 1995. Stellar evolution of low- and intermediate-mass stars. II. Post-AGB evolution. *A&A*, 299:755.

Bohigas, J., 2008. Photoionization Models Applied to Planetary Nebulae. *ApJ*, 674(2):954.

Bohigas, J., Escalante, V., Rodríguez, M., et al., 2015. Echelle spectroscopy and photoionization modelling of the entire planetary nebula NGC 6210. *MNRAS*, 447(1):817.

Bowen, I.S., 1928. The origin of the nebular lines and the structure of the planetary nebulae. *ApJ*, 67:1.

Burton, M.G., 1987. *The shock excitation of molecular hydrogen in the interstellar medium.* Ph.D. thesis, University of Edinburgh.

Burton, M.G., Hollenbach, D.J., and Tielens, A.G.G., 1992. Mid-infrared rotational line emission from interstellar molecular hydrogen. *ApJ*, 399:563.

Burton, M.G., Hollenbach, D.J., and Tielens, A.G.G.M., 1990. Line Emission from Clumpy Photodissociation Regions. *ApJ*, 365:620.

Cahn, J.H. and Kaler, J.B., 1971. The Distances and Distribution of Planetary Nebulae. *ApJ*, 22:319.

Cardelli, J.A., Clayton, G.C., and Mathis, J.S., 1989. The Relationship between Infrared, Optical, and Ultraviolet Extinction. *ApJ*, 345:245.

Carey, S.J., Noriega-Crespo, A., Mizuno, D.R., et al., 2009. MIPSGAL: A Survey of the Inner Galactic Plane at 24 and 70 μm. *PASP*, 121(875):76.

Casali, M., Adamson, A., Alves de Oliveira, C., et al., 2007. The UKIRT wide-field camera. *A&A*, 467(2):777.

Casali, M.M. and Eiroa, C., 1996. The photospheres of embedded young stellar objects. *A&A*, 306:427.

Cassinelli, J.P., 1979. Stellar winds. *Annual Review of Astronomy and Astrophysics*, 17:275.

Cazaux, S. and Tielens, A.G.G.M., 2002. Molecular Hydrogen Formation in the Interstellar Medium. *ApJ*, 575(1):L29.

Cazaux, S. and Tielens, A.G.G.M., 2004. H_2 Formation on Grain Surfaces. *ApJ*, 604(1):222.

Chambers, K.C., Magnier, E.A., Metcalfe, N., et al., 2016. The Pan-STARRS1 Surveys. *arXiv e-prints*, arXiv:1612.05560.

Cohen, M., Parker, Q.A., Green, A.J., et al., 2011. Multiwavelength diagnostic properties of Galactic planetary nebulae detected by the GLIMPSE-I. *Monthly Notices of the RAS*, 413:514.

Cohen, M., Tielens, A.G.G.M., Bregman, J., et al., 1989. The Infrared Emission Bands. III. Southern IRAS Sources. *ApJ*, 341:246.

Condon, J.J. and Kaplan, D.L., 1998. Planetary Nebulae in the NRAO VLA Sky Survey. *ApJ*, 117(2):361.

Currie, M.J., Berry, D.S., Jenness, T., et al., 2014. Starlink Software in 2013. In N. Manset and P. Forshay, editors, *Astronomical Data Analysis Software and Systems XXIII*, volume 485 of *Astronomical Society of the Pacific Conference Series*, page 391.

Davis, C.J., Smith, M.D., Stern, L., et al., 2003. Near-infrared spectroscopy of (proto)-planetary nebulae: molecular hydrogen excitation as an evolutionary tracer. *MNRAS*, 344:262.

De Marco, O., 2009. The Origin and Shaping of Planetary Nebulae: Putting the Binary Hypothesis to the Test. *Publications of the Astronomical Society of the Pacific*, 121:316.

Drew, J.E., Greimel, R., Irwin, M.J., et al., 2005. The INT Photometric Hα Survey of the Northern Galactic Plane (IPHAS). *Monthly Notices of the RAS*, 362:753.

Ellsworth-Bowers, T.P., Rosolowsky, E., Glenn, J., et al., 2015. The Bolocam Galactic Plane Survey. XII. Distance Catalog Expansion Using Kinematic Isolation of Dense Molecular Cloud Structures with ^{13}CO(1-0). *ApJ*, 799(1):29.

Ercolano, B., Barlow, M.J., Storey, P.J., et al., 2003. MOCASSIN: a fully three-dimensional Monte Carlo photoionization code. *MNRAS*, 340(4):1136.

Evans, A., 1994. *The dusty universe*.

Fang, X., Guerrero, M.A., Miranda, L.F., et al., 2015. Hu 1-2: a metal-poor bipolar planetary nebula with fast collimated outflows. *MNRAS*, 452(3):2445.

Fang, X., Zhang, Y., Kwok, S., et al., 2018. Extended Structures of Planetary Nebulae Detected in H_2 Emission. *ApJ*, 859(2):92.

Fazio, G.G., Hora, J.L., Allen, L.E., et al., 2004. The Infrared Array Camera (IRAC) for the Spitzer Space Telescope. *ApJ*, 154(1):10.

Ferland, G.J., Chatzikos, M., Guzmán, F., et al., 2017. The 2017 Release Cloudy. *RMxAA*, 53:385.

Frank, A., Balick, B., Icke, V., et al., 1993. Astrophysical Gasdynamics Confronts Reality: The Shaping of Planetary Nebuale. *ApJ*, 404:L25.

Frew, D.J., 2008. *Planetary Nebulae in the Solar Neighbourhood: Statistics, Distance Scale and Luminosity Function*. Ph.D. thesis, Department of Physics, Macquarie University, NSW 2109, Australia.

Frew, D.J., Bojičić, I.S., and Parker, Q.A., 2013. A catalogue of integrated Hα fluxes for 1258 Galactic planetary nebulae. *MNRAS*, 431(1):2.

Frew, D.J. and Parker, Q.A., 2010. Planetary Nebulae: Observational Properties, Mimics and Diagnostics. *Publications of the Astron. Soc. of Australia*, 27:129.

Frew, D.J., Parker, Q.A., and Bojičić, I.S., 2016. The Hα surface brightness-radius relation: a robust statistical distance indicator for planetary nebulae. *MNRAS*, 455(2):1459.

Froebrich, D., Davis, C.J., Ioannidis, G., et al., 2011. UWISH2 - the UKIRT Widefield Infrared Survey for H$_2$. *Monthly Notices of the RAS*, 413:480.

Froebrich, D., Makin, S.V., Davis, C.J., et al., 2015. Extended H$_2$ emission line sources from UWISH2. *Monthly Notices of the RAS*, 454:2586.

Gaia Collaboration, Brown, A.G.A., Vallenari, A., et al., 2018. Gaia Data Release 2. Summary of the contents and survey properties. *A&A*, 616:A1.

García-Hernández, D.A., Manchado, A., García-Lario, P., et al., 2002. Near-IR spectroscopy of planetary nebulae precursors. *A&A*, 387:955.

Garcia Lario, P., Manchado, A., Riera, A., et al., 1991. IRAS 22568+6141 : a new bipolar planetary nebula. *A&A*, 249:223.

García-Segura, G., Langer, N., Różyczka, M., et al., 1999. Shaping Bipolar and Elliptical Planetary Nebulae: Effects of Stellar Rotation, Photoionization Heating, and Magnetic Fields. *Astrophysical Journal*, 517:767.

Gillett, F.C., Low, F.J., and Stein, W.A., 1967. Infrared Observations of the Planetary Nebula NGC 7027. *ApJ*, 149:L97.

Gledhill, T.M. and Forde, K.P., 2015. Imaging the transition between pre-planetary and planetary nebulae: integral field spectroscopy of hot post-AGB stars with NIFS. *Monthly Notices of the RAS*, 447:1080.

Gledhill, T.M., Froebrich, D., Campbell-White, J., et al., 2018. Planetary nebulae in the UWISH2 survey. *MNRAS*, 479(3):3759.

Gómez, J.F., Niccolini, G., Suárez, O., et al., 2018. ALMA imaging of the nascent planetary nebula IRAS 15103-5754. *MNRAS*, 480(4):4991.

Groot, P.J., Verbeek, K., Greimel, R., et al., 2009. The UV-Excess survey of the northern Galactic plane. *MNRAS*, 399(1):323.

Guerrero, M.A., Toalá, J.A., Medina, J.J., et al., 2013. Unveiling shocks in planetary nebulae. *A&A*, 557:A121.

Guerrero, M.A., Villaver, E., Manchado, A., et al., 2000. H_2 and Brγ Narrowband Imaging of Bipolar Planetary Nebulae. *ApJ*, 127:125.

Hastings, W., 1970. Monte Carlo Sampling Methods using Markov Chains and their Applications. *Biometrika*, 57(1):97.

Herwig, F., 2005. Evolution of Asymptotic Giant Branch Stars. *Annual Review of Astronomy and Astrophysics*, 43(1):435.

Hoare, M.G., Purcell, C.R., Churchwell, E.B., et al., 2012. The Coordinated Radio and Infrared Survey for High-Mass Star Formation (The CORNISH Survey). I. Survey Design. *PASP*, 124(919):939.

Hoffmeister, V.H., Chini, R., Scheyda, C.M., et al., 2006. 2.3 μm CO emission and absorption from young high-mass stars in M 17. *Astronomy and Astrophysics*, 457:L29.

Hollenbach, D. and Natta, A., 1995. Time-Dependent Photodissociation Regions. *ApJ*, 455:133.

Hollenbach, D.J. and Shull, J.M., 1977. Vibrationally excited molecular hydrogen in Orion. *ApJ*, 216:419.

Hora, J.L., Latter, W.B., and Deutsch, L.K., 1999. Investigating the Near-Infrared Properties of Planetary Nebulae. II. Medium-Resolution Spectra. *ApJ*, 124:195.

Hubble, E.P., 1922. The source of luminosity in galactic nebulae. *ApJ*, 56:400.

Iben, Jr., I., 1995. Planetary nebulae and their central stars - origin and evolution. *Physics Reports*, 250:2.

Ingallinera, A., Trigilio, C., Umana, G., et al., 2014a. A radio characterization of Galactic compact bubbles. *MNRAS*, 437(4):3626.

Ingallinera, A., Trigilio, C., Umana, G., et al., 2014b. Study of the extended radio emission of two supernova remnants and four planetary nebulae associated with MIPSGAL bubbles. *MNRAS*, 445(4):4507.

Isella, A., Guidi, G., Testi, L., et al., 2016. Ringed structures of the hd 163296 protoplanetary disk revealed by alma. *Phys. Rev. Lett.*, 117:251101.

Ishihara, D., Kaneda, H., Onaka, T., et al., 2011. Galactic distributions of carbon- and oxygen-rich AGB stars revealed by the AKARI mid-infrared all-sky survey. *A&A*, 534:A79.

Jacob, R., Schönberner, D., and Steffen, M., 2013. The evolution of planetary nebulae. VIII. True expansion rates and visibility times. *A&A*, 558:A78.

Jones, A.M., Gledhill, T.M., Froebrich, D., et al., 2018. The excitation mechanisms and evolutionary stages of UWISH2 planetary nebula candidates. *MNRAS*, 480(2):1563.

Jones, E., Oliphant, T., Peterson, P., et al., 2001. SciPy: Open source scientific tools for Python.

Kaler, J.B., 1983. The evolution of large planetary nebulae and their central stars. (NB : PK 13+2 1=131+2 1, 214+14 1=217+14 1). *ApJ*, 271:188.

Karakas, A.I. and Lugaro, M., 2016. Stellar Yields from Metal-rich Asymptotic Giant Branch Models. *ApJ*, 825(1):26.

Kastner, J.H., Gatley, I., Merrill, K.M., et al., 1994. The Bipolar Symmetry of Ring-like Planetary Nebulae: Molecular Hydrogen Emission from Halos. *ApJ*, 421:600.

Kazarian, M.A., Parsamian, S., and Parrao, L., 1998. Spectrophotometry of five planetary nebulae. *Astrophysics*, 41(3):239.

Kerber, F. and Claeskens, J.F., 1997. Two planetary nebulae with tori of different development. *A&A*, 318:561.

Khromov, G.S., 1989. Planetary Nebulae. *Space Science Reviews*, 51(3-4):339.

Kingsburgh, R.L. and Barlow, M.J., 1994. Elemental abundances for a sample of southern galactic planetary nebulae. *MNRAS*, 271:257.

Kwok, S., 1982. From red giants to planetary nebulae. *Astrophysical Journal*, 258:280.

Kwok, S., 1993. Proto-planetary nebulae. *Annual Review of Astron and Astrophys*, 31:63.

Kwok, S., 2000. *The Origin and Evolution of Planetary Nebulae*.

Kwok, S., Purton, C.R., and Fitzgerald, P.M., 1978. On the origin of planetary nebulae. *Astrophysical Journal, Letters*, 219:L125.

Kwok, S., Zhang, Y., Koning, N., et al., 2008. Planetary Nebulae Detected in the Spitzer Space Telescope GLIMPSE Legacy Survey. *ApJ*, 174(2):426.

Lancon, A. and Rocca-Volmerange, B., 1992. A library of near-IR stellar spectra from 1.328 to 2.5 microns. *Astronomy and Astrophysics, Supplement*, 96:593.

Lawrence, A., Warren, S.J., Almaini, O., et al., 2007. The UKIRT Infrared Deep Sky Survey (UKIDSS). *MNRAS*, 379(4):1599.

Likkel, L., Dinerstein, H.L., Lester, D.F., et al., 2006. A Spectrophotometric Survey of K-Band Emission Lines in Planetary Nebulae. *AJ*, 131:1515.

Lucas, P.W., Hoare, M.G., Longmore, A., et al., 2008. The UKIDSS Galactic Plane Survey. *MNRAS*, 391(1):136.

Lucy, L.B., 1974. An iterative technique for the rectification of observed distributions. *AJ*, 79:745.

Luhman, K.L. and Rieke, G.H., 1996. High-Resolution Near-Infrared Spectroscopy of Hubble 12. *ApJ*, 461:298.

Lumsden, S.L., Puxley, P.J., and Hoare, M.G., 2001. Near-infrared spectra of compact planetary nebulae. *MNRAS*, 328:419.

Luridiana, V., Morisset, C., and Shaw, R.A., 2015. PyNeb: a new tool for analyzing emission lines. I. Code description and validation of results. *A&A*, 573:A42.

Magrini, L., Perinotto, M., Corradi, R.L.M., et al., 2003. Spectroscopy of planetary nebulae in M 33. *A&A*, 400:511.

Manchado, A., Guerrero, M.A., Stanghellini, L., et al., 1996. *The IAC morphological catalog of northern Galactic planetary nebulae*.

Manchado, A., Manchado, A., Barreto, M., et al., 2003. LIRIS (Long-slit Intermediate Resolution Infrared Spectrograph) Project status. In J.M. Rodriguez Espinoza, F. Garzon Lopez, and V. Melo Martin, editors, *Revista Mexicana de Astronomia y Astrofisica Conference Series*, volume 16, pages 43–45.

Manchado, A., Stanghellini, L., Villaver, E., et al., 2015. High-resolution Imaging of NGC 2346 with GSAOI/GeMS: Disentangling the Planetary Nebula Molecular Structure to Understand Its Origin and Evolution. *ApJ*, 808(2):115.

Marquez-Lugo, R.A., Guerrero, M.A., Ramos-Larios, G., et al., 2015. The excitation mechanism of H_2 in bipolar planetary nebulae. *MNRAS*, 453:1888.

Marquez-Lugo, R.A., Ramos-Larios, G., Guerrero, M.A., et al., 2013. On the relationship between the H_2 emission and the physical structure of planetary nebulae. *MNRAS*, 429(2):973.

Matsuura, M., Speck, A.K., McHunu, B.M., et al., 2009. A "Firework" of H_2 Knots in the Planetary Nebula NGC 7293 (The Helix Nebula). *ApJ*, 700(2):1067.

Matsuura, M., Speck, A.K., Smith, M.D., et al., 2007. VLT/near-infrared integral field spectrometer observations of molecular hydrogen lines in the knots of the planetary nebula NGC 7293 (the Helix Nebula). *MNRAS*, 382(4):1447.

Meixner, M., McCullough, P., Hartman, J., et al., 2005. The Multitude of Molecular Hydrogen Knots in the Helix Nebula. *AJ*, 130(4):1784.

Mellema, G. and Frank, A., 1995. Radiation gasdynamics of planetary nebulae - V. Hot bubble and slow wind dynamics. *MNRAS*, 273(2):401.

Mendez, R.H., 1991. Photospheric Abundances in Central Stars of Planetary Nebulae, and Evolutionary Implications. In G. Michaud and A.V. Tutukov, editors, *Evolution of Stars: the Photospheric Abundance Connection*, volume 145 of *IAU Symposium*, page 375.

Menzel, D.H., 1926. The Planetary Nebulae. *PASP*, 38(225):295.

Messier, C., 1781. Catalogue des Nébuleuses et des Amas d'Étoiles (Catalog of Nebulae and Star Clusters). Connoissance des Temps ou des Mouvements Célestes.

Metropolis, N., Rosenbluth, A.W., Rosenbluth, M.N., et al., 1953. Equation of State Calculations by Fast Computing Machines. *J. Chem. Phys*, 21(6):1087.

Miller Bertolami, M.M., 2016. New models for the evolution of post-asymptotic giant branch stars and central stars of planetary nebulae. *A&A*, 588:A25.

Milne, D.K. and Aller, L.H., 1982. Radio observations at 14.7 GHZ of southern planetary nebulae. *A&A Supp.*, 50:209.

Miszalski, B., Parker, Q.A., Acker, A., et al., 2008. MASH-II: more planetary nebulae from the AAO/UKST Hα survey. *MNRAS*, 384(2):525.

Mizuno, D.R., Kraemer, K.E., Flagey, N., et al., 2010. A Catalog of MIPSGAL Disk and Ring Sources. *AJ*, 139(4):1542.

Mora, A., Merín, B., Solano, E., et al., 2001. EXPORT: Spectral classification and projected rotational velocities of Vega-type and pre-main sequence stars. *Astronomy and Astrophysics*, 378:116.

Morisset, C., 2013. pyCloudy: Tools to manage astronomical Cloudy photoionization code.

Mullin, L.M. and Hardcastle, M.J., 2009. Bayesian inference of jet bulk-flow speeds in Fanaroff-Riley type II radio sources. *MNRAS*, 398(4):1989.

Murakami, H., Baba, H., Barthel, P., et al., 2007. The Infrared Astronomical Mission AKARI*. *PASJ*, 59:S369.

Natta, A. and Hollenbach, D., 1998. The evolution of the neutral gas in planetary nebulae: theoretical models. *A&A*, 337:517.

Neugebauer, G., Habing, H.J., van Duinen, R., et al., 1984. The Infrared Astronomical Satellite (IRAS) mission. *ApJ*, 278:L1.

Ney, E.P., Merrill, K.M., Becklin, E.E., et al., 1975. Studies of the infrared source CRL 2688. *ApJ*, 198:L129.

Nordhaus, J., Blackman, E.G., and Frank, A., 2007. Isolated versus common envelope dynamos in planetary nebula progenitors. *Monthly Notices of the RAS*, 376:599.

Novikov, I.D. and Smith, M.D., 2018. Numerical simulations of wind-driven protoplanetary nebulae - I. near-infrared emission. *MNRAS*, 480(1):75.

O'Dell, C.R., Sabbadin, F., and Henney, W.J., 2007. The Three-Dimensional Ionization Structure and Evolution of NGC 6720, The Ring Nebula. *AJ*, 134(4):1679.

Osterbrock, D.E. and Ferland, G.J., 2006. *Astrophysics of gaseous nebulae and active galactic nuclei*.

Otsuka, M., Kemper, F., Cami, J., et al., 2014. Physical properties of fullerene-containing Galactic planetary nebulae. *MNRAS*, 437(3):2577.

Otsuka, M., Ueta, T., van Hoof, P.A.M., et al., 2017. The Herschel Planetary Nebula Survey (HerPlaNS): A Comprehensive Dusty Photoionization Model of NGC6781. *ApJ*, 231(2):22.

Öttl, S., Kimeswenger, S., and Zijlstra, A.A., 2014. Ionization structure of multiple-shell planetary nebulae. I. NGC 2438. *A&A*, 565:A87.

Paczyński, B., 1970. Evolution of Single Stars. I. Stellar Evolution from Main Sequence to White Dwarf or Carbon Ignition. *Acta Astronomica*, 20:47.

Parker, Q.A., Acker, A., Frew, D.J., et al., 2006. The Macquarie/AAO/Strasbourg Hα Planetary Nebula Catalogue: MASH. *Monthly Notices of the RAS*, 373:79.

Parker, Q.A., Bojičić, I.S., and Frew, D.J., 2016. HASH: the Hong Kong/AAO/Strasbourg Hα planetary nebula database. In *Journal of Physics Conference Series*, volume 728 of *Journal of Physics Conference Series*, page 032008.

Parker, Q.A., Cohen, M., Stupar, M., et al., 2012. Discovery of planetary nebulae using predictive mid-infrared diagnostics. *Monthly Notices of the RAS*, 427:3016.

Parker, Q.A., Phillipps, S., Pierce, M.J., et al., 2005. The AAO/UKST SuperCOSMOS Hα survey. *Monthly Notices of the RAS*, 362:689.

Pazderska, B.M., Gawroński, M.P., Feiler, R., et al., 2009. Survey of planetary nebulae at 30 GHz with OCRA-p. *A&A*, 498(2):463.

Peimbert, M., Peimbert, A., and Delgado-Inglada, G., 2017. Nebular Spectroscopy: A Guide on Hii Regions and Planetary Nebulae. *PASP*, 129(978):082001.

Perek, L. and Kohoutek, L., 1967. *Catalogue of Galactic Planetary Nebulae*.

Perinotto, M., Schönberner, D., Steffen, M., et al., 2004. The evolution of planetary nebulae. I. A radiation-hydrodynamics parameter study. *A&A*, 414:993.

Phillips, J.P., 2003. The relation between Zanstra temperature and morphology in planetary nebulae. *MNRAS*, 344(2):501.

Phillips, J.P., 2004. Planetary nebula distances re-examined: an improved statistical scale. *MNRAS*, 353(2):589.

Phillips, J.P. and Marquez-Lugo, R.A., 2011a. Mid- and Far-Infrared Photometry of Galactic Planetary Nebulae with the AKARI All-Sky Survey. *RMxAA*, 47:83.

Phillips, J.P. and Marquez-Lugo, R.A., 2011b. MIPSGAL 24 μm observations of Galactic planetary nebulae. *MNRAS*, 410(4):2257.

Phillips, J.P. and Ramos-Larios, G., 2008. Mid-infrared imaging of 18 planetary nebulae using the Spitzer Space Telescope. *MNRAS*, 383(3):1029.

Piliugin, L.S. and Khromov, G.S., 1979. Evolution of planetary nebulae : the temperature of their central stars. *SOVAST*, 23:425.

Pottasch, S.R., 1984. *Planetary nebulae. A study of late stages of stellar evolution*, volume 107.

Priestley, F.D. and Barlow, M.J., 2018. OH$^+$ emission from cometary knots in planetary nebulae. *MNRAS*, 478(2):1502.

Proxauf, B., Öttl, S., and Kimeswenger, S., 2014. Upgrading electron temperature and electron density diagnostic diagrams of forbidden line emission. *A&A*, 561:A10.

Puspitaningrum, E. and Malasan, H.L., 2019. Photoionization modelling of the Wolf-Rayet planetary nebulae IC 4663 based on multiwavelength observations. In *Journal of Physics Conference Series*, volume 1231 of *Journal of Physics Conference Series*, page 012031.

Ramos-Larios, G., Guerrero, M.A., Sabin, L., et al., 2017. Pushing the limits: detecting H$_2$ emission from faint bipolar planetary nebulae in the IPHAS sample. *MNRAS*, 470:3707.

Rauch, T., 2003. A grid of synthetic ionizing spectra for very hot compact stars from NLTE model atmospheres. *A&A*, 403:709.

Rayner, J.T., Cushing, M.C., and Vacca, W.D., 2009. The Infrared Telescope Facility (IRTF) Spectral Library: Cool Stars. *ApJ*, 185(2):289.

Reich, W., Fuerst, E., Haslam, C.G.T., et al., 1984. A radio continuum survey of the galactic plane at 11cm wavelength. I. *A&A Supp.*, 58:197.

Reipurth, B. and Aspin, C., 1997. Infrared Spectroscopy of Herbig-Haro Energy Sources. *AJ*, 114:2700.

Richardson, W.H., 1972. Bayesian-based iterative method of image restoration∗. *J. Opt. Soc. Am.*, 62(1):55.

Rieke, G.H., Young, E.T., Engelbracht, C.W., et al., 2004. The Multiband Imaging Photometer for Spitzer (MIPS). *ApJ*, 154(1):25.

Robitaille, T.P., Meade, M.R., Babler, B.L., et al., 2008. Intrinsically Red Sources Observed by Spitzer in the Galactic Midplane. *AJ*, 136(6):2413.

Rubin, R.H., 1970. Radio observations of planetary nebulae and possible planetary nebulae. *A&A*, 8:171.

Ruffle, P.M.E., Zijlstra, A.A., Walsh, J.R., et al., 2004. Angular diameters, fluxes and extinction of compact planetary nebulae: further evidence for steeper extinction towards the bulge. *MNRAS*, 353(3):796.

Sabin, L., Parker, Q.A., Corradi, R.L.M., et al., 2014. First release of the IPHAS catalogue of new extended planetary nebulae. *Monthly Notices of the RAS*, 443:3388.

Sahai, R., 2020. Observing planetary and pre-planetary nebulae with the james webb space telescope. *Galaxies*, 8(61).

Schmidt-Voigt, M. and Koeppen, J., 1987a. Influence of stellar evolution on the evolution of planetary nebulae. I - Numerical method and hydrodynamical structures. *A&A*, 174:211.

Schmidt-Voigt, M. and Koeppen, J., 1987b. Influence of stellar evolution on the evolution of planetary nebulae. II. Confrontation of models with observations. *A&A*, 174:223.

Schoenberner, D., 1983. Late stages of stellar evolution. II. Mass loss and the transition ofasymptotic giant branch stars into hot remnants. *ApJ*, 272:708.

Schönberner, D., 2016. The dynamical evolution of planetary nebulae. In *Journal of Physics Conference Series*, volume 728 of *Journal of Physics Conference Series*, page 032001.

Schönberner, D., Jacob, R., and Steffen, M., 2005a. The evolution of planetary nebulae. III. Internal kinematics and expansion parallaxes. *A&A*, 441(2):573.

Schönberner, D., Jacob, R., Steffen, M., et al., 2005b. The evolution of planetary nebulae. II. Circumstellar environment and expansion properties. *A&A*, 431(3):963.

Shaw, G., Ferland, G.J., Abel, N.P., et al., 2005. Molecular Hydrogen in Star-forming Regions: Implementation of its Microphysics in CLOUDY. *ApJ*, 624(2):794.

Shklovsky, I.S., 1956. The nature of planetary nebulae and their nuclei. *Astronomicheskii Zhurnal*, 33:315.

Skrutskie, M.F., Cutri, R.M., Stiening, R., et al., 2006. The Two Micron All Sky Survey (2MASS). *AJ*, 131(2):1163.

Soker, N., 2006. Why Magnetic Fields Cannot Be the Main Agent Shaping Planetary Nebulae. *Publications of the ASP*, 118:260.

Speck, A.K., Meixner, M., Jacoby, G.H., et al., 2003. Molecular Hydrogen in the Ring Nebula: Clumpy Photodissociation Regions. *PASP*, 115(804):170.

Stanghellini, L., Corradi, R.L.M., and Schwarz, H.E., 1993. The correlations between planetary nebula morphology and central star evolution. *A&A*, 279:521.

Stanghellini, L., Villaver, E., Manchado, A., et al., 2002. The Correlations between Planetary Nebula Morphology and Central Star Evolution: Analysis of the Northern Galactic Sample. *ApJ*, 576(1):285.

Stasińska, G. and Tylenda, R., 1986. Intermediate mass stars undergoing a very hot phase : can we measure their temperatures ? *A&A*, 155:137.

Steffen, M., Szczerba, R., and Schoenberner, D., 1998. Hydrodynamical models and synthetic spectra of circumstellar dust shells around AGB stars. II. Time-dependent simulations. *A&A*, 337:149.

Stenholm, B. and Acker, A., 1987. Spectroscopic observations of faint and misclassified planetary nebulae. *A&A Supp.*, 68:51.

Sternberg, A. and Dalgarno, A., 1989. The infrared response of molecular hydrogen gas to ultraviolet radiation - High-density regions. *Astrophysical Journal*, 338:197.

Strömgren, B., 1939. The Physical State of Interstellar Hydrogen. *ApJ*, 89:526.

Sutherland, R., Dopita, M., Binette, L., et al., 2018. MAPPINGS V: Astrophysical plasma modeling code.

Tody, D., 1993. IRAF in the Nineties. In R.J. Hanisch, R.J.V. Brissenden, and J. Barnes, editors, *Astronomical Data Analysis Software and Systems II*, volume 52 of *Astronomical Society of the Pacific Conference Series*, page 173.

Tokunaga, A.T., 2000. *Infrared Astronomy*, page 143.

Treffers, R.R., Fink, U., Larson, H.P., et al., 1976. The spectrum of the planetary nebula NGC 7027 from 0.9 to 2.7 microns. *Astrophysical Journal*, 209:793.

Urquhart, J.S., Hoare, M.G., Purcell, C.R., et al., 2009. The RMS survey. 6 cm continuum VLA observations towards candidate massive YSOs in the northern hemisphere. *A&A*, 501:539.

van Hoof, P.A.M., van de Steene, G.C., Barlow, M.J., et al., 2010. Herschel images of NGC 6720: H_2 formation on dust grains. *A&A*, 518:L137.

van Winckel, H., 2003. Post-AGB Stars. *Annual Review of Astronomy and Astrophysics*, 41:391.

Vejar, G., Montez, Rodolfo, J., Morris, M., et al., 2019. Planetary Nebulae and How to Find Them: Color Identification in Big Broadband Surveys. *ApJ*, 879(1):38.

Volk, K. and Kwok, S., 1985. Dynamical evolution of planetary nebulae. *A&A*, 153:79.

Wallace, L. and Hinkle, K., 1997. Medium-Resolution Spectra of Normal Stars in the K Band. *Astrophysical Journal, Supplement*, 111:445.

Waters, C.Z., Magnier, E.A., Price, P.A., et al., 2016. Pan-STARRS Pixel Processing: Detrending, Warping, Stacking. *arXiv e-prints*, arXiv:1612.05245.

Wenger, M., Ochsenbein, F., Egret, D., et al., 2000. The SIMBAD astronomical database. The CDS reference database for astronomical objects. *Astronomy and Astrophysics, Supplement*, 143:9.

Woolf, N.J. and Ney, E.P., 1969. Circumstellar Infrared Emission from Cool Stars. *Astrophysical Journal, Letters*, 155:L181.

Wright, E.L., Eisenhardt, P.R.M., Mainzer, A.K., et al., 2010. The Wide-field Infrared Survey Explorer (WISE): Mission Description and Initial On-orbit Performance. *AJ*, 140(6):1868.

Zanstra, H., 1927. An Application of the Quantum Theory to the Luminosity of Diffuse Nebulae. *ApJ*, 65:50.

Zhang, C.Y., 1995. A Statistical Distance Scale for Galactic Planetary Nebulae. *ApJ*, 98:659.

Zijlstra, A.A., 2015. Planetary nebulae in 2014: A review of research. *Revista Mexicana de Astronomia y Astrofisica*, 51:221.

Zuckerman, B. and Gatley, I., 1988. Molecular Hydrogen Maps of Extended Planetary Nebulae: The Dumbell, the Ring, and NGC 2346. *ApJ*, 324:501.